

THE UNIVERSITY
of EDINBURGH

This thesis has been submitted in fulfilment of the requirements for a postgraduate degree (e.g. PhD, MPhil, DClinPsychol) at the University of Edinburgh. Please note the following terms and conditions of use:

This work is protected by copyright and other intellectual property rights, which are retained by the thesis author, unless otherwise stated.
A copy can be downloaded for personal non-commercial research or study, without prior permission or charge.
This thesis cannot be reproduced or quoted extensively from without first obtaining permission in writing from the author.
The content must not be changed in any way or sold commercially in any format or medium without the formal permission of the author.
When referring to this work, full bibliographic details including the author, title, awarding institution and date of the thesis must be given.

Photochemistry on Mars: Preparing for Data from the ExoMars Trace Gas Orbiter

Benjamin M. Taysum



Doctor of Philosophy

THE UNIVERSITY OF EDINBURGH

2021

Abstract

Our understanding of methane on Mars is insufficient to explain the spatial and temporal variability it has been reported to experience, and the 2021 detections of atmospheric hydrogen chloride (HCl) do not, as of yet, have an explanation. A comprehensive photochemistry scheme is required to study the processes operating within Mars' atmosphere, and to aid in reconciling modelling results with observations. To address these gaps in scientific understanding, I have developed a 1-D atmospheric photochemistry model to describe methane (CH_4), ethane (C_2H_6), their resulting oxidation products, and chlorine-containing trace gases in the Martian atmosphere. CH_4 and C_2H_6 are often emitted together in terrestrial surface releases. I report the first detailed study of the evolution of C_2H_6 in Martian conditions, and investigate the corresponding photochemical footprints of CH_4 and C_2H_6. Using my model I have identified that formaldehyde and formic acid are common oxidation products of CH_4 and C_2H_6, while acetaldehyde (CH_3CHO) and acetic acid (CH_3COOH) are unique oxidation products of C_2H_6. I also find that CH_3CHO photolysis can lead to CH_4 production at the surface.

Drawing on concepts pioneered in the Earth sciences, I developed the first Tangent Linear and Adjoint model for Martian atmospheric photochemistry, which enables the study of the sensitivity of atmospheric chemistry measurements to changes in precursor gases. I use this to assess the sensitivity of O_3 and H_2O_2 model columns to the models initial abundances of inorganic trace gas species, finding strong sensitivities of H_2O_2 to CO and H_2O vapour abundances. O_3 demonstrates strong and seasonally variable negative sensitivities to H_2O vapour and O_2, and strong positive sensitivities to H_2O ice in the polar winters.

Using aerosol and H_2O profiles from the ExoMars Trace Gas Orbiter, I built a simple heterogeneous chemistry scheme for chlorine chemistry to explain the HCl profiles measured in early 2021. Using uptake coefficients used for Earth stratosphere models, the routine can produce HCl at the required abundances and shape, but a more rigorous scheme will be required for future work.

Lay Summary

I extracted and developed the 1-D photochemistry submodule from the 3-D LMD-OU Mars General Circulation Model (MGCM) to help interpret data from the ExoMars Trace Gas Orbiter (TGO) which began collecting scientific observations in April 2018. I incorporated a chemical scheme to describe the oxidation of methane (CH_4), ethane (C_2H_6), and chlorine-containing gases in the atmosphere of Mars from the surface to 70 km.

Methane has been sporadically observed on Mars over the past 20 years by numerous ground-based telescopes, orbiters, and by instruments on the Curiosity Rover, but to explain observed variations of Martian CH_4 chemical models require a physical or chemical destruction mechanism 600 times larger than supported by current knowledge. On Earth, CH_4 has strong ties to biological processes and is often coupled with releases of C_2H_6 from surface sources. I use the 1-D photochemical model to assess the atmospheric lifetimes of CH_4 and C_2H_6, and to identify unique organic products from C_2H_6 that can be used to help identify types of organic surface releases.

I have also developed the first photochemical Tangent Linear and Adjoint model for a non-Earth atmosphere and use it to demonstrate the sensitivity of Mars' atmospheric hydrogen peroxide (H_2O_2) and ozone (O_3) columns to the 1-D models initial chemical abundances. The adjoint can also be used in future work to assess the necessary changes to the initial conditions of the 1-D model to improve the agreement between the model output of a desired gas and the observational measurements of it. I demonstrate the accuracy and flexibility of my adjoint model and show how it will be a beneficial tool for future assimilation of data from the ExoMars TGO.

I also use the 1-D photochemical model to study new hydrogen chloride (HCl) profiles observed by the Atmospheric Chemistry Suite (ACS) spectrometer aboard the TGO. These data represent the first confirmed sighting of any chlorine species in Mars' atmosphere. To interpret these data, I expanded the 1-D model to include the photochemistry of HCl and 12 other chlorine-containing gases and have developed a new gas-solid reaction (heterogeneous) scheme involving atmospheric dust grains and water ice crystals, based on laboratory data. I demonstrate that the reactions of OH and HO_2 molecules with dust in the atmosphere, releasing a Cl or ClO molecule in the process, and the loss of gas-phase HCl onto water ice crystals reproduces the observations of HCl made by the ACS well. I also find that abundances of HCl between 0.1—10 parts per billion (ppb), observed by the TGO instrumentation, can result in the chemical sink of CH_4 increasing in strength by a factor of 100—1700, highlighting

the importance of including a more detailed description of Mars' photochemistry in MGCMs. The introduction of chlorine chemistry into my model also results in better agreement with measurements of H_2O_2, but the release of chlorine from dust is currently too simplistic in the 1-D model be used for long-term studies.

Acknowledgements

I would first of all like to thank my supervisor Paul Palmer. You were a tremendous help throughout the entirety of the four years of my PhD, and I'm grateful to have had you for academic support. You helped raise my own confidence in my abilities in this field higher than first year me could have imagined, and helped me foster a genuine love for planetary science that I look forward to pursuing for years to come.

I want to also thank Séverine Robert, Ann Carine Vandaele, Justin Erwin, and the rest of the NOMAD team operating at the Royal Belgian Institute for Space Aeronomy for accommodating me on my three week visit back in February 2019. I had an amazing time working in the department and learning about the work you perform. The experience helped confirm my desire to pursue a career in planetary science after my PhD.

I would also like to thank Stephen Lewis and Manish Patel of the Open University for providing the initial model code for my project, extracted from the OU version of the LMD-GCM. You were both great helps for me during my first year too, answering questions regarding the model or Mars' atmosphere with great detail and clarity, making me feel like a welcome member of the scientific community from the start.

I owe a big debt to my fellow Crew members, especially Sam, Helen, Joffy, Matt, Spencer, James, and Alice. Without periodic coffee breaks downstairs and dumb conversations to lift me away from my desk every few hours, I may have gone insane. I honestly couldn't have asked for a more supportive group of friends during my PhD. I don't need to wish you all the best in your work when I'm gone, because I have no doubt you will all excel.

Thank you Stephen, for being the best personal hype-man anyone could ask for. Whenever I found myself dug deep in a mental trench, you would help pull me out of it in a seconds notice. You helped keep things in perspective at times when work was getting me down, and that helped more than I can say.

I'd like to take some sentences to thank my family too, for providing me with unparalleled support throughout these years. Mum and Dad, talking to you on the phone would make any work stress or fears dissipate as if by magic. Hannah, I hope your coming PhD experience will be as rewarding as I found mine, if not more.

Declaration

I declare that this thesis was composed by myself, that the work contained herein is my own except where explicitly stated otherwise in the text, and that this work has not been submitted for any other degree or professional qualification except as specified.

The research presented in Chapter 4 has been published, on 10/06/2020, in the Journal of Geophysical Research: Planets, entitled *Photochemistry of Methane and Ethane in the Martian Atmosphere* [Taysum and Palmer, 2020].

Benjamin M. Taysum

Contents

Abstract ii

Lay Summary iii

Acknowledgements v

Declaration vi

Figures and Tables x

1 Introduction 1

1.1 The Atmospheric Chemistry Suite . . . 10

1.2 Nadir and Occultation for Mars Discovery . . . 11

1.3 1-D Global Mean Models . . . 13

1.3.1 Time-Dependent 1-D Models . . . 15

1.4 Research Questions . . . 16

2 Martian Atmospheric Photochemistry 19

2.1 Inorganic Chemistry . . . 19

2.1.1 Carbon Dioxide . . . 22

2.1.2 Water Vapour and Hydrogen Chemistry . . . 26

2.1.3 Oxygen Chemistry . . . 31

2.2 Organic Chemistry . . . 37

2.2.1 Methane Observations . . . 37

2.2.2 Discrepancies between Observations and Modelling of Methane on Mars . . . 41

2.2.3 Organic Species as Biosignatures on Mars . . . 47

3 1-D Photochemistry Submodule 53

3.1 Tracer Transport . . . 54

3.2 Photochemistry . . . 54

3.2.1 Odd-Nitrogen Chemistry . . . 56

3.2.2 Gas-Phase Chemistry . . . 57

3.2.3 Heterogeneous Chemistry . . . 59

3.2.4 Semi-Implicit Backwards Euler Method . . . 60

3.2.5 HO_x and O_x Photochemical Equilibrium . . . 60

3.2.6 Photolysis . . . 65

3.2.7 Time-dependent meteorological boundary conditions 67

4 Photochemistry of Methane and Ethane in the Martian Atmosphere 68
4.1 Organic Photochemistry 70
4.2 Definition of Numerical Experiments 81
4.3 Results 82
4.3.1 Methane Oxidation in the Atmosphere of Mars 82
4.3.2 Production of Formaldehyde from CH_4 Oxidation 88
4.3.3 Production of Formic Acid from CH_4 Oxidation 92
4.3.4 Ethane Oxidation 94
4.3.5 Production of Formaldehyde and Formic Acid from C_2H_6 Oxidation . 98
4.3.6 Methane Production from the Oxidation of Acetaldehyde 98
4.4 Conclusion 100

5 Tangent Linear and Adjoint Model for Martian Photochemistry 103
5.1 Overview of Tangent Linear Models 103
5.2 General Derivation of the Tangent Linear Model 105
5.3 General Derivation of the Adjoint 108
5.4 Validation of the Tangent Linear Model 109
5.5 Sensitivity of H_2O_2 and O_3 to Inorganic Chemistry 116
5.6 Conclusion 121

6 Atmospheric Hydrogen Chloride on Mars 123
6.1 Search and Detection of Martian HCl 123
6.2 Chlorine Photochemistry Scheme 126
6.2.1 Heterogeneous Chlorine Chemistry 134
6.2.2 Surface Deposition of HCl 137
6.3 Chlorine Photochemistry from Heterogeneous Reactions 140
6.4 HCl from Heterogeneous Interactions 145
6.4.1 HCl Profile Comparisons 146
6.4.2 HCl Adjoint Sensitivities 151
6.4.3 Dust-Bound Chlorine Lifetime 158
6.4.4 HCl Atmospheric Lifetime with Ice Uptake 160
6.4.5 HCl Column Abundances 161
6.5 Heterogeneous Chlorine Impacts on H_2O_2 163
6.6 Heterogeneous Chlorine and Organic Chemistry 167
6.7 Conclusion 169

7 Conclusions and Future Work 172
7.1 Atmospheric Lifetimes of Organic Compounds 173

7.2 Model Improvements 174
7.3 Martian Photochemical Adjoint Sensitivity Analysis 176
7.4 Future Work 177
7.5 Summary 182

Appendices

A Appendix **183**
A.1 Equations Involved in the Tangent Linear Model 183
A.1.1 Linearised Vertical Transport 184
A.1.2 Linearised Photochemistry Equations 185

B Appendix **193**
B.1 ACS-MIR HCl and 1-D Model Comparisons 193

Bibliography **201**

Figures and Tables

Figures

1.1 Observations of the 2003 methane plume measured by the ground-based CSHELL/IRTF and NIRSPEC/Keck-2 spectroscopic telescopes and the geological structure of their locations on Mars. Approximately 19,000 tons of CH_4 gas are contained within them. Figure from Mumma et al. [2009]. 2

1.2 The ExoMars Trace Gas Orbiter and the locations of the ACS and NOMAD spectrometer suites. The positions of the other two instruments onboard, the Colour and Stereo Surface Imaging System (CaSSIS), and the Fine Resolution Epithermal Neutron Detector (FREND), are also shown. Taken from Medialab [2015]. 4

1.3 Schematic displaying the Solar Occultation method for atmospheric remote sensing. Below are two simulated transmittance spectras in the UV-Visible (Left) and the Infrared (Right) produced by the UV-Visible and Solar Occultation channels of the NOMAD instrument respectively. The two synthetic spectra are taken from Vandaele et al. [2015]. 6

1.4 Schematic highlighting Mars' location during its orbit around the Sun and the corresponding solar longitude, L_S (°). Aphelion, the point of Mars' furthest distance from the Sun, occurs at L_S 71°, and its perihelion, the point of closest approach, occurs at L_S 251°. Figure taken from P'al et al. [2019]. 8

1.5 The sensitivities of the NIR, MIR, and TIRVIM spectrometer channels of the ACS. From top to bottom: MIR lower detection limits of various trace gases; ASC-NIR and MIR sensitivities to various H_2O and HDO wavebands; ACS sensitivities to CO, CO_2, and O_2 with altitude. τ indicates atmospheric optical depth at measurement time. The fine dashed lines of the bottom plot indicate abundances predicted by the LMD GCM, extracted from the Mars Climate Database v5.2 [Millour et al., 2015]. Figure taken from Korablev et al. [2018]. 17

1.6 Detection limits for a number of trace gas species for the NOMAD spectrometer for three aerosol optical depth (AOD) cases: Solid lines: AOD = 0.0, dotted lines: AOD = 0.1, dash and dots: 1.0. A) CH_4 and two isotopologues; blue line indicates a VMR of 10 ppb, the maximum value observed by the MSL [Webster et al., 2015]. B) C_2H_2, C_2H_4, C_2H_6; black lines represent VMRs of 1 and 10 ppb. C) HCl, HCN, HCHO, OCS, H_2S, SO_2; black lines represent VMRs of 1 and 10 ppb. D) O_3; black lines represent results from the GEM-Mars model [Neary and Daerden, 2018]: solid: yearly average profile, dash and dots: maximum values at each altitude calculated by GEM-Mars. E) OH and HO_2. Pink (HO_2) and cyan (OH) lines are results of the GEM-Mars model. Solid: yearly average, dash and dots: maximum values at each altitude calculated by GEM-Mars. Figure taken from Vandaele and Rodriguez-Gomez [2013]. 18

2.1 Phase diagrams of a) H_2O and b) CO_2 with respect to atmospheric pressure and temperature. Conditions experienced in the atmosphere of Mars are highlighted in red. A typical Martian surface pressure is of magnitude 10^{-3} atm, and temperatures can reach lows of -150 °C during the polar nights, and highs of 20 °C at noon at the equator. 21

2.2 Condensation and sublimation of Mars' northern pole as seen by the Hubble Space Telescope . Figure taken from HST. 23

2.3 Seasonal variations in surface pressure measurements recorded by the Viking I and Viking II Lander produced by the condensation and sublimation of the CO_2 ice caps in the polar regions. Figure taken from Wood and Paige [1992]. 24

2.4 Seasonal variations in the water vapour column of Mars (in precipitable microns, pr. μm) as measured by the SPICAM spectrometer aboard the Mars Express orbiter over MY 27–31. Figure taken from Trokhimovskiy et al. [2015a]. 26

2.5 Results of the assimilation of TES measured water vapour columns over MY24 (a–e) and MY25 (f–h) displaying the zonally averaged vertical distribution of water vapour mass mixing ratios (g kg^{-1}) with latitude and their variances over one Mars year. White contours denote water ice mixing ratios with contour values [0.005, 0.01, 0.02, 0.03] g kg^{-1}; Black solid and dashed contours denote the mean meridional circulation in clockwise and anti-clockwise directions respectively, with contour values of [0.1, 0.5, 1.5] $\times 10^9$ kg s^{-1}. Figure taken from Steele et al. [2014]. 27

2.6 Vertical distribution profiles of H, OH, HO_2 and water vapour produced by the 1-D photochemistry model at 45° south at local noon. Left hand profiles are taken at aphelion, right hand profiles are taken at perihelion. 30

2.7 Inorganic reactions involved with molecular oxygen and the snapping of the O=O covalent bond. Green boxes: reaction returns O_2. Yellow boxes: reaction product maintains the O=O bond. Red boxes: O=O bond is severed in the reaction. Dashed line indicates that O_2 is the second product of the O_3 + OH reaction. 32
2.8 Column abundances of O_3 and H_2O vapour measured by the SPICAM spectrometer aboard the MEX as a function of solar longitude and planet latitude. O_3 column abundances are given in micron-atmospheres (μ-atm), and H_2O vapour abundances are given in precipitable microns (pr-μm). Figure taken directly from Lefèvre et al. [2021]. 34
2.9 Vertical distribution profiles of O_3 as measured by SPICAM aboard the MEX using the solar occultation remote sensing method and their variances with latitude and solar longitude. a) Latitude range 30–60° north, b) latitude range 0–30° north, c) latitude range 0–30° south, d) 30–60° south, and bottom plot contrasting these low-latitude distributions with the deep south latitude band 60–90° south. Figures taken directly from Lebonnois et al. [2006]. 36
2.10 Spatial distribution of CH_4 on Mars observed during the Martian northern hemisphere's summer (90–180°L_S) by a) the PFS aboard the MEX (figure taken from source [Geminale et al., 2011]) and b) the CSHELL ground-based spectrometer telescope (figure taken from Mumma et al. [2009]). 38
2.11 Figure extracted from Webster et al. [2018]. 40
2.12 Pressure and temperature stability plot of methane clathrate (thick solid curve) and water (thin solid lines), accompanied with three geothermal profiles of the Martian subsurface (dotted lines) of different surface material, and markers indicating depths in meters. Top: ice-cemented soil, middle: dry sandstone, bottom: loose soil. Figure extracted from Chastain and Chevrier [2007]. 44
2.13 Hypothesised sinks and sources of the atmospheric methane observed in the Martian atmosphere. Figure extracted from NASA [2018]. 46
2.14 Deuterium and carbon isotope delta-ratios of methane produced from terrestrial abiotic and biotic sources. Figure extracted from Etiope et al. [2013]. 49
2.15 Hypothesised sinks and sources of the atmospheric methane observed in the Martian atmosphere. Figure extracted from Etiope [2018]. 52

4.1 Primary stages of the CH_4 photochemistry that I use in my 1-D photochemistry model, taken from the CAABA/MECCA v4.0 chemical mechanism. 83
4.2 Photochemical loss factors (s^{-1}) CH_4 in my 1-D photochemistry model at latitude 2.5°N, local time 12:00, and solar longitudes 71° and 251° (Mars' aphelion and perihelion, respectively) as a function of altitude. 84

4.3 Local and vertically integrated photochemical lifetime of CH4 within the atmosphere of Mars and its variations with altitude (km) and solar longitude at latitudes 30° N, 2.5° N, and 30° S, respectively. All vertical segments are values from the 1-D photochemistry model at 12:00 LT. 86
4.4 Volume mixing ratio profiles of major photochemical products of 50 ppt of CH4 after one sol. These include formaldehyde (HCHO), formic acid (HCOOH), methanol (CH_3OH), methyl hydroperoxide (CH_3OOH), hydromethyl peroxy ($HOCH_2O_2$), and hydromethyl hydroperoxide ($HOCH_2OOH$) 87
4.5 Vertical profiles of HCHO (ppt) from the photochemistry of 50 ppt CH_4 within a zonal band centered on latitudes 30°N, 2.5°N, and 30°S, across all solar longitudes, as calculated by my 1-D photochemical model. 88
4.6 Photochemical production and loss rates for HCHO (molec $cm^{-3}s^{-1}$), associated with CH_4 photochemistry, as a function of altitude. Calculations are for L_S = 71°, 06:30 LT, and latitude 2.5°N. 90
4.7 Photochemical lifetime of HCHO within the atmosphere of Mars and its variations with altitude (km) and solar longitude at latitudes 30°N, 2.5 °N, and 30°S, respectively. All vertical segments are values from the 1-D photochemistry model at 12:00 LT. 91
4.8 As Figure 4.6 but for formic acid (HCOOH). 92
4.9 Photochemical lifetime of HCOOH and its variance with altitude and solar longitude as calculated by my 1-D photochemistry model. 93
4.10 Primary stages of the C_2H_6 photochemistry that I use in my 1-D photochemistry submodule, taken from the CAABA/MECCA v4.0 box model. 94
4.11 Photochemical loss factors for C_2H_6 as a function of altitude in my 1-D photochemistry model with altitude. Calculations are for L_S = 71° and 251°, 12:00 LT, at latitude 2.5°N. 95
4.12 Local and vertically integrated photochemical lifetime of C_2H_6 within the atmosphere of Mars and its variations with altitude (km) and solar longitude at latitudes 30°N, 2.5 °N, and 30°S, respectively. All vertical segments are values from the 1-D photochemistry model at 12:00 LT. 96
4.13 Volume mixing ratio profiles of oxidised organic products after one sol of introducing a uniform profile volume mixing ratio of 50 ppt of C_2H_6. 97
4.14 Photochemical production and loss rates (molec $cm^{-3}s^{-1}$) of HCHO and HCOOH in my 1-D photochemistry model associated with 50 ppt of C_2H_6. Values are for latitude 2.5°N, local time 12:00, and solar longitudes 71° and 251° as a function of altitude. 99
4.15 Photochemical production and loss rates for methane (molec $cm^{-3}s^{-1}$), associated with the UV photolysis of a 50 ppt column of CH_3CHO, as a function of altitude. Calculations are for L_S = 251°, 12:00 LT, and latitude 2.5°N. 100

5.1 Schematic of a Tangent Linear Model of some non-linear function dependent on one variable, f(x). The control state takes x_C as the input to yield f(x_C), and the change due to an altered input x_P can be calculated by two runs of the full model, f(x_P) - f(x_C), or approximated by the TLM of function f, TLM(x_P - x_C). 104
5.2 A simplified schematic of the non-linear 1-D photochemistry model (yellow) and the tangent linear model (purple) operating in parallel, linearising the 1-D processes with respect to tracer mass mixing ratios at the current model timestep (PQ^t). 107
5.3 Comparisons of the relative perturbations made to a control state in the 1-D model (Equation 5.17) as calculated via the full non-linear 1-D photochemistry model and their approximations from the TLM (Equation 5.10). 111
5.4 Temporal invariance of Equation 5.14 displayed by calculating the change in H_2O_2 column vmr caused by a 10% increase to the initial H_2O column using TLM calculated perturbation vectors and adjoint sensitivity vectors at every model timestep for a period of 10 sols (480 timesteps). 116
5.5 Percentage change in H_2O_2 column vmrs produced by a 10% increase to the column of inorganic trace gas species in the 1-D model, allowing for a 10 sol model spin up. 118
5.6 Percentage change in O_3 column vmrs produced by a 10% increase to the column of inorganic trace gas species in the 1-D model, allowing for a 10 sol model spin up. 119

6.1 Observations of HCl on Mars made by ACS-MIR during the 2018 global dust storm. A) Northern hemisphere observations between L_S 210–330°, B) Southern hemisphere observations between L_S 245–290°, C) Southern hemisphere observations between L_S 310–325°. The purple line and shading indicates the mean of the profiles and their standard deviations in each subfigure. D) All ACS-MIR occultations are shown with gray dots. Triangles indicate lower limits of HCl only, whereas detections of HCl are circles with the maximum vmr of the profile indicated by the colorbar. NOMAD-SO retrievals are indicated by diamonds. The mean dust opacity is presented in the background of the figure. E) The lowest height (tangent height) in km above the surface of the ACS-MIR solar occultation observations. Figures from Korablev et al. [2021]. 124
6.2 Photochemical lifetimes of chlorine-containing tracers in the 1-D photochemistry model assessed at noon (LT = 12:00 hrs) at latitudes 60° and -60° during Mars' aphelion (L_S 71°) and perihelion (L_S 251°). Red regions: steady-state approximation; Yellow regions: simple exponential solution; Green regions: semi-implicit backwards Euler method. 132
6.3 Loss rates of HCl at 60° north and L_S 71° using gas-phase chlorine chemistry only. 133

6.4 Relative humidity at the Phoenix lander's landing site . Figure from Fischer et al. [2019]. 135
6.5 The uptake coefficients involved with chlorine species in the 1-D model and their variations with Relative Humidity (%) and temperature (K). γ_{cl1}: OH + Dust $\longrightarrow$ ClO_x + Dust, γ_{cl2}: HO_2 + Dust $\longrightarrow$ ClO_x + Dust, γ_{cl3}: HCl + Ice $\longrightarrow$ Ice + Products. 136
6.6 Surface roughness lengths (cm) as inferred from MGS-TES rock abundance data. Figure taken from Hébrard et al. [2012]. 138
6.7 Turbulent and Quasi-Laminar layer resistances (R_a and R_b), HCl dry deposition velocities at the surface, and the resultant loss rate of HCl due to surface deposition as calculated by the 1-D model assuming a constant surface roughness of z_0 = 1 cm and bare soil (R_c = 0). 139
6.8 Diurnal variations of Cl and ClO at 20° north, 210° L_S, as modelled by the 1-D photochemistry model using the heterogeneous chlorine chemistry scheme. Upper row displays the vmrs in Log_{10} form, bottom row presents the vmrs with a linear colour scheme. 140
6.9 Diurnal variations of ClOO, OClO, ClCO, and Cl_2O_2 at 20° north, 210° L_S, as modelled by the 1-D photochemistry model using the heterogeneous chlorine chemistry scheme. 141
6.10 Diurnal variations of HCl, HOCl, Cl_2, and ClO_3 at 20° north, 210° L_S, as modelled by the 1-D photochemistry model using the heterogeneous chlorine chemistry scheme. 142
6.11 Diurnal variations of $HClO_4$ and ClO_4 at 20° north, 210° L_S, as modelled by the 1-D photochemistry model using the heterogeneous chlorine chemistry scheme. 144
6.12 HCl profiles produced by the 1-D photochemistry model through the heterogeneous chlorine chemistry routine using standard climatological aerosol and H_2O vapour profiles (dashed lines) and ACS-TIRVIM and MIR observed aerosol mass loadings and H_2O vapour profiles (solid lines) and their coincidences with the HCl observations performed by Korablev et al. [2021]. Subplot title indicate parameters of the ACS-MIR HCl observation, and the in-plot text denotes the differences with the ACS-TIRVIM aerosol profiles solar longitude (ΔL_S), latitude (ΔLat), longitude (ΔLong), and local time (ΔLT). 147
6.13 Similar to Figure 6.12. 148
6.14 Partial column vmr of HCl observed by the ACS-MIR (top) and those modelled by the 1-D photochemistry model using the heterogeneous chlorine scheme with ACS-TIRVIM observed ice and dust profiles and ACS-MIR H_2O vapour profiles. . 149

6.15 Reaction rates involving the production and loss of atmospheric HCl for two ACS-MIR observed profiles [Korablev et al., 2021] when dust and water ice profiles from ACS-TIRVIM are used in the 1-D photochemistry model. Heterogeneous reactions involved in producing ClO_x and adsorbing HCl are included. γ_{cl1} : OH + Dust $\longrightarrow$ ClO_x; γ_{cl2} : HO_2 + Dust $\longrightarrow$ ClO_x, γ_{cl3} : HCl + Ice. 150

6.16 Comparisons of the relative perturbations made to a control state in the 1-D model (Equation 5.17) as calculated via the full non-linear 1-D photochemistry model and their approximations from the TLM (Equation 5.10). Both cases include chlorine chemistry, with 31 tracers in total considered, and perturbations are recorded over three sols (144 model timesteps). 151

6.17 (a-b) 1-D model HCl profiles and observations made by the ACS-MIR. (c-d) Change experienced in the 1-D model HCl abundances (ppb) at each layer resulting from a 20% increase to dust mmrs 6 hours prior as calculated by the adjoint. (e-f) Change experienced in the 1-D model HCl abundances (ppb) at each layer resulting from a 20% increase to H_2O ice mmrs 6 hours prior as calculated by the adjoint . . . 153

6.18 Maximum changes to the HCl profiles of Figures 6.12,6.13, and Figures B.1–B.7 (Δ ppb) caused by a 20% change to the initial inorganic tracer concentrations of the 1-D model. 155

6.19 H_2O vapour column vmr in ppm and the lifetime of chlorine trapped within dust grains when the heterogeneous chlorine chemistry routine is active (h_{cl1} and h_{cl2}. The rate of HCl dry deposition to the Martian surface is also shown in molecules m^{-2} per Mars sol. 158

6.20 The photochemical lifetime of HCl with altitude at 60° S and solar longitude as calculated by the 1-D model excluding then including heterogeneous uptake of HCl on H_2O ice. 160

6.21 HCl column abundance (ppb) variations with latitude and solar longitude, using longitudinal mean meteorological boundary conditions, long-lived inorganic tracers (CO, O_2, H_2, CO_2, and H_2O vapour), and aerosol profiles as calculated by the 1-D photochemistry model using the heterogeneous chlorine chemistry scheme. The column mass of dust, the source of Cl and ClO molecules, and H_2O ice, the heterogeneous sink for HCl, are presented also. 161

6.22 HCl column vmrs (ppb) calculated by the 1-D model from Figure 6.21 (colour saturated at 6 ppb) with the median HCl vmrs observed by the TGO NOMAD throughout MY34–35 [Aoki et al., 2021] and the median HCl vmrs observed by the ACS-MIR throughout MY34 [Korablev et al., 2021] superimposed. Left hand colour bar displays ACS-MIR/NOMAD median HCl vmr, right hand colour bar displays the 1-D model HCl column vmr. 162

6.23 H_2O_2 column abundances and their variations with latitude and solar longitude as calculated by the 1-D model using model runs with no heterogeneous chemistry (top), and with the heterogeneous chlorine chemistry scheme active (middle). The bottom heatmap presents the resultant change (in percentage with respect to the chlorine-absent run) to the H_2O_2 column due to chlorine chemistry. 163
6.24 (a) Column mixing ratios of H_2O_2 as calculated by the 1-D photochemistry model with and without the heterogeneous chlorine chemistry routine active and (b) the 3-D General Circulation Models with and without heterogeneous uptake of OH and HO_2 on ice. Figure a does not include the upper limits of H_2O_2 produced by Encrenaz et al. [2019]. The original observations of Mars' H_2O_2 column by Encrenaz et al. [2004b], and the reanalysed values using the updated GEISA 2015 spectrographic records performed by Encrenaz et al. [2019] are presented in each plot. Figure b has been taken directly from Encrenaz et al. [2019]. 165
6.25 Net photochemical flux of H_2O_2 at 40°S, 210° L_S across one Mars sol with (left) no heterogeneous chemistry considered, (middle) OH and HO_2 uptake on H_2O ice particles, and (right) OH, HO_2 uptake on ice and the heterogeneous chlorine chemistry routine active. 166
6.26 Photochemical lifetime of CH_4 in terrestrial years and the variance across latitude and solar longitude on Mars without chlorine chemistry, and with the heterogeneous chlorine scheme active. 167
6.27 Photochemical loss rates of CH_4 for a chlorine-free model run (solid) and a run producing chlorine via the heterogeneous chlorine routine (dashed), and the vmr profiles of HCHO, HCOOH, and CH_3OOH at LT = 12:00 hrs after one sol of chlorine chemistry. 168

B.1 Observations of HCl via the ACS-MIR during MY34 and HCl profiles produced by the 1-D model using the heterogeneous chlorine chemistry routine with ACS-TIRVIM dust and ice profiles and ACS-MIR H_2O vapour profiles, and aerosol and H_2O profiles from the MCDv5.3 databases Standard Climatological dataset. . . . 194
B.2 Same as Figure B.1. 195
B.3 Same as Figure B.1. 196
B.4 Same as Figure B.1. 197
B.5 Same as Figure B.1. 198
B.6 Same as Figure B.1. 199
B.7 Same as Figure B.1. 200

Tables

1.1 Earth dates corresponding to the equinox's and northern hemisphere solstices of Mars for Mars Years (MY) 1–34. This table has been extracted from Cantor et al. [2010]. 9
1.2 Parameters of the three spectral channels inside the TGOs ACS spectrometer suite. 10

2.1 Inorganic trace gas species in the Martian atmosphere and measured abundances. i) [Belton and Hunten, 1966, Fedorova et al., 2009], ii) [Fedorova et al., 2021, Sindoni et al., 2011, Smith et al., 2021], iii) [Owen et al., 1977, Mahaffy et al., 2013], iv) [Trokhimovskiy et al., 2015a, Smith et al., 2009, Smith, 2002, Aoki et al., 2019], v) [Chaufray et al., 2008], vi) [Todd Clancy et al., 2013], vii) [Villanueva et al., 2013], viii) [Krasnopolsky and Feldman, 2001], ix) [Krasnopolsky et al., 1997, Encrenaz et al., 2008, 2004b], x) [Ritter et al., 2019, Qin, 2020, Chaufray et al., 2009], xi) [Hartogh et al., 2010, Sandel et al., 2015, Fedorova et al., 2021], xii) [Patel et al., 2021, Barth et al., 1973, Olsen et al., 2020] 19
2.2 Table displaying the most notable reported observations and non-detections of CH_4 on Mars, the instruments responsible for them, and the detection magnitudes or inferred upper limits. Red rows indicate non-detections which highlight the highly transient and temporally variable nature of the methane being reported in observational campaigns. 37

3.1 Trace gas species in the 1-D photochemistry submodule. All chlorine species and all organic compounds (bar CH_4 itself) are new additions to the model since it was received in September 2017. 54
3.2 Inorganic reaction rate coefficients within the 1-D photochemistry submodule. Bimolecular rate coefficient units are cm^3 $molec^{-1}$ s^{-1}. Values denoted by superscript a are three-body reactions with values taken with atmospheric number density complying to temperatures of T = 298 K and pressures of 660 Pa. γ denotes the uptake coefficient of the heterogeneous reaction. 62
3.3 Photolysis reactions in the 1-D photochemistry submodule already included at the point of the project start date. The rates presented are taken at aphelion ($L_S = 71^\circ$) at a solar zenith angle of 0° at the Martian equator. 66

4.1 Organic trace gas species handled by the 1-D Photochemistry Submodule 71
4.2 Chemical reactions and rate coefficients involved in the oxidation of CH_4 used in my 1-D photochemistry model. Bimolecular rate coefficient units are cm^3 $molec^{-1}$ s^{-1}. ^{a} are three-body reactions with values taken with atmospheric number density complying to temperatures of T = 298 K and pressures of 660 Pa. ^{b} are unimolecular rate coefficients with units s^{-1}. 74

4.3 Functions and constants used by the R-O_2 permutation reaction handling scheme extracted from the CAABA/MECCA v4.0 box model. 76

4.4 Chemical reactions and rate coefficients involved in the oxidation of C_2H_6 used in my 1-D photochemistry model. Bimolecular rate coefficient units are cm^3 $molec^{-1}$ s^{-1}. ^{a} are three-body reactions with values taken with atmospheric number density complying to temperatures of T = 298 K and pressures of 660 Pa. ^{b} are unimolecular rate coefficients with units s^{-1}. 78

4.5 Organic photolytic reactions used within the 1-D photochemistry submodule. Values (s^{-1}) are interpolated from an offline look-up table constructed by a modified TUV Madronich et al. [2002] model with respect to CO_2 and O_3 column abundances overheard, temperature, optical opacity and solar zenith angle. Values displayed are extracted for a solar zenith angle of 0°, L_S = 251° (perihelion). 81

5.1 Results from Cases 1–4 of the comparisons of perturbations to a control state as modelled by the non-linear 1-D photochemistry model and the TLM approximation. λ denotes the relative magnitude of the initial perturbations, R is the Pearson correlation coefficient, m the gradient of the linear line of best fit (L.o.B.F), and N is the total number of perturbations. 113

6.1 Chlorine species included in my 1-D photochemistry model. 126

6.2 Reactions involving chlorine species used in my 1-D photochemistry submodule. All rate coefficients calculated at T = 298 K are given in units of cm^3 $molec.^{-1}$ s^{-1}, with exceptions denoted with ^{a} that are first-order and in units of s^{-1}. Termolecular rate coefficients are calculated for an atmospheric temperature of 298 K and pressure of 660 Pa. 128

6.3 Photolysis reactions of chlorine tracers used in my 1-D photochemistry model. Reactions highlighted in green indicate new additions since I started my PhD. . . 131

6.4 Uptake coefficients for heterogeneous interactions involving chlorine species. ^{a}: A_{Des} = 1E13 s^{-1}, pre-exponential factor for the desorption of the adsorbed HCl precursor, E_{Des} = 28.0 kJ mol^{-1} HCl desorption activation energy, A_R = 1.2E4 s^{-1}, pre-exponential factor of HCl precursor reaction, ΔE = E_{Des} - E_R = 30.5 kJ mol^{-1}, energy difference between desorption and reaction of HCl on ice particle. RH denotes relative humidity (%). 134

6.5 Results of the comparisons of the TLM approximated and 1-D model calculated relative perturbations to a 1-D model control run with chlorine chemistry active. . 152

A.1 Coefficients used in the linearisation of NO and NO_2 number densities. 187

A.2 Coefficients used in Equation A.32–A.34 constructed of non-linear model control run values. 188

A.3 Coefficients used in the linearisation of odd-oxygen species (Equations A.40–A.44. 189
A.4 Coefficients used in the linearisation of odd-chlorine species (Equations A.48–A.50). 190
A.5 192

Chapter 1

Introduction

The Red Planet has captured significant public and scientific interest across the world over the past two decades due to numerous reported observations of methane (CH_4) within the atmosphere. On Earth, $\sim$90% of atmospheric CH_4 is produced through biological processes, which can be biogenic in nature, such as organic matter decomposition via methanogenic bacteria in rice paddies, swamps, and animal waste, or thermogenic, where CH_4 is produced in the breakdown of organic matter buried deep in the subsurface in high pressure and high temperature environment and enters the atmosphere via gas seepage in the surface [Saunois et al., 2020]. The remainder of Earth's methane is produced via abiotic geological methods [Conrad, 2009]. Because of these strong ties to terrestrial biology, CH_4 is referred to as a potential bio-signature of extraterrestrial life in the astrobiology community. Without a definitive source and an effective sink presently known to exist for CH_4 on Mars, there has been speculation as to whether or not biological processes could currently be active below the surface safe from the hazardous environments above.

As Mars is Earth's nearest neighbour and possesses a significantly less hostile atmosphere than the likes of Venus, the planet provides us with the opportunities to expand our knowledge within the fields of planetary science through landing platforms, orbiters, and rovers. Developing an understanding of Mars' current atmospheric behaviour, and its mysterious past, allows us to unlock information regarding processes and events that are not observed on Earth, and can aid in the studies of terrestrial planets that lie beyond our solar system. There is still much to be learnt about Mars; our current models fail to replicate the observed latitude variations in carbon monoxide (CO) [Smith et al., 2009, Smith et al., 2018], or accurately model water vapour existing in a super-saturated state 30–40 km above the surface [Maltagliati et al., 2011], and model estimates of ozone column and profile abundances still require work to improve coincidence with observations [Lefèvre et al., 2004b, 2008]. The 21st century detections of CH_4 [Krasnopolsky et al., 2004, Formisano et al., 2004, Encrenaz, 2008, Geminale et al., 2008, Mumma et al., 2009, Fonti and Marzo, 2010, Geminale et al., 2011, Krasnopolsky, 2012, Webster et al., 2015, Webster et al., 2018, Giuranna et al., 2019]have provided another mystery, as the gas could be linked to biological emission sources in an environment believed to be incredibly hostile to organic materials [Levin and Straat, 2009]. Even more unexpectedly, the variations in atmospheric CH_4 are consistent with a loss rate

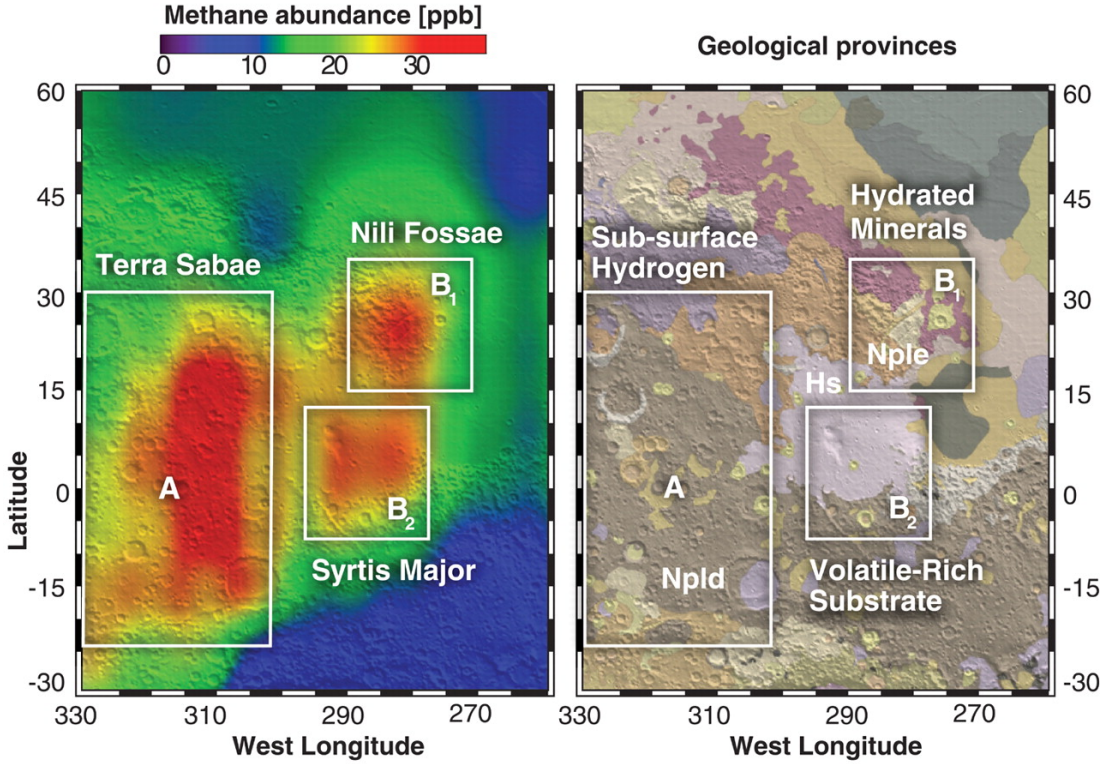


Figure 1.1: Observations of the 2003 methane plume measured by the ground-based CSHELL/IRTF and NIRSPEC/Keck-2 spectroscopic telescopes and the geological structure of their locations on Mars. Approximately 19,000 tons of CH_4 gas are contained within them. Figure from Mumma et al. [2009].

up to 600 times faster than any photochemical model currently predicts [Lefèvre and Forget, 2009, Taysum and Palmer, 2020]. Most recently, observations of hydrogen chloride (HCl) in the atmosphere of Mars [Korablev et al., 2021] have presented a new and unexpected puzzle for scientists studying Martian atmospheric photochemistry, again due to a lack of a known source or sink for chlorine chemistry on the Mars.

The first reported detection of CH_4 on Mars was made by the Infrared Spectrometer (IRS) aboard the Mariner 7 during the spacecraft's flyby in 1969 [Sullivan, 1969], which gathered a significant amount of interest within the biology community [Saltinski, 1971] due to the gases strong ties to biological life on Earth. The reported observation came from the IRS measurement of a strong absorption feature at a 3.3 μm wavelength, coupled with a weaker feature found at 3.0 μm, at the edge of the southern polar cap of Mars. Originally, the stronger 3.3 μm feature was thought to be caused by the third vibrational band (ν_3) of CH_4, however later research found that this same spectral absorption feature can be attributed to CO_2 ice [Herr and Pimentel, 1969] which falls heavily on the polar caps, capable of achieving depths of up to 1 m. Two years later in 1971, analysis of Mariner 9's flyby and IRS measurements placed an upper limit of CH_4 on Mars of $<$ 20 ppb [Maguire, 1977].

In 1993, solar occultation measurements were performed by the Phobos spacecraft that reported a detection of formaldehyde (HCHO) [Korablev et al., 1993], one of several compounds produced by the oxidation of CH_4 in the terrestrial atmosphere. This measurement reported HCHO in parts per million abundances between 20–30 km above the surface, a value which many scientists at the time believed to be unrealistically high. In 1997, researchers then used ground-based spectroscopic telescopes at the Kitt Peak National Observatory and the NASA Goddard Space Flight Center in 1997 to search for absorption features of CH_4. These results found no positive detection of HCHO, instead refining a 2-σ upper limit of $<$ 3 ppb on the molecule [Krasnopolsky et al., 1997], but did report the measurement of a 70 ppb column abundance of CH_4 detected by observing the spectral features between 3.6–3.8 μm and 8.0–8.1 μm wavelength ranges. Another study performed in 2000 of Mars of the same spectral region however failed to measure any CH_4 or HCHO spectral features [Lellouch et al., 2000], instead placing upper limits of 50 ppb and 150 ppb on the chemicals respectively.

The start of the 21st century marked a turning point for the astrobiology and Mars modelling community, as reports of successful observations of CH_4 started to appear. The first two reports of the decade appeared in late 2004, made by two independent teams through two seperate observational techniques. The first team used ground-based telescopes studying the 3.3 μm absorption band of CH_4 [Krasnopolsky et al., 2004] to measure CH_4 at a mixing ratio of 10 $\pm$ 3 ppb, while the second team found abundances varying between 0–30 ppb across the planet using the Planetary Fourier Spectrometer (PFS) aboard the Mars Express Orbiter [Formisano et al., 2004]. In 2008, an analysis of 30,561 PFS measurements of the 3.3 μm CH_4 absorption line was performed to study seasonal and spatial trends in CH_4, reporting an average abundance of 14 $\pm$ 5 ppb [Geminale et al., 2008]. The following year saw the publication of one of the most striking reports of CH_4 on Mars - a team of researchers using the CSHELL/IRTF and NIRSPEC/Keck-2 ground-based infrared spectrometer telescopes reported the appearance of a plume of CH_4 in the equatorial latitudes ranging between 20–60 ppb in abundance [Mumma et al., 2009], containing approximately 19,000 metric tons of CH_4 gas localised between roughly 30° south and 45° north. These observations are displayed in Figure 1.1. Shortly after this report, an analysis studying the ν_4 CH_4 vibrational band with a spectral feature at 7.7 μm in spectra recorded by the Thermal Emission Spectrometer (TES) aboard the Mars Global Surveyor (MGS) identified three localised spots with abundances varying across the globe within a range of 0–60 ppb [Fonti and Marzo, 2010], consistent with the previous positive detections of the 2000's.

These sporadic and spatially variable reports of CH_4 on Mars from both terrestrial telescopes and Mars orbiters prompted the establishment of the ExoMars program [Vago et al., 2006], a collaborative effort between the European Space Agency (ESA) and the Russian Roscosmos State Corporation for Space Activities designed to search for evidence of past or present biological activity on Mars. The ExoMars program consists of two parts: the ExoMars Trace

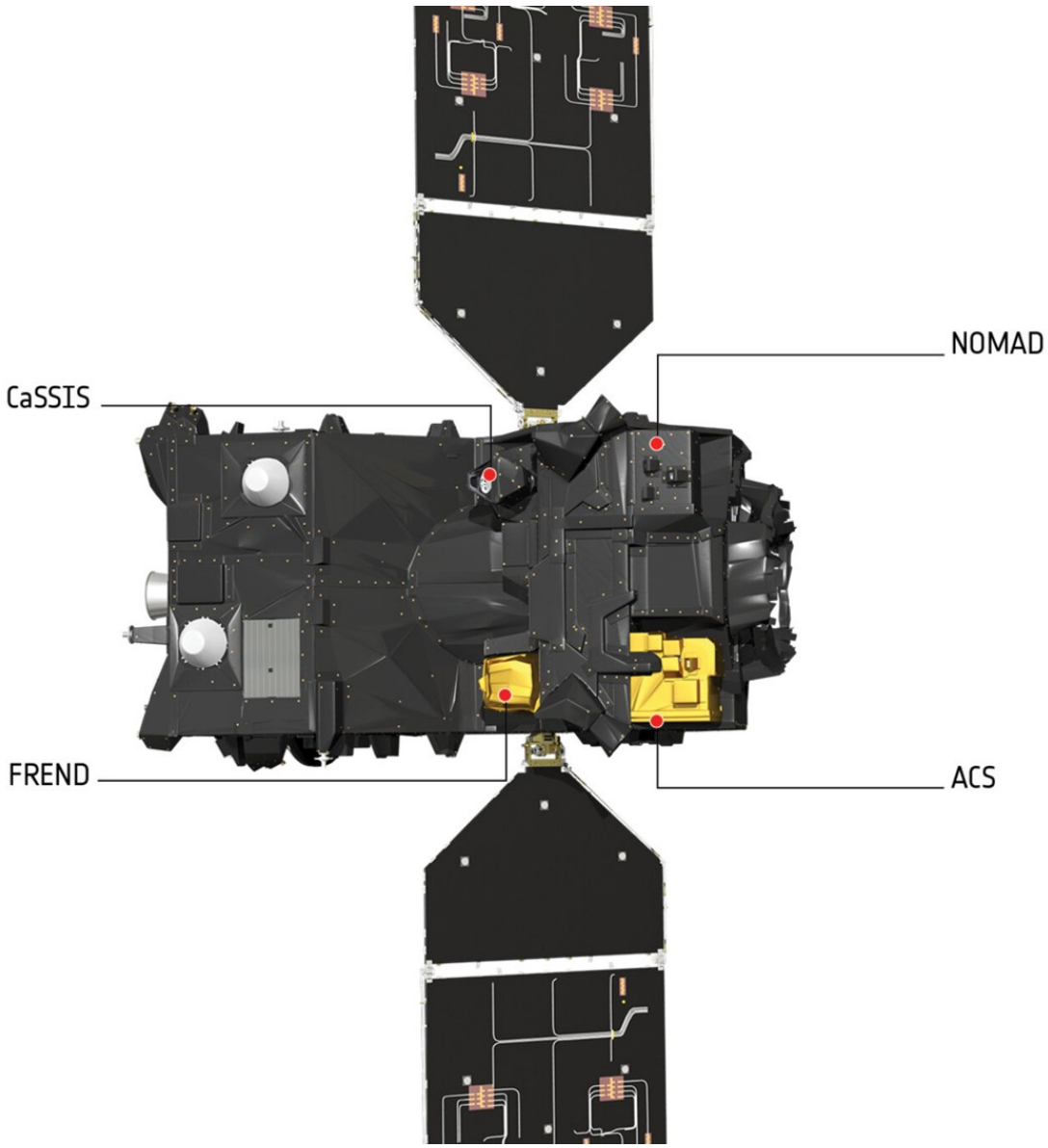


Figure 1.2: The ExoMars Trace Gas Orbiter and the locations of the ACS and NOMAD spectrometer suites. The positions of the other two instruments onboard, the Colour and Stereo Surface Imaging System (CaSSIS), and the Fine Resolution Epithermal Neutron Detector (FREND), are also shown. Taken from Medialab [2015].

Gas Orbiter (TGO) [Wall, 2018], launched on the 14th of March 2016 and in a stable orbit of approximately 400 km from the Martian surface as of 19th of October 2016 [Wall, 2018], and the ExoMars Rover [Patel et al., 2010], with a scheduled launch date of the 20th of September 2022 and an expected landing date of the 10th of June 2023.

The TGO is equipped with two spectrometer suites, the Atmospheric Chemistry Suite (ACS) and the Nadir and Occultation for Mars Discovery (NOMAD), that aim to study the chemical composition of the Martian atmosphere through limb, nadir, and solar occultation measurement methods with the highest spectral resolution of a Mars-orbiting craft to-date [Trokhimovskiy and Korablev, 2014, Thomas et al., 2016]. Their locations on-board the TGO are shown in Figure 1.2. The primary goals of the TGO and its set of instruments are to hunt for signs of past or presence biological activity, to assess how the geochemistry of the planet varies with time and space, and to locate any emission sources and sink sites should they exist [Vandaele et al., 2015].

The solar occultation method used by NOMAD and ACS allows the TGO to measure vertical profiles of trace gas species abundances, aerosol extinction, and physical atmospheric properties such as pressure, temperature, and density with a very high vertical resolution, less than or equal to 1 km. Both the NOMAD and ACS have been built by teams involved with the Venus Express mission [Korablev et al., 2018], and have based their solar occultation strategy on that employed by the Solar Occultation at Infrared (SOIR) channel of the Spectroscopy for Investigation of Characteristics of the Atmosphere of Venus (SPICAV) instrument [Vandaele et al., 2008]. The TGO aligns itself to face the Sun prior to sunset without any obstruction by the atmosphere, and captures a reference spectra in the spectral range of the pending observation. The spectrometers continuously record spectra as the Sun begins to fall behind the atmosphere, and stops when the line of sight is broken by the planet surface. Transmittance spectra are then produced by normalising this set of observed spectra by dividing by the previously taken reference spectra of the Sun. Figure 1.3 presents a schematic demonstrating the solar occultation measuring process. This set of absorption spectra can then be converted into a measurement of tracer abundances, optical extinction etc. by fitting the unique absorption spectra of various molecules in the observed bandwidth to the measured spectra, and through inverse modelling methods. These methods provide a numerical estimate of the abundances of each tracer or subject of interest required to best-fit the measured spectra sets, enabling the construction of vertical profiles. This method is subject to some limitations, as it requires a clear and transparent atmosphere for successful measurements which can be compromised by the presence of dust that has been lofted into the atmosphere.

The geometry of limb sounding measurements is similar to that of solar occultations. However, as opposed to measuring the solar radiation absorbed by the atmosphere limb sounding campaigns typically measure thermal emission lines originating from, or scattered by, the ‘limb’ of the atmosphere. Limb sounding has previously been used by the Mars Climate Sounder

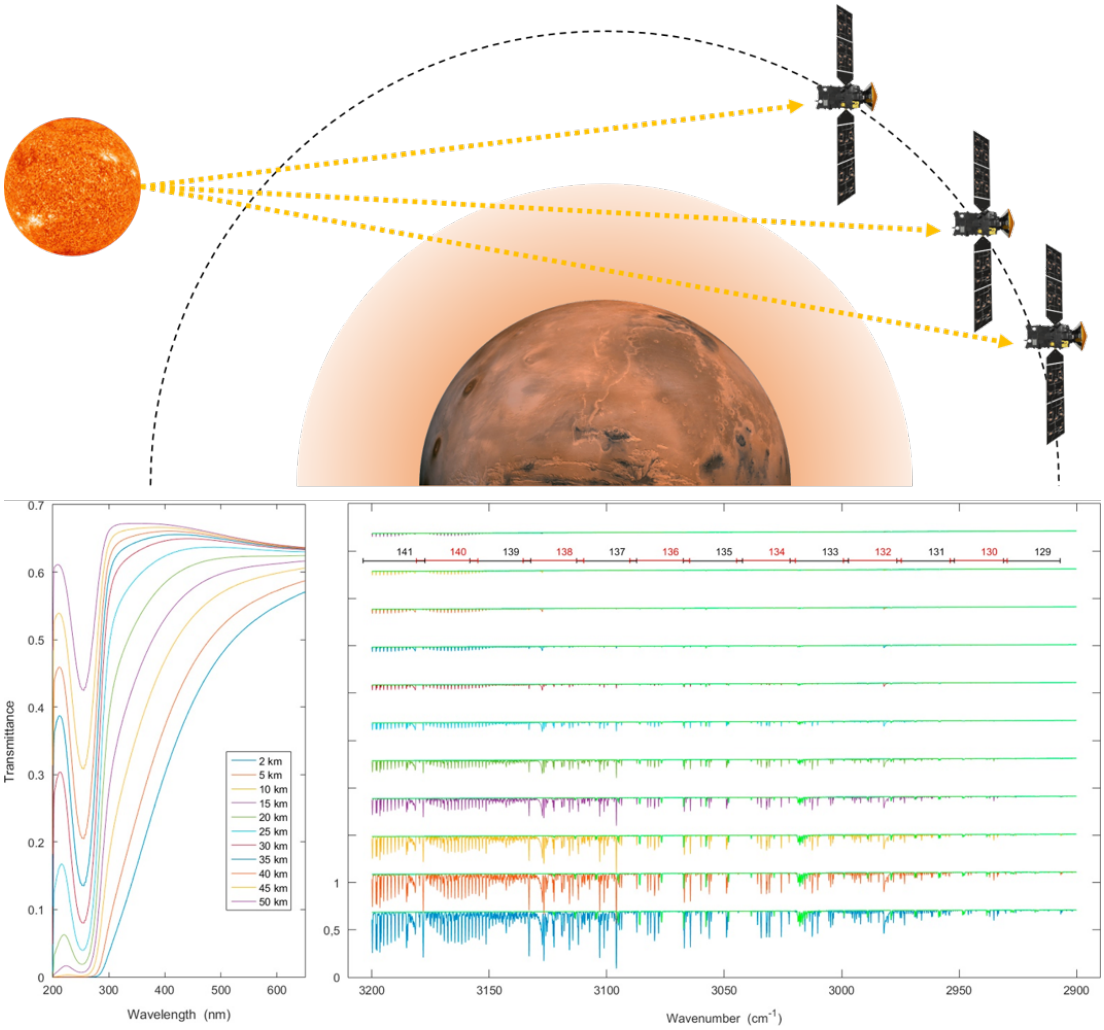


Figure 1.3: Schematic displaying the Solar Occultation method for atmospheric remote sensing. Below are two simulated transmittance spectras in the UV-Visible (Left) and the Infrared (Right) produced by the UV-Visible and Solar Occultation channels of the NOMAD instrument respectively. The two synthetic spectra are taken from Vandaele et al. [2015].

[McCleese et al., 2007] aboard the Mars Reconnaissance Orbiter in its campaign to measure seasonal and spatial variances in the vertical profiles of water vapour, dust abundances, and atmospheric parameters such as temperature and pressure [McCleese et al., 2007, Kleinböhl et al., 2009, McCleese et al., 2010].

Nadir observations have a unique geometry in which the observing equipment is pointed towards the planet surface anti-parallel to the zenith. During an observation, the spectrometers observe the ground directly below the satellite for a set integration time, and measure the atmospheric emission and scattering of solar radiation in the specified wavelength range to produce values of column abundances of trace gas species, surface temperatures and pressures, and optical opacity. These measurements help to construct a picture of the seasonal, latitudinal, and longitudinal variations across the entire planet.

The NOMAD and ACS spectrometer suites have the highest spectral resolution of any Mars orbiter equipment to date. The generally higher spectral resolutions enable the spectrometers to be more sensitive and capable of picking up absorption features produced by organic trace gas species in abundances as low as 25 ppt, and can distinguish the unique features of various molecular isotopologues - molecules with identical chemical structure but different number of neutrons. Measurements of these isotopologues provide the $^{17}O/^{16}O$ and $^{18}O/^{16}O$ isotopic ratios that detail the history of water vapour and various processes such as loss to the surface or into space that may have effected the ratios [Jakosky, 2021]. The only measurement of this ratio prior to the observations made by the ACS in 2019 [Alday et al., 2019b] was performed by the Curiosity Rover's Sample Analysis for Mars (SAM) instrument in 2013 [Webster et al., 2013] as part of the Mars Science Laboratory (MSL) mission. One of the chief aims of the MSL was the landing and operation of the Curiosity Rover, which successfully touched-down at Gale Crater on the 6th of August 2012. Curiosity and the MSL mission would go on to assess the habitability of Mars, the nature of organic compounds found within the Martian soil, and study the surrounding atmospheric composition at Gale Crater [Grotzinger et al., 2012], which the ExoMars program will continue and expand upon.

As well as being at the forefront of the search for bio-signatures on Mars, the TGO is expanding on previous work performed by older Mars orbiters and their studies into the atmosphere's chemical make-up. The Mars Express Orbiter and the Spectroscopy for the Investigation of the Characteristics of the Atmosphere of Mars (SPICAM) ultraviolet spectrometer [Bertaux et al., 2006] has produced an abundance of data since its arrival to Mars in late 2003, enabling scientists to better quantify the seasonal water vapour (H_2O) cycle that Mars experiences [Trokhimovskiy et al., 2015a], as well as the ozone (O_3) cycle and its anti-correlation with H_2O on Mars [Lebonnois et al., 2006, Lefèvre et al., 2007]. The TGO also aims to study the vertical and spatial distribution of Martian dust and water ice crystals suspended in the atmosphere to expand upon the observations performed by instrumentation such as the Thermal Emission Spectrometer (TES) [Pearl et al., 2001] on-board the Mars Global Surveyor that arrived at

Mars in 1997. An accurate knowledge of dust and ice particle physics and chemistry on Mars is integral for understanding many aspects of the atmosphere, such as the condensation and sublimation of carbon dioxide around dust nuclei [Nachbar et al., 2016], the development of water ice clouds [Laura et al., 2010] and their subsequent effects on radiative transfer and atmospheric temperatures [Wilson et al., 2008], and the possible involvement of water ice in heterogeneous chemical reactions that have the effect of improving General Circulation Model (GCM) predictions of O_3 when compared to observations made by SPICAM [Lefèvre et al., 2008].

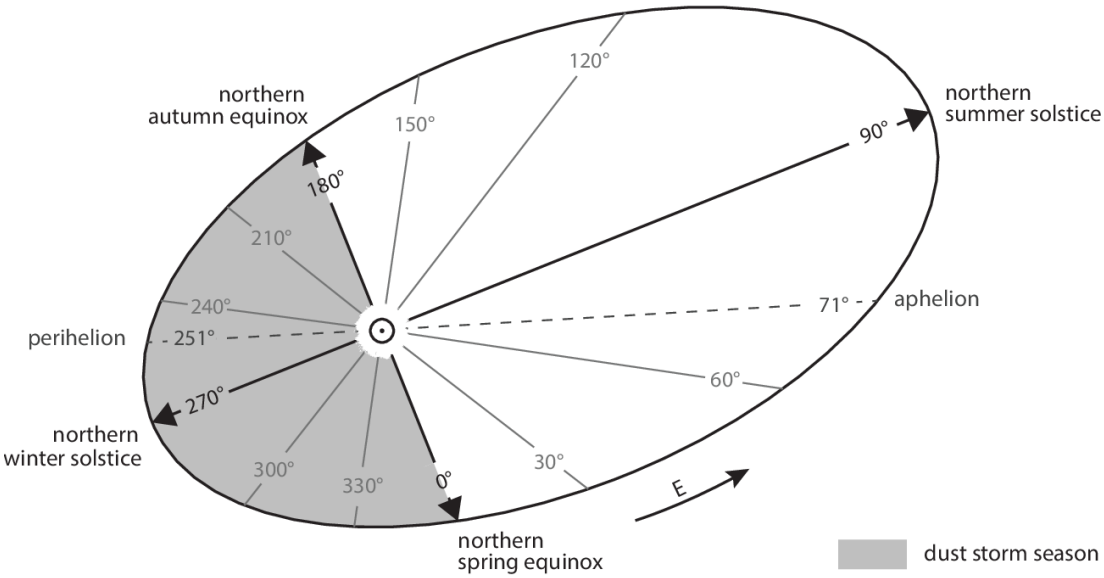


Figure 1.4: Schematic highlighting Mars' location during its orbit around the Sun and the corresponding solar longitude, L_S (°). Aphelion, the point of Mars' furthest distance from the Sun, occurs at L_S 71°, and its perihelion, the point of closest approach, occurs at L_S 251°. Figure taken from P'al et al. [2019].

Time-keeping on Mars is similar to that on Earth. The Martian day, a 'sol', lasts for 24 hours and 39 minutes, and the Martian year is broken up into four seasons corresponding to one quarter of the planets orbit. Figure 1.4 presents a schematic of the Martian orbit and its relationship with solar longitude, L_S. The northern hemisphere's spring is defined between L_S 0–90°, the northern summer between L_S 90–180°, the northern autumn between L_S 180–270°, and the northern winter between L_S 270–360°. The 'dust-storm season', times when global and local dust-storm frequencies are at a maximum on Mars, occurs during Mars' approach to perihelion roughly between 180–360°. A Martian year lasts for just under 687 Earth days, and it is standard convention in the scientific community to number the Mars Years (MY's) by defining the start of Mars Year 1 (MY1) at the spring equinox of Mars (0° L_S)

in 1955. This year was arbitrarily chosen by Clancy et al. [2000], but it does coincide with the appearance of a well observed global dust storm in 1956 [Kuiper, 1957]. A list of the Earth dates corresponding with MY1–MY36 and the northern hemisphere's equinox's and solstices is presented in Table 1.1.

Table 1.1: Earth dates corresponding to the equinox's and northern hemisphere solstices of Mars for Mars Years (MY) 1–34. This table has been extracted from Cantor et al. [2010].

Mars Year (MY)	Spring equinox (Ls = 0°)	Summer solstice (Ls = 90°)	Autumnal equinox (Ls = 180°)	Winter solstice (Ls = 270°)
01	Apr 11 1955	Oct 27 1955	Apr 27 1956	Sep 21 1956
02	Feb 26 1957	Sep 13 1957	Mar 15 1958	Aug 09 1958
03	Jan 14 1959	Aug 01 1959	Jan 31 1960	Jun 26 1960
04	Dec 01 1960	Jun 18 1961	Dec 18 1961	May 14 1962
05	Oct 19 1962	May 05 1963	Nov 05 1963	Mar 31 1964
06	Sep 05 1964	Mar 22 1965	Sep 22 1965	Feb 15 1966
07	Jul 24 1966	Feb 07 1967	Aug 10 1967	Jan 03 1968
08	Jun 10 1968	Dec 25 1968	Jun 27 1969	Nov 20 1969
09	Apr 28 1970	Nov 12 1970	May 15 1971	Oct 08 1971
10	Mar 15 1972	Sep 29 1972	Apr 01 1973	Aug 25 1973
11	Jan 31 1974	Aug 17 1974	Feb 17 1975	Jul 13 1975
12	Dec 19 1975	Jul 04 1976	Jan 04 1977	May 30 1977
13	Nov 05 1977	May 22 1978	Nov 22 1978	Apr 17 1979
14	Sep 23 1979	Apr 08 1980	Oct 09 1980	Mar 04 1981
15	Aug 10 1981	Feb 24 1982	Aug 27 1982	Jan 20 1983
16	Jun 28 1983	Jan 12 1984	Jul 14 1984	Dec 07 1984
17	May 15 1985	Nov 29 1985	Jun Jan 1986	Oct 25 1986
18	Apr 01 1987	Oct 17 1987	Apr 18 1988	Sep 11 1988
19	Feb 16 1989	Sep 03 1989	Mar 06 1990	Jul 30 1990
20	Jan 04 1991	Jul 22 1991	Jan 22 1992	Jun 16 1992
21	Nov 21 1992	Jun 08 1993	Dec 08 1993	May 04 1994
22	Oct 09 1994	Apr 26 1995	Oct 26 1995	Mar 21 1996
23	Aug 26 1996	Mar 13 1997	Sep 12 1997	Feb 06 1998
24	Jul 14 1998	Jan 29 1999	Jul 31 1999	Dec 25 1999
25	May 31 2000	Dec 16 2000	Jun 17 2001	Nov 11 2001
26	Apr 18 2002	Nov 03 2002	May 05 2003	Sep 29 2003
27	Mar 05 2004	Sep 20 2004	Mar 22 2005	Aug 16 2005
28	Jan 21 2006	Aug 08 2006	Feb 07 2007	Jul 04 2007
29	Dec 09 2007	Jun 25 2008	Dec 25 2008	May 21 2009
30	Oct 26 2009	May 13 2010	Nov 12 2010	Apr 08 2011

31	Sep 13 2011	Mar 30 2012	Sep 29 2012	Feb 23 2013
32	Jul 31 2013	Feb 15 2014	Aug 17 2014	Jan 11 2015
33	Jun 18 2015	Jan 03 2016	Jul 04 2016	Nov 28 2016
34	May 05 2017	Nov 20 2017	May 22 2018	Oct 16 2018
35	Mar 23 2019	Oct 08 2019	Apr 08 2020	Sep 02 2020
36	Feb 07 2021	Aug 25 2021	Feb 24 2022	Jul 21 2022

1.1 The Atmospheric Chemistry Suite

The ACS consists of three spectrometers capable of measuring across a range of infrared wavelengths spanning 0.7–17μm and observing trace gas species with volume mixing ratios at the parts per trillion (ppt) level [Korablev et al., 2018]. The spectral resolution, R, of a spectrometer is defined as the ratio of the wavelength, λ, being measured and the smallest wavelength interval distinguishable around this wavelength, $\Delta\lambda$. For all three channels, the values of R exceed 10,000, enabling absorption features seperated by wavelengths as small as $\sim$ 0.1 nm to be resolved.

The near-infrared channel (NIR) spans the spectral range of 0.7–1.6μm with a spectral resolution of approximately 20,000 [Trokhimovskiy et al., 2015b] and is primarily used for solar occultation measurements that record vertical distribution profiles of trace gas species. Its spectral range enables it to measure abundances of CO_2, CO, H_2O, and O_2, which has been used to observe large quantities of H_2O vapour existing in the upper regions of the atmosphere in super-saturated cells [Fedorova et al., 2020] as well as to derive O_2 density profiles within the 10–60 km altitude range [Fedorova et al., 2018]. The primary scientific goals of the NIR channel are to measure the distributions of dust and ice aerosols, water vapour, and the day and night side airglow that occur during the UV induced photo-dissociation of ozone that can be used to parameterise O_2 abundances.

	NIR	MIR	TIRVIM
Operational Modes	Nadir, SO, Limb	SO	Nadir, SO
Spectral Range (μm)	0.73-1.6	2.3-4.3	1.7-17
Resolving Power ($\lambda/\Delta\lambda$)	20,000-27,000	30,000-50,000	760-7600 (Nadir) 4520-45,200 (SO)
Signal to Noise Ratio (in SO)	4000	2500-5000	50-170

Table 1.2: Parameters of the three spectral channels inside the TGOs ACS spectrometer suite.

The mid-infrared channel (MIR) operates within the 2.3–4.3 μm wavelength range, and can reach resolving powers of up to 50,000, making it capable of measuring trace gas species within the Martian atmosphere to the highest level of precision to date. It is expected to be limited to solar occultation measurements, and has been used to measure oxygen isotopes of water vapour [Alday et al., 2019a], measure abundances of water ice suspended in the atmosphere [Stcherbinine et al., 2020], and make the first observation of O_3 within MIR wavelengths on Mars [Olsen et al., 2020]. Measurements of oxygen isotope ratios on Mars provide insights into the ancient geology of Mars, as all geological and atmospheric processes have different impacts on the fractionation of ^{16}O, ^{17}O, and ^{18}O [Franchi et al., 1999].The isotopic fractions of oxygen measured in H_2O for the first time by the ACS-MIR channel has also enabled the first vertical distributions of these fractions to be measured, allowing scientists to observe and investigate possible altitude-dependent fractionation processes, such as the photodissociation rates of HDO and H_2O and relative uptakes on dust to form water ice, for the first time on Mars. Water ice clouds were first observed by Mariner 9 [Hanel et al., 1972], and are known to have strong connections with the water cycle on Mars [Kahn, 1990, Whiteway et al., 2009]. They are also capable of absorbing and scattering solar radiation [Wilson et al., 2008], impacting the temperature structure and general circulation of the atmosphere, and are thus integral in our understanding of Martian atmospheric chemistry and dynamics. One of the spectral feature of O_3 observed lies within a wavelength range of 3.26–3.33 μm, which coincides with a prominent spectral feature of CH_4 (the third level vibration-rotation band) and has caused concern that it may interfere with attempted measurements of CH_4. The third spectrometer channel of the ACS is the thermal-infrared (TIRVIM) that spans the 1.7–17 μm spectral range and has the capacity to measure atmospheric temperature profiles [Guerlet et al., 2019], water and dust aerosols [Luginin et al., 2019], and clouds of condensed CO_2 ice [Luginin et al., 2021]. The performances of the three ACS spectrometers are summarised in Table 1.2, and their observational limitations for various trace gas species with altitude are presented in Figure 1.5.

1.2 Nadir and Occultation for Mars Discovery

The NOMAD spectrometer suite observes spectra within wavelength range of 0.2–0.65 μm and the 2.2–4. μm infrared wavelength range, performing spectroscopic measurements of the Martian atmospheres composition through solar occultations, limb, and nadir observations. Like the ACS, NOMAD is comprised of three channels, using them to monitor spatial and temporal changes in trace gas distributions, localise sinks and sources of trace gas species, and further our understanding of Mars' water and CO_2 cycles [Vandaele et al., 2015]. The Solar Occultation (SO) channel operates within the infrared spectral range of 2.3–4.3 μm, and can achieve spectral resolving powers of up to 20,000. The Limb, Nadir, and solar Occultation (LNO) channel also operates within the infrared (2.3–3.8 μm), which as the name implies also

has the capability of performing Nadir and Limb observations and can perform with spectral resolving power values of 10,000. Both the SO and the LNO channels are capable of providing trace gas profiles with vertical resolutions between 0.8–1 km. Operating in nadir mode, the LNO has an observational footprint varying between 0.5×68 km^2 and 17×51 km^2, and both the SO and LNO channels have spectral resolutions one magnitude greater than any other spectrometer past or present involved in Mars observation. The third channel covers ultraviolet and visible (UVIS) wavelengths, spanning a spectral range of 200–650 nm, and is capable of operating in all three observational modes. In nadir, the observational footprint is 5×56 km^2 , and solar occultation measurements in UVIS can be made with vertical resolution $<$ 300 m. The expected detection limits for a number of important trace gas species for the NOMAD and its SO channel are presented in Figure 1.6, and highlights their dependence on altitude and optical opacity.

NOMAD is also capable of distinguishing between various isotopologues of CH_4 and H_2O, e.g. $^{12}CH_4$, $^{12}CH_3D$ and HDO, where D refers to the deuterium hydrogen isotope ^2H. This enables NOMAD to become a valuable tool in identifying sources of planetary activity such as active volcanism and outgassing, and providing constraints on the nature (i.e. biological or geological) of any observed CH_4 releases. NOMAD has recently been used to produce the first measurements of the D/H ratios variance with altitude and the evolution of the profiles over the course of a Martian year [Villanueva et al., 2019, Villanueva et al., 2021]. However, extensive observational campaigns using the NOMAD have failed to observe any traces of CH_4 within the atmosphere since it began its scientific campaign in 2018 [Liuzzi et al., 2019, Korablev et al., 2019].

The spectrometer has also successfully measured profiles of ozone throughout MY34–35 [Patel et al., 2021], and recorded an enhancement of O_3 in the northern latitudes at high altitudes during the Northern hemispheres autumn–winter period for the first time. This set of O_3 profiles provided the most comprehensive account of the global distribution of O_3 on Mars to date, and provides the scientific community with enough data to further investigate the anti-correlative relationship between O_3 and water vapour and a means to develop a better insight into the odd-oxygen and odd-hydrogen photochemical cycles on Mars.

The SO channel has been performing a large number of observations of H_2O vapour during the MY34–35 period, over the course of which Mars experienced a global dust storm event [Sánchez-Lavega et al., 2019, Kass et al., 2020] that saw the entire planet enshrouded in a veil of fine uplifted dust grains. NOMAD measured a substantial increase in water vapour abundances in the mid-altitudes (40–100 km) during the peak of the global dust storm event [Aoki et al., 2019], and researchers have since used this data to conclude that the transport

of Martian dust to heights above 40 km increases atmospheric temperatures due to solar absorption, preventing the development of ice clouds in these high altitude, and enables water vapour to accumulate in greater volumes than in non-dust storm scenarios [Neary et al., 2020], a valuable insight into the relationship between the Marian dust and water cycles.

Nadir observations of carbon monoxide (CO) have been carried out by the NOMADs LNO channel [Smith et al., 2021], measuring spatial and seasonal variatons of the CO column mixing ratio across MY34–35. Comparisons of these measurements with model results using the same models that were used in the comparisons of the CO observations made by the Compact Reconnaissance Imaging Spectrometer for Mars (CRISM) aboard the MRO of MY28–33 [Smith et al., 2018] show an improvement in coincidence, which is primarily due to improvements in the technology between the NOMAD and CRISM. The accuracy and resolution of NOMAD makes it one of the strongest tools for remote sounding of Mars, and has helped expand our knowledge of Mars' atmosphere in the first three years of its operation alone.

1.3 1-D Global Mean Models

$$\frac{dn_i}{dt} = P_i - n_i L_i + \frac{d\theta_i}{dz} \tag{1.1}$$

The general equation that is used to calculate the change in the abundance, n_i, of trace gas species i within a 1-D atmospheric model is presented in Equation 1.1. P_i denotes the rate of chemical production of species i (molec. cm^{-3} s^{-1}), L_i denotes the rate of loss of i (s^{-1}), and θ_i denotes the flux due to vertical transport. Equation 1.1 distinguishes itself from other time-*in*dependent 1-D Mars models such as those used by McElroy and Donahue [1972], Nair et al. [1994], and Krasnopolsky [2010] that set the left hand side of Equation 1.1 to zero and task their models to calculate the resultant values of n_i. These models are used to study the globally averaged atmospheric state of Mars, which was an especially important pursuit prior to the abundance of observational data that only really started to accumulate in the 1990s. The globally averaged 1-D models were the first to theorise the responsibility of HO_x species in stabilising Mars' CO_2 and preventing the runaway build-up of O_2 and CO [McElroy and Donahue, 1972]. Their numerical results when compared to observations however are rather poor, especially when used to calculate the abundances of tracers with long atmospheric lifetimes. These discrepancies appear from a number of sources, an important one being the atmospheric temperature profiles assumed. Globally averaged 1-D models throughout the 1970's typically assumed a linear decrease in temperature from a prescribed surface temperature to an altitude at (what was then assumed) the boundary layer to a constant 150–200 K above [Parkinson and Hunten, 1972, McElroy and Donahue, 1972]. These types of

profiles would result in large abundances of water vapour being restricted to altitudes below 5–km, and a consequent lack of HO_x able to reform CO_2 from CO, resulting in model CO values exceeding observational constraints (CO columns between 900–1100 ppm) [Lefèvre and Krasnopolsky, 2017].

Attempts to improve global average 1-D model results, a temperature dependent CO_2 absorption cross-section was adopted which increased the photolysis rate of H_2O, but took the CO discrepancies the other way by over-producing HO_x and under-producing CO by up to a factor of 8 whilst producing good agreements for unstable tracers like O_3 and H_2O_2 Nair et al. [1994], Krasnopolsky [2010]. Other suggestions included the alteration of various HO_x chemical reaction rates to increase CO_2 reformation, but none of the changes were found to be supported by either future laboratory work [McCabe et al., 2001] or Earth atmospheric science [Jucks et al., 1998]. Heterogeneous chemistry between gas phase tracers and atmospheric dust and water ice were first studied using the 1-D model of Yung et al. [1988] equipped with uptake of H and HO_2 on dust and ice grains, and found that uptake coefficients from laboratory measurements were capable of strongly decreasing the abundance of HO_x [Anbar et al., 1993] and improving CO abundances [Krasnopolsky, 1993]. Later a global mean 1-D model used by Krasnopolsky [2006b] utilised updated chemical reaction rates, absorption cross-sections, and dust and ice profiles to show that the uptake coefficients required for HO_x species on ice have to be between 4 and 30 times greater than those recommended for use in Earth atmospheric studies to coincide the model CO with the observational constraint of 900-1100 ppm. Further, these required uptakes decreased the coincidence of the model's O_3 (too low) and H_2O_2 (too high) column and their latitudinal and seasonal variances.

Global mean 1-D models are specialised for the study of Mars' most stable trace gas species that have atmospheric lifetimes that span multiple decades (CO, O_2) to thousands of years (H_2), as time-dependent models would need to perform model runs over these long time periods to derive meaningful conclusions. These models however, solving for the global mean equilibrium atmospheric constitution, cannot account for the seasonal and latitudinal variances experienced by Mars' atmospheric water vapour, temperature, dust, or ice. These parameters can all produce extreme impacts on the HO_x distributions and abundances, which in turn will effect the catalytic recycling of CO over the Martian year and subject the globally averaged 1-D models to inaccuracies.

1.3.1 Time-Dependent 1-D Models

1-D models that utilise Equation 1.1, such as the 1-D photochemistry submodule used in this thesis, are referred to as being *time dependent*, and are capable of studying the impacts of physical atmospheric parameters that vary in time such as surface pressure, water vapour, and temperature on chemical abundances. This enables models to assess diurnal variations in short-lived trace gas species such as HO_x compounds and O_3, and seasonal variations when equipped with temporally varying H_2O and temperature profiles. As there are no considerations of horizontal advections, time-dependent 1-D models of Mars are subject to inaccuracies when used in extended runs to model trace gas species with longer chemical lifetimes such as H_2 and CO. Further, these models are only capable of studying specific local conditions, as opposed to the global means found using the models detailed in Section 1.3. One of the first time-dependent 1-D chemistry models for Mars was developed by Shimazaki and Shimizu [1979], using time dependent diurnally averaged surface temperature and water data recorded by the Viking Landers to model a seasonally varying ozone column that was found to be in close coincidence with prior observations made by the Mariner 9 observations Barth et al. [1973]. The same time-dependent model was used again by Shimazaki [1981], this time using the diurnal variances of temperature and water vapour, finding that model coincidences marginally improved in comparison to the earlier study [Shimazaki and Shimizu, 1979]. This time-dependent model, with a very short and sporadic dataset compared to modern standards, qualitatively predicted the formation of a layered structure for ozone that was later confirmed by the Phobos 2 UV spectrometer [Blamont and Chassefiere, 1993], and also predicted the decrease in O_3 in mid-latitudes during the northern summer-fall period due to the encroaching water vapour from sublimation of the polar caps seen much later by Mars Express' SPICAM [Lebonnois et al., 2006].

Utilizing an updated 1-D time-dependent model, Krasnopolsky [2006a] incorporated the temporally variable temperature and water vapour data recorded by the MGS TES to model a diurnally variable H_2O_2 abundance due to the effects of heterogeneous loss of HO_x on water ice with CO_2, H_2, and O_2 values as constants set to observational values. Krasnopolsky [2009] used a 1-D time-dependent photochemical model and displayed that the model was capable of reproducing O_3 column abundances as measured by MEX's SPICAM in the mid-latitude regions when the long-lived tracers of the region where held constant at their observed values.

1.4 Research Questions

The primary aim of my thesis is to develop a sophisticated 1-D photochemistry scheme to aid in the interpretation of retrievals of trace gas species by the NOMAD and ACS spectrometer suites aboard the ExoMars Trace Gas Orbiter. The following research questions are addressed within my thesis:

1. What are the bounds on the atmospheric lifetimes of methane and non-methane volatile organic compounds on Mars, given our current knowledge of its atmospheric photochemistry?
2. Does a more detailed one dimensional photochemistry submodule improve model agreements with observations of trace gas species?
3. Can a photochemical adjoint for Mars' atmosphere provide information regarding the sensitivity of inorganic and chlorine-containing trace gas species on Mars to the abundances of other trace gas species?

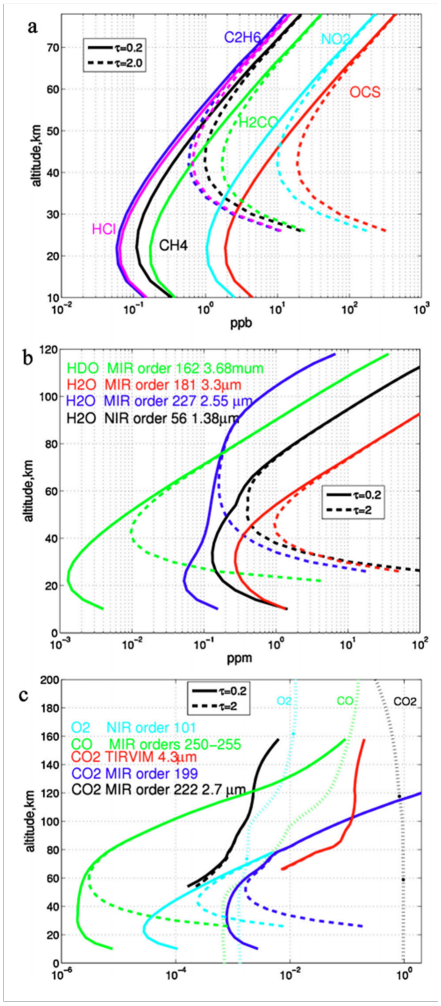


Figure 1.5: The sensitivities of the NIR, MIR, and TIRVIM spectrometer channels of the ACS. From top to bottom: MIR lower detection limits of various trace gases; ASC-NIR and MIR sensitivities to various H_2O and HDO wavebands; ACS sensitivities to CO, CO_2, and O_2 with altitude. τ indicates atmospheric optical depth at measurement time. The fine dashed lines of the bottom plot indicate abundances predicted by the LMD GCM, extracted from the Mars Climate Database v5.2 [Millour et al., 2015]. Figure taken from Korablev et al. [2018].

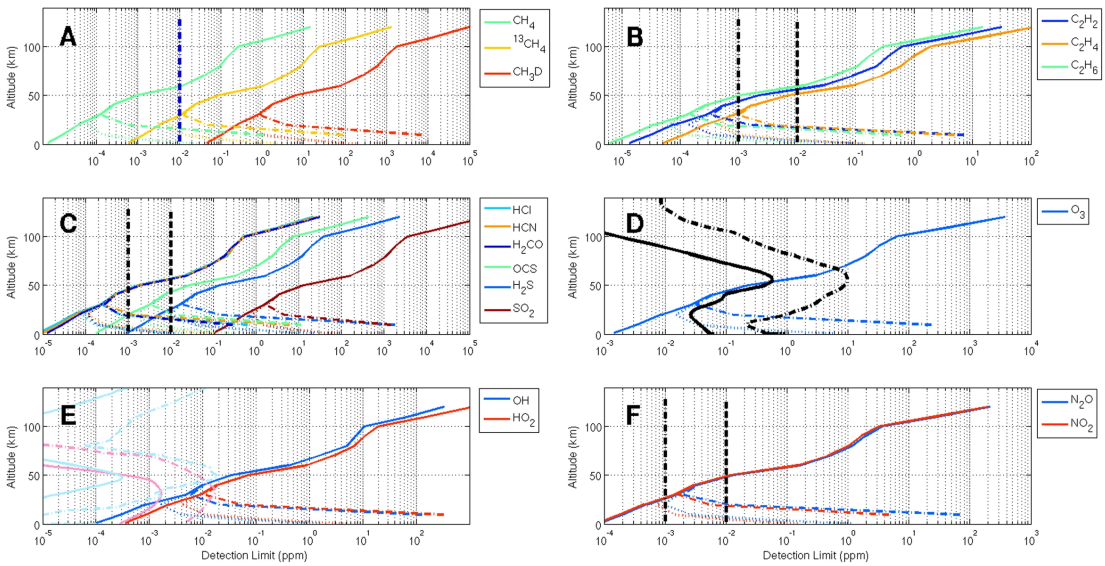


Figure 1.6: Detection limits for a number of trace gas species for the NOMAD spectrometer for three aerosol optical depth (AOD) cases: Solid lines: AOD = 0.0, dotted lines: AOD = 0.1, dash and dots: 1.0. A) CH_4 and two isotopologues; blue line indicates a VMR of 10 ppb, the maximum value observed by the MSL [Webster et al., 2015]. B) C_2H_2, C_2H_4, C_2H_6; black lines represent VMRs of 1 and 10 ppb. C) HCl, HCN, HCHO, OCS, H_2S, SO_2; black lines represent VMRs of 1 and 10 ppb. D) O_3; black lines represent results from the GEM-Mars model [Neary and Daerden, 2018]: solid: yearly average profile, dash and dots: maximum values at each altitude calculated by GEM-Mars. E) OH and HO_2. Pink (HO_2) and cyan (OH) lines are results of the GEM-Mars model. Solid: yearly average, dash and dots: maximum values at each altitude calculated by GEM-Mars. Figure taken from Vandaele and Rodriguez-Gomez [2013].

Chapter 2

Martian Atmospheric Photochemistry

2.1 Inorganic Chemistry

Tracer	Volume Mixing Ratio	Citations
CO_2	0.95	i
CO	300–1600 PPM	ii
N_2	0.018–0.027	iii
Ar	0.016–0.020	iii
H_2O	0–2000 PPM	iv
H	3–30$\times 10^4$ molec. cm^{-3}	v
OH	0.05–0.20 PPB	vi
HO_2	$<$ 200 PPB (Upper Limit)	vii
H_2	17 PPM	viii
H_2O_2	0–60 PPB	ix
O	0.0005–0.002	x
O_2	1800–5800 PPM	xi
O_3	0–450 PPB	xii

Table 2.1: Inorganic trace gas species in the Martian atmosphere and measured abundances. i) [Belton and Hunten, 1966, Fedorova et al., 2009], ii) [Fedorova et al., 2021, Sindoni et al., 2011, Smith et al., 2021], iii) [Owen et al., 1977, Mahaffy et al., 2013], iv) [Trokhimovskiy et al., 2015a, Smith et al., 2009, Smith, 2002, Aoki et al., 2019], v) [Chaufray et al., 2008], vi) [Todd Clancy et al., 2013], vii) [Villanueva et al., 2013], viii) [Krasnopolsky and Feldman, 2001], ix) [Krasnopolsky et al., 1997, Encrenaz et al., 2008, 2004b], x) [Ritter et al., 2019, Qin, 2020, Chaufray et al., 2009], xi) [Hartogh et al., 2010, Sandel et al., 2015, Fedorova et al., 2021], xii) [Patel et al., 2021, Barth et al., 1973, Olsen et al., 2020]

.

Between 4.5–3.7 billion years ago, Mars sustained a global magnetic field via a subsurface flow of liquid rock around the planetary core [Mittelholz et al., 2020], providing it with a form of protection against the continuous bombardment of charged particles emitted by the Sun in the solar winds. However, the magnetic dynamo could not be sustained for a longer period like the Earth's due to Mars' lower density and planet radius. The smaller mass of Mars ($\sim$0.107 M_{Earth}) resulted in a more rapid cooling of the outer core, which solidified and could not maintain the global magnetic field. The exposure of the atmosphere to the solar winds caused the Martian atmosphere to experience heavy rates of erosion from charged particles

stripping the gases away to space. Modern Mars currently experiences atmospheric loss rates of approximately 2 kg s^{-1} due to the solar winds, as measured by the Mars Atmosphere and Volatile Evolution (MAVEN) orbiter [Jakosky et al., 2018], and over a period of roughly 3.7 billion years surface pressures on the planet steadily dropped from 0.5 bar during the dynamo period [Jakosky et al., 2017] to varying spatially and seasonally between 4–9$\times 10^{-3}$ bar (400–900 Pa) today, having lost roughly 66% of its original mass.

The low-pressure atmosphere that remains today is dependent on a series of photochemical networks to maintain the stability of its primarily carbon dioxide ($\sim$ 95% by volume) atmosphere. The atmospheric pressures of Mar today are lower than water's vapour pressure at its triple point, which prevents water from condensing from the gas phase to the liquid phase. The phase diagram of H_2O, with surface pressures on Mars noted, is displayed in Figure 2.1a. The majority of Mars' H_2O is trapped as ice beneath the polar caps [Christensen, 2006], leaving between 0–70 precipital microns (pr μm) in the atmosphere as water vapour with strong spatial and seasonal variances [Fouchet et al., 2007, Trokhimovskiy et al., 2015a]. Both CO_2 and H_2O vapour are subject to strong photolysis all the way to the surface, which sees UV photons breaking CO_2 into carbon monoxide and atomic oxygen ($O(^3P)$ and $O(^1D)$), and H_2O vapour into hydrogen atoms (H) and hydroxyl radicals (OH). These highly reactive species chemically react with each other to form many other short-lived and inorganic tracers in a complex photochemical network, and makes Mars' atmosphere an oxidising environment. The most immediately noticeable result of the oxidising effects that these photolytic products have on Mars is the distinct red colour of the Martian surface, caused by the oxidation of nanophase ferric oxides contained in the soil [Bibring et al., 2006]. This red, rusted dust only has a typical depth of 0.1–11.1 μm on the surface however [Cantor, 2007], and is a dull grey where there has been no prominent exposure of the iron compounds to the oxidising atmosphere above.

The interactions between products produced by the UV photolysis of CO_2 and H_2O in the atmosphere produce a wide range of short-lived tracers that have been successfully observed by remote sensing measurements and *in-situ* instruments such as those the Curiosity and Perseverance rovers. Nitrogen (N_2) and argon (Ar) are also present with volume mixing ratios of 0.0189 and 0.0193 [Mahaffy et al., 2013], two species that are photochemically inert below altitudes roughly 120 km. Table 2.1 provides a list of the inorganic trace gas species found in Mars' atmosphere alongside typical volume mixing ratios measured by various orbiters and ground-based spectrometer telescopes.

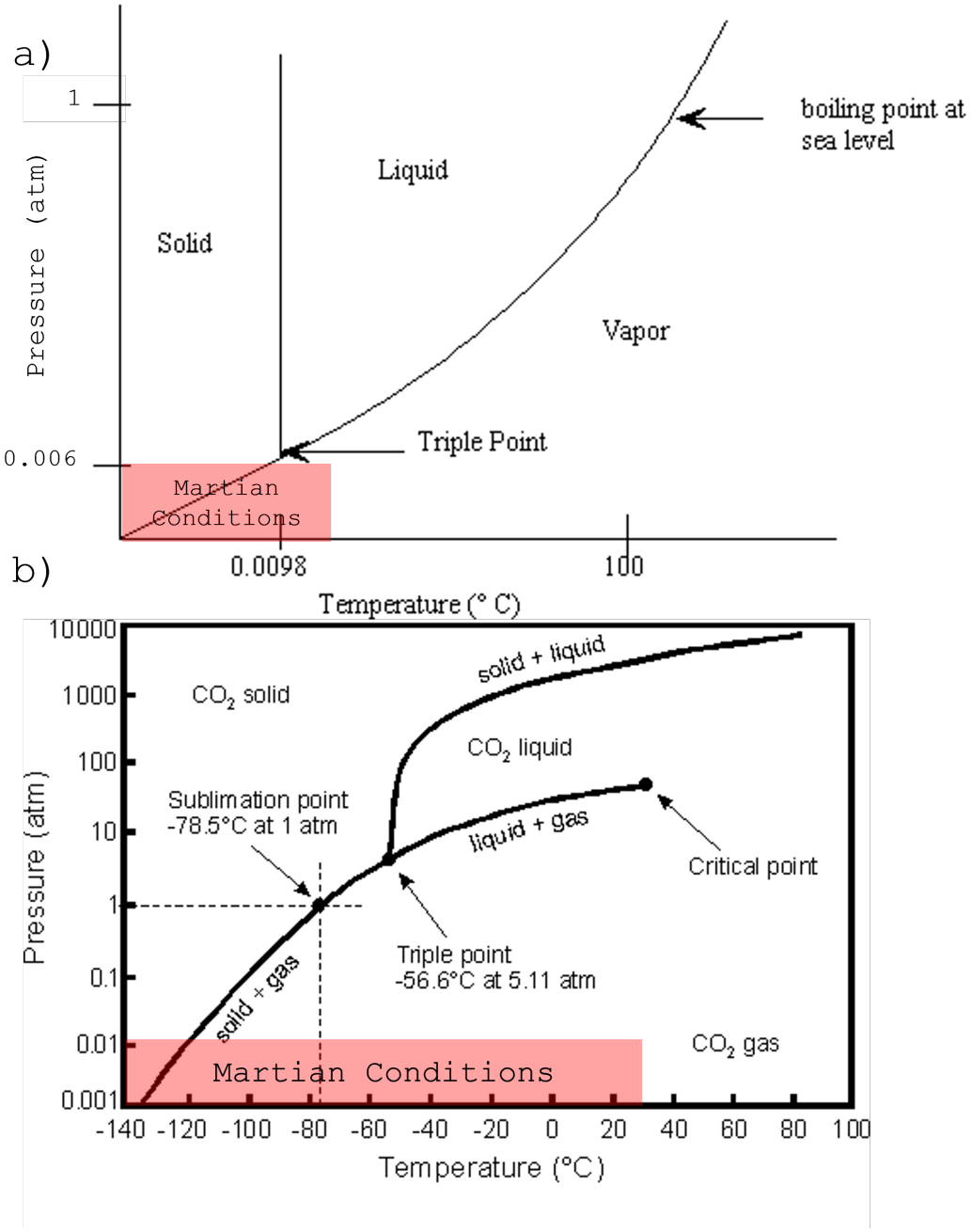


Figure 2.1: Phase diagrams of a) H_2O and b) CO_2 with respect to atmospheric pressure and temperature. Conditions experienced in the atmosphere of Mars are highlighted in red. A typical Martian surface pressure is of magnitude 10^{-3} atm, and temperatures can reach lows of -150 °C during the polar nights, and highs of 20 °C at noon at the equator.

2.1.1 Carbon Dioxide

Carbon dioxide is the most abundant gas in the atmosphere of Mars. In the presence of UV radiation from the Sun CO_2 is capable of photodissociating into CO and two forms of atomic oxygen, the ground-state, O(^{3}P), and the higher energy excited-state O(^{1}D), depending on the energy, and therefore wavelength (λ), of the radiation:

$$\begin{aligned} &(\mathrm{R1}) \quad CO_2 + h\nu \longrightarrow CO + O(^3P) \quad \lambda < 205\,nm \\ &(\mathrm{R2}) \quad CO_2 + h\nu \longrightarrow CO + O(^1D) \quad \lambda < 167\,nm. \end{aligned}$$

Without any additional trace gas species, the reactions R1 and R2 would result in the CO_2 dominant atmosphere breaking down to one composed primarily of CO and O_2 due to the reverse reaction involving a non-reacting third species, M, being spin-forbidden,

$$(\mathrm{R3}) \quad CO + O(^3P) + M \longrightarrow CO_2 + M,$$

in which the reactant and the product gases exist in two different spin states, raising the activation energy required of the reaction to form a stable product from the reactant, and in turn greatly decreasing the rate of reaction. The atomic oxygen atoms would then engage in the formation of O_2 molecules by colliding with one another in a three-body reaction,

$$\begin{aligned} &(\mathrm{R4}) \quad O(^1D) + M \longrightarrow O(^3P) + M \\ &(\mathrm{R5}) \quad O(^3P) + O(^3P) + M \longrightarrow O_2 + M. \end{aligned}$$

The rate at which O(^{3}P) atoms combine to form O_2 (R5) is up to 100 times greater than the rate at which they react with CO to reform CO_2 (R3). This proved difficult to reconcile in the 1960's prior to the postulation that water vapour may exist in Mars' atmosphere [Kliore et al., 1965, Belton and Hunten, 1966], as the only other reaction of note in a pure CO_2 atmosphere is the slow photolytic destruction of O_2 back to ground-state atomic oxygen atoms. The problem of CO_2's stability on Mars would find it's solution in 1972, when researchers postulated the theory that trace amounts of water in the atmosphere could produce odd-hydrogen (HO_x = H + OH + HO_2) through UV photolysis in quantities large enough to catalyse the reformation of CO to CO_2. The chemical network responsible for this recycling is expanded upon in greater detail in the next section.

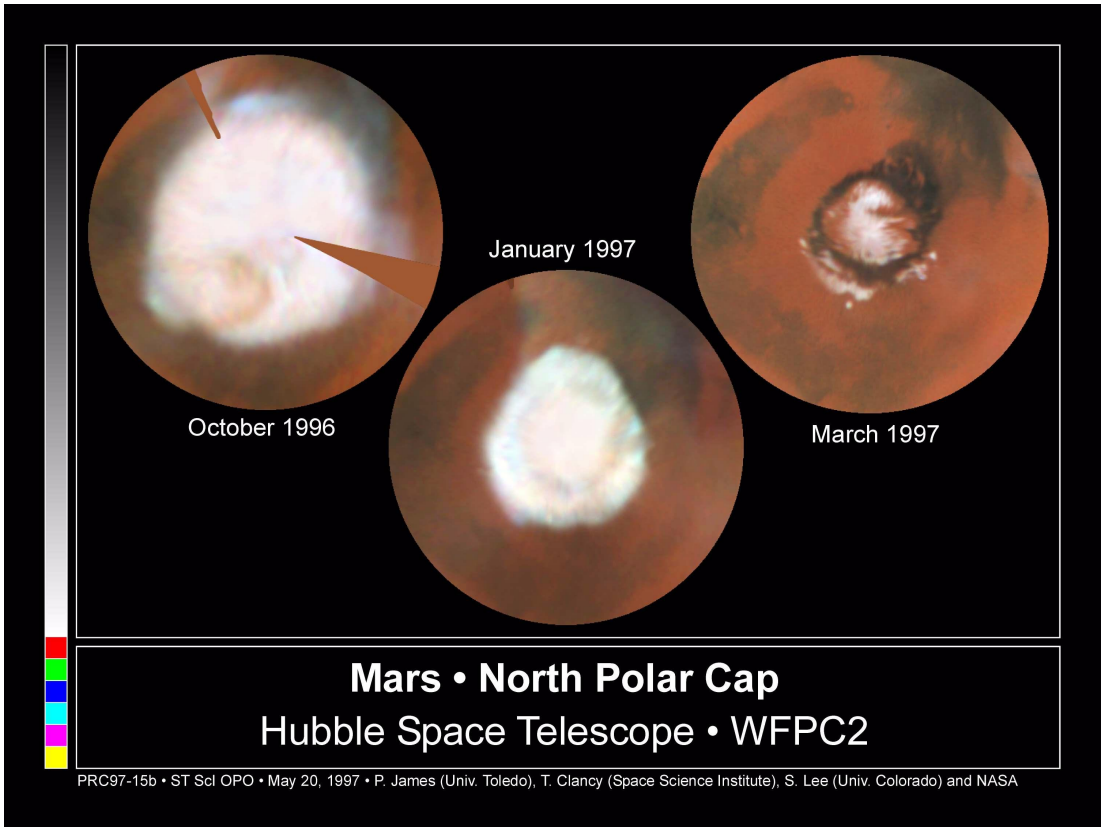


Figure 2.2: Condensation and sublimation of Mars' northern pole as seen by the Hubble Space Telescope . Figure taken from HST.

The low atmospheric pressures enable the condensation of CO_2 gas to solid CO_2 ice during each pole's respective winter period, producing clouds of CO_2 ice crystals which fall and gather at the polar caps. A phase diagram of CO_2 is presented in Figure 2.1b, with typical Martian atmospheric conditions highlighted in red. Pressures of $\sim$ 100 Pa (0.001 atm) are found roughly 20 km from the Martian surface, at which point the sublimation point of CO_2 is experienced at -136.8 $^{\circ}$C [Forget et al., 1998]. These temperatures are commonly found during the polar nights. The seasonally expanding and contracting CO_2 northern polar cap captured by the Hubble Space Telescope is presented in Figure 2.2. The presence of CO_2 ice clouds and CO_2 snowfall was first postulated in 1970 when Mariner 6 and 7 detected an absorption feature at 4.3 μm [Herr and Pimentel, 1970], a strong signature of CO_2 ice. In 1998, observations made by the Mars Pathfinder's lander [Smith et al., 1997] were combined with ground-based spectroscopic telescopes measurements to infer that an image taken of a blue whisp of cloud by the Imager for Mars Pathfinder (IMP) could be composed of CO_2 ice [Clancy and Sandor, 1998]. The TES aboard the MGS was used in the first observation campaigns with the intended aim of detecting CO_2 ice clouds in the early 2000s, and successfully detected their presence in the Martian mesosphere (40–100 km altitudes) [Clancy et al., 2003, 2007], which would be followed by the first unambiguous spectrometer detections

performed by the Mars Express Orbiter's Spectroscopy for Investigation of Characteristics of the Atmosphere of Mars (SPICAM) [Montmessin et al., 2006] in 2006 and the Observatoire pour la Minéralogie, l'Eau, les Glaces et l'Activité (OMEGA) in 2007 [Montmessin et al., 2007]. To date, Mars is the only terrestrial planet in the solar system known to produce clouds composed of its primary atmospheric constituent. The ExoMars TGO continues to add to the list of CO_2 ice cloud observations, having used the ACS NIR and TIRVIM channels to detect mesospheric CO_2 ice clouds in 2021 [Luginin et al., 2021], however the exact process responsible for the condensation of CO_2 gas is still poorly understood as few instruments, like MAVEN, are capable of observing the polar nights due to the nature of their orbits around the planet, which is where and when the majority of the CO_2 condensation and sublimation cycles are taking place.

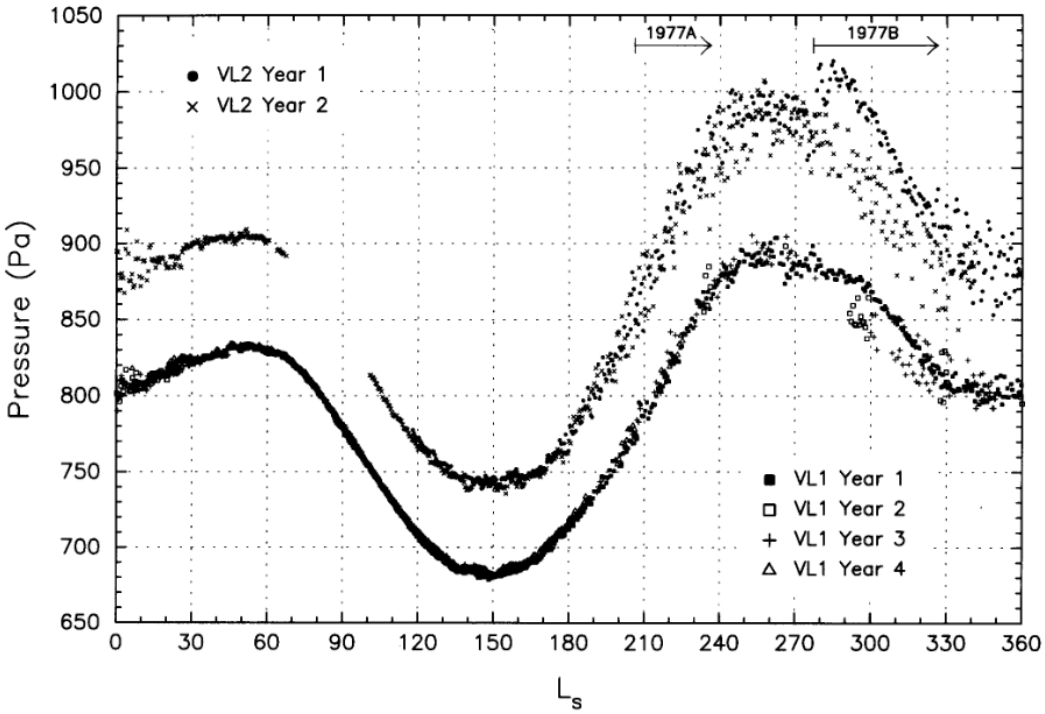


Figure 2.3: Seasonal variations in surface pressure measurements recorded by the Viking I and Viking II Lander produced by the condensation and sublimation of the CO_2 ice caps in the polar regions. Figure taken from Wood and Paige [1992].

The winter condensation of CO_2 ice, and the following sublimation when the polar caps are exposed to sunlight in the spring and summer season, has the effect of removing and resupplying up to 30% of the entire planet's atmospheric mass on a seasonal cycle, which results in strong seasonal variations in surface pressures across the globe as seen by the

Viking Landers in Figure 2.3. Global circulation models of Mars that incorporated a seasonal CO_2 ice condensation and sublimation routine [Pollack et al., 1990, 1993, Haberle et al., 2008] were capable of replicating the strong seasonal surface pressures observed by the Viking landers [Guo et al., 2009], but were unable to explain the residual southern cap.

The northern polar cap of Mars has a diameter of roughly 1100 km and is primarily composed of water ice, with radar measurements performed by orbiters such as the Mars Reconnaisance Orbiter revealing approximately 1.6 million km^3 of water ice below the northern polar cap [Carr and Head III, 2003, Smith et al., 2001]. Radar measurements performed by the Mars Advanced Radar for Subsurface and Ionospheric Sounding (MARSIS) aboard the Mars Express orbiter found a similar H_2O ice abundance, roughly 1.6 million km^3, within the southern polar cap [Plaut et al., 2007]. These polar ice sheets experience a seasonal deposition, and subsequent sublimation, of a roughly 1.5–2 m thick layer of CO_2 ice being deposited on the top. The southern polar cap, however, is significantly smaller than the northern cap, with a diameter of 400 km, with massive subsurface deposits of CO_2 ice revealed in 2011 by MRO radar observations [Phillips et al., 2011].

The CO_2-based atmosphere of Mars also produces some complications with regards to chemical rate coefficients used in the modelling of Martian photochemistry. Three-body rate coefficients require a bath gas, some species inert to the chemical reaction that absorbs excess energy the initially unstable product via collision to allow the product to exist in a stable state. Databases and sources containing rate coefficients calculated through laboratory experiments or numerical modelling approaches such as the NIST Chemical Kinetics Database [Manion et al., 2015] and the JPL Chemical Kinetics and Photochemical Data for Use in Atmospheric Studies evaluations [Burkholder et al., 2015] are extensively used for planetary modelling. Their values however often make use of N_2 as the system bath gas due to it being the primary constituent of Earth's atmosphere. The differences in molecular structure of N_2 and CO_2, where CO_2 has an additional bond available to absorb energy increasing the probability of a successful absorption collision, result in three-body rate coefficients being more efficient in the presence of a CO_2 bath gas than N_2.

To produce accurate abundances of CO, O_3, and O_2 when compared to observations, a 1-D photochemical model of Mars produced by Nair et al. in 1994 [Nair et al., 1994] found that multiplying all three-body rate coefficients calculated with N_2 as a bath gas by a factor of 2.5 greatly improved model and observation coincidences. Shortly afer, a laboratory study found that the three-body reaction involving the production of ozone from the reaction of atomic oxygen with molecular oxygen was roughly 2.075 times faster in the presence of CO_2 than N_2 [Sehested et al., 1995].

2.1.2 Water Vapour and Hydrogen Chemistry

Water can only exist in liquid form on Mars below the surface, as atmospheric pressures above ground lie below water's vapour pressure at its triple point (see Figure 2.1a) - at temperatures below the freezing point of water, vapour immediately condenses to the solid ice state, and above freezing temperatures, water ice sublimates back to the vapour state. The north and south polar caps store roughly 1.6 million cubic kilometers of water ice below the seasonally variable CO_2 ice layer respectively [Smith et al., 2001, Carr and Head III, 2003], and their periodic exposure to sunlight enables the sublimation of water ice to vapour that activates a seasonal water vapour cycle, displayed in Figure 2.4.

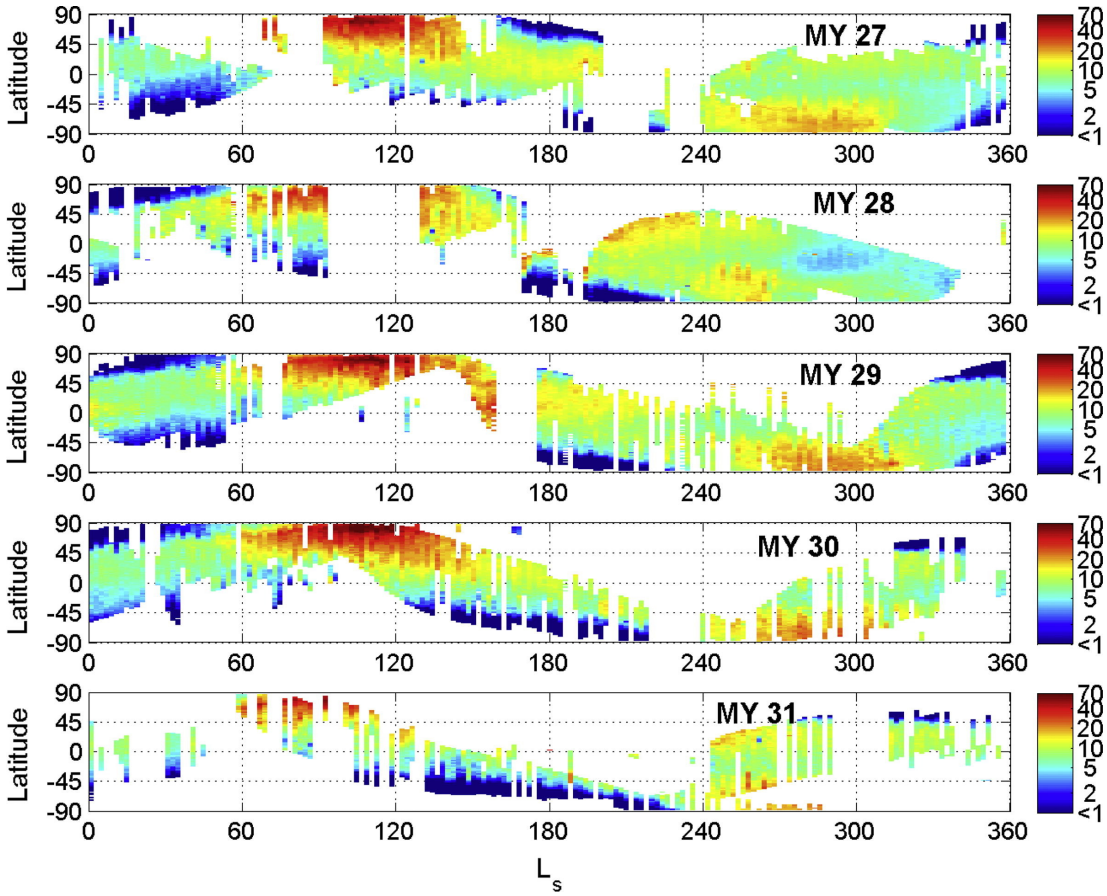


Figure 2.4: Seasonal variations in the water vapour column of Mars (in precipitable microns, pr. μm) as measured by the SPICAM spectrometer aboard the Mars Express orbiter over MY 27–31. Figure taken from Trokhimovskiy et al. [2015a].

The northern polar cap is the most dominant driver of the seasonal variances as seen in Figure 2.4, where exposure to sunlight during the northern hemisphere's spring and summer (0–180° L_S) causes the sublimation of CO_2 and H_2O ice, greatly elevating the H_2O column abundances from $\sim$ 10 pr. μm to highs of 70 pr. μm in the high northern latitudes. These

high abundances are gradually transported to the lower latitudes in the equatorial regions. A prominent asymmetry can be noticed too between the maximum abundances produced between the northern and southern caps during their respective summers, where the southern hemisphere's summer starts at 270° L_S.

The vertical distribution of Mars' water vapour has been extensively measured through remote sensing campaigns over the past two decades, with notable advancements made by the Mars Express' Planetary Fourier Spectrometer (MEX-PFS) [Fouchet et al., 2007, Tschimmel et al., 2008, Sindoni et al., 2011] and SPICAM spectrometers [Maltagliati et al., 2011, Trokhimovskiy et al., 2015a, Maltagliati et al., 2013] that conducted the first annual survey of water vapour's vertical structure. The TES produced a significant number of column abundance measurements of H_2O across the globe over the MGS satellite's 10 year science campaign from 1996 to 2006 [Smith, 2002, Wolkenberg et al., 2011, Smith, 2004], enabling an intensive data assimilation procedure to model the seasonal variations in the vertical distribution of water over a climatological mean Mars year lacking any major global dust storm events [Steele et al., 2014], the results of which are displayed in Figure 2.5. The TGO has recently conducted studies of the water vapour distribution and it's variance during global dust storm events [Belyaev et al., 2021, Aoki et al., 2019], and its strong correlations with the very recent observations of hydrogen chloride (HCl) [Aoki et al., 2021].

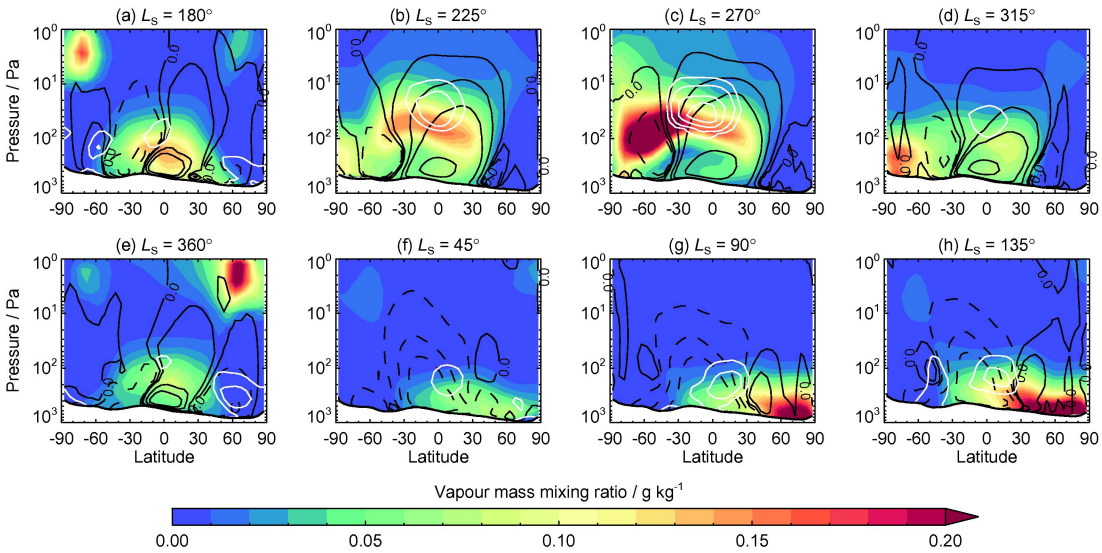


Figure 2.5: Results of the assimilation of TES measured water vapour columns over MY24 (a–e) and MY25 (f–h) displaying the zonally averaged vertical distribution of water vapour mass mixing ratios (g kg^{-1}) with latitude and their variances over one Mars year. White contours denote water ice mixing ratios with contour values [0.005, 0.01, 0.02, 0.03] g kg^{-1}; Black solid and dashed contours denote the mean meridional circulation in clockwise and anti-clockwise directions respectively, with contour values of [0.1, 0.5, 1.5] $\times 10^9$ kg s^{-1}. Figure taken from Steele et al. [2014].

The seasonal changes in the water vapour distribution is primarily caused by the orbital alignment of Mars. Mars' orbital eccentricity is greater than that of Earth's (0.0934 and 0.0167 respectively), resulting in more pronounced seasonal changes in solar irradiation to the planet. During 180–270°, Mars' southern polar cap is exposed to sunlight triggering the sublimation of H_2O ice deposited on the surface back into the atmosphere, whereas the northern cap is in darkness, experiencing colder temperatures, causing the condensation of H_2O and a drier northern hemisphere. At perihelion (251° L_S) Mars is at its closest approach to the Sun, and the dust content of the atmosphere increases during the dust-storm season. The dust grains readily absorb IR radiation from the Sun and can heat the surrounding air by up to 35 °C hotter than equivalent dust-free air [Kass et al., 2016]. The rising atmospheric temperatures in the south rise cause the water vapour saturation level (hygropause) to elevate, restricting water vapour to altitudes below 40–50 km. It has been discovered only in the past decade that water vapour can exist in a super-saturated state above the Martian hygropause [Maltagliati et al., 2011, Fedorova et al., 2020], which occurs at the same time as the uplifting of dust into the upper atmosphere. 3-D Martian GCMs have been capable of producing water vapour in abundances above saturation at this time by transporting dust to altitudes above roughly 40 km [Neary et al., 2020], which absorbs solar radiation and increases the local atmospheric temperatures preventing the condensation of water vapour to ice clouds, and enabling water vapour to exist in a supersaturated state at high altitudes.

As Mars exits perihelion, and begins to move away from the Sun over 315–90° L_S air temperatures decrease with the drop in solar radiation intensity, and the northern polar cap becomes exposed to sunlight while the southern cap enters it's autumn and winter periods. North pole water ice sublimates to gas, whilst south pole vapour condenses to ice, causing the southern hemisphere to become drier, whilst the northern hemisphere becomes more moist. The decreasing atmospheric temperatures trigger a drop in the saturation level of water vapour in the northern hemisphere, lowering from 40–50 km to between 10–15 km. The lower levels of atmospheric dust during this period also prevent the accumulation of water vapour at supersaturated levels above the hygropause in the northern spring and summer.

The UV photolysis and oxidation via reactions with $O(^1D)$ produced of water vapour molecules is the dominant source of odd-hydrogen (HO_x = H + OH + HO_2) species below the hygropause, producing atomic hydrogen and hydroxyl radicals,

$$\text{(R6)} \quad H_2O + h\nu \longrightarrow H + OH \quad \lambda < 200\,nm$$
$$\text{(R7)} \quad H_2O + O(^1D) \longrightarrow 2OH \quad ,$$

which go on to form a chemical network responsible for the photochemical stability of the Martian atmosphere [Atreya and Gu, 1995]. The absorption cross-sections of CO_2 and H_2O reach their peak in the same UV spectra region ($120 < \lambda < 180$ nm), so the rate of H_2O photolysis greatly increases with altitude as the CO_2 column density overhead decreases. In drier regions, such as altitudes above $\sim$ 100 km or during the polar winter nights, the production of HO_x can become dominated by the oxidation of molecular hydrogen by $O(^1D)$ atoms produced by CO_2 photolysis,

$$(\mathrm{R8}) \quad H_2 + O(^1D) \longrightarrow OH + H \quad .$$

In the lower 100 km of the atmosphere, the OH produced in these reactions can react with CO to form CO_2, is upwards of 10^4 times more efficient at 298 K at the surface than the spin-forbidden reaction of $O(^3P)$ with CO. The H atom produced here as the second product is then capable of reacting via a three-body reaction with molecular oxygen to form hydroperoxyl radicals, HO_2, which proceed to react quickly with $O(^3P)$ atoms generated by the photolysis of CO_2, and recycles OH back into the atmosphere. This photochemical cycle was first postulated in 1972 and was one of the strongest theoretical inferences that O_2 could exist in the Martian atmosphere prior to conclusive observations [McElroy and Donahue, 1972],

$$\begin{aligned}
(\mathrm{R9}) \quad & CO + OH \longrightarrow CO_2 + H \\
(\mathrm{R10}) \quad & H + O_2 + CO_2 \longrightarrow HO_2 + CO_2 \\
(\mathrm{R11}) \quad & HO_2 + O(^3P) \longrightarrow OH + O_2 \\
\mathrm{Net:} \quad & CO + O(^3P) \longrightarrow CO_2 \quad ,
\end{aligned}$$

and is responsible for 85% of the total recycling of carbon monoxide back to CO_2 [Nair et al., 1994]. Modelling studies have shown that the total column loss of CO to the reaction with OH (R9) occurs at a rate approximately 100 times faster than the rate at which HO_x is produced via the UV photolysis of water vapour, implying that each OH molecule produced by the breakdown of an H_2O molecule is used in this cycle 100 times, acting as a very efficient atmospheric catalyst for CO_2 restoration.

HO_2 molecules produced within this cycle are also able to engage in chemical reactions with each other, producing hydrogen peroxide, H_2O_2. H_2O_2 was first hypothesised to exist on Mars as an explanation for the absence of organic compounds in the Martian soil measured by the Viking Landers in 1977 [Biemann et al., 1976, Oyama and Berdahl, 1977], due to its abilities as a powerful chemical oxidiser that may have sterilised the upper layers of the Martian surface [Bullock et al., 1994]. It took over 30 years for the first confirmed detections of hydrogen

peroxide on Mars to be made [Encrenaz et al., 2004a, Clancy et al., 2004]. The production and subsequent UV photolysis of H_2O_2 to two OH molecules produces a second odd-hydrogen cycle that modelling studies have shown recycle a further 8% [Krasnopolsky, 2010] of CO_2 photolysed to CO.

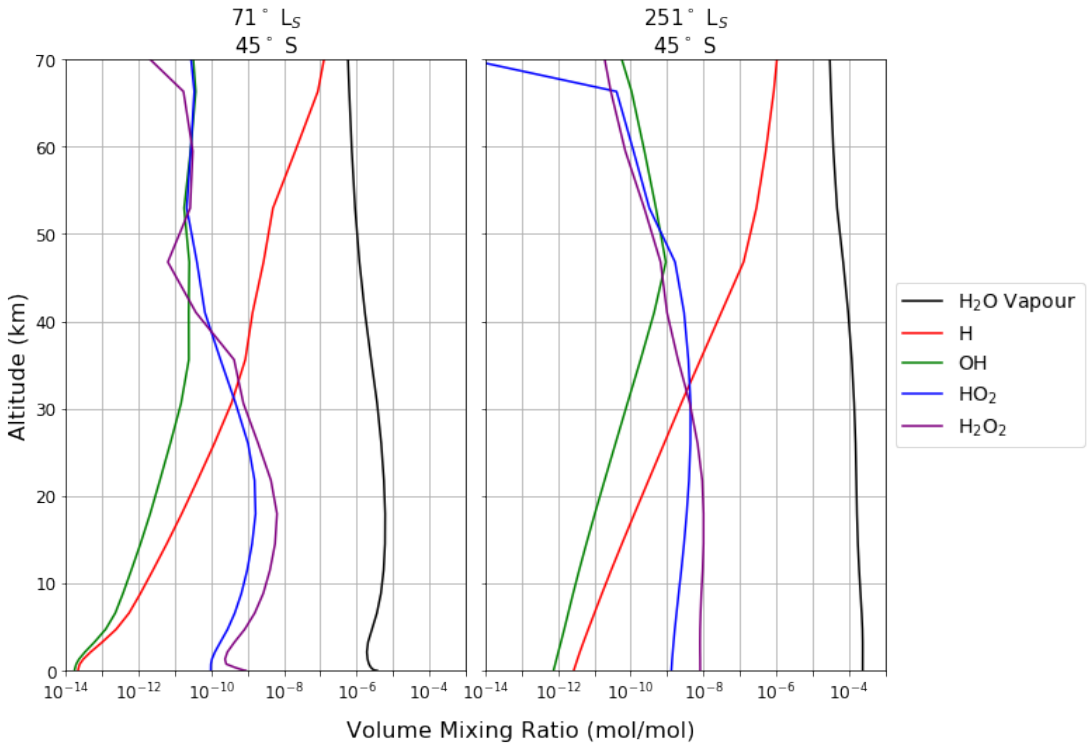


Figure 2.6: Vertical distribution profiles of H, OH, HO_2 and water vapour produced by the 1-D photochemistry model at 45° south at local noon. Left hand profiles are taken at aphelion, right hand profiles are taken at perihelion.

Figure 2.6 presents the volume mixing ratios of odd-hydrogen species and H_2O_2 produced by longitudinal mean water vapour profiles from the LMD-GCM at latitude 45° south, as calculated by the 1-D photochemistry model. Due to its production being controlled by the self-reaction of HO_2 molecules, the profile of H_2O_2 is expected to be similar in shape to that of HO_2 (Figure 2.6), with stronger deviations appearing above the hygropause where HO_2 abundances start to decline and UV photolysis of H_2O_2 increases with a clearer atmospheric column above.

These recycling cycles available for CO to convert back to CO_2 are prevented from repeating by three inorganic chemical reactions,

$$\begin{aligned}
&(\mathrm{R12}) \quad OH + HO_2 \longrightarrow H_2O + O_2 \\
&(\mathrm{R13}) \quad H + HO_2 \longrightarrow H_2 + O_2 \\
&(\mathrm{R14}) \quad H + HO_2 \longrightarrow H_2O + O(^3P) \quad ,
\end{aligned}$$

which mediate the abundance of HO_x in the atmosphere. Hydrogen atoms effectively become trapped when converted to molecular form on Mars, as the only available chemical sinks below 100 km are O(^{1}D) and OH. H_2 is also stable under UV radiation, resulting in photochemical lifetimes of multiple centuries, and can vertically diffuse into the Martian ionosphere above 100 km where ion interactions strip it back down to atomic hydrogen, which can be supplied with enough energy to escape the Martian atmosphere entirely [Chaffin et al., 2017]. Modelling studies have also found that night time temperatures and pressures across the Martian globe enable the condensation of atmospheric H_2O_2 [Moudden, 2007], which provides a sink at the Martian surface for HO_x chemistry that improves the accuracy of 3-D GCMs when H_2O_2 abundances are compared to observations [Daerden et al., 2019].

2.1.3 Oxygen Chemistry

The presence of oxygen on Mars is not to be confused as a biosignature due its production being entirely based in atmospheric photochemical processes, in stark contrast to the 50–70% of Earth's O_2 produced via marine life [Lindsey et al., 2010]. O_2 has been observed on Mars directly by ground-based telescopes [Hartogh et al., 2010, Trauger and Lunine, 1983, Belton and Hunten, 1968], satellites [Lebonnois et al., 2006, Fedorova et al., 2021], and *in-situ* by the Curiosity Rover [Trainer et al., 2019]. O_2 can also be observed indirectly via observations of O_2 dayglow [Conway, 1981, Fedorova et al., 2006, Gérard et al., 2020], a phenomena that occurs in higher altitudes when an O_2 molecule produced in an excited state via the UV photolysis of ozone stabilizes itself by releasing a 1.27 μm photon.

As detailed in Section 2.1.1, the atmosphere produces O(^{3}P) and O(^{1}D) atoms through photolysis of CO_2. These are capable of producing molecular oxygen through two primary reactions,

$$\begin{aligned}
&(\mathrm{R15}) \quad OH + O(^3P) \longrightarrow O_2 + H \\
&(\mathrm{R16}) \quad O(^3P) + O(^3P) + CO_2 \longrightarrow O_2 + CO_2 \quad ,
\end{aligned}$$

the former of the two producing 90% of Mars' O_2 [Krasnopolsky, 1993]. The covalent bond between the two oxygen atoms in an O_2 molecule is strong, and is unbroken in many photochemical reactions. The termolecular reactions of O_2 with H atoms and O(^{3}P),

$$\text{(R17)} \quad H + O_2 + CO_2 \longrightarrow HO_2 + CO_2$$
$$\text{(R18)} \quad O(^3P) + O_2 + CO_2 \longrightarrow O_3 + CO_2 \quad ,$$

produce products with photochemical lifetimes shorter than 30 minutes in daylight. O_3 breaks down rapidly back to oxygen atoms and O_2 through photolysis across a large spectral domain, and several efficient chemical reactions involving HO_2 almost instantly return O_2 without snapping the covalent bond. To effectively remove oxygen from the atmosphere the O=O covalent bond has to be snapped within the chemical reaction, which is predominantly performed by the UV photolysis of O_2 molecules themselves. No reaction with ozone is capable of breaking the bond directly, but multiple paths for O=O breaking can be found in HO_2. Reactions of HO_2 with H have three pathways, 2 of which split O=O with a branching ratio of approximately 91%, the other returning O_2. A final inorganic pathway for O=O removal in the Martian atmosphere is the UV breakdown of hydrogen peroxide into two OH molecules. This reaction network is displayed in Figure 2.7.

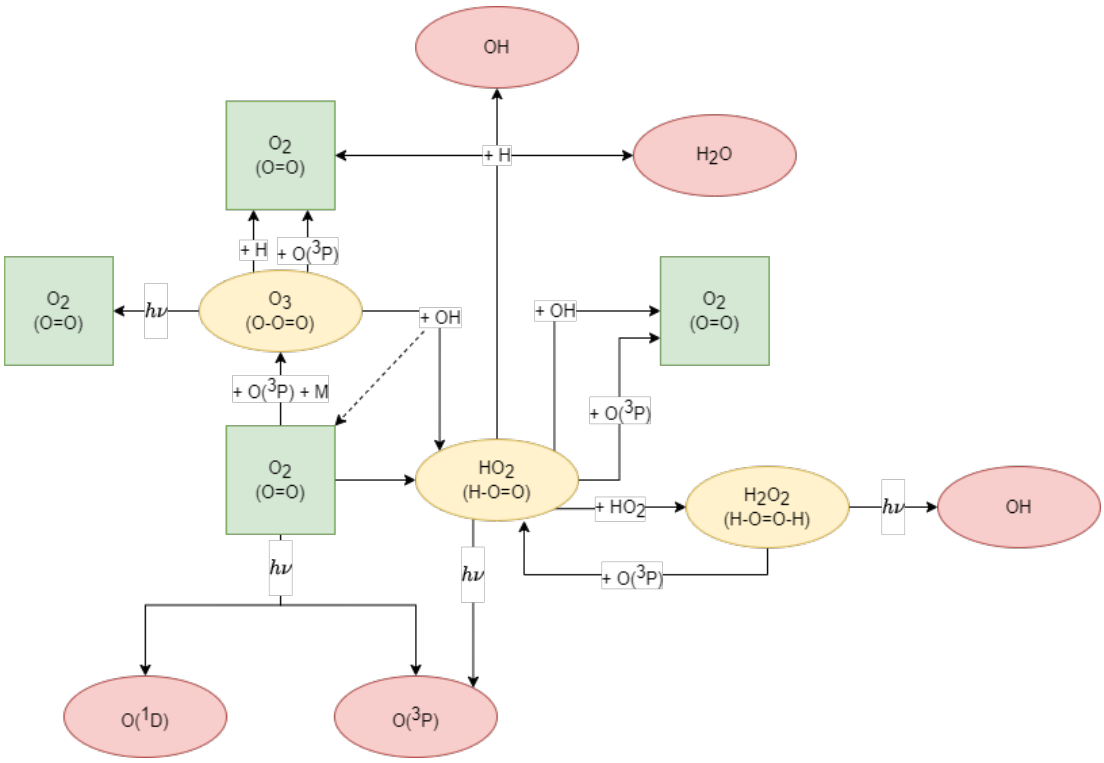


Figure 2.7: Inorganic reactions involved with molecular oxygen and the snapping of the O=O covalent bond. Green boxes: reaction returns O_2. Yellow boxes: reaction product maintains the O=O bond. Red boxes: O=O bond is severed in the reaction. Dashed line indicates that O_2 is the second product of the O_3 + OH reaction.

This network results in O_2 being photochemically stable in the Martian atmosphere according to models, having chemical lifetimes that span between 10–70 years [Krasnopolsky, 1993, 2010, 2017]. This is significantly greater than the mean ventilation time of the lower $\sim$ 20–km of the atmosphere according to GCM modelling [Barnes et al., 1996] and observational measurements [Santee and Crisp, 1995] of roughly 40 sols , implying that O_2 should have a uniform distribution controlled by transport processes and therefore abide to a seasonal cycle controlled by the polar CO_2 condensation and sublimation cycles. Measurements made by the Sample Analysis at Mars (SAM) mass spectrometer aboard the Curiosity rover situated at the surface of Gale crater have recently shown that this cycle is incomplete in our models [Trainer et al., 2019]. SAM's observations revealed that an additional 10^{20} molec. cm^{-2} ($\sim$ 400–ppm) are required in GCM model columns to match measurements acquired in the 0–150° L_S period, and an O_2 chemical lifetimes in the range of 100–1000 days to replicate steep drops in VMR observed in the 300–360° L_S region. Ground-based measurements in 2010 also revealed that a vertically homogeneous O_2 profile does not produce an optimum fit for retrievals of O_2 column densities [Hartogh et al., 2010], implying that our current photochemical models are missing some currently unknown atmosphere-surface mechanisms that could be responsible for producing a seasonally variable surface reservoir for O_2.

Ozone is a product of this oxygen and hydrogen cycle on Mars, assumed to exist in photochemical equilibrium with O(^{3}P) during daylight when exposed to UV radiation. With strong IR (λ = 9.6μm) and UV (0.25 μm) absorption bands, O_3 has been extensively observed since the first detection made by the Mariner 9's UV spectrometer [Barth et al., 1973]. Observations from the Hubble Space Telescope in the late 1990's [Clancy et al., 1999], ground-based telescopes in the mid-2000's [Fast et al., 2006], and vertical profile retrievals from satellite spectrometers such as SPICAM [Perrier et al., 2006, Willame et al., 2017] have helped to provide multi-annual studies of the seasonal variability of O_3 and it's strong anti-correlations to water vapour [Lefèvre et al., 2021].

The anti-correlation to water vapour arises from the fast reactions of O_3 with odd-hydrogen compounds,

$$\begin{aligned}
&(\mathrm{R19}) \quad O_3 + H \longrightarrow OH + O_2 \\
&(\mathrm{R20}) \quad O_3 + OH \longrightarrow HO_2 + O_2 \\
&(\mathrm{R21}) \quad O_3 + HO_2 \longrightarrow OH + 2O_2 \quad ,
\end{aligned}$$

and the reaction of:

$$(\mathrm{R22}) \quad HO_2 + O(^3P) \longrightarrow OH + O_2 \quad ,$$

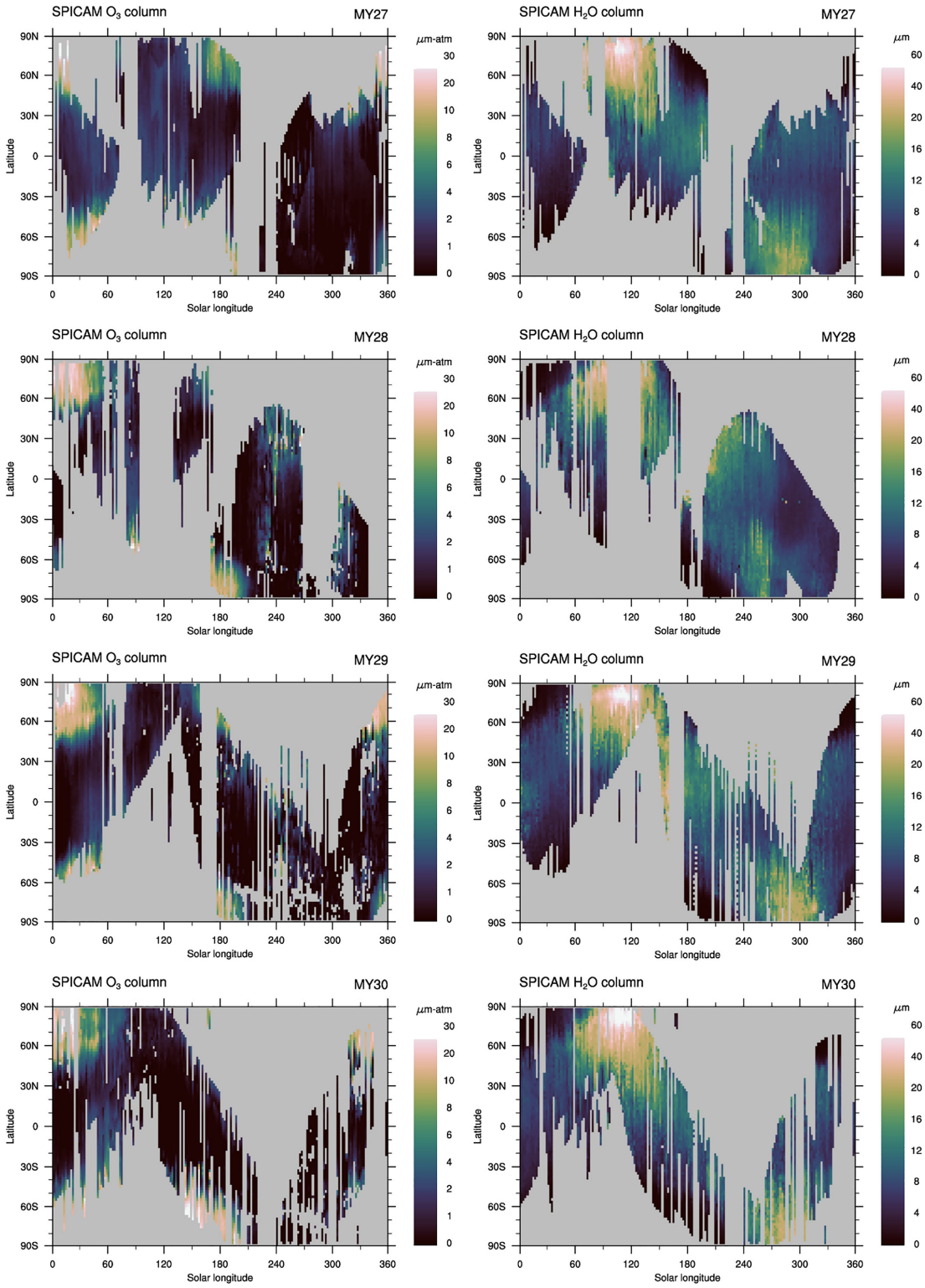


Figure 2.8: Column abundances of O_3 and H_2O vapour measured by the SPICAM spectrometer aboard the MEX as a function of solar longitude and planet latitude. O_3 column abundances are given in micron-atmospheres (μ-atm), and H_2O vapour abundances are given in precipitable microns (pr-μm). Figure taken directly from Lefèvre et al. [2021].

which greatly depletes the abundance of atomic oxygen available for the production of O_3 via the termolecular reaction with O_2. With water vapour displaying strong seasonal variability as discussed in Section 2.1.2, ozone too experiences strong seasonal and spatial variability. Figure 2.8 presents observations of O_3 and H_2O as observed by SPICAM on the MEX orbiter over the course of 5 Mars years [Lefèvre et al., 2021]. In the deep latitudes during each hemisphere's respective winter when the air is dry, less HO_x is present to destroy O_3 and suppress it's production, resulting in column abundances increasing. Photochemical lifetimes in the polar regions during winter rise from below one hour to multiple sols due to the lack of H_2O photolysis. In the summer, with water vapour sublimating at the poles the resulting elevation of HO_x radicals causes a dip in O_3 column abundances by factors of magnitude 10^2.

In the lower latitudes outside of the extremes of the polar regions, the anti-correlation between the integrated column abundances of H_2O and O_3 becomes less pronounced. Instead, O_3 abundances are primarily dictated by the vertical structure of H_2O, not the total integrated column content. During Mars' aphelion water vapour is predominantly stored below the hygropause at $\sim$ 20–km, which provides a window for O_3 development in a 20–40 km altitude pocket, where above the reactions of H_2 with $O(^1D)$ provides a steady sink of H atoms (Figure 2.6). As Mars' orbit advances towards perihelion, the elevation of the hygropause with increasing atmospheric temperatures and the supersaturation of altitude pockets due to dust interactions closes this O_3 production window with the consequent rise of HO_x in the higher altitudes. The result is a seasonally repeating ozone layer throughout the solar longitude range of roughly 50–120°, observable in Figure 2.9. This shape of this layer is well replicated by current GCM models, but the column abundances are underestimated during Mars' aphelion by factors of roughly 2, implying that HO_x chemistry is too efficient in our current models [Lefèvre et al., 2004b, Lefèvre et al., 2021] or that heterogeneous interactions between O_3, HO_x tracers, and water ice aerosols may be present.

When OH and HO_2 uptake on water ice crystals is incorporated into GCM photochemistry routines, GCM outputs do improve when compared to the observations of O_3 columns made by SPICAM especially in the aphelion season when model columns rise by a factor of almost 2, and successfully replicate almost all aphelion O_3 peaks observed by SPICAM [Lefèvre et al., 2008]. However, the seasonal variations in H_2O_2 were found to be in excess of observations by a factor of 3 when heterogeneous uptake on water ice is included, indicating that these heterogeneous processes are still not sufficiently understood but are crucial for a comprehensive understanding of the Martian atmosphere.

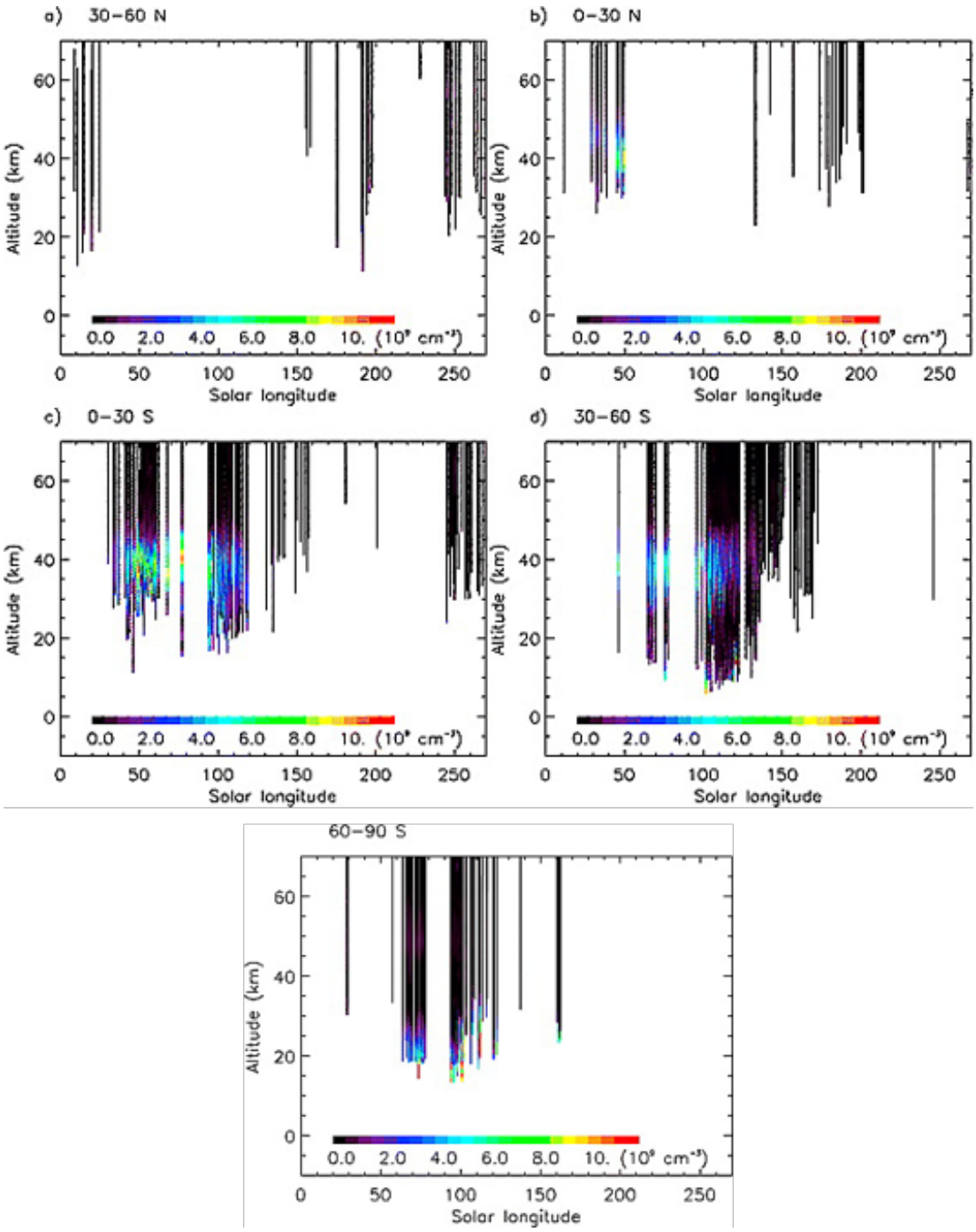


Figure 2.9: Vertical distribution profiles of O_3 as measured by SPICAM aboard the MEX using the solar occultation remote sensing method and their variances with latitude and solar longitude. a) Latitude range 30–60° north, b) latitude range 0–30° north, c) latitude range 0–30° south, d) 30–60° south, and bottom plot contrasting these low-latitude distributions with the deep south latitude band 60–90° south. Figures taken directly from Lebonnois et al. [2006].

2.2 Organic Chemistry

2.2.1 Methane Observations

Instrument	Observation Type	CH_4 Abundance	Measurement Type	Year	Citation
Canada-France-Hawaii Telescope	Ground-Based	10 ± 3 PPB	Global Mean	2004	[Krasnopolsky et al., 2004]
PFS	Satellite (Mars Express)	10 ± 5 PPB	Global Mean	2004	[Formisano et al., 2004]
Texas Echelon Cross Echelle Spectrograph	Ground-Based	No Detection (Upper Lim. 20 PPB)	No Detection	2006	[Encrenaz et al., 2006]
PFS	Satellite	20 ± 10 PPB	Localised Hotspot	2008	[Encrenaz, 2008]
PFS	Satellite	14 ± 5 PPB (Mean)	Global and Annual Mapping	2008	[Geminale et al., 2008]
CSHELL	Ground-Based	45 PPB (Peak)	Plume	2009	[Mumma et al., 2009]
TES	Satellite (Mars Global Surveyor)	5–60 PPB	Global and Annual Mapping (Discredited)	2009	[Fonti and Marzo, 2010]
PFS	Satellite	0–30 PPB (15 PPB Mean)	Global and Annual Mapping	2011	[Geminale et al., 2011]
CSHELL	Ground-based	3–10 PPB	Global Mapping	2012	[Krasnopolsky, 2012]
SAM	Rover (MSL Curiosity)	No Detection (Upper Lim. 1.3 PPB)	No Detection	2013	[Webster et al., 2013]
CSHELL, CRIRES, NIRSPEC	Ground-Based	No Detection (Upper Lim. 7.8 PPB)	No Detection	2013	[Villanueva et al., 2013]
SAM	Rover	7.2 ± 2.1 PPB (0.69 ± 0.25 PPB Mean)	Annual *In-Situ*	2015	[Webster et al., 2015]
SOFIA/EXES	Ground-Based	No Detection (Upper Lim. 1–9 PPB)	No Detection	2018	[Aoki et al., 2018]
SAM	Rover	0.24–0.65 PPB (0.41 ± 0.16 PPB Mean)	Multi-Annual *In-Situ*	2018	[Webster et al., 2018]
NOMAD and ACS	Satellite (ExoMars TGO)	No Detection (Upper Lim. 0.05 PPB)	No Detection	2019	[Korablev et al., 2019]
PFS	Satellite	15.5 ± 2.5 PPB	Localised Hotspot (1^{st} Independent Confirmation with SAM [Webster et al., 2018])	2019	[Giuranna et al., 2019]
NOMAD and ACS	Satellite	No Detection (Upper Lim. 0.06 PPB)	No Detection	2021	[Knutsen et al., 2021]

Table 2.2: Table displaying the most notable reported observations and non-detections of CH_4 on Mars, the instruments responsible for them, and the detection magnitudes or inferred upper limits. Red rows indicate non-detections which highlight the highly transient and temporally variable nature of the methane being reported in observational campaigns.

As detailed earlier in Section 1, the observations of CH_4 by Earth-based telescopes, Mars orbiters, and *in-situ* equipment such as the MSL Curiosity Rover were the motivating cause for the development of the ExoMars program [Vago et al., 2006]. The CO_2-based oxidising atmosphere of Mars offers no pathways for CH_4 production through atmospheric chemistry, and the modelled lifetimes of $> 10^2$ years imply that it is being actively produced. Table 2.2 presents a summarised list of the most important observations of CH_4 since the first modern sighting in 2004 [Krasnopolsky et al., 2004].

The PFS aboard the MEX orbiter has been responsible for many detections of CH_4 prior to 2011 [Formisano et al., 2004, Encrenaz, 2008, Geminale et al., 2008, 2011], and like all satellites orbitting Mars it has the benefit of a lack of contamination within its spectrographic records of trace gas species in Earth's atmosphere that is present in observations made using ground-based equipment. However, the MEX was launched in 2003, and there have been major improvements in satellite observational techniques since. The spectral resolution

of both the short-wavelength (1.2–5.5 μm) and long-wavelength (5.5–45 μm) of the PFS is 1.3 cm^{-1}, resulting in observing powers of $\sim$ 5500, and have vertical resolutions that span 7–12 km [Formisano et al., 2005]. A comparison with the NOMAD spectrometer aboard the TGO, with a spectral resolution of 0.12–0.5 cm^{-1}, resolving power of 10,000-20,000, and vertical resolutions of $<$ 1 km, shows just how far advancements in the field of remote sensing have come. The spectral resolution of older orbiters and their equipment was one of the first caveats noted by scientists with regards to the validity of the measured methane abundances [Zahnle et al., 2011]. Four spectral absorption features of methane located at wavenumbers 1300, 3000, 4400, and 6000 cm^{-1} lie within the PFS' spectral range, but only the ν_3 band (centred on 3018 cm^{-1}) was chosen due to signal to noise ratio limitations across the other bands, but the signal studied was still too weak for a direct detection, and was instead inferred from fitting a 10–60 ppb abundance of CH_4 to their atmospheric models to improve fits only at 3018 cm^{-1}. Further, this ν_3 band feature of methane has a width of $\sim$ 3 cm^{-1} enabling up to three PFS spectra elements to be used, yet the fit of the CH_4 only improves one, and strong deviations remain across other wavelengths that do not improve when CH_4 is added to their model.

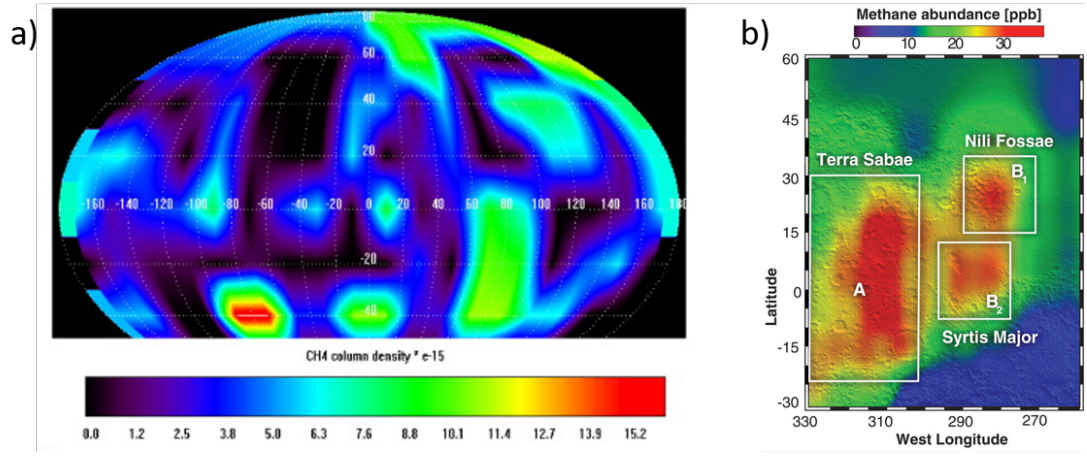


Figure 2.10: Spatial distribution of CH_4 on Mars observed during the Martian northern hemisphere's summer (90–180°L_S) by a) the PFS aboard the MEX (figure taken from source [Geminale et al., 2011]) and b) the CSHELL ground-based spectrometer telescope (figure taken from Mumma et al. [2009]).

The TES aboard the MGS reported detections of CH_4 ranging between 5–60 ppb with a strong spatial and temporal variances. However, the TES measurement arrived from the analysis of the 1300 cm^{-1} CH_4 absorption feature (centered on 1306 cm^{-1}) [Fonti and Marzo, 2010], which becomes problematic due to the close proximity of CO_2 and H_2O absorption features that risk a false identification due to the TES' low spectral resolution, ranging between 5–10 cm^{-1} [Christensen et al., 1992]. The observational limitations of these craft did not warrant immediate dismissal, but instead motivated a greater abundance of resources to be supplied to future campaigns for the search for organic chemistry on Mars.

Ground-based telescopes were also used to search for CH_4 in Mars' atmosphere, with multiple teams reporting detections [Krasnopolsky et al., 2004, Mumma et al., 2009, Krasnopolsky, 2012], and others reporting no methane but providing inferred upper limits [Encrenaz et al., 2006, Villanueva et al., 2013]. The reported detections, from both ground-based telescopes and orbiting satellites, have added reliability due to their values all coinciding in the same magnitude (0–70 ppb) and arriving from independent teams and instruments. The ground-based measurements however have the complication of needing to subtract the spectral features of Earth's own atmosphere directly overhead. Follow up research, making use of HITRAN [Rothman et al., 2009] spectrography simulations, noted that Earth-based telescopes only reported CH_4 on Mars during time periods when Mars was approaching Earth in it's orbital configuration, which blue-shifts light radiating from it. When blue-shifted, absorption features of terrestrial water vapour and methane are in close proximity to the Martian features being measured. This opens up the possibility that the CH_4 observed in these periods is not from the atmosphere of Mars, but instead from an imprecise account for CH_4 in the terrestrial atmospheric column above the telescopes. Further, the spatial localities of these independent reports are rather conflicting. Observations of CH_4 made by the PFS, shown in Figure 2.10a, revealed a strong abundance of 45 ppb of CH_4 around the northern pole during the northern summer [Geminale et al., 2011], at which point CO_2 and H_2O ice is sublimating. The team theorised that this could be a sign of CH_4 trapped within the pole escaping during the sublimation processes, and could be considered as a source of CH_4. However, the ground-based CSHELL observations of a 45 ppb plume of CH_4 confined to the region around Syrtis Major ranging from 20° south to 35° north during the northern summer [Mumma et al., 2009] shown in Figure 2.10b contradicts the PFS measurements, as no strong CH_4 signal was observed in the polar region. If CH_4 is trapped beneath the polar ice caps, then the appearance of a polar CH_4 hotspot should be an annual feature for Mars detectable by any observer.

On the 6th of August 2012 the MSL Curiosity Rover touched down on Mars at Gale Crater, and the Tunable Laser Spectrometer (TLS) within the Sample Analysis at Mars (SAM) package became the first *in-situ* instrument on Mars capable of measuring CH_4 with a spectral resolution multiple orders of magnitude finer than any orbiter at 0.0002 cm^{-1}. Curiosity's first attempts at observing methane at the Gale Crater surface were published in 2013, and failed to report a conclusive abundance, instead constraining an upper limit to 1.3 ppb [Webster et al., 2013]. This was highly unexpected, as Mars models predicted that dispersion of the high abundance plumes from only a few years prior [Mumma et al., 2009] would have created a global mean abundance of $\sim$ 6 ppb [Krasnopolsky et al., 2004, Lefèvre and Forget, 2009] owing to CH_4's expected multi-century chemical lifetime. The rover continued its operations, and periodically sampled the air at Gale Crater for whiffs of methane. Twenty months after the very first measurement attempt, the SAM team had amassed enough data to report the detection of CH_4 at a mean background value of 0.69 $\pm$ 0.25 ppb, with four consecutive

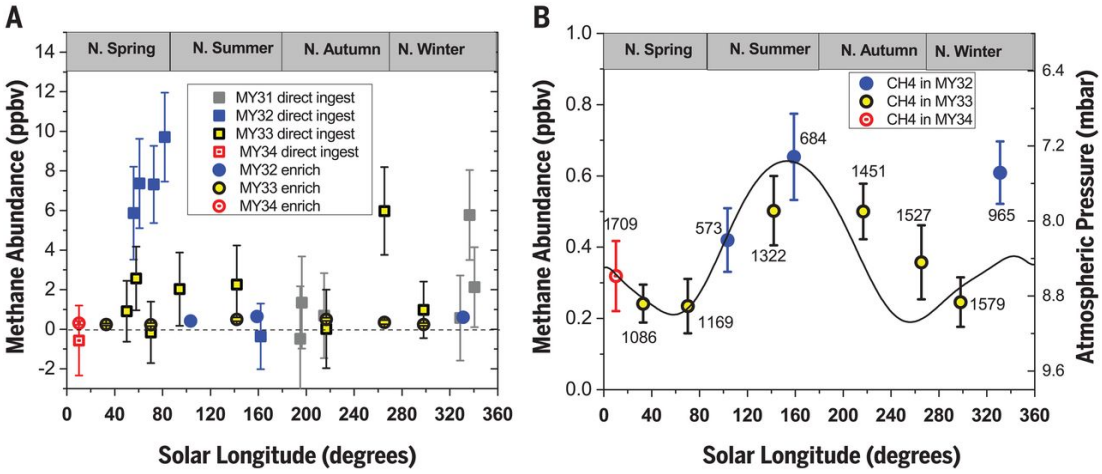


Figure 2.11: Figure extracted from Webster et al. [2018].

measurements over a 60 sol period finding elevated abundances of methane rising to as high as 7.2 $\pm$ 2.1 ppb [Webster et al., 2015]. They employed a new method of analysis with SAM by concentrating the methane ingested into the device by removing CO_2 and H_2O from the sampling chamber, enabling the TLS to detect CH_4 abundances of as low as 100 ppt [Kerr, 2012]. These first ever *in-situ* detections of CH_4 on a planet beyond Earth were later put under scrutiny with suggestions that the methane was being produced by the rover itself [Zahnle, 2015]. These issues were then contested by the MSL team who noted that to produce the elevations of approximately 7 ppb of methane the rover would need to generate upwards of 10^{24} CH_4 molecules over the 2 month period experiencing the elevated readings. A source of CH_4 of this strength within the rover could not be identified [Webster et al., 2018].

In 2018, Curiosity unveiled measurements of CH_4 over a 5 year period at Gale Crater, reporting a mean background of 0.41 $\pm$ 0.16 ppb and an apparent strong seasonal variation with values ranging between 0.24–0.65 ppb [Webster et al., 2018]. Figure 2.11a presents all measurements of CH_4 recorded by the TLS over this 5 year period and their variance with solar longitude, and Figure 2.11b presents what are regarded as the 'background' level measurements, produced through the CH_4 enrichment method that enables the TLS to observe CH_4 at the 100 ppt level that the authors claim demonstrates a seasonal cycle with sporadic enhancements across the year. In 2020 however, a statistical analysis of the data recorded by TLS contested the claims that these background fluctuations resemble a seasonal cycle [Gillen et al., 2020]. They note that the small number of data points recorded and presented in the paper, and that the folding of the data to a 1-year period as-per Figure 2.11b inherently weights the shape to favour that of a seasonal cycle, and that there is no indication from the data itself that it abides to a seasonal cycle instead of stochastic variations, or variations abiding to another time period.

In 2019, a new study of data acquired via the MEX PFS produced a major milestone for the Martian methane tale - the first independent confirmation of an observation of CH_4 on Mars by two different instruments [Giuranna et al., 2019]. The data studied was collected by the PFS across the same time period as the Curiosity rover's first $\sim$ 20 months at Gale Crater, utilising a new observing method referred to as *spot-tracking*. Spot-tracking separates itself from nadir observations by tracking a single surface feature of Mars during its flyover, as opposed to pointing anti-parallel to the zenith for its duration as-per nadir passes. This enables the PFS to produce hundreds of spectra measurements over one singular area over 10–90 minutes and have the capability of observing methane with a lower-limit column averaged vmr of 5 ppb. This method produced a detection of a 15.5 $\pm$ 2.5 ppb column average of CH_4 above Gale Crater only one day after Curiosity's TLS measured a 5.78 $\pm$ 2.27 ppb spike of methane at the Gale Crater surface.

In the same year however, the ExoMars TGO presented it's first findings after searching for CH_4 since the satellite's arrival at Mars in late 2016 - no confirmed detections of CH_4, with a refined upper limit of 0.05 ppb [Korablev et al., 2019]. The TGO, with the most sensitive remote sensing equipment on an orbiter around Mars to-date, and specially tailored for the observation of organic compounds, has now been in operation for over four years and has still yet to report a successful detection of CH_4 on Mars [Knutsen et al., 2021]. This wildly sporadic appearance and disappearance of CH_4 challenges our current knowledge and understanding of Martian atmospheric chemistry, and requires an extremely powerful oxidising source or physical process that is as-of-yet unknown to us.

2.2.2 Discrepancies between Observations and Modelling of Methane on Mars

The vertical mixing timescale from the Martian surface to 70–km, through the calculation of z^2/K for altitude z and eddy diffusion coefficient K (2×10^7–4×10^8 cm^2 s^{-1} [Rodrigo et al., 2009] between 30–200 km), is less than 30 days, and the global mixing timescale is found to be roughly half a year [Barnes et al., 1996]. In current photochemistry models of Mars, the chemical lifetime of CH_4 is expected to be multiple hundreds of years [Wong et al., 2003, Krasnopolsky, 2006b]. UV photolysis of CH_4 is only effective at altitudes above $\sim$ 60–km, and below OH, O(^{3}P), and O(^{1}D) are the only currently known atmospheric chemical sinks. This implies that any methane present on Mars should be homogeneously spread across the globe. The sporadic nature of the CH_4 being reported by the various orbiters, ground-based telescopes, and *in-situ* devices requires an atmospheric lifetime of less than 200 days, which is almost 600 times quicker than current models predict [Lefèvre and Forget, 2009]. This creates two vital questions that need to be addressed to help coincide GCM modelled organic chemistry with observations: where does the methane on Mars come from, and where does it go?

One route for CH_4 to appear on Mars that has been postulated is the production from comet impacts [Kress and McKay, 2004], making the argument that the dust condensing after the initial impact on the planet surface is capable of catalysing the production of CH_4 from atmospheric CO and H_2 during the cooldown period of the impact fireball. This theory was applied to the CH_4 observed by the Canada–France–Hawaii Telescope telescope in 2004 that observed a mean abundance of 10 $\pm$ 3 ppb and required a production of 270 tonnes per year to explain [Krasnopolsky et al., 2004] (very low when compared to Earth's estimated 570 million tonnes per year). Comets in the Oort cloud have been observed to have roughly 1% of their ice mass composed of CH_4 [Gibb et al., 2003], and by estimating the frequency of comet impacts with Mars they are only capable of transferring $\sim$ 5 tonnes of CH_4 per year to the Martian atmosphere. Factoring in gas phase chemistry and dust condensing in the impact fireball, this value is further constrained to about 0.8% of the necessary production (2 tonnes per year), and has a probability of being the cause of the 2004 observations of only 0.0011 [Krasnopolsky, 2006b], effectively ruling out cometary impacts as the source of Martian CH_4.

CH_4 is a common product of terrestrial outgassing events, such as microseepage through the planetary surface or volcanism events, and is often accompanied by various other chlorine and sulfur-based trace gas species, e.g. SO_2 and HCl. There is no evidence of modern volcanic activity at the surface, the most recent feature of volcanic activity is estimated to have been produced between 53–210 thousand years ago [Horvath et al., 2021], just short of 1000 times longer than the expected lifetime of CH_4 in the atmosphere. This long lull of volcanism compared to the significantly shorter lifetime of CH_4 rules out volcanism as the source of the observations of CH_4. Further, there have been no observations by orbiting craft of any strong temperature anomalies at the surface of Mars, which would be expected in the vicinity of active volcanism. SO_2 typically appears in the plumes of terrestrial volcanoes in abundances that are of the order of $\sim$ 1% [von Glasow, 2010], whereas the CH_4 emitted is closer to magnitudes of a few parts per million [Etiope and Klusman, 2002]. There have been no successful observations of sulfur chemistry on Mars, with the most recent upper limits being measured by ground-based spectrometer as 3.1 ppb [Khayat et al., 2017]. Taking the ratios of SO_2 and CH_4 production in terrestrial volcanism and applying them to this upper SO_2 limit, volcanism on Mars could only be expected to produce up to 1 tonne of CH_4 per year [Krasnopolsky, 2005], significantly short of the rate required to produce any of the observations of the past 20 years.

A second geological process postulated, also devoid of any biological activity, involves the serpentization of subsurface olivine rock, a crystal structure composed of Mg_2SiO_4 and Fe_2SiO_4 [Oze and Sharma, 2005]. Upon contact with liquid water in subsurface conditions, the crystal mixture is capable of chemically reacting to produce H_2. The H_2 produced in the subsurface can then react with subsurface gas-phase CO_2 to produce CH_4 in the the Sabatier reaction,

$$4H_2 + CO_2 \leftrightarrow CH_4 + H_2O,$$

which is optimal in temperature ranges of 200–400 °C and pressures of 30–100 atm [Gao et al., 2012], which exist at depths of 0.1–1 km below Mars' surface [Jones et al., 2011]. This process, like volcanism, has the benefit of potentially explaining the spatial variability of Mars' CH_4, as it's production would be fully dependent on areas having the relevant unique geological features. Serpentization processes can theoretically be supported on Mars as olivine has been detected in substantial quantities at the Martian surface [Hamilton and Christensen, 2005], and evidence of liquid water existing in subterranean lakes has been collected by the MEX's MARSIS radar instrument [O'Callaghan, 2020]. The reaction however is only effective at large temperatures that are not found close to the surface of Mars, and instead is expected to be only effective at depths of roughly 10–15 km [Krasnopolsky, 2006b]. At a depth of 5 km, the time taken for diffusion through the Martian regolith to produce a surface abundance of 1 ppb has been modelled to be within 307,000–3,340,000 Mars years [Stevens et al., 2017], which would make them incapable of being the cause for large episodic rises in CH_4.

A third geological subsurface source for Martian CH_4 under consideration is the destabilisation of methane clathrate deposits [Chastain and Chevrier, 2007, Gloesener et al., 2021]. Within low temperature and high pressure environments, liquid water molecules can solidify and form a clathrate structure which can effectively trap gaseous molecules of other species. The water mass fraction within the Martian soil has been observed by the MEX orbiter's OMEGA, a visible and infrared mineralogical mapping spectrometer, to vary between 30–70% in the polar regions and between 2–10% within lower latitudes [Milliken et al., 2006], but it is still unknown as to whether or not thermodynamics within the soil would have enabled the formation of methane clathrate structures. However, recent modelling of the Martian subsurface has revealed that the present-day Martian subsurface can provide large zones in which methane clathrate can exist in a stable condition [Gloesener et al., 2021], where the top of the stability zones 30–70 meters in the lower latitudes and depths can be as large as $\sim$ 15–km. Clathrates are capable of storing large abundances of CH_4 gas within them, with 1–m^3 of clathrate capable of holding 116 kg (164 m^3 at 298 K and 10^5 Pa) of methane. The destabilisation of a 1–m thick layer of methane clathrate across an area of roughly 2300 m^2 would therefore be capable of releasing 270 tonnes of methane [Chastain and Chevrier, 2007] as required for the first reports of CH_4 on Mars [Krasnopolsky et al., 2004]. This destabilisation could be triggered by a number of factors, such as the seasonal variations in the subsurface temperature, or shallow seismic activity that has recently been monitored by the NASA InSight Lander [Lognonné et al., 2020]. The release of CH_4 to the atmosphere of Mars via destabilisation of subsurface clathrate distributions still leaves the question of methane's true origins unanswered - the original production process could be the

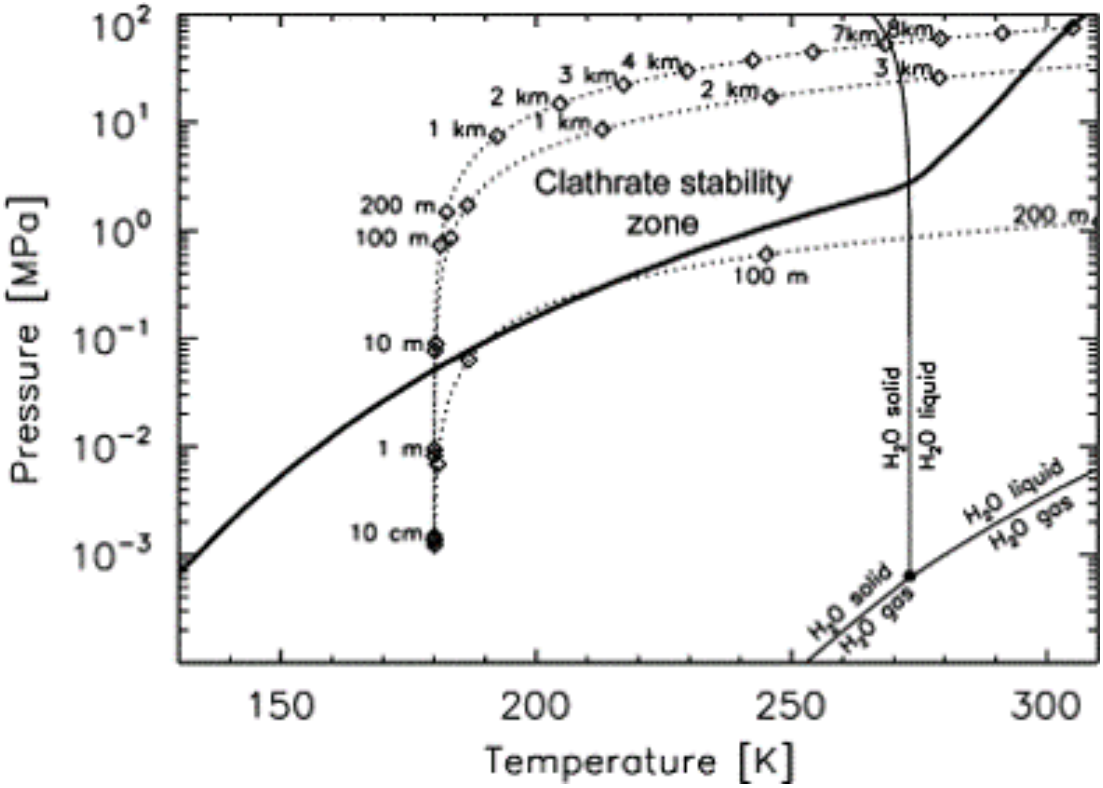


Figure 2.12: Pressure and temperature stability plot of methane clathrate (thick solid curve) and water (thin solid lines), accompanied with three geothermal profiles of the Martian subsurface (dotted lines) of different surface material, and markers indicating depths in meters. Top: ice-cemented soil, middle: dry sandstone, bottom: loose soil. Figure extracted from Chastain and Chevrier [2007].

previously described serpentization process ongoing below the clathrate stability layer, where sequestration of CH_4 produced into the clathrate structures acts as a regulator between the subsurface and the atmosphere, or, more excitingly, the production via an extinct or currently active subsurface biosphere sheltered from the irradiated and oxidant-heavy soil above.

Variations of observed atmospheric CH_4 also require strong changes in the loss processes. Current GCM predictions of CH_4 lifetimes of $\sim$ 300 years need to be drastically cut down to magnitudes of $\sim$ 200 terrestrial days, and even further down to timescales of $\sim$ 1 hour if the missing sink is confined to the surface [Lefèvre and Forget, 2009]. The current loss processes in these GCM models are solely UV photolysis (effective only at altitudes above $\sim$ 60–km), and chemical reactions with O(^{1}D), O(^{3}P), and OH. Heterogeneous interactions with methane and the Martian surface have been considered as a new sink, however reactions like these that are non-reactive are typically slow. Reanalysis of data taken by the Viking Landers revealed an organic content of $\sim$ 1–ppm in Martian soils in the mid-latitudes [Navarro-González et al., 2010], and the MSL Curiosity rover reported the detection of organic compounds preserved in mudstone at Gale Crater [Eigenbrode et al., 2018], which opens the door for an atmosphere-surface deposition scheme for Mar's atmospheric methane to be investigated. Modelling studies have been conducted investigating CH_4 adsorption into the regolith as a non-chemical sink [Gough et al., 2010], with 3-D GCM results showing that global spatial and temporal variability is difficult to produce with realistic atmospheric parameters [Meslin et al., 2011], but 1-D models recently showing that the observed variable background at Gale can be somewhat replicated by this atmosphere-surface process [Moores et al., 2019a]. H_2O_2 that has condensed onto dust grains and fallen to the surface has been postulated as a chemical sink at the surface for CH_4, however modelling studies found that H_2O_2 must exist in unrealistically large abundances from the surface to depths of $\sim$ 500 m to have a chance at lowering CH_4's lifetime to below 4 years [Gough et al., 2011, Atreya et al., 2006].

Dust-storms and dust-devils have also been considered as the missing sink for Mars' atmospheric methane. In these events dust particles become charged due to friction with each other (the triboelectric effect), and vertical winds can elevate lighter grains to greater heights than heavier grains. Lighter grains favour developing negative charges, whereas heavier grains favour positive, and their separation can produce an electric field that can reach Martian atmospheric breakdown voltages of $\sim$ 25 keV [Jackson et al., 2010]. An electron avalanche can then occur, with electron densities becoming large enough to engage in the following reactions [Farrell et al., 2006]:

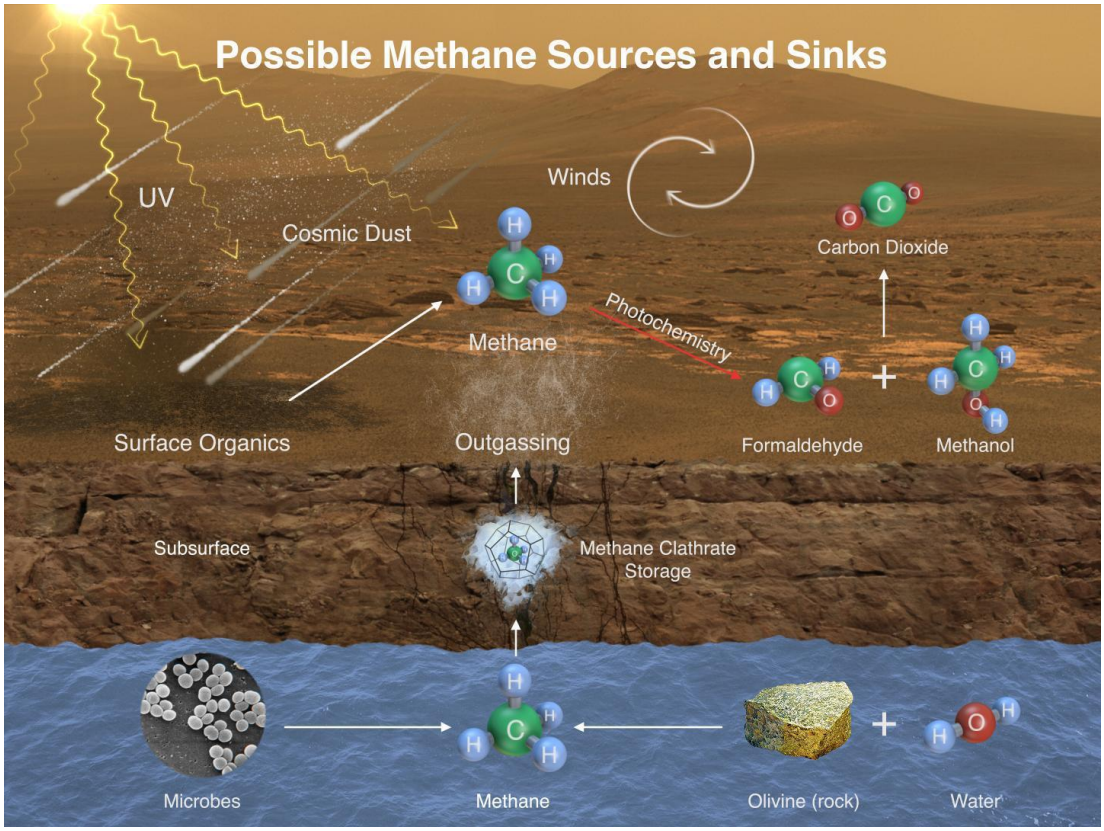


Figure 2.13: Hypothesised sinks and sources of the atmospheric methane observed in the Martian atmosphere. Figure extracted from NASA [2018].

$$
\begin{aligned}
CO_2 + e^- &\longrightarrow CO + O(^3P) \\
H_2O + e^- &\longrightarrow OH + H \\
CH_4 + e^- &\longrightarrow CH_3 + H \quad .
\end{aligned}
$$

The increased abundance of H_2O_2 from electrochemistry due to electrochemical breakdown of H_2O, capable of producing 10^4 times the amount of H_2O_2 than standard models, may result in saturation occuring at 200 times the rate of photochemistry [Atreya et al., 2006] causing H_2O_2 to condense around dust-grains and deposit on the surface, producing a strong oxidiser in the soil for CH_4 [Atreya et al., 2007]. However, this reaction scheme was found to have only a small impact on the global CH_4 lifetime, and produces an over-abundance of H_2O_2 whereas models considering gas-phase chemistry reproduce H_2O_2 observations reasonably well [Lefèvre et al., 2008]. The large electric field strengths required to initiate this electrochemistry are also doubted to develop and be sustained at this level, with E-fields found to be limited to $\sim$15–20 kV/m by modelling studies [Kok and Renno, 2009].

In addition to triboelectric effects, the Martian dust itself has also been hypothesised as the missing CH_4 sink. The dust of Mars has been observed to contain a significant amount of quartz (SiO_2) by Curiosity's Alpha Particle X-ray Spectrometer (APXS), where a mean soil content of 45.41 is measured at Gale Crater [Berger et al., 2016]. Performing tumbling experiments in a sealed container with SiO_2 and olivine rock that replicate wind erosion with materials traveling at speeds of $\sim$ 1 m/s [Knak Jensen et al., 2014]. CH_4 inserted into this container was found to form covalent bonds of Si-CH_3 when active Si- sites are unveiled by the erosion process, and remained stable up to temperatures of 250 °C. These experiments found that a mass of 10^6 tonnes of active quartz would be capable of removing 270 tonnes [Krasnopolsky et al., 2004] of CH_4 within 100–200 days. The total mass of dust suspended in the Martian atmosphere has been estimated to reach $\sim 10^8$ tonnes during dust-storm events [Martin, 1995], in excess of the calculated amount. The Curiosity Rover itself reported some anti-correlations between it's measurements of CH_4 and the atmosphere's optical opacity [Webster et al., 2015], which provides more evidence pointing towards dust as the missing sink. However, these laboratory studies failed to consider chemistry within the soil that on Mars contains strong chemical oxidants, which the authors themselves admit may result in the Si-CH_3 bond being a temporary sink that may strongly alter its capacity as an effective remover of CH_4. Figure 2.13 presents a cartoon summarizing these proposed sources and sinks of CH_4, and I will now move on to address the potential of CH_4 as evidence for the existence of extraterrestrial microbial life.

2.2.3 Organic Species as Biosignatures on Mars

One of the most exciting hypotheses regarding methane's origins on Mars is the presence of methanogenic bacteria which, if present and found, would be the first instance of biological activity to be discovered beyond Earth. Methanogenic bacteria produce CH_4 as a product of their metabolism in the following reactions [Summers et al., 2002]:

$$\begin{aligned} CO_2 + 4H_2 &\longrightarrow CH_4 + 2H_2O + 39.35 \text{ kcal mol}^{-1} \\ 2H_2O + 3CO &\longrightarrow CH_4 + 2CO_2 + 11.04 \text{ kcal mol}^{-1} \quad , \end{aligned}$$

in which CO and H_2 can be supplied to subterranean bacterial colonies from the atmosphere through diffusion through the regolith. Numerous types of methanogenic bacteria have been studied in laboratories with Mars soil analogues and have been found capable of existing and producing methane in the presence of CO_2, H_2 and water [Kral et al., 2004], and some are even capable of surviving and adapting to Mars soil analogues with 1–5% of their mass contaminated with perchlorate (ClO_4^-) [Kral et al., 2016], a powerful oxidiser first detected in the Martian soil by the Phoenix lander [Hecht et al., 2009b]. Studies using a 1-D photochemistry

model found that the maximum loss flux of atmospheric H_2 to the soil are 2×10^7 cm^{-2} s^{-1}, as larger values cause model calculations of H_2 to deviate to far from observed values. The largest permissible CO flux was similarly calculated as 6×10^7 cm^{-2} s^{-1}, which would result in a surface CO VMR drop of approximately 25% [Weiss et al., 2000]. The fluxes of H_2 and CO that a methanogenic colony may require to produce $\sim$ 15 ppb of CH_4 at the surface at a 10–m depth were found to be much larger, 1.1×10^{10} and 8.8×10^9 cm^{-2} s^{-1} respectively. These models also failed to take into account the presence of oxidising species within the soil, which could greatly impact the rate at which the reductants CO and H_2 can travel to the bacterial colonies through the Martian regolith, and limit the colony to a subsurface depth of 10–m and assume a 10% efficiency of the bacteria's metabolism.

A more recent study conducted $\sim$ 19 years after made use of observational parameters such as surface temperature, atmospheric composition, and pressure from the MSL Curiosity rover and an updated and more comprehensive photochemistry model to assess the plausibility of various bacterial colonies making use of H_2 and CO atmosphere-surface fluxes as their energy source. Two methanogenic pathways making use of H_2 and CO were studied and found to experience a maximum flux of 1.9×10^5 and 1.6×10^5 cm^{-2} s^{-1} respectively before atmospheric CH_4 reached $\sim$ 1–ppb levels [Sholes et al., 2019]. Fluxes of this magnitude could be reached at depths greater than 10–km that has pressures and temperatures at which laboratory studies have demonstrated that some methonogenic bacteria, such as the methanothermobacter wolfeii, can survive and multiply [Sinha et al., 2017].

The possibility of life on Mars is very exciting and heavily researched by the astrobiology community. However, how is it possible to differentiate between CH_4 that has its origins in abiotic processes like volcanism and serpentization, and CH_4 produced via biological activity? The largest drill currently on Mars belongs to the Insight lander, boasting a length of just short of 5 meters, but with potential CH_4 depths in excess of 10 km digging into the Martian soil is an unfeasible approach. The best approach available is the study of the methane itself, its isotopologues (molecules of the same chemical structure but differing in ion composition), and the atmospheric chemistry close to the emission site at the surface.

One method would be to search for localised variations in H_2, commonly used as a food-source for methanogenic bacteria and a fuel for abiotic serpentization. As detailed earlier, olivine rock is capable of reducing liquid water and producing H_2 gas below ground, which in turn can abiotically reduce carbon compounds and produce CH_4. The H_2/CH_4 ratios produced via abiotic serpentization were reported to regularly be greater than 40 at temperatures and pressures found at $\sim$ 5–km depths, with lower values being a preliminary indicator of biological activity [Oze et al., 2012]. Taking the value of H_2 of 17–ppm given in Table 2.1, ignoring the missing CH_4 sink required for now, a CH_4 abundance of $\gtrapprox$ 415–ppb would be a potential indicator of Martian biological activity. With upper limits from the TGO being set at 50–ppt [Korablev et al., 2019], this hypothesised indicator of life comes up negative. Importantly, these

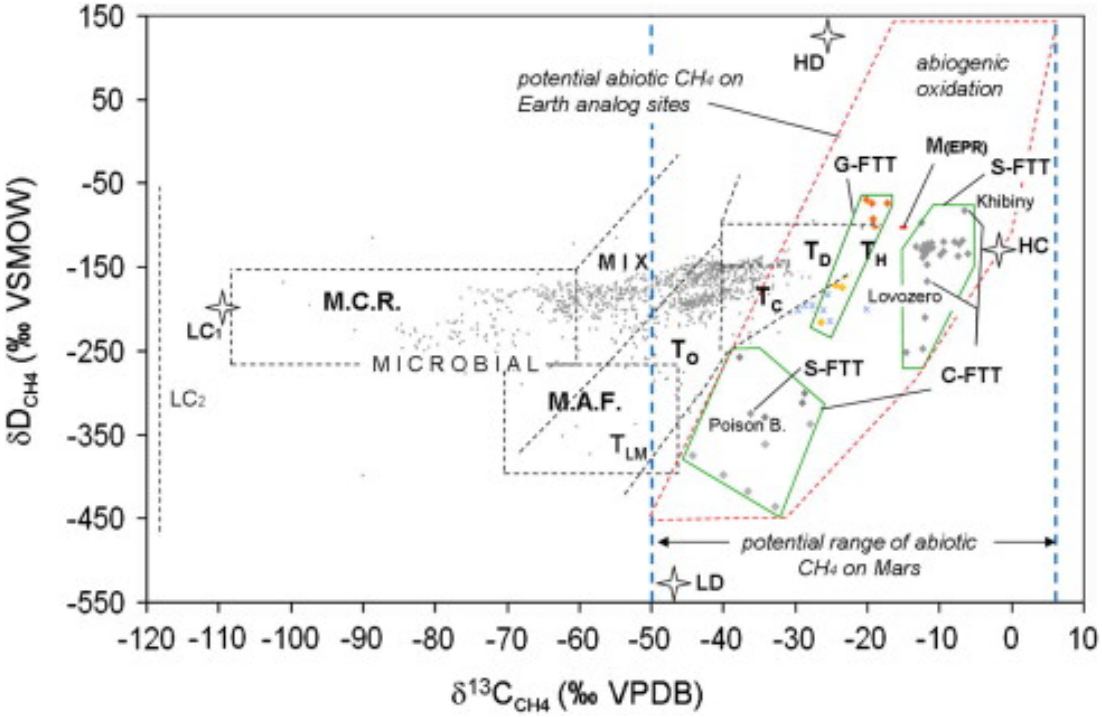


Figure 2.14: Deuterium and carbon isotope delta-ratios of methane produced from terrestrial abiotic and biotic sources. Figure extracted from Etiope et al. [2013].

experiments neglect the impacts of regolith diffusion and consequent impacts of subsurface chemistry and transport rates of different molecular species. Any reports of biological activity derived from this consideration therefore need to be confirmed by additional methods before taken seriously.

Another proposal is to study the isotopic composition of the methane molecules themselves. Different pathways for the production of methane occur at different pressures, temperatures, and a wide range of other important parameters that govern the amount of energy available in the chemical system. These different factors are manifested in the energy stored within the chemical products themselves, where more energetic production systems tend to yield heavier carbon and hydrogen atoms. Stable methane exists with two C isotopes, ^{12}C and the heavier ^{13}C, and can have up to four hydrogen atoms in the deuterium state, ^{2}H, in place of the lighter ^{1}H atom. The ratio of the isotopes are presented as values of $\delta^{1}3$C and δD, which are calculated using the Vienna Pee Dee Belemnite (VPDB) reference value of $(^{13}C/^{12}C)_{VPDB}$= 0.01123720 and the Vienna Standard Mean Ocean Water (VSMOW) reference value of $(D/^{1}H)_{VSMOW}$= 155.7$\times 10^{-6}$:

$$\delta^{13}C = \left(\frac{(^{13}C/^{12}C)_{Sample}}{(^{13}C/^{12}C)_{VPDB}} - 1\right) \times 1000\%_0$$
$$\delta D = \left(\frac{(D/^{1}H)_{Sample}}{(D/^{1}H)_{VSMOW}} - 1\right) \quad \times 1000\%_0 \quad .$$

Figure 2.14 presents a large collection of δD versus $\delta^{13}C$ values measured at the emission sites of a large number of methane produced via microbial and abiotic processes. This plot shows a loose relationship between the two values and the nature of the methane source, highlighting that abiotic processes do tend to favour the generation of heavier C and H atoms with $\delta^{13}C$ values typically > 40 ‰$_0$. This is not a definitive relation however, as some microbial processes are capable of generating $\delta^{13}C$ values seen in abiotic processes. Moreover, studies of methane's transport through the Martian regolith have shown that interactions between CH_4 and compounds in the regolith are capable of greatly altering the isotopic composition to the point that a source at a depth of 1–km can be altered in both $\delta^{13}C$ and δH by up to -1000 ‰$_0$ [Stevens et al., 2017], enabling an abiotic source to disguise itself as a biotic one if assessed by Figure 2.14. The only process identifiable by the study of the release sites isotopologue ratios on their own was found to be a shallow and abiotic process with a $\delta^{13}C$ of $\gtrapprox 0$.

On Earth, methane emissions are occasionally coupled with trace amounts of ethane (C_2H_6). C_2H_6 requires a greater amount of energy to produce, and is more often associated with abiotic production methods [Etiope, 2018]. If CH_4 is detected by the TGO without any C_2H_6, or a very high C/C_2 ratio is found, then this could be a preliminary indicator of a biological method of production. However, the subsurface breakdown of organic matter in thermogenic gas production is seen on Earth to also result in the production of large amounts of C_2H_6, and again the impact of the ratios can be subject to alterations as the gas mix diffuses through the Martian regolith as it has been seen to do so on Earth [Etiope et al., 2009].

As emphasised in Figure 2.15, there is no singular method available to remote sensing campaigns or *in-situ* measurements for the differentiation of deep subsurface sources of CH_4 with complete certainty. Isotopologue measurements and C/C_2 ratios on their own have microbial, thermogenic, and abiotic methods producing a range of values that overlap one another, but together they could help to infer information regarding the temperature and pressure ranges they could feasibly be produced at, and help to constrain the hypotheses put out by the scientific community. NASA and ESA have expressed interest in a collaborative sample-return mission to Mars [Muirhead et al., 2020], albeit without official commitments at the time of writing this thesis, that would seek to collect soil and regolith samples of Mars to be returned to Earth for laboratory testing. Being able to experiment with Martian soil and regolith directly would yield a significant level of information that could be used to constrain the effects of gas diffusion through Mars' surface, and aid in assessing the abundances of

isotopes and other gas products at the point of production. At present, we lack an adequate amount of data to rule out either biological or abiotic CH_4 production, however the ongoing work in the planetary science and astrobiology community moves ever-forward in attempting to find answers.

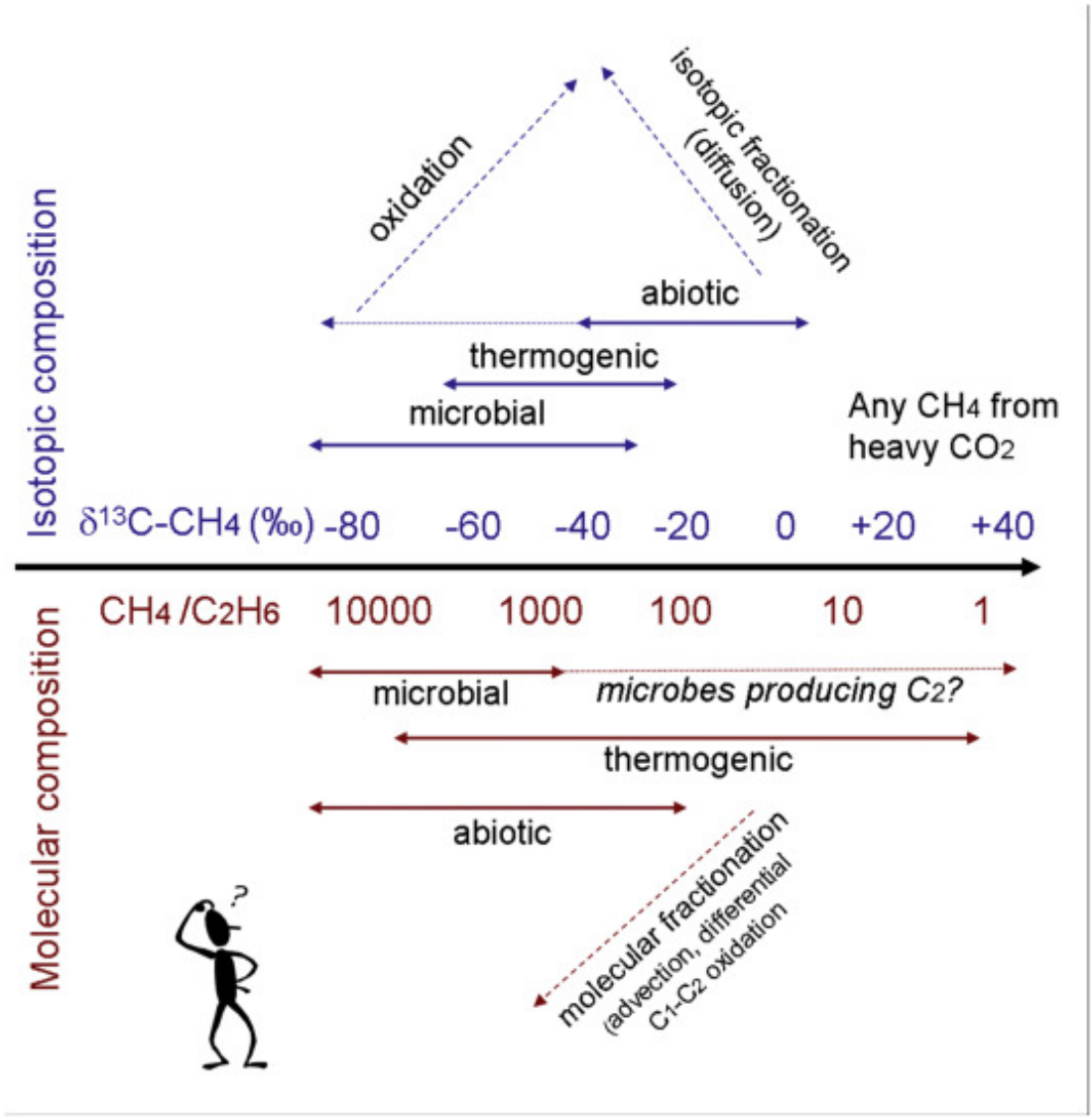


Figure 2.15: Hypothesised sinks and sources of the atmospheric methane observed in the Martian atmosphere. Figure extracted from Etiope [2018].

Chapter 3

1-D Photochemistry Submodule

Throughout the following chapters, I make use of the one dimensional (1-D) time-dependent photochemistry submodule originally developed by researchers at the Laboratoire de Météorologie Dynamique (LMD) for their 3-D Mars General Circulation Model (MGCM) [Hourdin et al., 1993, Forget et al., 1999]. The original photochemistry submodule was developed at LMD by taking the photochemical reaction network for Mars created by Nair et al. [1994] and applying it to the Reactive Processes Ruling the Ozone Budget in the Stratosphere (REPROBUS) model, a terrestrial stratospheric chemistry model produced in the early 1990s at LMD and detailed in Lefevre et al. [1994]. The Mars photochemistry submodule was then attached to the 3-D LMD MGCM by Lefèvre et al. [2004b] to create the first three dimensional simulation of Mars' atmosphere with photochemical reactions.

The 1-D photochemistry model was supplied to me from the UK's Open University, who have developed their own version of the LMD's 3-D MGCM code Lewis et al. [1999]. The principle differences between the UK's version and the original LMD version lie within the advection schemes employed, in which the UK version is equipped with an expansive dust transport package [Newman et al., 2002a,b], and calculates horizontal movement through the spherical harmonic numerical approach [Hoskins, 1973] and finite-difference methods vertically, whereas the original LMD code utilises the finite-difference scheme across all spatial dimensions.

Without the presence of horizontal transport, the time-dependent model equation to be solved by the 1-D photochemistry submodule of this work is:

$$\frac{dn_i}{dt} = P_i - n_i L_i + \frac{d\theta_i}{dz} \tag{3.1}$$

in which n_i, P_i, and L_i denote the number density (molec. cm^{-3}), chemical rate of production (molec. cm^{-3} s^{-1}) and loss (s^{-1}) of trace gas species *i*, and θ_i denotes the vertical flux.

3.1 Tracer Transport

The LMD-UK and LMD MGCM's calculates the vertical displacement of trace gas species via atmospheric turbulence and molecular diffusion through the same packages that use the second-order finite volume scheme detailed by Hourdin and Armengaud [1999] and a turbulent mixing scheme within the planetary boundary layer described in detain in Forget et al. [1999]. The van-Leer advection scheme is used by the LMD MGCM to simulate the larger-scale atmospheric transport of tracers included in this work, and is comprehensively detailed in the works of Newman et al. [2002a] and Newman et al. [2002b].

3.2 Photochemistry

The model originally arrived with photochemical reactions governing the evolution of 15 inorganic trace gas species and methane, listed at the top of Table 3.1. This work focuses on the atmospheric chemistry of the lower atmosphere, in which I restrict the altitude of the 1-D model to approximately 70 km. This was chosen to limit computational expense, and to enable the project to focus on the wide range of ongoing questions relevant to the lower atmosphere of Mars. The exclusion of the ionosphere and thermosphere also removes the need for ion and electron reactions to be considered and updated, and allowed me to focus the project resources on photochemical interactions only. A full list of all trace gas species handled by my 1-D model that studies the oxidation of methane and ethane, and the interactions of chlorine-containing species, is presented in Table 3.1.

Table 3.1: Trace gas species in the 1-D photochemistry submodule. All chlorine species and all organic compounds (bar CH_4 itself) are new additions to the model since it was received in September 2017.

Inorganic Species	
Name	Formula
CO_2	Carbon Dioxide
CO	Carbon Monoxide
$O(^1D)$	Atomic Oxygen (Excited Singlet)
$O(^3P)\equiv O$	Atomic Oxygen (Ground State)
O_2	Molecular Oxygen
O_3	Ozone
H	Atomic Hydrogen
OH	Hydroxyl
HO_2	Hydroperoxyl
H_2O_2	Hydrogen Peroxide

H_2O (Vapour)	Water Vapour
H_2O (Ice)	Water Ice
N_2	Nitrogen
Ar	Argon
Organic Species (Methane Oxidation)	
CH_4	Methane
CH_3	Methyl Radical
CH_3O_2	Methyl Peroxy-radical
CH_3OOH	Methyl Hydroperoxide
CH_3OH	Methanol
CH_3O	Methoxide
HCHO	Formaldehyde
HCOOH	Formic Acid
$HOCH_2O_2$	Hydromethyl Peroxy
$HOCH_2OH$	Methanediol
$HOCH_2OOH$	Hydromethyl Hydroperoxide
HCO	Formyl Radical
Organic Tracers (Ethane Oxidation)	
C_2H_6	Ethane
C_2H_5	Ethyl Radical
$C_2H_5O_2$	Ethyldioxy Radical
C_2H_5OOH	Ethyl Peroxy
C_2H_5OH	Ethanol
$HOCH_2CH_2O_2$	–
$HOCH_2CH_2O$	–
Ethgly ($(CH_2OH)_2$)	Ethylene Glycol
Hyetho2h ($C_2H_6O_3$)	Hydroperoxyethanol
CH_3CHO	Acetaldehyde
CH_2CHOH	Ethenol
CH_3CHOHO_2	Hydroxy Ethyl Peroxy Radical
CH_3COOH	Acetic Acid
$CH_3CHOHOOH$	–
$CH_3C(O)$	Acetyl Radical
$CH_3C(O)OOH$	Peracetic Acid
$HCOCH_2O_2$	–
Glyox (OCHCHO)	Glyoxal

HCOCO	–
$HOOCH_2CHO$	Hydroperoxy Acetaldehyde
$HOCH_2CHO$	Glycoaldehyde
HOCHCHO	Hydroxyl-vinoxy Radical
$HOCH_2CO$	–
$HOCH_2CO_3$	–
$HOCH_2CO_2H$	Glycolic Acid
$HCOCO_2H$	–
$HCOCO_3H$	–
$HCOCO_3$	–
$HOCH_2CO_2H$	–
Chlorine Species	
Cl	Atomic Chlorine
Cl_2	Molecular Chlorine
ClO	Chlorine Monoxide
OClO	–
Cl_2O_2	Chlorine Peroxide
HCl	Hydrogen Chloride
HOCl	Hypochlorous Acid
ClOO	Chloroperoxyl
CH_3OCl	Methyl Hypochlorite
ClCO	Chloroformyl Radical
ClO_3	Chlorine Trioxide
$HClO_4$	Perchloric Acid
ClO_4	Perchlorate

3.2.1 Odd-Nitrogen Chemistry

Odd-nitrogen (NO_x = NO + NO_2) chemistry also favours the atmosphere above 120–km, the point at which the very stable N_2 molecule can undergo photolysis. Below, the N_2 band is chemically stable with reactions with $O(^1D)$ being negligible at Martian pressures and temperatures [Krasnopolsky, 1993], and the abundance of NO_x is determined via downward diffusion from the thermosphere. The Mars Express observations of NO nightglow [Bertaux et al., 2005] highlighted that the supply of odd-nitrogen from high altitudes is significantly impacted by horizontal transport that my 1-D model is incapable of modelling. As a result my model holds NO + NO_2 abundances at an upper limit of 0.6–ppb, as per the work of Lefèvre

et al. [2004b]. This abundance was selected as three modelling studies of low-mid altitude ($<$ 70 km) NO_x performed by Nair et al. [1994], Krasnopolsky [1993], and Krasnopolsky [1995] all found NO_x abundances uniformly mixed with volume mixing ratios of roughly 0.6–ppb. The odd-nitrogen reactions accounted for in my 1-D photochemistry model are:

$$\begin{aligned} NO_2 + O &\longrightarrow NO + O_2 \\ NO + HO_2 &\longrightarrow NO_2 + OH \\ NO_2 + h\nu &\longrightarrow NO + O \\ NO + O_3 &\longrightarrow NO_2 + O_2 \quad , \end{aligned}$$

as done by Lefèvre et al. [2004b] and Krasnopolsky [2006a]. This is chiefly due to their inclusion resulting in better model O_3 column coincidences with early Mars O_3 observations due to their impacts on odd-hydrogen formation. NO and NO_2 are not included in the code as tracers for transport. Krasnopolsky [1995] found that out of 33 reaction rates involving NO_x only the first three listed above yield column rates greater than 10^{10} cm^{-2} s^{-1}, with all others with magnitudes less than 10^8 cm^{-2} s^{-1}. Compared to a CO_2 column density of $\sim 10^{23}$ molecules cm^{-2} on Mars, these other reactions are deemed negligible in the lower atmosphere. The reaction of NO with O_3 is included due to ozone having a very short lifetime, rendering it sensitive to chemical reactions with small rate coefficients. Moreover, any assumption of downward flux from the top of the model without thermosphere and ionosphere calculations above would result in inaccuracies and problematic inferences of the impacts of NO_x in the lower atmosphere.

3.2.2 Gas-Phase Chemistry

Compounds in the gas-state are capable of reacting through bi-molecular and termolecular, also known as three-body, reactions. In bi-molecular reactions, two species come into contact and react at a rate dependent on the concentrations of the reactants, and the temperature of the system. Their equations take the forms:

$$\begin{aligned} A + B &\longrightarrow AB \\ AB + C &\longrightarrow AC + B \quad , \end{aligned}$$

and the rate they occur at is typically found by employing the Arrhenius equation:

$$k(T) = A \exp\left(-\frac{E_a}{RT}\right) \quad \mathrm{cm^3\,molecule^{-1}\,s^{-1}} \quad , \tag{3.2}$$

in which E_a is the reaction activation energy (the energy threshold of the system required to trigger the reaction), A is the reaction's constant pre-exponential factor, R is the universal gas constant (J K^{-1} mol^{-1}) and T the atmospheric temperature (K). These are calculated experimentally through laboratory work and compiled in various sources such as JPL's 'Chemical Kinetics and Photochemical Data for Use in Atmospheric Studies' handbook [Burkholder et al., 2019] and the online NIST 'Chemical Kinetics Database' [Manion et al., 2015]. Some reaction rates are found to deviate from Equation 3.2 in laboratory experiments across the studied temperature ranges, in which case the three-parameter expression:

$$k(T) = A\left(\frac{T}{298}\right)^n \times \exp\left(-\frac{E_a}{RT}\right) \quad , \tag{3.3}$$

is used to accommodate for the deviation.

Termolecular reactions involve the presence of a third compound that remains unchanged in the reaction, with a general formula of:

$$A + B + M \longrightarrow AB + M \quad .$$

In these reactions, the initial product, AB, is produced in an excited state and will almost immediately decompose back to the original reactants. The inert body of the reaction, M, absorbs the excess energy of the product via collisions and stabilises it. On Mars, CO_2 acts as M, whereas on Earth N_2 performs this role. This poses some complications. The vast majority of termolecular reaction rates are calculated using N_2 as the bath gas, M, for use in Earth tropospheric and stratospheric modelling. CO_2 molecules have 2 chemical bonds available to adsorb energy in the collisions, as opposed to N_2's single bond, which results in an increased efficiency as an absorbing molecule [Kaufman and Kelso, 1967]. To accommodate this, the termolecular rate coefficients quoted in literature are multiplied by a factor of 2.5 as originally postulated by Nair et al. [1994], with the exception of rate a_1 of Table 3.2 which is multiplied by 2.075 as discovered experimentally by Sehested et al. [1995].

Three-body reactions supplied by sources such as Burkholder et al. [2019] are given in terms of a high and low pressure rate coefficient, k_∞ and k_0 respectively. In most cases at Martian atmospheric temperatures and pressures the differences between the two are negligible, so the value of k_0 is used in the model. This is not the case however for reactions c_{11} and c_{16} in Table 3.2. For these reactions, the Troe formula is used to produce a second-order approximation:

$$k_0(T) = k_0^{300}\left(\frac{T}{300}\right)^{-n} \quad \text{cm}^6\text{molecule}^{-2}\text{s}^{-1} \tag{3.4}$$

$$k_\infty(T) = k_\infty^{300}\left(\frac{T}{300}\right)^{-m} \quad \text{cm}^3\text{molecule}^{-1}\text{s}^{-1} \tag{3.5}$$

$$k_{3rd}(k_0^{300}, n, k_\infty^{300}, m) = \frac{k_0[M]\times 2.5}{1+\frac{k_0[M]\times 2.5}{k_\infty}} 0.6^{\left[1+[\log_{10}\frac{k_0[M]\times 2.5}{k_\infty}]^2\right]^{-1}} \quad , \tag{3.6}$$

which I have modified to include the 2.5 factor to account for CO_2's greater efficiency as a bath gas. The values of k_0^{300}, k_∞^{300}, n, and m are supplied by the rate coefficient sources [Sander et al., 2015, 2019, Manion et al., 2015]. The chemical and photolysis reactions used by the 1-D model to simulate the oxidation of CH_4 and C_2H_6 will be detailed in Chapter 4, and those involved in the simulation of atmospheric chlorine chemistry will be detailed in Chapter 6.

3.2.3 Heterogeneous Chemistry

The 1-D photochemistry submodule arrived with two heterogeneous chemical reactions, h_1 and h_2 in Table 3.2, that cover the uptake of OH and HO_2 radicals onto water ice particles. The rate coefficient values are calculated by the equation:

$$h_X = \frac{1}{4} v_{therm} \gamma S \quad ,$$

in which v_{therm} is the thermal velocity of the uptaking gas (cm s^{-1}), γ is the uptake coefficient of the reaction, representing the probability of a molecule colliding with the aerosol adsorbing onto the solid surface, and S is the surface area per unit volume (cm^2 cm^{-3}) of the aerosol involved in the reaction. To calculate the value of S for water ice or dust aerosols, the mass mixing ratio (MR) of the aerosol, in kg/kg, needs to be converted to number density, $N_{aerosol}$, in particles cm^{-3} within the model. This is done as follows:

$$N_{aerosol} = \frac{\rho_{atm}}{V_{aerosol}\rho_{aerosol}}\text{MR}$$
$$V_{aerosol} = \frac{4}{3}\pi r_{eff}^3 \quad ,$$

where r_{eff} is the aerosols effective radius in cm, and ρ_{atm} and $\rho_{aerosol}$ are the atmospheric and aerosol densities in g cm^{-3}. In this work, ρ_{Dust} is assumed to be 2.5 g cm^{-3} [Perko et al., 2006] and ρ_{Ice} is taken as 0.92 g cm^{-3}.

3.2.4 Semi-Implicit Backwards Euler Method

The photochemical lifetime of a species is defined as the time taken for it to lower to 1/e = 0.3679 of its original abundance through photochemical reactions. For trace gas species with lifetimes in the model that are greater than the model's chemistry timestep (600 s), the 1-D model uses the semi-implict backwards Euler method (SIBEM) to calculate the rates of change to the gases caused by photochemical interactions. The rates of production and loss for tracer i, P_i and L_i respectively, are calculated using tracer abundances in number density units (molec. cm^{-3}), denoted [i], using values at the current model timestep t. To calculate the abundance of [i] at the following model timestep using chemistry timestep value Δt_c, the equation:

$$
\begin{aligned}
P_i &= \sum_a \sum_b k_{ab}[a]^t[b]^t + \sum_c J_c[c]^t \quad (\text{molec.cm}^{-3}\text{s}^{-1}) \\
L_i &= \sum_d k_d[d]^t + \sum_i J_i \quad (\text{s}^{-1}) \\
[i]^{t+1} &= \frac{[i]^t + P_i \Delta t_c}{1 + L_i \Delta t_c} \quad ,
\end{aligned}
$$

is used. When used to calculate long-lived species, the equations abide to mass conservation. There are two cases involving inorganic chemistry that this scheme does not apply to: species in the O_x family, composed of O and O_3, and HO_x, composed of H, OH, and HO_2.

3.2.5 HO_x and O_x Photochemical Equilibrium

The scheme that handles the chemical modelling of O_x and HO_x was originally given in Lefèvre et al. [2004b]. During the day (defined as points where the solar zenith angle is less than 95°), O_x has a lifetime less than the chemistry timestep below $\sim$ 60 km [Krasnopolsky and Lefèvre, 2013]. Above, O and H can have lifetimes greater than 1 month. At night, without UV photolysis of O_3, O and O_3 can individually be handled by the SIBEM equation while maintaining mass conservation. With HO_x however, the species lifetime is always less than the chemistry timestep regardless of the solar zenith angle. O_3, OH, and HO_2 are assumed to be in photochemical equilibrium, and their individual abundances can be derived from their summed abundances HO_x and O_x respectively. For HO_x:

$$
\begin{aligned}
[HO_{\mathrm{x}}]^t &= [H]^t + [OH]^t + [HO_2]^t \\
[H]^t &= \frac{[HO_{\mathrm{x}}]^t}{1 + \frac{(1+[OH]^t/[HO_2]^t)}{[H]^t/[HO_2]^t}} \\
[HO_2]^t &= \frac{[H]^t}{[H]^t/[HO_2]^t} \\
[OH]^t &= [HO_2]^t \times [OH]^t/[HO_2]^t \quad ,
\end{aligned}
$$

and for O_x during daylight:

$$
\begin{aligned}
[O_{\mathrm{x}}]^t &= [O]^t + [O_3]^t \\
[O_3]^t &= \frac{[O_{\mathrm{x}}]^t}{[O]^t/[O_3]^t} \\
[O]^t &= [O_3]^t \times [O]^t/[O_3]^t \quad ,
\end{aligned}
$$

in which the ratios $[H]^t/[HO_2]^t$, $[OH]^t/[HO_2]^t$, and $[O]^t/[O_3]^t$ are from here referred to as the partition functions rh_ho2, roh_ho2, and ro_o3 respectively. The summed abundances, [O_x] and [HO_x], have lifetimes greater than the chemistry timestep, enabling their evolution to be modelled via the SIBEM equation.

Table 3.2: Inorganic reaction rate coefficients within the 1-D photochemistry submodule. Bimolecular rate coefficient units are cm^3 $molec^{-1}$ s^{-1}. Values denoted by superscript a are three-body reactions with values taken with atmospheric number density complying to temperatures of T = 298 K and pressures of 660 Pa. γ denotes the uptake coefficient of the heterogeneous reaction.

Key	Reaction	Formula	Rate at T = 298 K	Reference
		Reactions with O		
a_1	$O+O_2+M \rightarrow O_3+M$	2.075×6.00E-34(T/300)$^{-2.4}$	2.23E-16 ^{a}	Sander et al. [2015]
a_2	$O+O+M \rightarrow O_2+M$	2.50×9.46E-34exp(485/T)	2.10E-15 ^{a}	Campbell and Gray [1973]
a_3	$O+O_3 \rightarrow O_2+O_2$	8.00E-13exp(-2060/T)	7.96E-16	Sander et al. [2015]
		Reactions with O(^{1}D)		
b_1	$O(^1D)+CO_2 \longrightarrow O+CO_2$	7.40E-11exp(120/T)	1.11E-10	Sander et al. [2015]
b_2	$O(^1D)+H_2O \longrightarrow OH+OH$	1.63E-10exp(60/T)	1.99E-10	Sander et al. [2015]
b_3	$O(^1D)+H_2 \longrightarrow OH+H$	1.20E-10	1.20E-10	Sander et al. [2015]
b_4	$O(^1D)+O_2 \longrightarrow O+O_2$	3.30E-11exp(55/T)	3.97E-11	Sander et al. [2015]
b_5	$O(^1D)+O_3 \longrightarrow O_2+O_2$	1.20E-11	1.20E-11	Sander et al. [2015]
b_6	$O(^1D)+O_3 \longrightarrow O_2+O+O$	1.20E-11	1.20E-11	Sander et al. [2015]
b_7	$O(^1D)+CH_4 \longrightarrow CH_3+OH$	0.75×1.75E-10	1.31E-10	Sander et al. [2015]
b_8	$O(^1D)+CH_4 \longrightarrow CH_3O+H$	0.20×1.75E-10	3.50E-11	Sander et al. [2015]
b_9	$O(^1D)+CH_4 \longrightarrow HCHO+H_2$	0.05×1.75E-10	8.75E-12	Sander et al. [2015]
		Reactions with Hydrogen Compounds		
c_1	$O+HO_2 \longrightarrow OH+O_2$	3.00E-11exp(200/T)	5.87E-11	Sander et al. [2015]
c_2	$O+OH \longrightarrow O_2+H$	1.80E-11exp(180/T)	3.29E-11	Sander et al. [2015]
c_3	$H+O_3 \longrightarrow OH+O_2$	1.40E-10exp(-470/T)	2.89E-11	Sander et al. [2015]
c_4	$H+HO_2 \longrightarrow OH+OH$	7.20E-11	7.20E-11	Sander et al. [2015]
c_5	$H+HO_2 \longrightarrow H_2+O_2$	6.90E-12	6.90E-12	Sander et al. [2015]

Table 3.2 continued from previous page

c_6	$H + HO_2 \longrightarrow H_2O + O$	1.60E-12	1.60E-12	Sander et al. [2015]
c_7	$OH + HO_2 \longrightarrow H_2O + O_2$	4.80E-11exp(250/T)	1.11E-10	Sander et al. [2015]
c_8	$HO_2 + HO_2 \longrightarrow H_2O_2 + O_2$	1.50E-12exp(19/T)	1.60E-12	Christensen et al. [2002]
c_9	$OH + H_2O_2 \longrightarrow H_2O + HO_2$	1.80E-12	1.80E-12	Sander et al. [2015]
c_{10}	$OH + H_2 \longrightarrow H_2O + H$	2.80E-12exp(-1800/T)	6.67E-15	Sander et al. [2015]
c_{11}	$H + O_2 + M \longrightarrow HO_2 + M$	k_3rd(2.5×4.4E-32, -1.3, 7.5E-11, 0.2)	1.88E-14 [a]	Sander et al. [2015]
c_{12}	$O + H_2O_2 \longrightarrow OH + HO_2$	1.40E-12exp(-2000/T)	1.70E-15	Sander et al. [2015]
c_{13}	$OH + OH \longrightarrow H_2O + O$	1.80E-12	1.80E-12	Sander et al. [2015]
c_{14}	$OH + O_3 \longrightarrow HO_2 + O_2$	1.50E-12exp(-880/T)	7.83E-14	Sander et al. [2015]
c_{15}	$HO_2 + O_3 \longrightarrow OH + O_2 + O_2$	1.00E-14exp(-490/T)	1.93E-15	Sander et al. [2015]
c_{16}	$HO_2 + HO_2 + M \longrightarrow H_2O_2 + O_2 + M$	2.50×2.10E-33exp(920/T)	2.01E-14 [a]	Sander et al. [2015]
c_{17}	$OH + OH + M \longrightarrow H_2O_2 + M$	k_3rd(2.5×6.9E-31,-1, 2.60E-11, 0)	2.70E-13 [a]	Sander et al. [2015]
c_{18}	$H + H + M \longrightarrow H_2 + M$	2.5×1.80E-30/T	2.64E-14 [a]	Baulch et al. [2005]
		Odd-Nitrogen		
d_1	$NO_2 + O \longrightarrow NO + O_2$	5.1E-12exp(210/T)	1.03E-11	Sander et al. [2015]
d_2	$NO + O_3 \longrightarrow NO_2 + O_2$	3.0E-12exp-1500/T	1.9E-14	Sander et al. [2015]
d_3	$NO + HO_2 \longrightarrow NO_2 + OH$	3.3E-12exp270/T	8.17e-12	Sander et al. [2015]
		Carbon Compounds		
e_1	$OH + CO \longrightarrow CO_2 + H$	Details in Joshi and Wang [2006]	1.47E-13	Joshi and Wang [2006]
e_2	$O + CO + M \longrightarrow CO_2 + M$	2.5×6.50E-33exp(-2184/T)	1.87E-18 [a]	Tsang and Hampson [1986]
		Heterogeneous Reactions		
h_1	$HO_2 + \text{Ice} \longrightarrow \text{Ice} + \text{Products}$	γ = 0.025	Cooper and Abbatt [1996]	

Table 3.2 continued from previous page

h_2	$OH + \text{Ice} \longrightarrow \text{Ice} + \text{Products}$	γ = 0.03	Cooper and Abbatt [1996]

3.2.6 Photolysis

The general form of a photolysis reaction is shown in Equation 3.7, in which a gas molecule absorbs a photon that causes molecular decomposition. The rates at which gas molecules breakdown under electromagnetic (EM) radiation is dependent on the total actinic flux of the local environment, the molecules energy and often temperature-dependent adsorbtion cross-section, and the probability of the molecule breaking down in the adsorption process, commonly called the reaction's quantum yield.

$$AB + h\nu \longrightarrow A + B \tag{3.7}$$

The actinic flux of the atmosphere is the total amount of EM radiation originating from the Sun, both directly from the solar beam and indirectly from scattering off the surroundings. This value is highly dependent on numerous variables in the Martian atmosphere, namely the total atmospheric column overhead (molecules cm^{-2}), the atmospheric temperature, O_3 column density, the solar zenith angle, and the optical opacity above. The radiative transfer calculations required to calculate this flux requires significant computational calculations at each model timestep that would cause the model to become too computationally expensive. To ease computational expense, whilst still considering the effects of the atmosphere's composition on photolytic frequencies, my model interpolates photolytic frequencies (s^{-1}) from an offline dataset. The model interpolates from this dataset with respect to total and O_3 column densities above, temperature, solar zenith angle and dust opacity at each model altitude step.

The values in the offline dataset are produced by a modified Earth model, the Tropospheric Ultraviolet (TUV) model [Lefèvre et al., 2004a], in the same process that was used to produce the original photochemistry routine developed by Lefèvre et al. [2004b]. To replicate the Martian environment in the TUV the VMR of CO_2 is raised to $\sim$ 0.95, O_2 is lowered from 20.95% of the total air density to 1.5×10^{-3}%, SO_2 is removed, and NO_2 is set to 0.6 PPB per the assumption of NO_x detailed in Section 3.2.1. Climatological temperature and pressure profiles from the MCDv5.3 are used as inputs for the TUV also. My 1-D model interpolates the calculated frequencies with respect to surface temperatures ranging from 160 K to 260 K, which covers temperatures from high latitudes in sunlight during the northern hemisphere's winter to the southern hemisphere's summer. The table has a vertical resolution of roughly 1–km down to a surface pressure of 10 hPa, and the resolution of the solar zenith angle array ranges from steps of 5° from 0–90°, then steps of 1° up to 95° to account for the strong variances in values during sunset and sunrise. The O_3 column abundances considered range from 0.1–50 μm-atm, which adequately covers the 2–30 μm-atm abundances seen in the northern poles by Perrier et al. [2006] during the dry northern winter, where O_3 is at a maximum. Finally, optical opacity values considered in the interpolation scheme range from 0–4, which covers standard Martian climates and dust-storm events.

Table 3.3: Photolysis reactions in the 1-D photochemistry submodule already included at the point of the project start date. The rates presented are taken at aphelion (L_S = 71°) at a solar zenith angle of 0° at the Martian equator.

Key	Reaction	Rate at 4.80 km (s^{-1})	Rate at 75.90 km (s^{-1})
Inorganic Photolysis			
j_o2_o	$O_2 + h\nu \longrightarrow O + O$	3.23E-10	3.02E-8
j_o2_o1d	$O_2 + h\nu \longrightarrow O + O(^1D)$	0.	1.68E-8
j_co2_o	$CO_2 + h\nu \longrightarrow CO + O$	4.23E-12	7.62E-10
j_co2_o1d	$CO_2 + h\nu \longrightarrow CO + O(^1D)$	0.	6.76E-12
j_o3_o1d	$O_3 + h\nu \longrightarrow O_2 + O(^1D)$	2.9E-3	3.08E-3
j_o3_o	$O_3 + h\nu \longrightarrow O_2 + O$	4.83E-5	5.06E-5
j_h2o	$H_2O + h\nu \longrightarrow OH + H$	2.74E-10	6.37E-8
j_h2o2	$H_2O_2 + h\nu \longrightarrow OH + OH$	3.72E-5	4.11E-5
j_ho2	$HO_2 + h\nu \longrightarrow OH + O$	2.36E-4	2.51E-4
j_no2	$NO_2 + h\nu \longrightarrow NO + O$	3.25E-3	3.33E-3
Organic Photolysis			
j_ch4_ch3	$CH_4 + h\nu \longrightarrow CH_3 + H$	0.	5.30E-10
j_ch4_1ch2_h2	$CH_4 + h\nu \longrightarrow ^1CH_2 + H_2$	0.	1.06E-9
j_ch4_3ch2_h_h	$CH_4 + h\nu \longrightarrow ^3CH_2 + H + H$	0.	1.00E-10
j_ch4_ch_h2_h	$CH_4 + h\nu \longrightarrow CH + H_2 + H$	0.	1.23E-10
j_ch3o2h	$CH_3OOH + h\nu \longrightarrow CH_3O + OH$	2.12E-5	2.22E-5
j_ch2o_hco	$HCHO + h\nu \longrightarrow HCO + H$	3.29E-5	3.39E-5
j_ch2o_co	$HCHO + h\nu \longrightarrow CO + H_2$	3.44E-5	3.56E-5
j_ch3oh	$CH_3OH + h\nu \longrightarrow CH_3O + H$	2.26E-7	1.14E-6
j_c2h6	$C_2H_6 + h\nu \longrightarrow$ Products	0.	1.54E-9
Chlorine Photolysis			
j_hcl	$HCl + h\nu \longrightarrow H + Cl$	1.15E-7	6.49E-7
j_hocl	$HOCl + h\nu \longrightarrow OH + Cl$	1.89E-4	1.94E-4
j_clo	$ClO + h\nu \longrightarrow Cl + O$	2.20E-3	2.32E-3

3.2.7 Time-dependent meteorological boundary conditions

To drive the 1-D photochemistry model, I use time-dependent lateral atmospheric boundary conditions of temperature, wind, water vapour volume mixing ratios, and surface pressure from the Mars Climate Database v5.3 (MCD) Millour et al. [2017]. I interpolate the 3-D meteorological fields from the MCD dataset, taking into account latitude, solar longitude, and local time, enabling photochemical calculations to be performed by the 1-D model over diurnal periods at any desired location.

Throughout this work, all interpolated values from the MCD dataset are longitudinal means, calculated independently by myself, acknowledging that there are only small longitudinal variations of meteorological parameters that are due primarily to topographical features. I take advantage of this so that the horizonal footprint of my model is representative of a zonal band of 3.75° in latitude, which is the latitudinal resolution of the MCD dataset. Zonal and meridional transport is not accounted for by the 1-D model. I use an interpolation routine for trace gases that have atmospheric chemistry lifetimes greater than the e-folding residence times associated with meridional advection of trace gases out of the zonal band, which is approximately 0.5–2 sols. I use this approach to drive the model with vertical profiles of CO_2, CO, O_2, H_2, and water vapour, ensuring the photochemical environment is consistent with the meteorological fields from the MCD, allowing the 1-D model to be accurately representative of the temporally and spatially variable oxidising environment. Seasonal water vapour profiles from MCD are especially important for the 1-D photochemical calculations as the photolysis of Martian H_2O is the source of the highly reactive odd-hydrogen species, HO_x = H + OH + HO_2, which help drive the oxidation of organic species and O_3 chemistry [Lefèvre et al., 2004b].

The overarching purpose of using these boundary conditions is that I can describe detailed 1-D atmospheric chemistry, including diurnal and seasonal changes associated with Mars' atmosphere, without the computational overhead of solving the 3-D dynamical equations. In particular, the boundary conditions help to maintain realistic values and variations of wind profiles that underpin vertical diffusion calculations that correspond to calculating vertical transport.

Chapter 4

Photochemistry of Methane and Ethane in the Martian Atmosphere

There is considerable debate in the community about the validity and robustness of detections of atmospheric methane (CH_4) on Mars. Detections of atmospheric CH_4 have been reported by teams analysing data obtained by numerous satellites [Formisano et al., 2004, Geminale et al., 2008, 2011, Giuranna et al., 2019], Earth-based telescopes [Krasnopolsky et al., 2004, Mumma et al., 2009], and *in situ* instruments [Moores et al., 2019b, Webster et al., 2015, Webster et al., 2018]. These reports of CH_4 on Mars are not universally corroborated however, as other teams using satellites have failed to detect any at all [Korablev et al., 2019, Liuzzi et al., 2019] or have contradicted the findings of prior reports such as those made using the TES by Fonti and Marzo [2010] [Fonti et al., 2015, Zahnle et al., 2011]. There have also been numerous observation campaigns using Earth-based telescopes that reported no detections of CH_4 [Krasnopolsky, 2007, 2012, Krasnopolsky et al., 1997, Villanueva et al., 2013], which casts doubt on the actual existence of CH_4 on Mars [Zahnle et al., 2011] .

This debate highlights the difficulty of measuring atmospheric CH_4 on Mars, and the gaps in our current understanding of the production and loss terms that determine atmospheric CH_4 on Mars should it exist. In this chapter, I explore how the presence of CH_4 could be determined by its oxidation products and in the process discuss how abiotic CH_4 could be potentially produced by organic chemistry.

Detections of atmospheric CH_4 at the Gale crater by the NASA Curiosity Rover were observed episodically rising from mean volume mixing ratios (VMRs) of 0.69 ± 0.25 parts per billion (ppb) to 7.20 ± 2.10 ppb across a 60-sol period [Webster et al., 2015]. The diurnal variations of CH_4 observations via Curiosity have recently been substantiated by the ExoMars Trace Gas Orbiter's Nadir and Occultation for Mars Discovery (NOMAD) spectrometer and Atmospheric Chemistry Suite (ACS)[Korablev et al., 2019, Moores et al., 2019b]. These measurements by NOMAD and ACS constrained the upper limit of CH_4 in the Martian atmosphere to 0.05 ppb.

Ground-based telescopes reported a signal of a plume that contained approximately 19,000 tonnes of CH_4 [Mumma et al., 2009] near the Syrtis Major region during Mars' northern hemisphere's midsummer, consistent with an estimated 0.60 kg $m^{-2}s^{-1}$ seasonal point source of organic compounds. Other searches for CH_4 on Mars have conversely failed to detect the compound [Webster et al., 2013], including the Trace Gas Orbiter's year and a half long search [Moores et al., 2019b]. This highlights the possibility of methane being significantly more temporally variable than current models predict [Lefèvre and Forget, 2009]. This inconsistency with regards to CH_4's detection has also ignited some polemic against the existance of the gas on Mars [Zahnle et al., 2011]. Recent analysis of data from the Planetary Fourier Spectrometer (PFS) aboard the Mars Express orbiter identified the presence of CH_4 in the Martian atmosphere that was confirmed via independent observations by Giuranna et al. [2019]. These results appear to confirm Curiosity's detection of CH_4 at the Gale Crater. The team retrieved column integrated VMRs of 15.5 $\pm$ 2.50 ppb above the Gale Crater only 1 Martian day (sol) after the Curiosity rover's measurement of a 5.78 $\pm$ 2.27 ppb [Webster et al., 2015].

To further study these possible emissions of CH_4, and to also provide a more detailed series of observations of the vertical structure and composition of Mars' atmosphere, the ExoMars mission program was established by the European Space Agency (ESA) [Vago et al., 2015] and the Russian Roscosmos State Corporation for Space Activities. The first mission conducted within this program was the launch of the Trace Gas Orbiter (TGO) in 2016, that included two suites of spectrometers, the Nadir and Occultation for MArs Discovery (NOMAD) spectrometer [Vandaele et al., 2018] and the Atmospheric Chemistry Suite (ACS) [Korablev et al., 2018]. The TGO underwent 11 months of aerobraking to reduce its orbital speed and altitude, eventually establishing an approximately circular orbit of altitude roughly 400 km allowing scientific observations to start in April 2018 [Vandaele et al., 2019]. Over the first year, no successful observations of CH_4 were reported by the TGO instrumentation [Korablev et al., 2019]. I developed my investigation bearing in mind the capabilities of TGO instruments, especially the solar occultation channels of NOMAD (NOMAD-SO) and ACS (ACS-MIR). The NOMAD-SO instrument has been designed to be sensitive to CH_4 abundances as low as 0.025 ppb when observed in solar occultation mode [Robert and et. al, 2016]. This expected detection limit was compared to the experimental values in Vandaele et al. [2019]. The TGO instruments improved the experimental upper limit of previous instrumentation to reach a limit of roughly 0.05 ppb for methane. A few profiles reported in Korablev et al. [2019] and obtained via ACS-MIR, measured in clear northern conditions, were able to achieve the most precise detection limits of 0.012 ppb down to an altitude of roughly 3 km.

Previous studies using 1-D photochemical models [Wong et al., 2003, Summers et al., 2002] calculate the photochemical lifetime of CH_4 to be roughly 300 years below 70 km. In the absence of a strong surface loss process, surface emissions of CH_4 will then become homogeneously distributed across the planet after being introduced into the atmosphere. This inconsistency between models and data means that the available atmospheric data is misinterpreted, and/or there is a loss mechanism that we do no not currently consider in models [Krasnopolsky, 2006b]. Previous calculations using a global 3-D general circulation model have determined that to reconcile models and data we need a CH_4 loss process that is up to 600 times faster than any known process [Lefèvre and Forget, 2009]. That additional sink would lower the atmospheric lifetime of CH_4 from centuries to less than 200 days. With the advent of the TGO, another approach we can take is to analyse observed spatial and temporal variations of the oxidation products of atmospheric CH_4. This requirement of an exceptionally strong chemical or physical sink for CH_4 to corroborate our models with the reported observations is another source of doubt for the validity of the reported CH_4 detections over the past two decades.

In this study, I describe the development of the 1-D photochemistry submodule from the LMD-UK General Circulation Model (GCM) [Forget et al., 1999, Lewis et al., 1999] to include organic chemistry and run it as an independent model to study photochemistry on Mars. I describe results from a series of numerical experiments that describe how the presence of CH_4 affects photochemistry on Mars. I also report photochemical results when I replace CH_4 with ethane (C_2H_6) to show this longer-chain hydrocarbon produced richer atmospheric chemistry but also allows us to consider an abiotic source of atmospheric CH_4 from the oxidation of acetaldehyde. In the next section I briefly detail the 1-D model of Mars' organic photochemistry. I then report results from my numerical experiments. I conclude the chapter with a discussion on the implications of my results for broadly understanding atmospheric chemistry on Mars but in particular the implications for detecting the presence of CH_4 and C_2H_6 on Mars using their oxidation products.

4.1 Organic Photochemistry

I build on the chemical mechanism by including 41 new organic compounds, guided by previous studies [Wong et al., 2003, Summers et al., 2002] and also the theoretical measurement capabilities of the NOMAD instrument [Robert and et. al, 2016], to improve understanding of Mars' atmospheric chemistry. I include CH_4, C_2H_6 and its photochemical products. The chemistry scheme does not consider the photochemistry of the CH and CH_2 radical species, which are included in previous modelling studies [Wong et al., 2003]. This is due to their

production being dominated by the UV photolysis of CH_4, which, as I shall so, only becomes efficient above $\sim$ 70 km. Their inclusion in the following work will therefore only serve to increase the computational expense of the model, but their inclusion will be necessary for the study of organic photochemistry of the thermosphere.

The extended chemical mechanism represents an additional 106 chemical reactions (Table 4.2 holds 36 reactions involved in CH_4 oxidation, Table 4.4 holds 70 involved in C_2H_6 oxidation) and 29 photolysis reactions (Table 4.5). A complete list of the organic trace gas species within the 1-D model is provided in Table 4.1. In the following work, I present the first analysis of C_2H_6 oxidation products in the Martian atmosphere.

Table 4.1: Organic trace gas species handled by the 1-D Photochemistry Submodule

Formula	Name
Organic Tracers (Methane Oxidation)	
CH_4	Methane
CH_3	Methyl Radical
CH_3O_2	Methyl Peroxy-radical
CH_3OOH	Methyl Hydroperoxide
CH_3OH	Methanol
CH_3O	Methoxide
HCHO	Formaldehyde
HCOOH	Formic Acid
$HOCH_2O_2$	Hydromethyl Peroxy
$HOCH_2OH$	Methanediol
$HOCH_2OOH$	Hydromethyl Hydroperoxide
HCO	Formyl Radical
Organic Tracers (Ethane Oxidation)	
C_2H_6	Ethane
C_2H_5	Ethyl Radical
$C_2H_5O_2$	Ethyldioxy Radical
C_2H_5OOH	Ethyl Peroxide
C_2H_5OH	Ethanol
$HOCH_2CH_2O_2$	-
$HOCH_2CH_2O$	-
Ethgly ($(CH_2OH)_2$)	Ethylene Glycol
Hyetho2h ($C_2H_6O_3$)	-
CH_3CHO	Acetaldehyde
CH_2CHOH	Ethenol
CH_3CHOHO_2	Hydroxy Ethyl Peroxy Radical
CH_3COOH	Acetic Acid

$CH_3CHOHOOH$	-
$CH_3C(O)$	Acetyl Radical
$CH_3C(O)OO$	-
$CH_3C(O)OOH$	Peracetic Acid
$HCOCH_2O_2$	-
Glyox (OCHCHO)	Glyoxal
HCOCO	-
$HOOCH_2CHO$	Hydroperoxy Acetaldehyde
$HOCH_2CHO$	Glycolaldehyde
HOCHCHO	Hydroxyl-Vinoxy Radical
$HOCH_2CO$	-
$HOCH_2CO_3$	-
$HOCH_2CO_2H$	Glycolic Acid
$HCOCO_2H$	-
$HCOCO_3H$	-
$HCOCO_3$	-
$HOCH_2CO_3H$	-

For these additional trace 41 organic tracers, I have added an additional 107 gas-phase reactions for the modelling of CH_4 and C_2H_6 oxidation in the atmosphere of Mars. I take the organic chemistry rate coefficients from the CAABA/MECCA v4.0 atmospheric box model [Sander et al., 2019], which is used to model organic chemistry within Earth's atmosphere. I have modified the mechanism to include HCO and C_2H_5 radicals. The CAABA/MECCA v4.0 model neglects these radicals as products, and instead includes the products of the radicals with molecular oxygen, O_2. This approximation is sufficient for Earth, where O_2 is present at 21% mass fraction, but on Mars it is present only at a mass fraction of 10^{-3}. Including these radicals allows us to improve the description of organic chemistry. All three-body reaction rate coefficients in the submodule are multiplied by a factor of 2.5, following Nair et al. [1994], to account for the increase in efficiency that CO_2 displays when used as a bath gas in comparison to N_2 or dry air, commonly used in laboratories for the calculation of these coefficients.

Peroxy-radicals, organic species with the generic chemical formula R-O_2 where R denotes a sequence of C, H, and O atoms, can engage in a significant number of different reactions with one another. These 'permutation' reactions occur between two R-O_2 compounds of the same species (self-reactions), and also between two different R-O_2 species (cross-reactions). Far too many possible pertmutation reactions exist for a numerical scheme to explicitly calculate, so the CAABA/MECCA v4.0 organic oxidation routines makes use of the permutation formalism detailed in Jenkin et al. [1997], which is an approach developed originally by Madronich

and Calvert [1990] with a simplification that assumes the primary co-reactant of reactions with R-O_2 species is CH_3O_2. To ease computational expense, the total abundance of peroxy-radicals is found at the start of each model timestep. The rate of the reactions of individual R-O_2 compounds, such as reaction cab_{44} in Table 4.4, are found by treating the summed R-O_2 abundance as one of the reactants. The reactions of R-O_2 species can produce up to three product channels, the branching ratios of which vary depending on the specific R-O_2 species molecular geometry, and can be temperature dependent. Table 4.3 presents the coefficients and parameters used in the permutation routine for organic atmospheric chemistry found in Sander et al. [2019] that I have incorporated into the 1-D photochemistry model and use to produce the results of the following chapter.

I limit my calculations to latitudes less than 30°, where most recent observations of CH_4 on Mars have been reported [Mumma et al., 2009, Webster et al., 2015, Webster et al., 2018]. At latitudes higher than 40° in both hemispheres, the MCD boundary conditions also allow us to describe the large-scale seasonal changes in atmospheric temperature that result from condensation, deposition and sublimation of CO_2, which produce significant changes in surface pressure. However, at these latitudes meridional wind profiles above the planetary boundary layer can become large enough to lower the tracer e-folding timescales to values too small for the 1-D model to neglect while still producing reliable model results. At latitudes less than 30°, the 1-D model in this work can be used to produce time-dependent tracer profiles for periods limited to 2 sols.

Table 4.2: Chemical reactions and rate coefficients involved in the oxidation of CH_4 used in my 1-D photochemistry model. Bimolecular rate coefficient units are cm^3 $molec^{-1}$ s^{-1}. [a] are three-body reactions with values taken with atmospheric number density complying to temperatures of T = 298 K and pressures of 660 Pa. [b] are unimolecular rate coefficients with units s^{-1}.

Methane Reaction Scheme				
Key	Reaction	Formula	Rate at T = 298 K	Reference
cab_1	$CH_4 + OH \longrightarrow CH_3 + OH$	1.85E-20exp(2.82LOG(T) - 987./T)	6.40E-15	Sander et al. [2019]
cab_2	$CH_4 + O \longrightarrow 0.51 * CH_3 + 0.51 * OH + 0.49 * CH_3O + 0.49 * H$	6.03E-18($T^{2.17}$)exp(-3619/T)	7.50E-18	Sander et al. [2019]
cab_3	$CH_3 + O_2 + M \longrightarrow CH_3O_2 + M$	k_3rd(7.00E-31, 3., 1.80E-12, -1.1)	1.14E-13 [a]	Sander et al. [2019]
cab_4	$CH_3 + O_3 \longrightarrow 0.956 * HCHO + 0.956 * H + 0.044 * CH_3O + O_2$	5.10E-12exp(-210/T)	2.52E-12	Sander et al. [2019]
cab_5	$CH_3 + O \longrightarrow 0.83 * HCHO + 0.83 * H + 0.17 * CO + 0.17 * H_2 + 0.17 * H$	1.30E-10	1.3E-10	Sander et al. [2019]
cab_6	$CH_3O_2 + HO_2 \longrightarrow CH_3OOH + O_2$	3.8E-13exp(780/T) /(1 + 1/(498exp(1160/T)))	5.21E-12	Sander et al. [2019]
cab_7	$CH_3O_2 + HO_2 \longrightarrow HCHO + H_2O + O_2$	3.8E-13exp(780/T) /(1 + 498exp(-1160/T)))	4.67E-13	Sander et al. [2019]
cab_8	$CH_3O_2 + R - O_2 \longrightarrow CH_3O + 0.5 * O_2$	2×7.40E-13exp(-520/T)	2.59E-13	Sander et al. [2019]
cab_9	$CH_3O_2 + R - O_2 \longrightarrow 0.5 * HCHO + 0.5 * CH_3OH + 0.5 * O_2$	2×(k_ch3o2 - 7.40E-13exp(-520/T))	4.43E-13	Sander et al. [2019]
cab_{10}	$CH_3O_2 + O_3 \longrightarrow CH_3O + O_2 + O_2$	2.90E-16exp(-1000/T)	1.01E-17	Sander et al. [2019]
cab_{11}	$CH_3O_2 + OH \longrightarrow CH_3O + HO_2$	1.40E-10	1.40E-10	Sander et al. [2019]
cab_{12}	$CH_3O_2 + O \longrightarrow CH_3O + O_2$	4.30E-11	4.30E-11	Sander et al. [2019]
cab_{13}	$CH_3OH + OH \longrightarrow 0.85 * HCHO + 0.85 * HO_2 + 0.15 * CH_3O + H_2O$	6.38E-18(T^2)exp(144/T)	9.19E-13	Sander et al. [2019]
cab_{14}	$CH_3OOH + OH \longrightarrow 0.6 * CH_3O_2 + 0.4 * HCHO + 0.4 * OH + H_2O$	k_ch3ooh_oh	1.00E-11	Sander et al. [2019]
cab_{15}	$CH_3O + O_2 \longrightarrow HO_2 + HCHO$	1.30E-14exp(-633/T)	1.55E-15	Sander et al. [2019]
cab_{16}	$CH_3O + O_3 \longrightarrow CH_3O_2 + O_2$	2.53E-14	2.53E-14	Sander et al. [2019]

cab_{17}	$CH_3O + O \longrightarrow 0.75 * CH_3 + 0.75 * O_2 + 0.25 * HCHO + 0.25 * OH$	2.50e-11	2.50E-11	Sander et al. [2019]
cab_{18}	$HCHO + OH \longrightarrow HCO + H_2O$	5.50E-12exp(-125/T)	3.60e-12	Sander et al. [2011]
cab_{19}	$HCHO + HO_2 \longrightarrow HOCH_2O_2$	9.70E-15exp(625/T)	7.90E-14	Sander et al. [2019]
cab_{20}	$HCHO + O \longrightarrow HCO + OH$	2.99E-11exp(-1529/T)	1.77E-13	Herron [1988]
cab_{21}	$HCO + O \longrightarrow CO + OH$	5.00E-11	5.00E-11	Baulch et al. [1992]
cab_{22}	$HCO + CH_3 \longrightarrow CH_4 + CO$	4.40E-11	4.40E-11	Mulenko [1987]
cab_{23}	$HCO + CH_3 \longrightarrow CH_3CHO$	4.42E-11	4.42E-11	Mulenko [1980]
cab_{24}	$HCO + HCO \longrightarrow HCHO + CO$	4.48E-11	4.48E-11	Friedrichs et al. [2002]
cab_{25}	$HCO + OH \longrightarrow CO + H_2O$	1.69E-10	1.69E-10	Baulch et al. [1992]
cab_{26}	$HCO + O_2 \longrightarrow CO + HO_2$	5.20E-12	5.20E-12	Sander et al. [2011]
cab_{27}	$HCO + H \longrightarrow CO + H_2$	1.83E-10	1.83E-10	Friedrichs et al. [2002]
cab_{28}	$HOCH_2O_2 \longrightarrow HCHO + HO_2$	2.40E12exp(-7000/T)	150.89 [b]	Sander et al. [2019]
cab_{29}	$HOCH_2O_2 + HO_2 \longrightarrow 0.5 * HOCH_2OOH + 0.5 * HCOOH + 0.2 * OH + 0.2 * HO_2 + 0.3 * H_2O + 0.8 * O_2$	5.6E-15exp(2300/T)	1.26E-12	Sander et al. [2019]
cab_{30}	$HOCH_2O_2 + R - O_2 \longrightarrow HCOOH + HO_2$	$2\times$(k_ch3o2$\times$5.50E-12)$^{0.5}$	2.78E-12	Sander et al. [2019]
cab_{31}	$HOCH_2O_2 + R - O_2 \longrightarrow 0.5 * HCOOH + 0.5 * HOCH_2OH + 0.5 * O_2$	$2\times$(k_ch3o2$\times$5.70E-14 $\times$exp(750/T))$^{0.5}$	9.95E-13	Sander et al. [2019]
cab_{32}	$HCOOH + OH \longrightarrow CO_2 + HO_2 + H_2O$	2.94E-14exp(786/T) + 9.85E-13exp(-1036/T)	4.42E-13	Sander et al. [2019]
cab_{33}	$HOCH_2OOH + OH \longrightarrow HOCH_2O_2$	k_roohro	6.02E-12	Sander et al. [2019]
cab_{34}	$HOCH_2OOH + OH \longrightarrow HCOOH + H_2O + OH$	k_rohro + k_s$\times$f_soh$\times$f_sooh	2.59E-11	Sander et al. [2019]
cab_{35}	$HOCH_2OH + OH \longrightarrow HO_2 + HCOOH + H_2O$	$2\times$k_rohro + k_s$\times$f_soh^2	1.13E-11	Sander et al. [2019]
cab_{107}	$CH_3 + OH + M \longrightarrow CH_3OH + M$	2.5$\times$dens$\times$2.48E-27exp(298./t)$^{3.8}$	9.92E-10	Fagerström et al. [1994]

Table 4.3: Functions and constants used by the R-O_2 permutation reaction handling scheme extracted from the CAABA/MECCA v4.0 box model.

CAABA/MECCA v4.0 Reaction Rate Parameters		
Key	Formula	Notes and Citations
Radical Arrhenius Equations		
k_ch3o2	1.03E-13*exp(365/T)	CH_3O_2 Self-reaction [Sander et al., 2019]
k_ch3ooh	5.30E-12*exp(190/T)	CH_3OOH + OH Reaction [Sander et al., 2019]
k_ch3co2h	4.00E-14*exp(850/T)	CH_3CO_2H + OH Reaction [Sander et al., 2019]
k_ro2ho2_1	2.91E-13*exp(1300/T)*(1 - exp(-0.245*1))	RO_2 + HO_2 (One carbon atom) [Sander et al., 2019]
k_ro2ho2_2	2.91E-13*exp(1300/T)*(1 - exp(-0.245*2))	RO_2 + HO_2 (Two carbon atoms) [Sander et al., 2019]
Arrhenius Equations for H Abstraction by OH		
k_s	4.50E-18*T^2*exp(253./T)	Taraborrelli [2010], Sander et al. [2019]
k_t	2.12E-18*T^2*exp(696/T)	Taraborrelli [2010], Sander et al. [2019]
k_rohro	2.10E-18*T^2*exp(-85/T)	Taraborrelli [2010], Sander et al. [2019]
k_roohro	0.60*k_ch3ooh	Taraborrelli [2010], Sander et al. [2019]
k_co2h	0.7*k_ch3co2h	Taraborrelli [2010], Sander et al. [2019]
kdec	1.00E6	Atkinson et al. [2006], Sander et al. [2019]
Updated Rate Constants for RO_3 + HO_2 Reactions		
kapho2	5.20E-13*exp(980/T)*1.865	Groß et al. [2014], Sander et al. [2019]
Arrhenius Equations for Permutation Reactions		
k_ro2soro2	2*(7.70E-15*exp(1330/T)*k_ch3o2)$^{0.5}$	Sander et al. [2019]
k_ro2rco3	4.00E-12*exp(500/T)	Sander et al. [2019]
k_ro2poro2	2*7.50E-14*exp(500/T)	Sander et al. [2019]
Substituent Factors		
f_soh	3.44	Taraborrelli [2010], Sander et al. [2019]
f_sooh	8.00	Taraborrelli [2010], Sander et al. [2019]
f_pch2oh	1.29	Taraborrelli [2010], Sander et al. [2019]
f_tooh	8.00	Taraborrelli [2010], Sander et al. [2019]
f_toh	2.68	Taraborrelli [2010], Sander et al. [2019]
f_o	8.15	Taraborrelli [2010], Sander et al. [2019]
f_cho	0.55	Taraborrelli [2010], Sander et al. [2019]

f_co2h	1.67	Taraborrelli [2010], Sander et al. [2019]
	Branching Ratios for RO_2 + HO_2 Reactions	
rco3_o3	0.10	Groß et al. [2014], Sander et al. [2019]
rco3_oh	0.69	Groß et al. [2014], Sander et al. [2019]
rco3_ooh	0.21	Groß et al. [2014], Sander et al. [2019]
rchoch2o2_oh	0.10	Sander et al. [2019]
rcoch2o2_oh	0.15	Sander et al. [2019]
rcoch2o2_ooh	0.85	Sander et al. [2019]

Table 4.4: Chemical reactions and rate coefficients involved in the oxidation of C_2H_6 used in my 1-D photochemistry model. Bimolecular rate coefficient units are cm^3 $molec^{-1}$ s^{-1}. [a] are three-body reactions with values taken with atmospheric number density complying to temperatures of T = 298 K and pressures of 660 Pa. [b] are unimolecular rate coefficients with units s^{-1}.

Ethane Reaction Scheme				
Key	Reaction	Formula	Rate at T = 298 K	Reference
cab_{36}	$C_2H_6 + OH \longrightarrow C_2H_5 + H_2O$	7.66E-12exp(-1020/T)	2.50E-13	Sander et al. [2015]
cab_{37}	$C_2H_6 + O \longrightarrow C_2H_5 + OH$	2.21E-15(T/298)$^{6.5}$exp(-132/T)	1.42E-15	Cohen and Westberg [1991]
cab_{38}	$CH_3 + CH_3 + M \longrightarrow C_2H_6$	Details in Cody et al. [2003]	5.12E-11 [a]	Cody et al. [2003]
cab_{39}	$C_2H_5 + O_2 + M \longrightarrow C_2H_5O_2$	2.5$\times$1.50E-28(298/T)^3$\times$dens	6.02E-11 [a]	Sander et al. [2015]
cab_{40}	$C_2H_5 + C_2H_5 \longrightarrow C_2H_4 + C_2H_6$	2.01E-12	2.01E-12	Dobis and Benson [1991]
cab_{41}	$C_2H_5 + O_2 \longrightarrow C_2H_4 + HO_2$	1.90E-14	1.90E-14	Sander et al. [2015]
cab_{42}	$C_2H_5 + H \longrightarrow CH_3 + CH_3$	7.95E-11exp(-132/T)	5.11E-11	Pratt and Wood [1984]
cab_{43}	$C_2H_5O_2 + HO_2 \longrightarrow C_2H_5OOH + O_2$	7.50E-13exp(700/T)	7.86E-12	Sander et al. [2019]
cab_{44}	$C_2H_5O_2 + RO_2 \longrightarrow 0.8 * CH_3CHO + 0.6 * HO_2 + 0.2 * C_2H_5OH + O_2$	2(7.60E-14*k_ch3o2)$^{0.5}$	3.27E-13	Sander et al. [2019]
cab_{45}	$C_2H_5OOH + HO_2 \longrightarrow C_2H_5OOH + O_2$	k_roohro	6.02E-12	Sander et al. [2019]
cab_{46}	$C_2H_5OOH + OH \longrightarrow CH_3CHO + OH$	k_s*f_sooh	7.47E-12	Sander et al. [2019]
cab_{47}	$C_2H_5OH + OH \longrightarrow 0.95 * C_2H_5O_2 + 0.95 * HO_2 + 0.05 * HOCH_2CH_2O_2 + H_2O$	3.00E-12exp(20/T)	3.21E-12	Sander et al. [2019]
cab_{48}	$HOCH_2CH_2O_2 + RO_2 \longrightarrow 0.6 * HOCH_2CH_2O + 0.2 * HOCH_2CHO + 0.2 * ETHGLY$	2*(7.80E-14exp(1000/T)*k_ch3o2)$^{0.5}$	1.77E-12	Sander et al. [2019]
cab_{49}	$HOCH_2CH_2O_2 + HO_2 \longrightarrow HYETHO2H$	1.53E-13exp(1300/T)*(1-k_rchohch2o2_oh)	1.08E-11	Sander et al. [2019]
cab_{50}	$HOCH_2CH_2O_2 + HO_2 \longrightarrow HOCH_2CH_2O + OH$	1.53E-13exp(1300/T)*k_rchohch2o2_oh	1.20E-12	Sander et al. [2019]
cab_{51}	$HOCH_2CH_2O + O_2 \longrightarrow HO_2 + HOCH_2CHO$	6.00E-14exp(-550/T)	9.48E-15	Sander et al. [2019]
cab_{52}	$HOCH_2CH_2O \longrightarrow HO_2 + HCHO + HCHO$	9.5E13exp(-5988/T)	1.78E5 [b]	Sander et al. [2019]
cab_{53}	$ETHGLY + OH \longrightarrow HOCH_2CHO + HO_2 + H_2O$	2*k_s*f_soh*f_pch2oh + 2*k_rohro	8.57E-12	Sander et al. [2019]
cab_{54}	$HYETHO2H + OH \longrightarrow HOCH_2CH_2O_2 + H_2O$	k_roohro	6.02E-12	Sander et al. [2019]
cab_{55}	$HYETHO2H + OH \longrightarrow HOCH_2CHO + OH + H_2O$	k_s*f_sooh*f_pch2oh	9.64E-12	Sander et al. [2019]
cab_{56}	$HYETHO2H + OH \longrightarrow HOOCH_2CHO + HO_2 + H_2O$	k_s*f_soh*f_pch2oh + k_rohro	4.29E-12	Sander et al. [2019]

cab_{57}	$CH_3CHO + OH \longrightarrow CH_3C(O) + H_2O$	4.40E-12exp(365/T)*0.95	1.42E-11	Sander et al. [2019]
cab_{58}	$CH_3CHO + OH \longrightarrow HCOCH_2O_2 + H_2O$	4.40E-12exp(365/T)*0.05	7.48e-13	Sander et al. [2019]
cab_{59}	$CH_3CHO + HO_2 \longrightarrow CH_3CHOHO_2$	3.46E12exp(-12500/(1.98*T)) / 6.34E26*exp(-1470/(1.98*T))	4.77E-22	Sander et al. [2019]
cab_{60}	$CH_3CHO + HCOOH \longrightarrow CH_2CHOH + HCOOH$	(1.17E-19*$T^{2.209}$)exp(-556/(1.987T))	1.34E-14	Sander et al. [2019]
cab_{61}	$CH_2CHOH + OH \longrightarrow HCOOH + OH + HCHO$	4.30E-11	4.30E-11	Sander et al. [2019]
cab_{62}	$CH_2CHOH + OH \longrightarrow HOCH_2CHO + HO_2$	2.40E-11	2.40E-11	Sander et al. [2019]
cab_{63}	$CH_2CHOH + HCOOH \longrightarrow CH_3CHO + HCOOH$	(4.67E-26*$T^{3.286}$)exp(-556/(T*1.987))	2.47E-18	Sander et al. [2019]
cab_{64}	$CH_3CHOHO_2 \longrightarrow CH_3CHO + HO_2$	3.46E12exp(-12500/(T*1.98))	2.18E3 [b]	Sander et al. [2019]
cab_{65}	$CH_3CHOHO_2 + HO_2 \longrightarrow 0.5 * CH_3CHOHOOH + 0.3 * CH_3COOH + 0.2 * CH_3 + 0.2 * HCOOH + 0.2 * OH + O_2$	5.60E-15exp(2300/T)	1.26E-11	Sander et al. [2019]
cab_{66}	$CH_3CHOHO_2 + RO_2 \longrightarrow CH_3 + HCOOH + OH$	k_ro2soro2	9.68E-13	Sander et al. [2019]
cab_{67}	$CH_3COOH + OH \longrightarrow CH_3 + CO_2 + H_2O$	4.00E-14exp(850/T)	6.93E-13	Sander et al. [2019]
cab_{68}	$CH_3CHOHOOH + OH \longrightarrow CH_3COOH + OH$	k_t*f_tooh*f_toh + k_rohro	4.19E-11	Sander et al. [2019]
cab_{69}	$CH_3CHOHOOH + OH \longrightarrow CH_3CHOHO_2$	k_roohro	6.02E-12	Sander et al. [2019]
cab_{70}	$CH_3C(O) + O_2 + M \longrightarrow CH_3C(O)OO + M$	5.10E-12(1 - 1/(1 + 9.48E-18*dens*2.5))	4.04E-12 [a]	Sander et al. [2019]
cab_{71}	$CH_3C(O) + O_2 + M \longrightarrow OH + HCHO + CO + M$	5.10E-12/(1 + 9.48E-18*dens*2.5))	1.06E-12 [a]	Sander et al. [2019]
cab_{72}	$CH_3C(O)OO + HO_2 \longrightarrow OH + CH_3 + CO_2$	5.20E-13exp(980/T)*1.507*0.61	1.28E-11	Sander et al. [2019]
cab_{73}	$CH_3C(O)OO + HO_2 \longrightarrow CH_3C(O)OOH$	5.20E-13exp(980/T)*1.507*0.23	4.83E-12	Sander et al. [2019]
cab_{74}	$CH_3C(O)OO + HO_2 \longrightarrow CH_3COOH + O_3$	5.20E-13exp(980/T)*1.507*0.16	3.36E-12	Sander et al. [2019]
cab_{75}	$CH_3C(O)OO + RO_2 \longrightarrow CH_3 + CO_2$	k_ro2rco3*0.9	1.93E-11	Sander et al. [2019]
cab_{76}	$CH_3C(O)OO + RO_2 \longrightarrow CH_3COOH$	k_ro2co3*0.1	2.14E-12	Sander et al. [2019]
cab_{77}	$CH_3C(O)OOH + OH \longrightarrow CH_3C(O)OO + H_2O$	k_roohro	6.02E-12	Sander et al. [2019]
cab_{78}	$HCOCH_2O_2 + RO_2 \longrightarrow 0.6 * HCHO + 0.6 * CO + 0.6 * HO_2 + 0.2 * GLYOX + 0.2 * HOCH_2CHO$	k_ro2poro2	8.03E-12	Sander et al. [2019]
cab_{79}	$HCOCH_2O_2 + HO_2 \longrightarrow HOOCH_2CHO$	k_ro2ho2_2*rcoch2o2_ooh	7.52E-12	Sander et al. [2019]
cab_{80}	$HCOCH_2O_2 + HO_2 \longrightarrow HCHO + CO + HO_2 + OH$	k_ro2ho2_2*rcoch2o2_oh	1.33E-12	Sander et al. [2019]
cab_{81}	$GLYOX + OH \longrightarrow HCOCO + H_2O$	3.10E-12exp(340/T)	9.70E-12	Sander et al. [2019]
cab_{82}	$HCOCO \longrightarrow HCO + CO$	1.40E12exp(-3159/T)	3.54E7 [b]	Orlando and Tyndall [2001]

cab_{83}	$HCOCO + O_2 \longrightarrow HCOCO_3$	5.00E-12*3.2*exp(-550/T)	2.53E-12	Sander et al. [2019]
cab_{84}	$HCOCO + O_2 \longrightarrow OH + CO + CO_2$	5.00E-12(1 - 3.2exp(-550/T))	2.47E-12	Sander et al. [2019]
cab_{85}	$HOOCH_2CHO + OH \longrightarrow HCOCH_2O_2 + H_2O$	k_roohro	6.02E-12	Sander et al. [2019]
cab_{86}	$HOOCH_2CHO + OH \longrightarrow HCHO + CO + OH + H_2O$	0.8*8.00E-12	6.40E-12	Sander et al. [2019]
cab_{87}	$HOOCH_2CHO + OH \longrightarrow GLYOX + OH + H_2O$	0.55*k_s*f_sooh*f_cho	2.26E-12	Sander et al. [2019]
cab_{88}	$HOCH_2CHO + OH \longrightarrow HOCH_2CO + H_2O$	0.8*8.00E-12	6.40E-12	Sander et al. [2019]
cab_{89}	$HOCH_2CHO + OH \longrightarrow HOCHCHO + H_2O$	0.2*8.00E-12	1.60E-12	Sander et al. [2019]
cab_{90}	$HOCHCHO \longrightarrow GLYOX + HO_2$	kdec	1.00E6 [b]	Sander et al. [2019]
cab_{91}	$HOCH_2CO + O_2 + M \longrightarrow HOCH_2CO_3 + M$	5.10E-12*(1 - 1/(1 + 1.85E-18*dens*2.5))	2.17E-12 [a]	Sander et al. [2019]
cab_{92}	$HOCH_2CO + O_2 + M \longrightarrow OH + HCHO + CO_2 + M$	5.10E-12*(1 + 1.85E-18*dens*2.5)	8.89E-12 [a]	Sander et al. [2019]
cab_{93}	$HOCH_2CO_3 + RO_2 \longrightarrow HCHO + CO_2 + HO_2$	k_ro2rco3*0.9	1.93E-11	Sander et al. [2019]
cab_{94}	$HOCH_2CO_3 + RO_2 \longrightarrow HOCH_2CO_2H$	k_ro2rco3*0.1	2.14E-12	Sander et al. [2019]
cab_{95}	$HOCH_2CO_3 + HO_2 \longrightarrow HCHO + OH + HO_2 + CO_2$	kapho2*rco3_oh	9.25E-12	Sander et al. [2019]
cab_{96}	$HOCH_2CO_3 + HO_2 \longrightarrow HOCH_2CO_3H$	kapho2*rco3_ooh	2.82E-12	Sander et al. [2019]
cab_{97}	$HOCH_2CO_3 + HO_2 \longrightarrow HOCH_2CO_2H + O_3$	kapho2*rco3_o3	1.34E-12	Sander et al. [2019]
cab_{98}	$HOCH_2CO_2H + OH \longrightarrow 0.09 * HCHO + 0.91 * HCOCO_2H + HO_2 + H_2O$	k_co2h + k_s*f_soh*f_co2h	5.50E012	Sander et al. [2019]
cab_{99}	$HCOCO_2H + OH \longrightarrow CO + HO_2 + CO_2 + H_2O$	k_co2h + k_t*f_o*f_co2h	2.66E-11	Sander et al. [2019]
cab_{100}	$HOCH_2CO_3H + OH \longrightarrow HOCH_2CO_3 + H_2O$	k_roohro	6.02E-12	Sander et al. [2019]
cab_{101}	$HOCH_2CO_3H + OH \longrightarrow HCOCO_3H + HO_2$	k_s*f_soh*f_co2h	5.37E-12	Sander et al. [2019]
cab_{102}	$HCOCO_3H + OH \longrightarrow HCOCO_3 + H_2O$	k_roohro	6.02E-12	Sander et al. [2019]
cab_{103}	$HCOCO_3H + OH \longrightarrow CO + CO_2 + H_2O + OH$	k_t*f_o*f_co2h	2.65E-11	Sander et al. [2019]
cab_{104}	$HCOCO_3 + RO_2 \longrightarrow CO + HO_2 + CO_2$	k_ro2rco3*0.9	1.93E-11	Sander et al. [2019]
cab_{105}	$HCOCO_3 + RO_2 \longrightarrow HCOCO_2H + O_2$	k_ro2rco3*0.1	2.14E-12	Sander et al. [2019]
cab_{106}	$HCOCO_3 + HO_2 \longrightarrow HO_2 + CO + CO_2 + OH$	kapho2	1.34E-11	Sander et al. [2019]

Table 4.5: Organic photolytic reactions used within the 1-D photochemistry submodule. Values (s^{-1}) are interpolated from an offline look-up table constructed by a modified TUV Madronich et al. [2002] model with respect to CO_2 and O_3 column abundances overheard, temperature, optical opacity and solar zenith angle. Values displayed are extracted for a solar zenith angle of 0°, L_S = 251° (perihelion).

Key	Reaction	J(z = 0.50 km)	J(z = 42.67 km)	J(z = 69.81 km)
$j_{CH_4 \rightarrow CH_3}$	$CH_4 + h\nu \longrightarrow CH_3 + H$	0.00	0.00	8.12E-10
$j_{CH_4 \rightarrow {}^1CH_2}$	$CH_4 + h\nu \longrightarrow {}^1CH_2 + H_2$	0.00	0.00	1.63E-9
$j_{CH_4 \rightarrow {}^3CH_2}$	$CH_4 + h\nu \longrightarrow {}^3CH_2 + H + H$	0.00	0.00	1.53E-10
$j_{CH_4 \rightarrow CH}$	$CH_4 + h\nu \longrightarrow CH + H_2 + H$	0.00	0.00	1.95E-10
j_{CH_3OOH}	$CH_3OOH + h\nu \longrightarrow CH_3O + OH$	2.23E-5	2.90E-5	2.97E-5
$j_{HCHO \rightarrow HCO}$	$HCHO + h\nu \longrightarrow HCO + H$	3.54E-5	4.62E-5	4.74E-5
$j_{HCHO \rightarrow CO}$	$HCHO + h\nu \longrightarrow H_2 + CO$	3.71E-5	4.88E-5	5.01E-5
j_{CH_3OH}	$CH_3OH + h\nu \longrightarrow CH_3O + H$	1.59E-7	1.12E-6	1.64E-6
$j_{C_2H_6}$	$C_2H_6 + h\nu \longrightarrow Products$	0.00	0.00	2.39E-9
$j_{CH_3CHO \rightarrow CH_3}$	$CH_3CHO + h\nu \longrightarrow CH_3 + HCO$	2.43E-5	3.40E-5	3.44E-5
$j_{CH_3CHO \rightarrow CH_4}$	$CH_3CHO + h\nu \longrightarrow CH_4 + CO$	5.46E-6	6.80E-6	6.81E-6
j_{HOCH_2OOH}	$HOCH_2OOH + h\nu(+O_2) \longrightarrow HCOOH + HO_2 + OH$	4.43E-5	5.43E-5	5.43E-5
$j_{HOCH_2CHO \rightarrow HCO}$	$HOCH_2CHO + h\nu \longrightarrow CH_3O + HCO$	4.08E-5	5.04E-5	5.05E-5
$j_{HOCH_2CHO \rightarrow CO}$	$HOCH_2CHO + h\nu \longrightarrow CH_3OH + CO$	4.91E-6	6.07E-6	6.09E-6
$j_{HOCH_2CHO \rightarrow OH}$	$HOCH_2CHO + h\nu(+O_2) \longrightarrow HCOCH_2O_2 + OH$	3.44E-6	4.25E-6	4.26E-6
$j_{Glyox \rightarrow HCO}$	$Glyoxal + h\nu \longrightarrow HCO + HCO$	7.84E-5	8.49E-5	8.5E-5
$j_{Glyox \rightarrow H_2}$	$Glyoxal + h\nu \longrightarrow H_2 + CO + CO$	1.90E-5	2.19E-5	2.20E-5
$j_{Glyox \rightarrow HCHO}$	$Glyoxal + h\nu \longrightarrow HCHO + CO$	2.79E-5	3.13E-5	3.14E-5
j_{CH_3COOH}	$CH_3COOH + h\nu \longrightarrow CH_3 + COOH$	7.77E-6	9.43E-6	9.44E-6
$j_{CH_3C(O)OOH}$	$CH_3C(O)OOH + h\nu \longrightarrow CH_3 + OH + CO_2$	3.85E-5	4.73E-6	4.75E-5

Proxies			
Key	Reaction	Proxy	Source
$j_{HOCH_2CO_3H}$	$HOCH_2CO_3H + h\nu \longrightarrow HCHO + HO2 + OH + CO2$	j_{CH_3OOH}	Sander et al. [2014]
j_{HCOCO_2H}	$HCOCO_2H + h\nu \longrightarrow 2HO_2 + CO + CO_2$	$3.95 \times j_{HCHO \rightarrow CO}$	Kuhlmann et al. [2003]
$j_{CH_3CHOHOOH}$	$CH_3CHOHOOH + h\nu \longrightarrow CH_3 + HCOOH + OH$	j_{CH_3OOH}	Sander et al. [2014]
$j_{Hyetho2h}$	$Hyetho2h + h\nu \longrightarrow HO_2 + CO + OH + CO_2$	$j_{CH_3OOH} + j_{HOCH_2CHO \rightarrow HCO} + j_{HOCH_2CHO \rightarrow CO} + j_{HOCH_2CHO \rightarrow OH}$	Sander et al. [2014]
j_{HCOCO_3H}	$HCOCO_3H + h\nu \longrightarrow HO_2 + CO + OH + CO2$	$j_{Hyetho2h}$	Sander et al. [2014]
j_{HOOCH_2CHO}	$HOOCH_2CHO + h\nu \longrightarrow HCHO + OH + HO2 + CO$	$j_{Hyetho2h}$	Sander et al. [2014]

4.2 Definition of Numerical Experiments

I use the 1-D model to determine vertical profiles of organic compounds that evolve from a hypothetically fixed and vertically uniform 50 ppt profile of CH_4. I chose this value because it was consistent with the upper limit of Martian CH_4 determined by data collected from the ACS/NOMAD instruments aboard the TGO [Korablev et al., 2019].

For this calculation, I initialise the model 10 sols prior to the point where solar longitude L_S = 0° with initial meteorological conditions and tracer profiles of CO_2, CO, O_2, water vapour, and H_2 from the previously detailed MCD v5.3 look-up table, and 50 ppt of CH_4 distributed evenly across all 25 atmospheric layers ranging from the surface to approximately 70 km. I then run the 1-D over one Mars year, 668 sols, following a 10 sol spin-up period, taking into account diurnal and seasonal (orbital) variations in solar zenith angle and corresponding changes in solar flux and photolytic frequencies. I report calculations at latitudes of 30°N, 2.5°N, and 30°S to investigate possible spatial variations in organic product profiles.

Following this investigation into the annual variations of the products produced by the steady and homogeneous CH_4 background, I use the 1-D model to investigate time-dependent photochemical processes that result from oxidation of CH_4 and C_2H_6. For these experiments, I initialise the 1-D model at the required latitude and solar longitude at 00:00 local time (LT) with 0 ppt CH_4 and other non-methane organic compounds. I use a five-day spin-up period at a constant solar longitude when I use trace gas profiles of CO_2, CO, O_2, H_2, and water vapour from the MCD v5.3 and diurnally-varying atmospheric parameters. This spin-up enables the HO_x and O_x chemistry to partition to the solar-longitude environment. After five sols, I add a vertically-uniform 50 ppt profile of CH_4 at 00:00 LT. I then let the model run freely for one further sol, and present the photochemical products at a local time of 18:00 LT when solar occultation measurements are typically collected. I adopt a similar approach to examine the photochemistry of C_2H_6.

4.3 Results

I use the 1-D model described in the previous section to understand the seasonal chemical composition of the Martian atmosphere as a function of latitude that corresponds to a fixed, uniform vertical distribution of atmospheric CH_4. I present a similar set of calculations that correspond to a uniform vertical distribution of atmospheric C_2H_6.

4.3.1 Methane Oxidation in the Atmosphere of Mars

Figure 4.1 describes the photochemical oxidation steps of atmospheric CH_4 on Mars. The dominant atmospheric losses of CH_4 are oxidation by the hydroxyl radical (OH) and the excited singlet oxygen ($O(^1D)$), and photolysis. The loss rates for atmospheric CH_4 vary as a function of solar longitude. There are a number of high-yield oxidation products that are produced rapidly, potentially allowing us to colocate elevated values with CH_4 emissions, and that are observable from orbiting instruments. In this chapter I will restrict my analysis to the production of formaldehyde (HCHO) and formic acid (HCOOH).

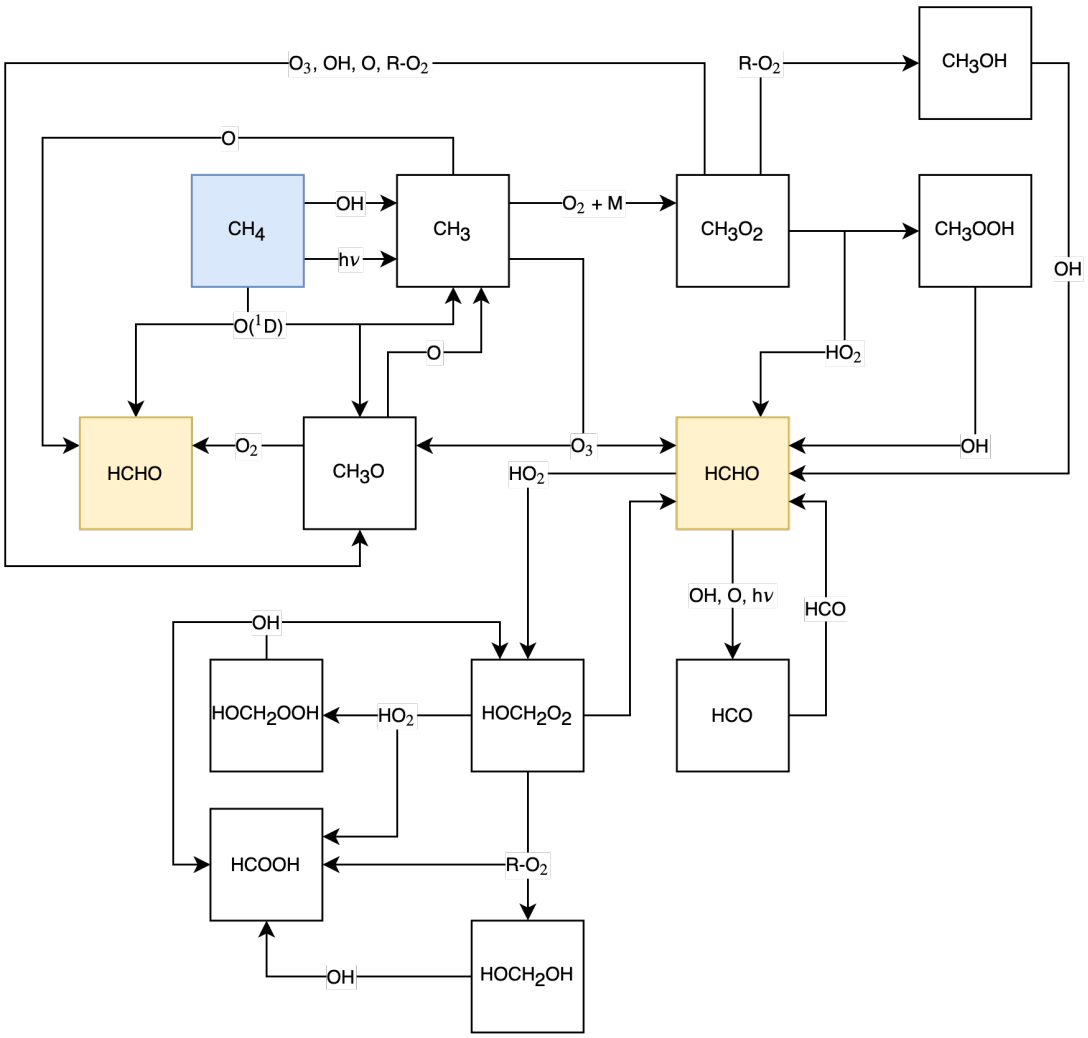


Figure 4.1: Primary stages of the CH_4 photochemistry that I use in my 1-D photochemistry model, taken from the CAABA/MECCA v4.0 chemical mechanism.

Figure 4.2 shows an illustrative vertical distribution of CH_4 loss factors (s^{-1}) at the solar longitudes of 71° and 271°, times at which Mars' orbit is furthest from and closest to the Sun, respectively. Loss factors, units of s^{-1}, are distinguished from loss rates, units of molec $cm^{-3}s^{-1}$, as loss factors provide a better insight into the reactivity of the surrounding environment. These values after being multiplied by CH_4 number densities equate to the rate of photochemical loss of CH_4 (molec $cm^{-3}s^{-1}$), i.e. the loss rate.

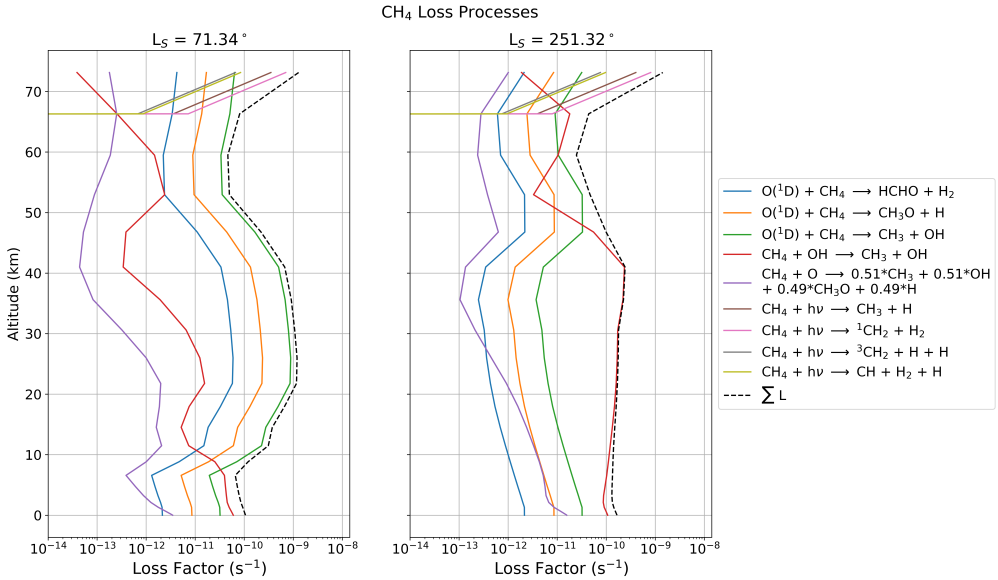


Figure 4.2: Photochemical loss factors (s^{-1}) CH_4 in my 1-D photochemistry model at latitude 2.5°N, local time 12:00, and solar longitudes 71° and 251° (Mars' aphelion and perihelion, respectively) as a function of altitude.

From the Martian surface to the top of the Martian hygropause, approximately 10 km at L_S 71° and 45 km at L_S 251°,the dominant loss process for CH_4 is from oxidation by OH. Consequently, at these altitudes the rate of OH production, driven by the photolysis of water vapour, are larger than outside this altitude range. Above these altitudes, the abundance of $O(^1D)$ increases, reflecting the drop in its loss from reaction with water vapour. Between the top of the hygropause and roughly 60 km, $O(^1D)$ becomes the dominant loss of atmospheric CH_4. There are three oxidation channels associated with this reaction (Table 4.2), the most efficient producing CH_3 and OH. Photolysis of CH_4 becomes significant only at altitudes higher than 60 km. The decreasing abundance of $O(^1D)$ atoms in the upper atmosphere results in a small vertical region, 50–60 km, where CH_4 loss rates decline before photolysis becomes important at higher altitudes. Below 60 km, the effect of UV radiation on CH_4 is negligible, and photochemical contributions made by methyl radical isotopologues can be disregarded. This

highlights that the primary atmospheric sinks of CH_4 change seasonally, with O(^1D) dominating in the aphelion seasons, and OH dominating in the perihelion. The stronger reaction rates of O(^{1}D) with CH_4 can thus be expected to produce greater abundances of potentially observable organic species within the aphelion seasons of Mars.

The local atmospheric lifetime of CH_4, incorporating all chemical loss terms (Figure 4.2), varies as a function of latitude and solar longitude. Differences between latitudes are determined by the solar radiation being received, which is a function of solar longitude and Mars' obliquity. Local atmospheric lifetimes range from 25 to 1700 years (Figure 4.3). These values, with a significant and localized surface loss process, would generate a large, slowly varying background value for CH_4 that would be difficult to attribute to individual surface sources. Local atmospheric lifetimes reach a minimum of 25–200 years between the top of the hygropause and approximately 50 km due to the larger abundance of the O(^{1}D) atom. Below the hygropause where OH is the dominant sink, local atmospheric lifetimes vary between 200 and 425 years. The longest local lifetimes of 1000–1700 years lie between 50 and 60 km during winter (L_S = 270–360°), as described above, where the OH and O(^{1}D) loss processes decline and before photolysis dominates above 60 km.

These local atmospheric photochemical lifetimes are significantly longer than the corresponding atmospheric transport timescales across all altitudes and solar longitudes. I study the variance of these local photochemical lifetimes with solar longitude, altitude, and Mars latitude to understand where are the most photochemically active regions for CH_4 (and below for C_2H_6) and consequently where I expect the largest production rates for their oxidation products. Calculating the vertically integrated photochemical lifetime of CH_4 with the 1-D model (Figure 4.3) yields timescales that correspond well to those calculated in previous studies [Lefèvre and Forget, 2009, Krasnopolsky et al., 2004, Summers et al., 2002], with the 1-D model producing values ranging between 250–550 terrestrial years across the latitude ranges studied here of 30° south to 30° north.

Figure 4.4 shows vertical profiles of the volume mixing ratios of organic compounds, radicals, peroxy-radicals, and long-lived species from left to right, that result from the oxidation of a fixed, uniformly distribution 50 ppt of atmospheric CH_4. For this calculation I initialise the 1-D model with 0 ppt of CH_4 across all vertical layers at L_S = 71° and L_S = 251°, 00:00 LT, at a latitude of 2.5°, the latitude at which a CH_4 plume has been previously observed [Mumma et al., 2009]. I spin-up for five sols using detailed MCD v5.3 tracer profiles. I then insert a fixed, uniform profile of 50 ppt of CH_4 into the model and run forward for one sol. I sample the model at 18:00 LT on sol 6, allowing sufficient time (18 hours) for products to be produced but a short enough time to ensure these products are not advected out of the column. This allows us to study the resulting CH_4 oxidation product concentrations. We show values for CH_4, HCHO, HCOOH, methanol, methyl hydroperoxide (CH_3OOH), hydromethyl peroxy ($HOCH_2O_2$), and hydromethyl hydroperoxide ($HOCH_2OOH$). The two products with the highest photochemical

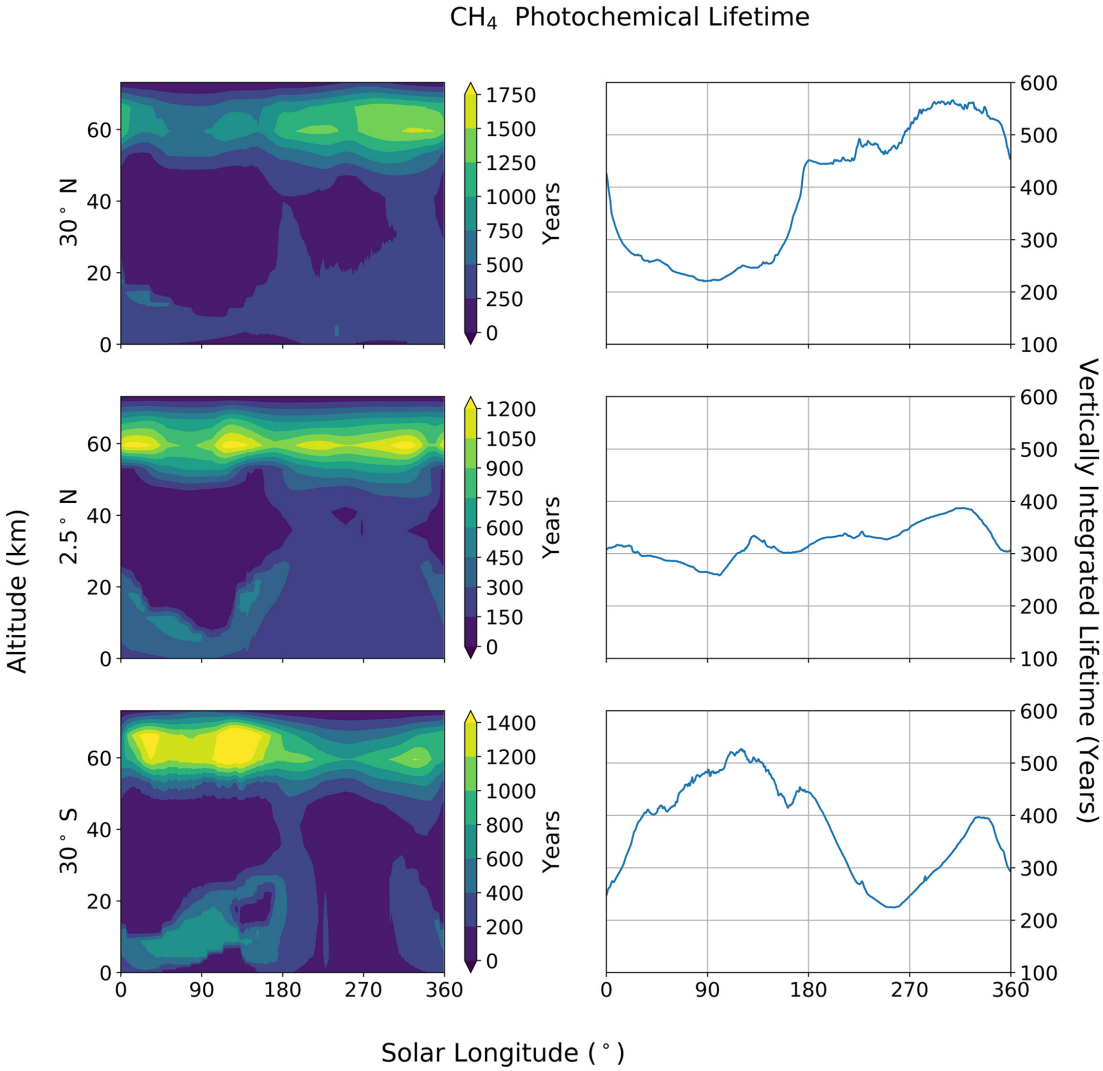


Figure 4.3: Local and vertically integrated photochemical lifetime of CH4 within the atmosphere of Mars and its variations with altitude (km) and solar longitude at latitudes 30° N, 2.5° N, and 30° S, respectively. All vertical segments are values from the 1-D photochemistry model at 12:00 LT.

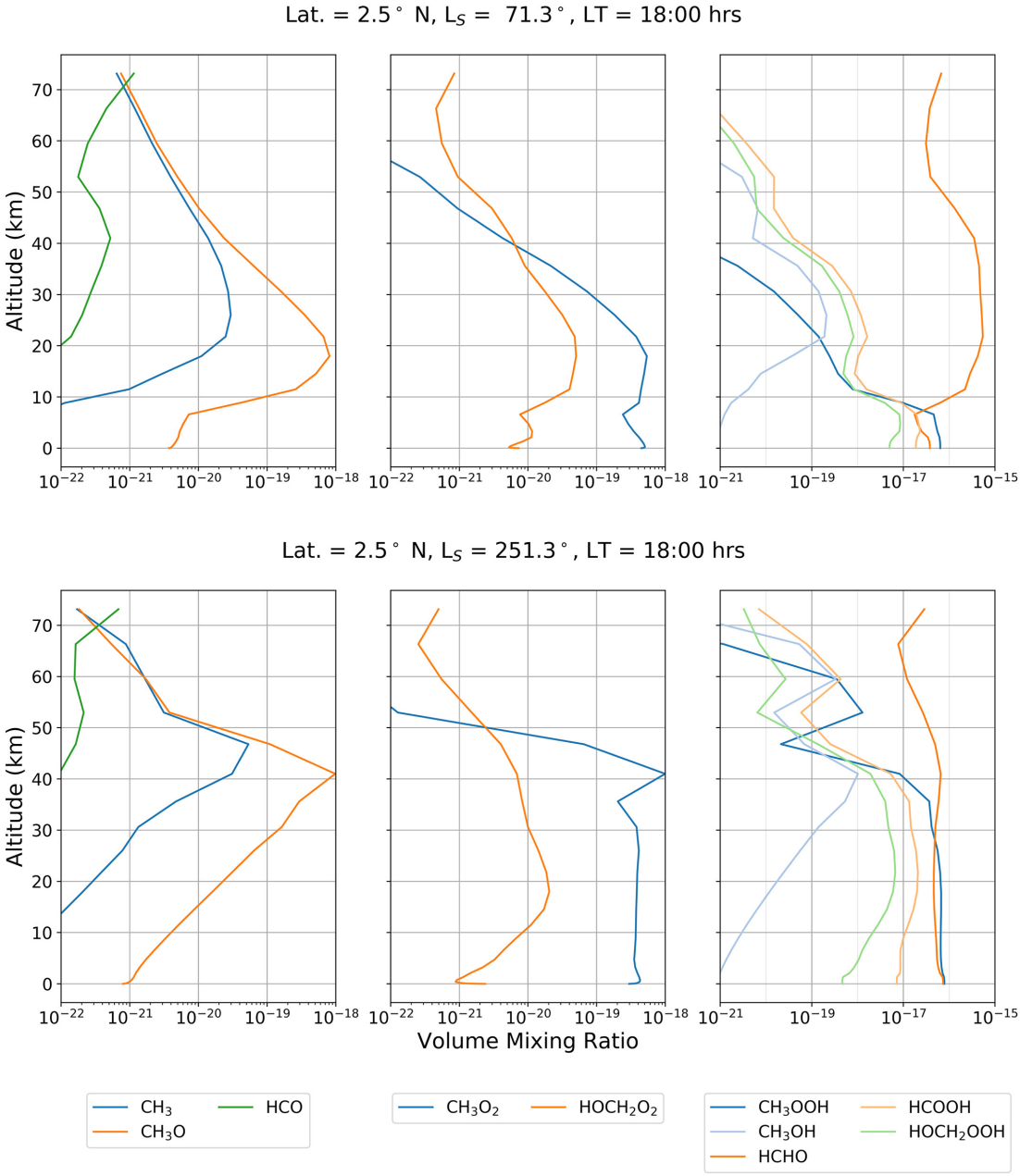


Figure 4.4: Volume mixing ratio profiles of major photochemical products of 50 ppt of CH4 after one sol. These include formaldehyde (HCHO), formic acid (HCOOH), methanol (CH_3OH), methyl hydroperoxide (CH_3OOH), hydromethyl peroxy ($HOCH_2O_2$), and hydromethyl hydroperoxide ($HOCH_2OOH$)

yields are HCHO and HCOOH. I find that HCHO has column averaged mixing ratios of 5.43×10^{-16} and 7.41×10^{-17} molecule/molecule at L_S = 71° and 251°, respectively. HCOOH has a column averaged mixing ratio of 2.31×10^{-17} and 2.08×10^{-17} molecule/molecule at L_S = 71° and 251°, respectively. I describe below the responsible production and loss rates associated with these two compounds.

Production rates of methanol are small in my 1-D model, which is driven by a realistic 50 ppt of CH_4. Previous studies that have used a much larger 100 ppm profile of CH_4 (e.g. Wong et al. [2003]) have still struggled to produce Martian methanol above ppt values. CH_3OH has prominent features at IR wavelengths, making it a valuable observed species to help constrain our understanding of organic chemistry. My 1-D model calculates CH_3OH column average mixing ratios of 2.09×10^{-19} and 1.01×10^{-18} molecule/molecule at L_S = 71° and 251°, respectively. These small quantities are due to the two main production terms for CH_3OH (Table 4.2) involving CH_3O_2 and CH_3 radicals that are not produced in large quantities by 50 ppt of CH_4. Consequently, I will only discuss CH_3OH in context of HCHO and HCOOH.

4.3.2 Production of Formaldehyde from CH_4 Oxidation

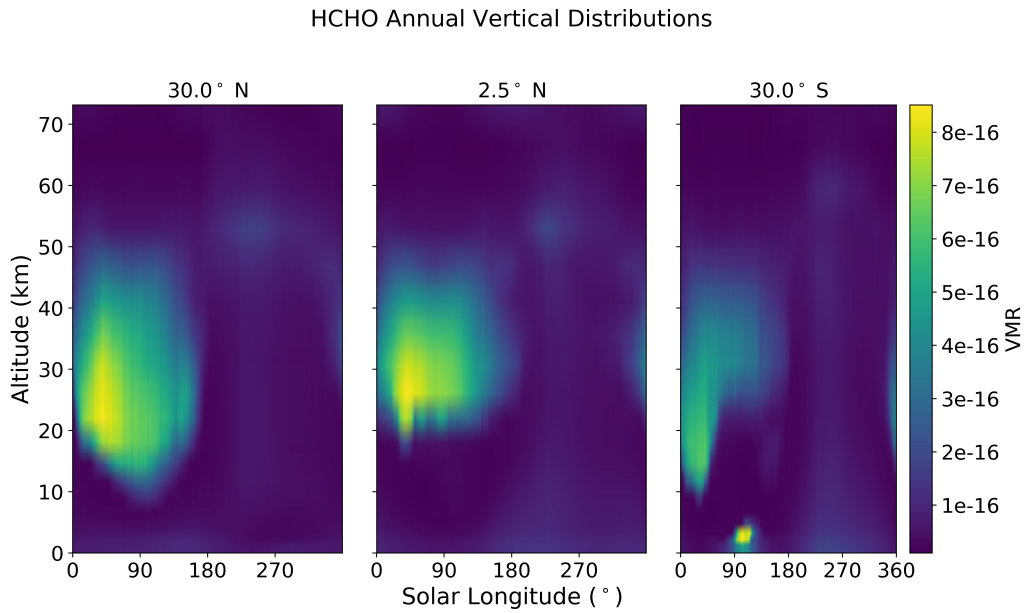


Figure 4.5: Vertical profiles of HCHO (ppt) from the photochemistry of 50 ppt CH_4 within a zonal band centered on latitudes 30°N, 2.5°N, and 30°S, across all solar longitudes, as calculated by my 1-D photochemical model.

HCHO is a high-yield oxidation product of CH_4 on Mars that is observable by the NOMAD and ACS spectrometers aboard the Trace Gas Orbiter. Figure 4.5 shows vertical distributions of HCHO volume mixing ratios, corresponding to a fixed vertical profile of 50 ppt CH_4, at 18:00 LT over all solar longitudes to determine when we might expect HCHO to be observable during one Martian year. HCHO production peaks during spring months when there is sufficient production of $O(^1D)$ in the middle atmosphere to oxidize CH_4 but not water vapour in the lower atmosphere. My model finds only small variations in the HCHO produced across

the three latitudes, where HCHO consistently remains below 10^{-3} ppt. This lies well below the expected detection limit of 30–40 ppt for the TGO NOMAD instrument [Vandaele and Rodriguez-Gomez, 2013] and of 0.17–1.70 ppb for the TGO ACS instrument [Korablev et al., 2018].

Figure 4.6 shows individual and net production and loss rates of HCHO as a function of altitude at 06:30 LT, L_S = 71°, and latitude 2.5°N. I find net production peaks at 06:30 LT as the Sun begins to rise above the horizon. Figure 4.6a shows two distinct regions where HCHO production peaks. Below the hygropause, at roughly 15 km at this L_S, reaction between water vapour and excited atomic oxygen result in HCHO production dominated by the reaction of CH_3O_2 and HO_2. Above the hygropause at 15 km, the HCHO production is from atomic oxygen reacting with methyl and methoxy radicals. Figure 4.6b show the HCHO loss rates. I find that HCHO is lost rapidly by photolysis through the atmospheric column. Below the hygropause, HCHO is lost by reaction with HO_2 which produced the $HOCH_2O_2$ peroxy radical. Above the hygropause, the dominant HCHO sink is reaction with atomic oxygen. At solar zenith angles between 60 and 85°, abundances of $O(^3P)$, CH_3, and CH_3O radicals are large enough at the top of the hygropause to overcome the loss of HCHO from photolysis. At lower solar zenith angles, the rate of formaledhyde photolysis is too great to allow significant net production.

The resulting atmospheric lifetime of HCHO for all Martian seasons is 2–6 hours at latitudes less than 30° (Figure 4.7), consistent with previously published results [Wong et al., 2003]. As a result, a detection of HCHO below 70 km in the Martian atmosphere will require a strong active release of CH_4 in the local vicinity. My calculations suggest that HCHO will be most likely detected at mid-altitudes (15–30 km) across the tropics during Mars northern spring and summer months. This is due to the lower abundance of water vapor and the increased levels of odd-oxygen species available for reactions with organic radicals, and also coincides with the altitude regions where the TGO instruments are expected to display the greatest level of sensitivity [Korablev et al., 2018].

Using a 1-D steady-state model driven by a profile of 100 ppm CH_4, Wong et al. [2003] report an increase in HCHO above 50 km. My 1-D calculations are time-dependent, driven by a more realistic CH_4 value (published since Wong et al. [2003]), and by interpolated atmospheric parameters that include optical opacity and long-lived inorganic tracers from a 3-D dataset. As such, I believe my approach provides a more comprehensive and realistic modelling environment to describe atmospheric photochemistry on Mars. The photolysis loss rates for HCHO in my model at latitude 2.5° are comparable to those used by Wong et al. [2003]. Differences between my calculations and those reported by Wong et al. [2003] are

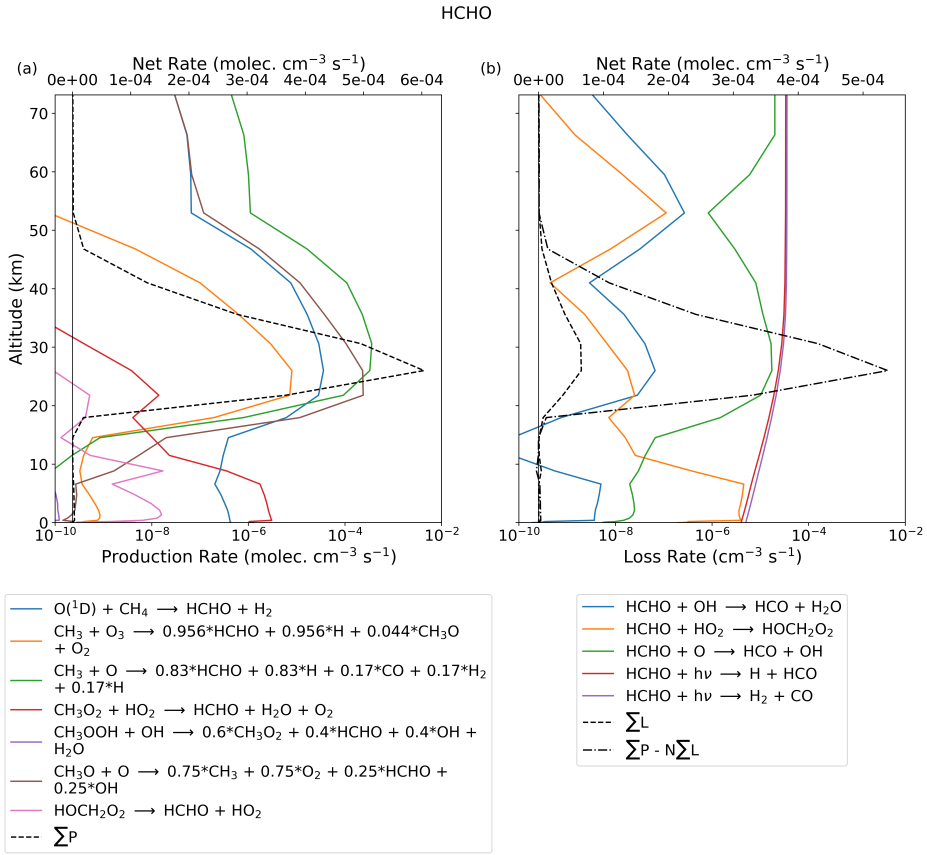


Figure 4.6: Photochemical production and loss rates for HCHO (molec cm^{-3}s^{-1}), associated with CH_4 photochemistry, as a function of altitude. Calculations are for L_S = 71°, 06:30 LT, and latitude 2.5°N.

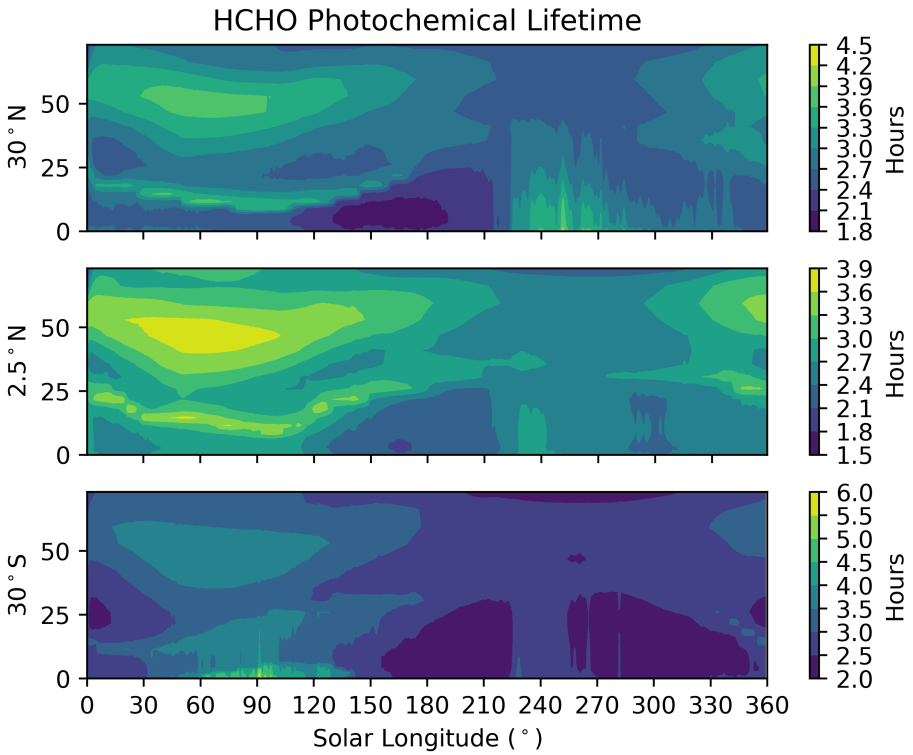


Figure 4.7: Photochemical lifetime of HCHO within the atmosphere of Mars and its variations with altitude (km) and solar longitude at latitudes 30°N, 2.5 °N, and 30°S, respectively. All vertical segments are values from the 1-D photochemistry model at 12:00 LT.

chiefly due to my model not including the $^3CH_2$ and $^1CH_2$ radicals that are only produced through UV photolysis of CH_4 above altitudes of roughly 70 km (reactions $j_{CH4 \longrightarrow 1CH2}$ and $j_{CH4 \longrightarrow 3CH2}$ of Table 4.5). Wong et al. [2003] found that CH_2 radicals directly produce HCHO through their reactions with CO_2:

$$CH_2 + CO_2 \longrightarrow HCHO + CO,$$

which produces a large quantity of HCHO that increases with altitude from roughly 55 km. In my model, $^3CH_2$ and $^1CH_2$ radicals will only be produced when CH_4 reaches the top model layer (altitude of roughly 70 km) at a very slow rate with CH_4 photolysis rates there at $\sim 10{-}9$ s^{-1} (Table 4.5). Inclusion of these smaller organic radicals will be important for investigations above 70 km, but their consideration below 70 km will produce negligible differences in results.

4.3.3 Production of Formic Acid from CH_4 Oxidation

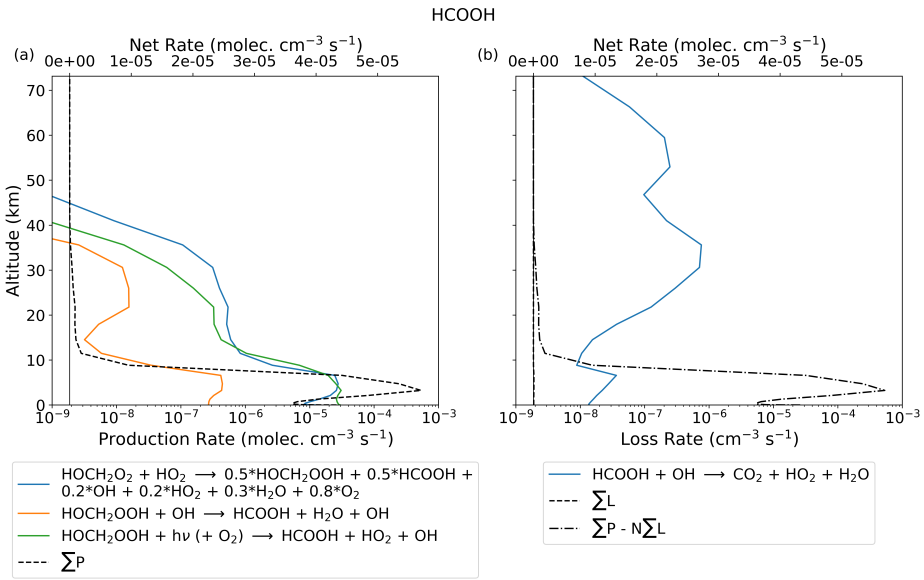


Figure 4.8: As Figure 4.6 but for formic acid (HCOOH).

The oxidation of HCHO via HO_2 radicals leads to pathways that produce HCOOH (Figure 4.1). HCHO reacts with HO_2 to produce the $HOCH_2O_2$ peroxy radical, which can either decay into its original reactants, or react with HO_2 to produce HCOOH directly or to produce hydroxymethyl hydroperoxide that subsequently reacts with OH to produce formic acid or $HOCH_2O_2$, with a branching ratio, $k_{HOCH_2O_2}/k_{HCOOH}$, of 0.233 at 298 K. $HOCH_2OOH$ can also photolyse under UV radiation to produce $HOCH_2O$ and OH. The $HOCH_2O$ radical proceeds to

react with molecular oxygen to produce formic acid and HO_2. The only sink of HCOOH in the Martian atmosphere is via oxidation by OH. This reaction is slow, and limits loss of HCOOH to regions below the point of the hygropause. In regions where OH concentrations are at a maximum, typically during L_S = 150–340° at the top of the water vapour saturation point, HCOOH has a photochemical lifetime that range between 1 and 10 sols. From the surface to roughly 8 km, values range between 70 sols and 220 sols throughout the year in the northern hemisphere, but values in the south increase to magnitudes of 10^3 sols during the northern summer (L_S = 90–180° with the lower abundances of atmospheric H_2O.

Figure 4.8 shows the net and individual production and loss rates for HCOOH for L_S = 71°, latitude 2.5°N, and LT = 18:00 due to a fixed, uniformly distribution of 50 ppt CH_4. The largest production rate of HCOOH is from $HOCH_2O_2$ reacting with HO_2 and from the photolysis of $HOCH_2OOH$. The loss of HCOOH from OH oxidation is slow compared to the production rates. My calculations therefore suggest that a detection of HCOOH would be related to the photochemical loss of HCHO. The resulting atmospheric lifetime of HCOOH, presented in Figure 4.9, is temporally and spatially variant, with lows of 2–5 sols at the tip of the hygropause, increasing to 75–100 sols closer to the surface where the abundances of OH fall.

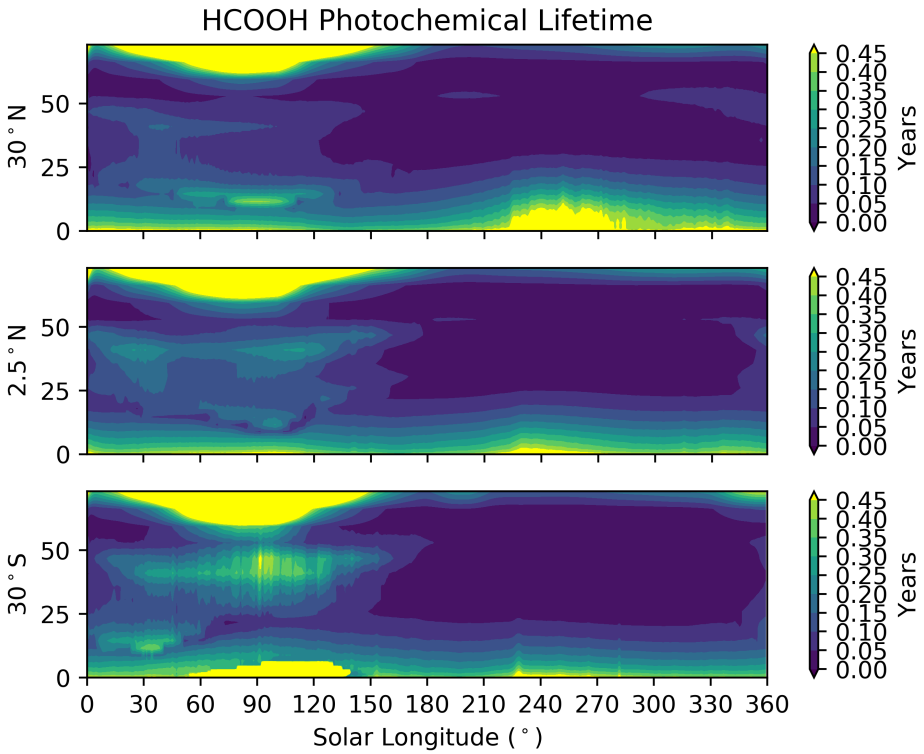


Figure 4.9: Photochemical lifetime of HCOOH and its variance with altitude and solar longitude as calculated by my 1-D photochemistry model.

4.3.4 Ethane Oxidation

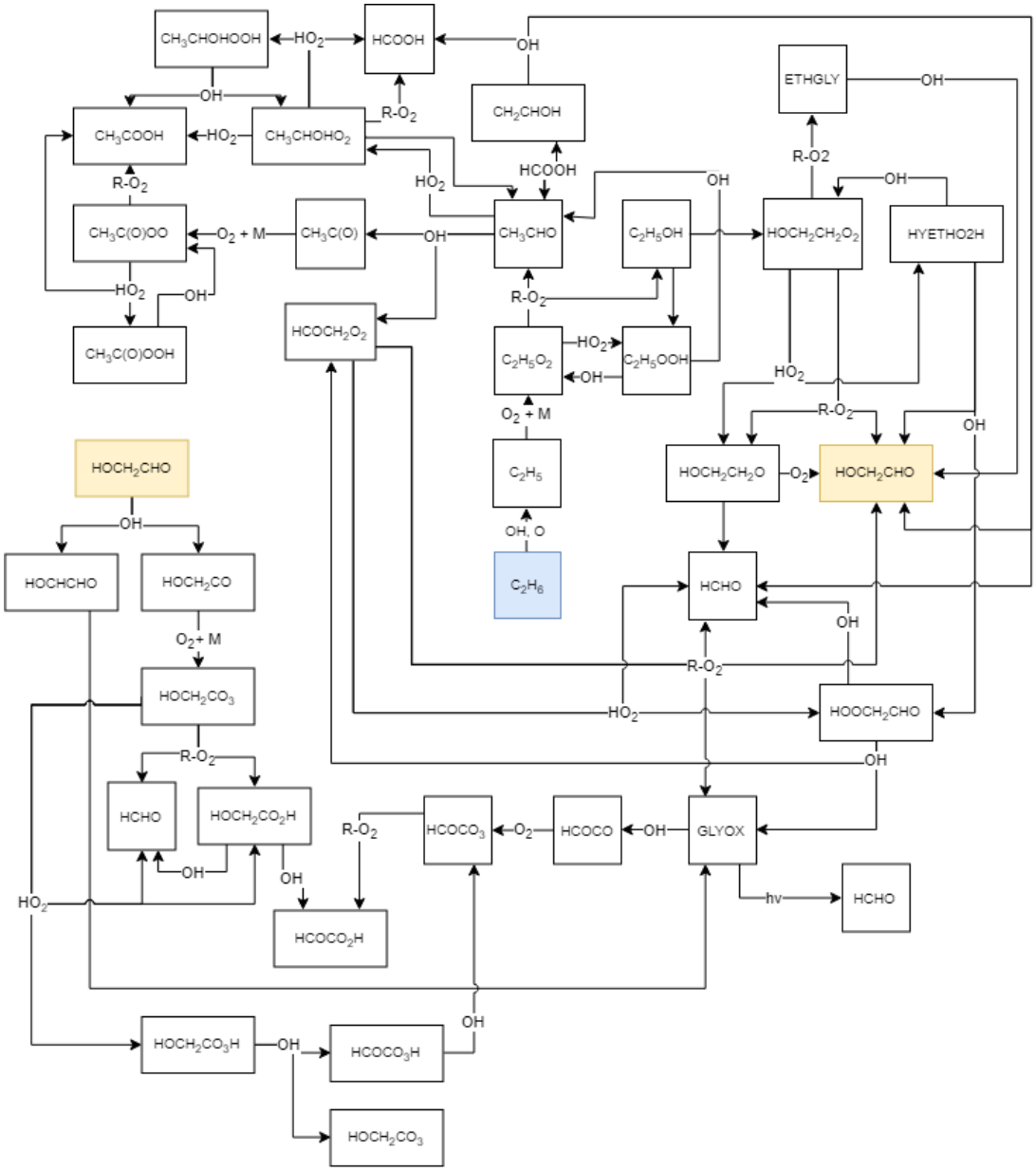


Figure 4.10: Primary stages of the C_2H_6 photochemistry that I use in my 1-D photochemistry submodule, taken from the CAABA/MECCA v4.0 box model.

Here I consider the impact of C_2H_6 on Mars' photochemistry. The impetus for these calculations is that on Earth, emissions of CH_4 are accompanied by emissions of higher-chain hydrocarbon such as C_2H_6 [Horita and Berndt, 1999, Guenther et al., 2000]. C_2H_6 is also listed as an observable compound through the NOMAD-SO and ACS-MIR instrument, with detection limits between 0.02 and 0.03 ppb [Vandaele et al., 2018] and 0.06–6 ppb [Korablev et al., 2018]. Current knowledge puts an upper limit of 0.20 ppb on C_2H_6 [Krasnopolsky, 2012, Villanueva et al., 2013].

Figure 4.10 shows that the photochemistry for C_2H_6 is more complicated than for CH_4 (4.2), but follows the same general routes. It is oxidized by OH and O(^{1}D) that initiates a series of chemical reactions that result in high yield products of HCHO and HCOOH among other compounds. One of the initial C_2H_6 oxidation product is the C_2H_5 radical, which is not described explicitly by the CAABA mechanism. I have used independent sources for reaction rates that involve the C_2H_5 radical (Table 4.4).

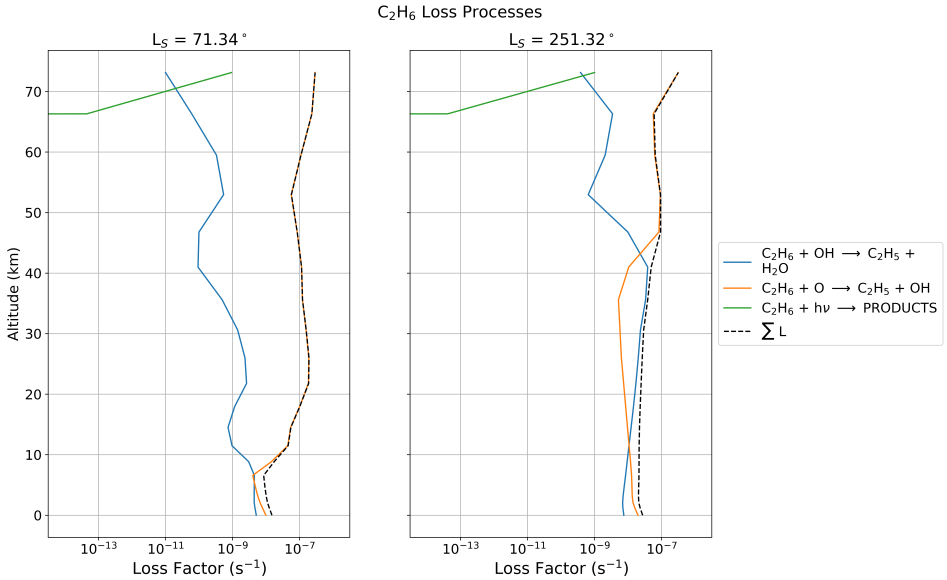


Figure 4.11: Photochemical loss factors for C_2H_6 as a function of altitude in my 1-D photochemistry model with altitude. Calculations are for L_S = 71° and 251°, 12:00 LT, at latitude 2.5°N.

Figure 4.11 shows the photochemical loss factors for C_2H_6 in the Martian atmosphere at noon, L_S 71° and 251°, and at latitude 2.5°N. My photolysis calculations, based on values from the TUV model Madronich et al. [2002] and adjusted for the Sun–Mars distance, suggest this loss process is insignificant below 70 km. Similar to CH_4, below the Martian hygropause OH is the dominant loss process for C_2H_6, and above the hygropause O(^{3}P) is the dominant loss process for C_2H_6, with the $C_2H_5O_2$ peroxy radical being a common oxidation product that results in a cascade of photochemical reactions, as described in Figure 4.10. The resulting photochemical lifetime of C_2H_6 is typically between 1 and 3.5 years below altitudes of 5 km and much shorter (50–450 sols) above the hygropause. Figure 4.12 shows that C_2H_6 has longer photochemical lifetimes below the points of H_2O saturation, where I find typical values that range from 3 to 5 years. In the middle atmosphere, the large abundance of O(^{3}P) reduced the lifetime to 30–450 sols. Based on these calculations, I suggest that any detection of C_2H_6 made by the TGO instruments will be due to an active release.

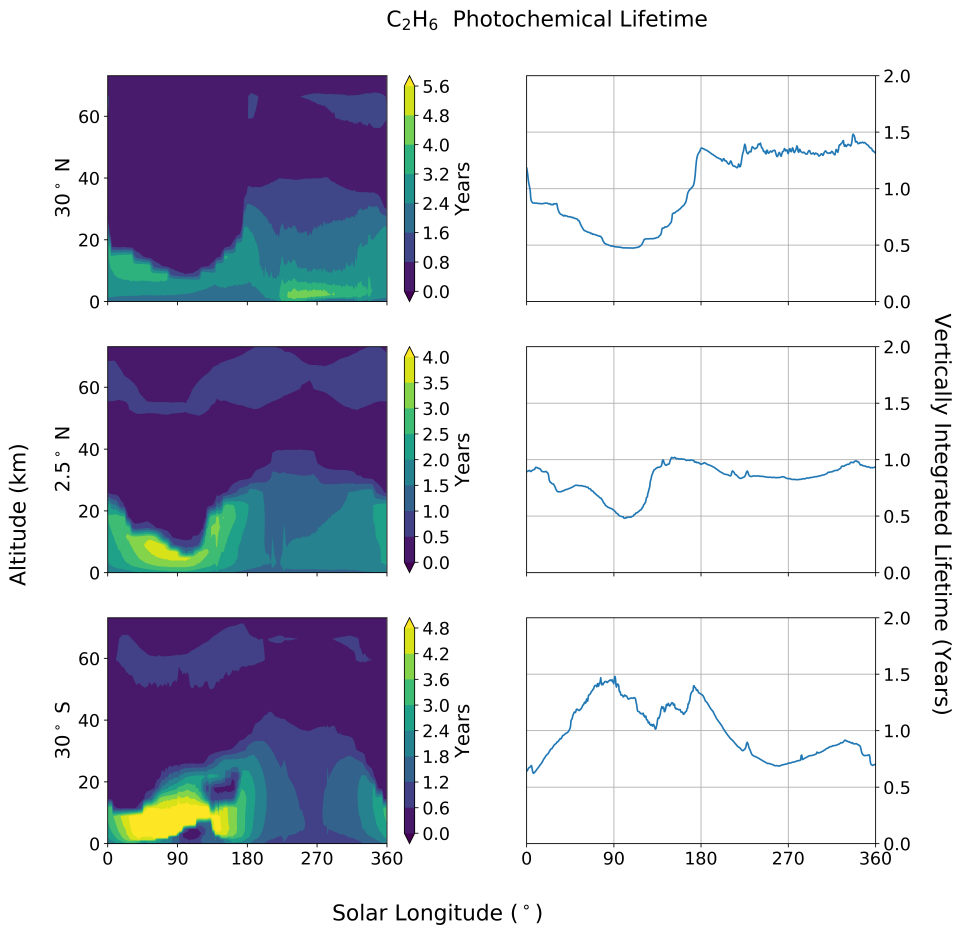


Figure 4.12: Local and vertically integrated photochemical lifetime of C_2H_6 within the atmosphere of Mars and its variations with altitude (km) and solar longitude at latitudes 30°N, 2.5 °N, and 30°S, respectively. All vertical segments are values from the 1-D photochemistry model at 12:00 LT.

Figure 4.13 shows the vertical profiles of organic compounds produced by the oxidation of 50 ppt of C_2H_6 after one sol at L_S 71° and 251°, latitude 2.5° sampled at 18:00 LT, to allow comparisons against the methane investigation of Figure 4.4. The introduction of longer chain peroxy-radicals via the $C_2H_5O_2$ radical increases the richness of photochemical products that are produced from CH_4 oxidation. In particular, the oxidation of C_2H_6 results in CH_3CHO column averaged mixing ratios of 7.24×10^{-16} molecule/molecule at aphelion conditions, elevating to 3.18×10^{-15} molecule/molecule at perihelion conditions. UV photolysis of CH_3CHO is a source of CH_4 and carbon monoxide. I find that UV photolysis of 50 ppt

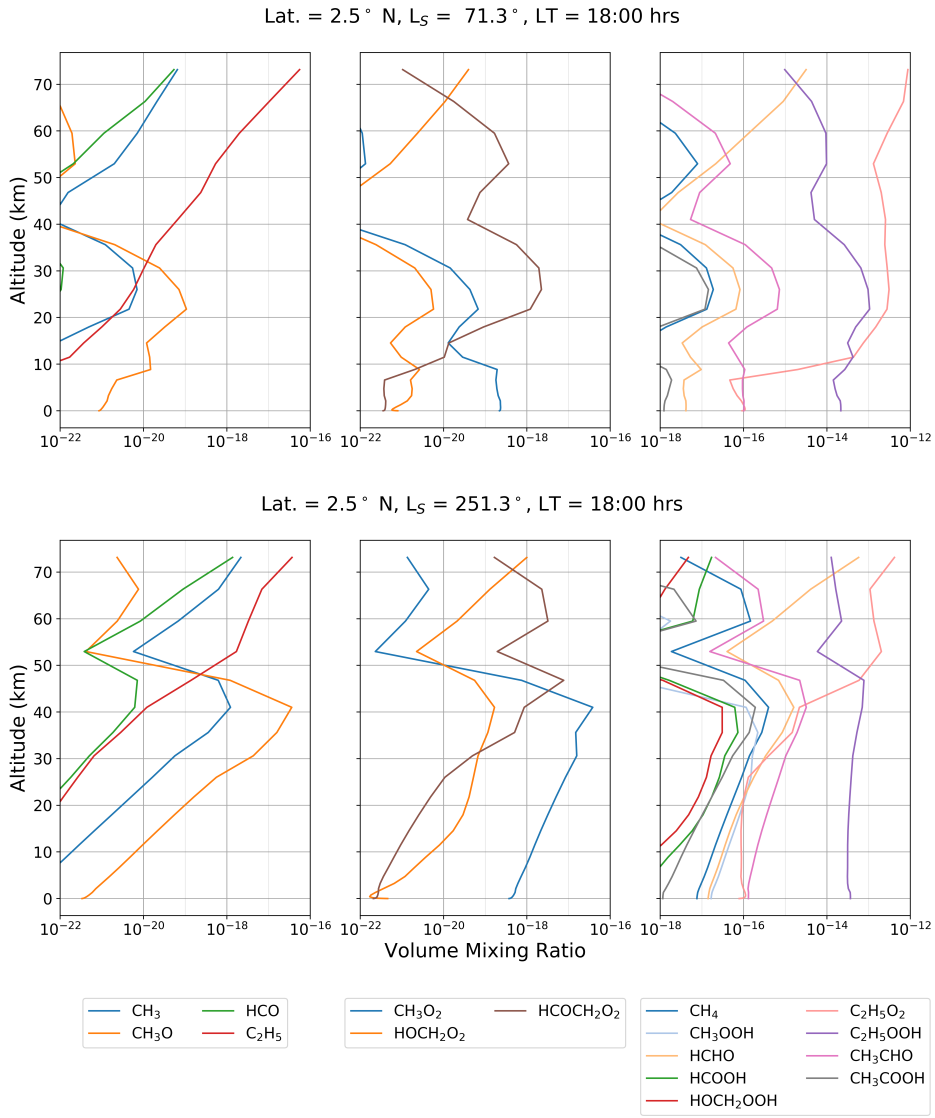


Figure 4.13: Volume mixing ratio profiles of oxidised organic products after one sol of introducing a uniform profile volume mixing ratio of 50 ppt of C_2H_6.

homogeneous column of C_2H_6 produces a CH_4 column averaged mixing ratio of 1.87×10^{-17} molecule/molecule at aphelion, and 3.97×10^{-16} molecule/molecule at perihelion. The ratios of CH_4/C_2H_6 at aphelion and perihelion are 3.71×10^{-7} and 7.86×10^{-6}, respectively, and the ratio of CH_4/CH_3CHO at these two orbital points are 2.58×10^{-2} and 1.25×10^{-1}, respectively.

Formaldehyde is produced with a much higher yield for C_2H_6 oxidation than for CH_4 oxidation, resulting in a column averaged mixing ratio of 3.16×10^{-15} and 5.74×10^{-14} molecule/molecule at aphelion and perihelion, respectively. These yields are $\simeq$6 times and 777 times higher than those made by CH_4 at aphelion and at perihelion, respectively. These higher yields of HCHO from C_2H_6 oxidation are due to a larger number of production pathways compared to the CH_4 oxidation mechanism. Production of HCOOH from C_2H_6 photochemistry during perihelion, column mixing ratio 7.30×10^{-17} molecule/molecule, is comparable with values from CH_4 oxidation, but is much smaller than CH_4 oxidation during aphelion with a column mixing ratio of 1.34×10^{-18} molecule/molecule. Lower production of HCOOH from C_2H_6 oxidation during aphelion is due to lower production pathways for $HOCH_2OOH$ and $HOCH_2O_2$, which drive subsequent production of HCOOH.

4.3.5 Production of Formaldehyde and Formic Acid from C_2H_6 Oxidation

Figure 4.14 shows the production and loss rates for HCHO and HCOOH from the oxidation of 50 ppt of C_2H_6. The largest production rate of HCHO is below the hygropause from the reaction of CH_3O_2 peroxy radical with HO_2, comparable to values from CH_4 oxidation. However, above the hygropause at 20 km the three-body reaction $CH_3C(O)+O_2+M$ and the CH_3 radical reaction with atomic oxygen are the primary sources of HCHO. Combined, the HCHO production rate is an order of magnitude larger than the rate from CH_4 oxidation.

The higher reactivity of C_2H_6 produces a larger quantity of $HOCH_2O_2$ peroxy radicals and hydroperoxy radicals in the regions just above the hygropause compared to CH_4 oxidation. With no additional loss processes, the increased net production rate results in larger concentrations of HCOOH, with production falling off rapidly towards the surface.

4.3.6 Methane Production from the Oxidation of Acetaldehyde

Figure 4.15 shows production and loss rates of CH_4 associated with a 50 ppt homogeneous column of CH_3CHO at L_S = 251°, latitude 2.5°, and at local noon to study the importance of UV photolysis of CH_3CHO. I calculate the photolysis loss rate using the TUV model, finding that UV photolysis penetrates efficiently to the surface. Net CH_4 production rates peak at 31.13 molec cm^{-3} s^{-1}, corresponding to an increase in CH_4 mixing ratio of 1.69×10^{-16} molecule/molecule s^{-1}, at $\simeq$1.30 km above the Martian surface at this time of day. To our current knowledge, this photolytic source of atmospheric CH_4 is the only proposed source that may be possible within the CO_2-dominated atmosphere of Mars.

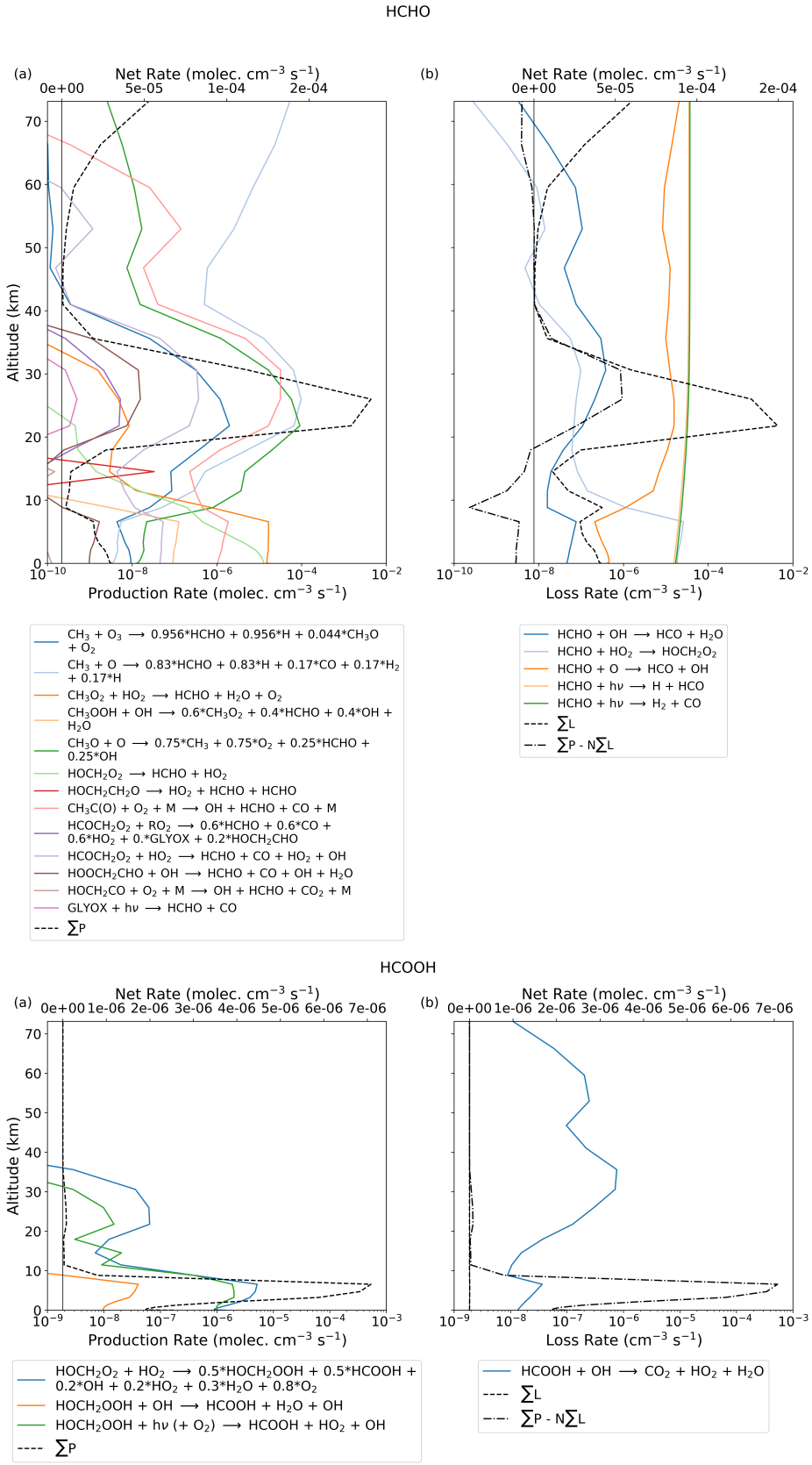


Figure 4.14: Photochemical production and loss rates (molec cm^{-3}s^{-1}) of HCHO and HCOOH in my 1-D photochemistry model associated with 50 ppt of C_2H_6. Values are for latitude 2.5°N, local time 12:00, and solar longitudes 71° and 251° as a function of altitude.

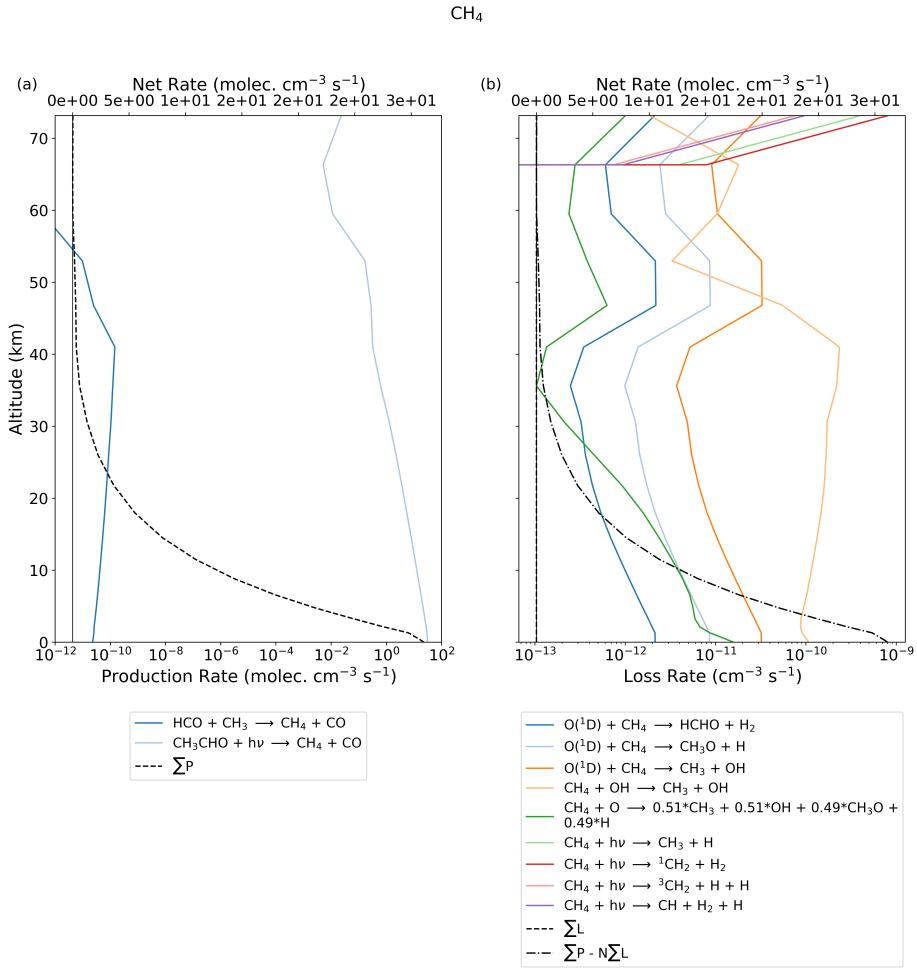


Figure 4.15: Photochemical production and loss rates for methane (molec $cm^{-3}s^{-1}$), associated with the UV photolysis of a 50 ppt column of CH_3CHO, as a function of altitude. Calculations are for L_S = 251°, 12:00 LT, and latitude 2.5°N.

4.4 Conclusion

I find that the oxidation of atmospheric CH_4 in the Martian atmosphere, at magnitudes similar to reported observations, produce formaldehyde and formic acid as photochemical products but at volume mixing ratios too low for successful detection via remote sensing by the NOMAD and ACS spectrometers aboard the ExoMars Trace Gas Orbiter. The photochemical lifetimes of formaldehyde calculated by my 1-D model are consistent with previous studies (e.g., [Wong and Atreya, 2004]), but I have also reported variations as a function of altitude and solar longitude. My use of the MCD v5.3 atmospheric parameters and tracer profiles enabled us to deduce that the largest atmospheric lifetimes of HCHO at latitudes less than 30° are

typically around 4 hours during the northern spring and summer above the point of H_2O vapour saturation. My model expands upon the findings from the steady state model by revealing the layered seasonal structure of HCHO that can develop, whilst refining the modelled lifetimes and revealing the seasonal variability of the compound.

My 1-D model refines the vertical structure and seasonal variability of the CH_4 within the equatorial regions of Mars, revealing that altitudes with low water vapour content can provide $O(^1D)$ abundances large enough to suppress the local atmospheric lifetime of CH_4 to between 50–100 years. I reveal a region in the upper section of the 1-D model, corresponding to 50–70 km where the absence of OH, $O(^1D)$, and lower UV photolysis increases the local CH_4 lifetimes to 400–800 years during the northern spring, and to 800–1300 years during the mid-northern summer to northern winter. Lifetimes close to the surface and below the hygropause (0–30 km) are invariant with latitude during the northern spring, but display variations between the north and southern hemisphere throughout the rest of the year, controlled by the sublimation of the respective hemispheres polar caps water ice content.

I find that the photochemical lifetime of C_2H_6 is correlated to the atmospheric water vapour content on Mars. Within the hygropause, lifetimes are found to be within 3–4 years, where OH is the dominant photochemical sink. At higher altitudes, these local atmospheric lifetimes are reduced to 100–400 Mars sols (0.15–0.6 years), due to the higher abundance of atomic oxygen. The lifetimes of acetaldehyde reach values of approximately one sol close to the Martian surface across all equatorial latitudes during the northern spring, that lower to roughly 0.5 sols in the northern hemisphere summer to winter periods. Acetic acid displays a similar seasonal trend, with lifetimes in the northern spring being between 3 and 4 sols below the hygropause , and lowering to between 0.2–1 sol with the elevation of the water saturation point. Oxidation of C_2H_6 in the Martian atmosphere results in a distinct profile of acetaldehyde, as well as greater yields of HCHO and HCOOH, compared to CH_4 oxidation. The 1-D model predicts atmospheric lifetimes of between 15 and 32 hours below altitudes of 25 km during L_S = 0–135°, lowering to 4–12 hours outside of this time frame across all equatorial latitudes, for CH_3CHO. I therefore propose that any instrument detection of CH_3CHO can be attributed to a surface release of C_2H_6 within the immediate local environment of the site of observation.

My more comprehensive description of atmospheric chemistry, involving 135 organic reactions, significantly expands on the schemes used by Wong and Atreya [2004] and Summers et al. [2002]. No formic acid was reported by the model of Wong and Atreya [2004] for their 1-D steady state model with 100 ppm of CH_4, whereas I report volume mixing ratios of similar magnitude to HCHO below the hygropause with CH_4 abundances of 50 ppt, the upper limit on Mars derived in Korablev et al. [2019]. This discrepancy can be explained by my more detailed description of peroxy radical chemistry that is taken from the CAABA/MECCA v4.0 chemistry scheme. In my 1-D model, photochemical lifetimes of HCOOH are inversely proportional to the abundance of OH available. At the top of the hygropause, local lifetimes have magnitudes of

1 - 10 sols. Below, the lifetimes vary substantially depending on the water vapour availability. Below 5 km, the local photochemical lifetimes in the drier southern latitudes can reach values exceeding 10^3 sols, whereas in the north, values between 10 and 100 are commonly found. These long photochemical lifetimes of HCOOH, in comparison to HCHO, makes it the most likely photochemical product of CH_4 oxidation that could provide independent verification of CH_4. Spectral features of HCOOH lie within the IR wavelengths measured by the ACS aboard the TGO, and the long wave channel of the PFS covers the wavenumber range of 250–1700 cm^{-1} [Formisano et al., 2005] that includes two absorption features of the HCOOH molecule [Gordon et al., 2017].

I find that the introduction of CH_4 at magnitudes similar to an empirically derived upper limit ($<$50 ppt) fails to produce significant perturbations to CO, O_3, or H_2O vapour (not shown) that will observable by instruments aboard the TGO. CH_4 reactions with O(^{1}D) above the hygropause and below 50 km have the net effect of increasing OH concentrations by magnitudes of $10^{-3}\%$ after one sol of exposure, which results in catalyzing the conversion of CO to CO_2 via reaction e_1 of Table 3.2. The increase in OH arises from the previously described reactions of O(^{1}D) atoms reacting with CH_4 in the drier altitudes, most notably reaction b_7. CO experiences relative perturbations of -$10^{-6}\%$ in the mid-altitudes, which will be lost within instrumental noise. This rise in OH, and the loss of O(^{1}D) to CH_4 interactions and O(^{3}P) with organic radical interactions, results in a drop in O_3 production in this region and increased O_3 loss. These perturbations are small, however, with drops of $10^{-3}\%$ after one sol, an amount that is below instrument signal-to-noise values. This highlights that source regions of CH_4 will not be identifiable by perturbations made to inorganic trace gas species observable to the ExoMars Trace Gas Orbiter.

Finally, my model highlights the possible existence of an atmospheric source of CH_4 from the photolysis of CH_3CHO, an oxidation product of C_2H_6. Photolysis of CH_3CHO in the Martian atmosphere is capable of producing trace amounts of CH_4 at all altitudes above the surface. I find that 50 ppt of CH_3CHO is capable of producing CH_4 at a volume mixing ratio rate of 4.54×10^{-16} s^{-1}.

This opens up the possibility of further studying CH_3CHO as a possible source for CH_4 detection on Mars. Although no evidence exists for CH_3CHO on Mars, one hypothetical source could be due to a sub-surface acetylene hydratase [Rosner and Schink, 1995] enzyme that converts acetylene (C_2H_2) to CH_3CHO through reactions with liquid water.

Chapter 5

Tangent Linear and Adjoint Model for Martian Photochemistry

In this chapter, I detail the development of the first Tangent Linear Model (TLM) for Martian atmospheric photochemistry, and demonstrate the resultant adjoint model through a sensitivity study of atmospheric O_3 and H_2O_2 with respect to inorganic, organic, and chlorine chemistry, and the sensitivity to aerosol profiles. I begin by giving a brief overview of what TLM and adjoint models are and what applications they have in the context of Earth atmospheric modelling studies. I'll then proceed to give a description of the general mathematics behind the TLM and adjoint models prior to discussing the specifics of the 1-D photochemistry model's TLM and adjoint, and will move on to demonstrate the accuracy of the 1-D TLM by comparing the evolution of a perturbed trace gas species calculated via the TLM with the same perturbation modelled via the full 1-D photochemistry model. Finally, I shall use the adjoint of the 1-D photochemistry model to assess the sensitivity of O_3 and H_2O_2 profiles and columns to the abundances of other trace gas species within the model.

5.1 Overview of Tangent Linear Models

A mathematical model takes some input variables, which can be denoted in vector notation as $\vec{X}^{t=0}$, and calculates their evolution (not necessarily over time) to produce values of $\vec{X}^{t}$ for a desired number of model timesteps t. For my 1-D photochemistry model, the initial input vector is composed of the mmrs (kg/kg) of I trace gas species across L model layers, and these values are modelled as they change over time due to photochemical interactions and vertical diffusion. A TLM of a non-linear model instead takes as input a change to the initial input vector of the non-linear model, $\Delta\vec{X}^{t=0}$, and calculates how these initial pertrubations evolve over the model's time domain to yield $\Delta\vec{X}^{t}$. In the case of my 1-D model, the TLM will calculate how a change to the initial mmr of tracer species i at model layer l will evolve over the model run and how it impacts all other model variables. This is done by making a linear approximation of the non-linear model in parallel with the non-linear model run. Figure 5.1 presents a simple schematic of a single variable function that illustrates how a TLM for it

would work. The non-linear model, the black curve, can be regarded as a function of some variable, X. For a 'control' run, the model takes X_C as input, and returns the value f(X_C). A second non-linear model run could opt to take X_P as input instead, returning the value f(X_P). The TLM is calculated during the control run, represented by the orange linear function of Figure 5.1, a 'linear' approximation in 'tangent' to the non-linear model curve at the control variable X_C. The TLM is then used to approximate the difference of f(X_P) and f(X_C), producing the value TLM(X_P - X_C). As demonstrated in the figure, the validity of the TLM approximation hinges on the non-linear function being continuously differentiable, and the TLM accuracy is dependent on the severity of the original model's non-linearity. These changes to the model output can be found by running the non-linear models many times, making small changes to their input variables, and subtracting the differences from the control run. However, the actual desired output of the TLM is the TLM matrix, explained in greater detail in Section 5.2, that can be used to produce an adjoint model, a very powerful tool that can be used in model sensitivity analysis. The adjoint is used to study a desired output at the end of the non-linear model, e.g. O_3 at 45 km after 2 sols, and iterates backwards through time, and finds the sensitivity of that desired output with respect to the initial conditions of the model, e.g. the sensitivity of O_3 at 45 km with respect to every trace gas species across every model timestep. The adjoint of the full model has a further use in the field of data assimilation in which it can be used to generate gradients of cost-functions made of differences between GCM model outputs and observed measurements to find an ideal input state for the GCM models, one that fits all data over some space and time domain.

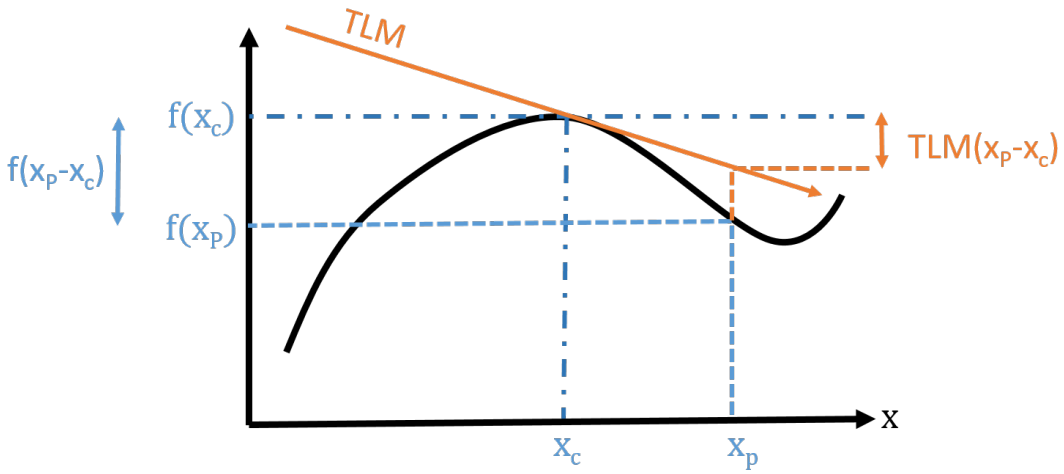


Figure 5.1: Schematic of a Tangent Linear Model of some non-linear function dependent on one variable, f(x). The control state takes x_C as the input to yield f(x_C), and the change due to an altered input x_P can be calculated by two runs of the full model, f(x_P) - f(x_C), or approximated by the TLM of function f, TLM(x_P - x_C).

TLM's and the resultant adjoints of photochemical systems have been developed for a number of Earth general circulation models [Tian and Zou, 2020, Zhang et al., 2013, Henze et al., 2007, Yang and Navon, 1996], but none have been produced for the study of Martian atmospheric photochemistry. Adjoints of atmospheric photochemical models on Earth have been used to study the sensitivity of various pollutants in major cities, such as Paris, to find that model results were only sensitive to a few reaction rate coefficients, enabling model simplifications to be made, important rate coefficients to be refined, and to identify strategies to minimize pollution [Menut et al., 2000]. They've also been used to assess the sensitivity of O_3 on Earth to various volatile organic compounds such as isoprene [Paulot et al., 2012], and in localised environments with respect to emissions made on a large continental scale [Schmidt and Martin, 2003]. To date, there have been no proper TLM developments for Martian atmospheric science. An approximation of the TLM method was used by Houben [1999] in their assimilation of TES temperature retrievals with a GCM describing physical processes but with no considerations of photochemistry, but no full TLM for Mars has been produced to-date. I chose to produce the first TLM of the Martian atmosphere for use alongside my 1-D photochemistry submodule as I believe that TLM's are a very valuable tool readily available for planetary science but have been neglected. A TLM, and resultant adjoint, of my 1-D model could provide insights into the highly non-linear photochemical processes that strongly influence Mars' atmospheric composition that go otherwise unnoticed. It will also help to understand the photochemically incomplete datasets being collected by the ExoMars TGO and other satellites. I now move on to the derivation of the general formula for the TLM of a time-dependent function like that of my 1-D photochemistry model.

5.2 General Derivation of the Tangent Linear Model

The 1-D photochemistry model can be regarded as a time-dependent function that takes a vector composed of all tracer species' mass mixing ratios (mmr), in units of kg/kg, across all model layers which is denoted here and throughout as $\vec{\mathrm{PQ}}$. A control run of the 1-D model uses initial mmr values $\vec{\mathrm{PQ}}_C{}^{t=0}$, with t denoting the model timestep. A second run (referred to as the perturbation run) begins with a slightly altered initial state vector:

$$\vec{\mathrm{PQ}}_P{}^{t=0} = (1+\vec{\lambda})\vec{\mathrm{PQ}}_C{}^{t=0} \quad ,$$

where $\vec{\lambda} \longrightarrow 0$ is a vector of scalars. A 'perturbation vector' can be established, and it is defined in Equation 5.1 simply as the difference between the perturbation run and the control run vectors at any model timestep. The full non-linear model equations of the two model runs can be re-written as Equations 5.2 and 5.3 below.

$$\vec{\mathrm{PQ}}\text{''}^{t} = \vec{\mathrm{PQ}}_P{}^{t} - \vec{\mathrm{PQ}}_C{}^{t} \tag{5.1}$$

$$\frac{\partial \vec{\mathrm{PQ}}_C{}^{t}}{\partial t} = F_{1D}(\vec{\mathrm{PQ}}_C{}^{t}) \tag{5.2}$$

$$\frac{\partial \vec{\mathrm{PQ}}_P{}^{t}}{\partial t} = F_{1D}(\vec{\mathrm{PQ}}_P{}^{t}). \tag{5.3}$$

A first-order Taylor expansion can be made around the control run, in which H.O.T denotes the neglected higher order terms, and $|_C$ denotes the linearisation around control state variables:

$$F_{1D}(\vec{\mathrm{PQ}}_P{}^{t}) - F_{1D}(\vec{\mathrm{PQ}}_C{}^{t}) = \left(\vec{\mathrm{PQ}}_P{}^{t} - \vec{\mathrm{PQ}}_C{}^{t}\right)\frac{\partial F_{1D}}{\partial \vec{PQ}}|_C + \mathrm{H.O.T.} \tag{5.4}$$

The perturbation vector, Equation 5.1, can be substituted immediately into the right hand side of Equation 5.4. The left hand side of Equation 5.4 is also simply the derivative of Equation 5.1 with respect to time. Equation 5.4 can therefore be rewritten as:

$$\frac{\partial \vec{\mathrm{PQ}}\text{''}^{t}}{\partial t} \approx \vec{\mathrm{PQ}}\text{''}^{t}\frac{\partial F_{1D}}{\partial \vec{PQ}}|_C, \tag{5.5}$$

in which the higher order terms are discarded. To produce the TLM of the 1-D photochemistry model, Equation 5.5 requires discretization with respect to time to carry the perturbations experienced at timestep t to timestep $t+1$. The discretized form of Equations 5.2 and 5.3, advanced by the model timestep Δt is provided in Equation 5.6. Equation 5.7, the discretized form of the perturbation vector advancement, immediately follows.

$$\vec{\mathrm{PQ}}^{t+1} = \vec{\mathrm{PQ}}^{t} + F_{1D}\left(\vec{\mathrm{PQ}}^{t}\right)\Delta t \tag{5.6}$$

$$\vec{\mathrm{PQ}}\text{''}^{t+1} = \vec{\mathrm{PQ}}\text{''}^{t} + \frac{\partial \vec{\mathrm{PQ}}\text{''}^{t}}{\partial t}\Delta t. \tag{5.7}$$

Equation 5.5 can then easily be substituted into Equation 5.7 to produce the equation for the TLM and construct the TLM matrix $\mathbf{A}^t$:

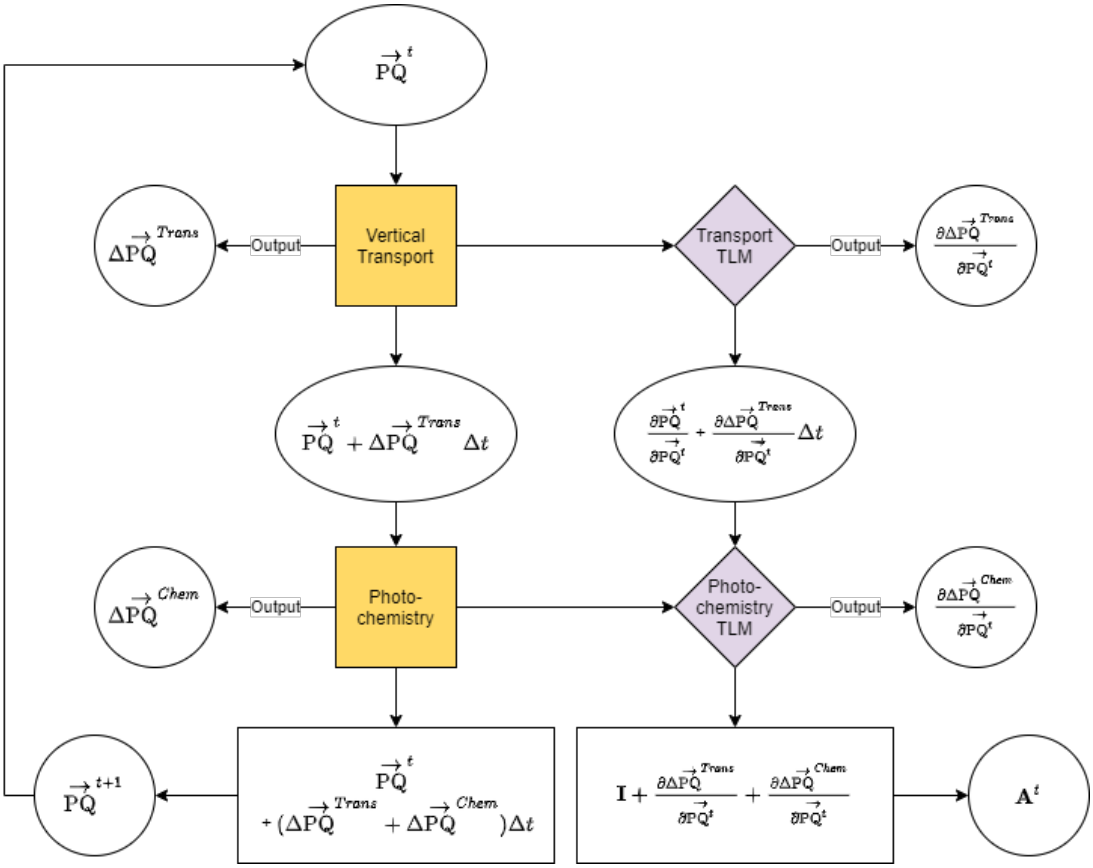


Figure 5.2: A simplified schematic of the non-linear 1-D photochemistry model (yellow) and the tangent linear model (purple) operating in parallel, linearising the 1-D processes with respect to tracer mass mixing ratios at the current model timestep (PQ^t).

$$\vec{\mathrm{PQ}}^{,t+1} = \vec{\mathrm{PQ}}^{,t} + \vec{\mathrm{PQ}}^{,t} \frac{\partial F_{1D}}{\partial \vec{PQ}} |_C \Delta t \tag{5.8}$$

$$\vec{\mathrm{PQ}}^{,t+1} = (\mathbf{I} + \frac{\partial F_{1D}}{\partial \vec{PQ}} |_C \Delta t) \vec{\mathrm{PQ}}^{,t} \tag{5.9}$$

$$\vec{\mathrm{PQ}}^{,t+1} = \mathbf{A}^t \vec{\mathrm{PQ}}^{,t}. \tag{5.10}$$

If there are I tracers in the model with L model layers, the perturbation vectors will be of size IL and the TLM matrix will be of shape $IL \times IL$. Figure 5.2 presents a schematic demonstrating how the TLM code operates in parallel with the full non-linear model run, takings control run variables as an input. A detailed explanation of the TLM for the 1-D photochemistry model and the linear equations derived from the vertical transport and photochemistry routines is provided in Section A.1.

5.3 General Derivation of the Adjoint

Recalling Equation 5.10, the TLM calculates the evolution of the perturbation vector $\vec{\mathrm{PQ}}$"^{t} forwards from model timestep t to timestep $t+1$. The perturbation vector at timestep t is itself produced from the TLM equation from the preceeding model timestep, $t-1$, a process that repeats until the initial timestep $t=0$. Written down this takes the appearance of Equation 5.11,

$$\vec{\mathrm{PQ}}"^{t+1} = \mathbf{A}^t \vec{\mathrm{PQ}}"^{t} = \mathbf{A}^t \mathbf{A}^{t-1} \vec{\mathrm{PQ}}"^{t-1} = \mathbf{A}^t \mathbf{A}^{t-1} \mathbf{A}^{t-2} ... \mathbf{A}^{t=0} \vec{\mathrm{PQ}}"^{t=0}. \tag{5.11}$$

The sequence of matrix multiplications $\mathbf{A}^t \mathbf{A}^{t-1} \mathbf{A}^{t-2} ... \mathbf{A}^{t=0}$ can be redefined as the model's transition matrix, $\mathbf{P}^{t+1}$, which can immediately carry the initial perturbations to the control model forward to the desired model timestep in a single calculation. This transition matrix is the primary objective of the TLM, and is what the adjoint matrix requires to conduct sensitivity studies and cost-function gradient construction.

A specific variable of interest is chosen for sensitivity studies, which shall be referred to as the forecast aspect and is denoted J. This could be the number density (molec. cm^{-3} s^{-1}) of O_3 at 30 km during the evening, the column abundance of H_2O_2 (molec. cm^2 s^{-1}) during the day, or the vmr of methane (mol/mol) at the surface as examples. It is important to note that the 1-D model and TLM operates in units of mmr (kg/kg), and therefore TLM and adjoint results will require conversion to appropriate units dependent on the chosen forecast element. This will be discussed towards the end of this section.

The change in J between a control model calculation and a perturbed model calculation at a desired forecast timestep t_N can be written as $dJ^{t_N} = J_P^{t_N} - J_C^{t_N}$. As J^{t_N} is a function of the mmr vector, this difference can be expanded via the first-order Taylor series once again:

$$\Delta J^{t_N} \approx \sum_{i=1}^{I} \sum_{l=1}^{L} \mathrm{PQ}"^{t}_{i,l} \frac{\partial J^{t_N}}{\partial \mathrm{PQ}^{t}_{i,l}}, \tag{5.12}$$

for all tracers i at all model layers l at some model timestep $0 \leq t \leq t_N$. Equation 5.12 can be read as follows - for a change in the forecast element at timestep t_N to occur, there must be a non-zero perturbation to species i at model layer l at some prior time t ($\mathrm{PQ}"^{t}_{i,l}$), and a non-zero sensitivity of the forecast element J^{t_N} to this species at this timestep ($\frac{\partial J}{\partial \mathrm{PQ}^{t}_{i,l}}$). These sensitivity values are what the adjoint model aims to calculate. For presentation, the sensitivity vector will be rewritten as Equation 5.13 which takes the form of a vector of size IL for I species across L model layers:

$$\hat{J}^t = \frac{\partial J^{t_N}}{\partial \vec{\mathrm{PQ}}^t}. \tag{5.13}$$

The sensitivity vector can be initialised at the forecast timestep, t_N. Using the perturbation vector and the sensitivity vector at the forecast timestep, Equation 5.12 becomes:

$$\Delta J^{t_N} \approx \sum_{i=1}^{I} \sum_{l=1}^{L} \mathrm{PQ}'^{t_N}_{i,l} \frac{\partial J^{t_N}}{\partial \mathrm{PQ}^{t_N}_{i,l}}. \tag{5.14}$$

To produce an instantaneous change in the forecast element from the forecast timestep, Equation 5.14 requires the sensitivity vector,$\hat{J}^{t_N}$, to be trivial. The only non-zero value found in $\hat{J}^{t_N}$ is that corresponding to the location of the forecast element in the perturbation vector. For Equation 5.14 to be true, this non-zero value is equal to 1, as this element of the sensitivity vector represents the partial derivative of J^{t_N} with respect to J^{t_N}.

$$\left(\vec{a}, \mathbf{A}\vec{b}\right) = \left(\mathbf{A}^T \vec{a}, \vec{b}\right) \tag{5.15}$$

To make the adjoint model iterate backwards through time, the 'adjoint property' has to be employed, presented in Equation 5.15, in which parentheses denote matrix multiplication, and is applicable for a linear operator in Euclidean space. Equation 5.10 is altered such that the perturbation vectors are replaced with the sensitivity vectors $\hat{\mathbf{J}}^t$ and $\hat{\mathbf{J}}^{t+1}$, and the TLM matrix is transposed and placed on the opposite side, yielding:

$$\hat{\mathbf{J}}^t = \mathbf{A}_{\mathrm{t}}^{\mathrm{T}} \hat{\mathbf{J}}^{t+1}, \tag{5.16}$$

which is the adjoint equation that iterates backwards in time to a desired backtrace timestep from the sensitivity vector initialised at the forecast timestep.

5.4 Validation of the Tangent Linear Model

The accuracy of an adjoint model is completely dependent on the accuracy of the TLM from which it is derived. To assess my TLM accuracy, I perform a series of comparisons between perturbations made to a control state as calculated by the full 1-D photochemistry model and the approximations made by the TLM. I define the 'relative perturbations' to a control state calculated by the full non-linear model as:

$$\Delta_{\%} \mathrm{PQ}^t_{i,l} = \frac{\mathrm{PQ}^t_{i,l,P} - \mathrm{PQ}^t_{i,l,C}}{\mathrm{PQ}^t_{i,l,C}} \tag{5.17}$$

for mmr (PQ) of trace gas species i at model layer l during timestep t, where subscripts P and C denote 'perturbed run' and 'control run' respectively. At the start of the perturbed runs (t = 0), I adjust the mmr of a select tracer at model layers l by a scalar magnitude (λ) such that:

$$\mathrm{PQ}^{t=0}_{i,l,P} = \mathrm{PQ}^{t=0}_{i,l,C} + \lambda \mathrm{PQ}^{t=0}_{i,l,C}, \tag{5.18}$$

and allow the 1-D model to operate for 2 sols (96 timesteps). A period of 2 sols is chosen to demonstrate that the TLM is capable of accurate multi-sol analysis, and is also the timescale used in the work of Chapter 3. A perturbation vector is then constructed for the TLM, initialising itself as a vector of 0's, with non-zero values equal to Equation 5.18 in the locations corresponding to the initial perturbations.

I have conducted four case studies in my assessment of my TLM's accuracy, each operating in different spatial and temporal scenarios with various chemistry routines active to highlight the flexibility of the TLM. Case One operates at 20° north at 234° L_S, and studies perturbations of H_2O_2 in the bottom four layers of the model (5–190 m above the surface) across the magnitude range 10^{-4}–10^{-1}, and only considers inorganic gas phase chemistry (16 tracers). Case 2 moves the model to 45° south at 70° L_S, includes gas phase chemistry of inorganic species and CH_4 and its oxidation products (27 tracers), and perturbs CH_4 across the larger magnitude range 10^{-3}–10^{0} at layers 8–10 (2.10–4.72 km) in the model. Case 3 studies inorganic chemistry only, and also includes the heterogeneous uptake of HO_2 and OH on H_2O ice. In case 3, the model works in the high north at 70° north at 196° L_S, and H_2O ice is perturbed across layers 12–15 (11.5–18 km) and across the magnitude range of -10^{-4}–10^{-1}. Case 4 sees the model moved into the deep south latitudes at 75° south at 70° L_S, working with inorganic chemistry, CH_4 oxidation, and the uptake of OH and HO_2 on ice. Again, ice is perturbed across the range -10^{-4}–10^{-1}, but across model layers 6–8 (0.8–2.1 km). In Cases 2 and 4, CH_4 is initialised at a vmr of 20 ppt across all model layers in accordance with the most recent upper limits derived from TGO-NOMAD observations [Knutsen et al., 2021].

Figure 5.3 presents scatter plots displaying the comparisons of the resultant cascade of tracer mmr perturbations as modelled by the full non-linear 1-D model (y-axis) and the TLM approximation (x-axis). If the TLM approximation perfectly replicates the perturbations calculated by the 1-D model, all points will lie on the dashed red diagonal line. Table 5.1 presents the quantitative results of Figure 5.3, displaying the Pearson correlation coefficient (R), which I use here as a measure of the 'tightness' of the shape of the distribution plotted, the gradient (m) of the linear line of best fit (L.o.B.F), and the total number of perturbations modelled (N). The non-linear 1-D model operates in single precision, whereas the analysis of the TLM is conducted in Python, which uses double precision floating points in matrix calculations. To

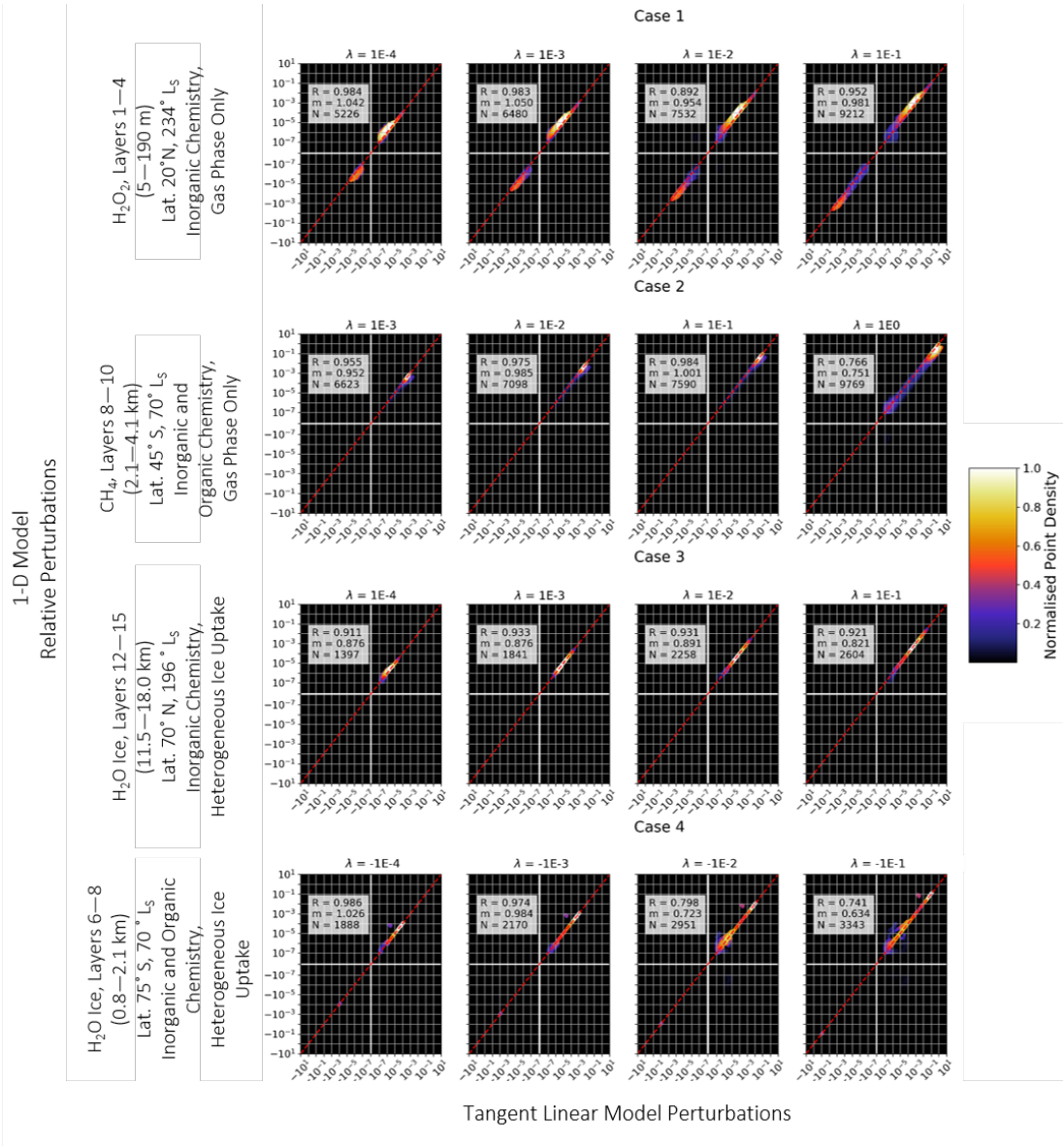


Figure 5.3: Comparisons of the relative perturbations made to a control state in the 1-D model (Equation 5.17) as calculated via the full non-linear 1-D photochemistry model and their approximations from the TLM (Equation 5.10).

account for this, I limit the study to perturbations of relative magnitudes $\geq |10^{-7}|$, as the 1-D model is not able to calculate these. Relative perturbations less than this limitation are also suppressed to 0 in the analysis stage in Python, to prevent smaller perturbations cascading into larger ones that the full non-linear model cannot account for.

The TLM developed by me can be seen to approximate the perturbations to the chemical system in the 1-D model very well across a full range of latitudes, solar longitudes, and for any combination of tracers and heterogeneous chemistry studied here. As expected from a model based upon a first-order Taylor expansion, the results gradually decrease in accuracy

with increasing initial perturbations as these result in the higher order terms neglected by Equation 5.5 becoming non-negligible. Cases 1 and 3, studying only inorganic chemistry and modelling 11 tracers less than 2 and 4, display the best results - this is due to the increasing number of variables in the TLM approximation decreasing the approaches accuracy, which is again to be expected from a first-order Taylor expansion. In Figure 5.3, the strongest discrepancies between the non-linear model calculated perturbations and those found via the TLM approximation appear mainly in the $< |10^{-4}|$ ranges. Errors in calculating perturbations lower than 0.01% of the control run values are primarily due to issues with machine precision. The TLM code, written in Fortran and in parallel with the 1-D model, operates using single precision calculations, wheres the analysis of the TLM, performed in Python, operates using double precision calculations. Errors may also appear due to the inability of the TLM method to consider changes to photolysis rates caused by changes in O_3 column densities. As detailed in Chapter 3, the photolysis rates are interpolated from an offline dataset that the TLM cannot account for in the linearised code. As such, small changes to photolysis rates will occur in the 1-D non-linear model in the presence of O_3 perturbations, which will go unrecorded in the TLM approximation, causing small errors to accumulate. Despite these differences in precision and the neglect of changing photolysis rates, the TLM can be seen performing very well with high levels of accuracy for perturbations of magnitudes up to 100%, with the majority of errors appearing for very small perturbations (< 0.01%). Perturbations of < 0.01% to trace gas species in the 1-D model will be almost inconsequential, and these discrepancies, when they appear, between the 1-D model and the TLM that I have developed can be disregarded.

Case one of Figure 5.3 and Table 5.1 only studies inorganic gas phase chemistry at 20° north in the northern fall (234° L_S), with CH_4 included, but without tracer support for oxidised non-methane VOCs described in Chapter 4. H_2O_2 was chosen for an initial perturbation, as it readily breaks down under UV conditions to perturb the highly non-linear HO_x abundances. Altitudes close to the surface (5–190 m) where chosen for the perturbation location, as these are the most turbulent regions of the atmosphere, experiencing highly non-linear transport mechanics. The high correlation coefficients, ranging between 0.89–0.98, and the gradients of the linear lines of best fits, ranging from 0.95–1.05, show that the TLM that I have produced is a very strong linear approximation of the highly non-linear photochemistry and transport routines within the 1-D model for the most reactive species in the model, at the most turbulent region of the atmosphere.

Case two expands the TLM to include the CH_4 oxidation scheme described in Chapter 4, initialised with a homogeneous 20 ppt profile, in line with the most recent upper limits inferred by the ExoMars TGO in Knutsen et al. [2021]. The TLM is re-positioned to 45° south as 70° L_S, a colder and drier environment than case one. I also expand the perturbation strengths to $\lambda = 10^0$, i.e. a perturbation of 100%. CH_4 is chosen to study the accuracy of the TLMs approximations of the organic oxidised products, and the perturbation is performed between

Table 5.1: Results from Cases 1–4 of the comparisons of perturbations to a control state as modelled by the non-linear 1-D photochemistry model and the TLM approximation. λ denotes the relative magnitude of the initial perturbations, R is the Pearson correlation coefficient, m the gradient of the linear line of best fit (L.o.B.F), and N is the total number of perturbations.

Case 1			
H_2O_2, Layers 1–4 (5–190 m)			
Lat. 20° N, 234° L_S			
Inorganic Chemistry, Gas Phase Only			
Initial Perturbation Magnitude (λ)	Correlation Coefficient (R)	Gradient of Linear L.o.B.F (m)	Total Number of Perturbations (N)
10^{-4}	0.98	1.04	5226
10^{-3}	0.98	1.05	6480
10^{-2}	0.89	0.95	7532
10^{-1}	0.95	0.98	9212
Case 2			
CH_4, Layers 8–10 (2.10–4.72 km)			
Lat. 45° S, 70° L_S			
Inorganic and Organic Chemistry, Gas Phase Only			
λ	R	m	N
10^{-3}	0.96	0.95	6623
10^{-2}	0.98	0.99	7098
10^{-1}	0.98	1.00	7590
10^{0}	0.77	0.75	9769
Case 3			
H_2O Ice, Layers 12–15 (11.5–18 km)			
Lat. 70° N, 196° L_S			
Inorganic Chemistry, Gas Phase + Heterogeneous Ice Uptake of OH and HO_2			
-10^{-4}	0.91	0.88	1397
-10^{-3}	0.93	0.88	1841
-10^{-2}	0.93	0.89	2258
-10^{-1}	0.92	0.82	2604
Case 4			
H_2O Ice, Layer 6–8 (0.8–2.1 km)			
Lat. 75° S, 70° L_S			
Inorganic and Organic Chemistry, Gas Phase + Heterogeneous Ice Uptake of OH and HO_2			
-10^{-4}	0.99	1.03	1888
-10^{-3}	0.97	0.98	2170
-10^{-2}	0.80	0.72	2951
-10^{-1}	0.74	0.63	3343

2.1–4.7 km. For perturbations < 10^{-1} in magnitude, the R values are very close to unity (R = 0.95–0.98), and the line of best fit is almost exactly a straight diagonal line through Figure 5.3 (m = 0.95–1.00). Stronger discrepancies begin to appear when the perturbations become of equivalent size to the control run values, as expected from a model based upon a first-order Taylor Expansion.

Case three goes back to considering inorganic chemistry only, but with the addition of uptake of OH and HO_2 radicals on water ice. The TLM is not equipped to handle the linearisation of ice particle development in the atmosphere, a process dependent on conditional statements that require relative humidity considerations. As such, the TLM matrix components for H_2O ice, and dust particles, is devised such that the perturbation vector of Equation 5.1 has the same relative value to the control state across the model run, i.e. an initial 10% increase to dust at 5 m will stay exactly 10% larger than the control run dust abundance at 5 m. The resultant TLM equation, for both dust and ice (tracer i) at model layer l for timestep t becomes:

$$\Delta \mathrm{PQ}_{i,l}^{t+1} = \frac{\mathrm{PQ}_{i,l}^{t+1}|_C}{\mathrm{PQ}_{i,l}^{t}|_C} \Delta \mathrm{PQ}_{i,l}^{t}. \tag{5.19}$$

The strong correlation coefficients (R = 0.91–0.93) and linear gradients of lines of best fits (m = 0.82–0.89) from perturbations to H_2O ice indicate that the linearised heterogeneous chemistry I have developed is a good approximation of the non-linear scheme of the 1-D model. Case three is placed in the high north of Mars, latitude 70° north during the northern fall (196° L_S), where H_2O ice in the atmosphere is more abundant due to the lack of sunlight and the low atmospheric temperatures. This is an ideal location to study the effectiveness of the linearised heterogeneous chemistry scheme included into my TLM of the 1-D photochemistry model. The relative perturbations to the ice profiles in case three are kept constant throughout the non-linear model run, in line with TLM handling in Equation 5.19. The introduction of heterogeneous uptake of OH and HO_2 produces perturbations directly to the HO_x chemistry in the 1-D model, which is highly non-linear and could be subject to strong inaccuracies when a linear approximation, like that of the TLM, is applied. Figure 5.3 shows that these inaccuracies, for perturbations to the ice profile of 10% magnitudes, are very small and the linear approximation is adept at approximating the impacts of atmospheric ice on the 1-D model's HO_x routine.

Case four moves to the deep south, 75° south, during the northern spring close to the point of Mars' orbital aphelion (70° L_S), and includes the heterogeneous uptake of OH and HO_2 on ice, as well as the oxidation products of CH_4. The model is initialised with 20 ppt of CH_4 again, in line with the most recent upper limits produced by the ExoMars TGO [Knutsen et al., 2021]. The TLM approximation performs the worst out of the four case studies presented here. For perturbations to ice below 0.1% ($\lambda = 10^{-3}$), R ranges between 0.97–0.99 and m between 0.984–1.03. Greater perturbations however see the R values drop to

values ranging from 0.74–0.80 and m falls to 0.63–0.72. As per case three, the primary gas-phase perturbations from an initial ice perturbation are made to the HO_x distributions. In case three, these HO_x perturbations evolve to predominantly impact O_3 and H_2O_2. In case four, the introduction of the oxidised organic tracers from CH_4 produces significantly more species capable of being influenced by HO_x changes. From Chapter 4, the yields of oxidised organic compounds such as HCHO and HCOOH (destroyed via OH in reactions cab_{18} and cab_{32} respectively), are inconsequentially small with vmrs ranging from 10^{-5}–10^{-3} ppt. Small changes to the HO_x abundances from perturbations to ice will lead to perturbations to oxidised organic compounds that are likewise incredibly small, often verging on single precision levels ($< 10^{-7}$). The changes to compounds like HCHO will therefore suffer from inaccuracies in the differences between the double precision of the analysis in Python to perform the TLM calculations, and the single precision of the 1-D model's non-linear calculations. The resulting errors however are limited to non-methane VOCs at magnitudes inconsequential to the remaining atmospheric photochemistry - they are too small to be observed via satellites or ground-based telescopes, and they exist at too low an abundance to influence the chemistry of well-observed species such as O_3 and H_2O_2. This can be seen in Figure 5.3 for case four, as the differences between the TLM and the 1-D model are predominantly found within the $< |10^{-5}|$ range.

These four case studies demonstrate that the photochemical TLM that I have constructed is an accurate approximation of the full non-linear 1-D photochemistry submodule for any combination of inorganic, organic, gas-phase, and heterogeneous chemistry used in the model. To assess the validity of the adjoint matrix that is derived from the TLM, I consider the temporal invariance of Equation 5.14. This equation should yield the same product, the difference in the chosen forecast element ΔJ at forecast timestep t_N, from the TLM calculated perturbation vector $\vec{PQ}$" and the adjoint derived sensitivity vector for any model timestep $0 \leq t \leq t_N$. The values of ΔJ^{tN} calculated using TLM and adjoint vectors across all prior model timesteps should be identical for the adjoint derived from the TLM to be valid.

Figure 5.4 presents the results of this temporal invariance study. I choose to perturb H_2O vapour by 10% across all model layers, and calculate the resulting change to the H_2O_2 column vmr at a forecast timestep 10 sols later. I then use the TLM calculated perturbations and the adjoint sensitivity vector of H_2O_2 at each model timestep t prior to the forecast timestep. I then compare the resultant values of ΔJ^{tN} to those found using the first model timestep. These results show that performing Equation 5.14 at any model timestep prior to the forecast timestep over a period as long as 10 sols in the model produces results that vary by magnitudes of machine precision ($< 10^{-14}$). These results demonstrate that the TLM I have developed for Martian atmospheric photochemistry is accurate and mathematically sound.

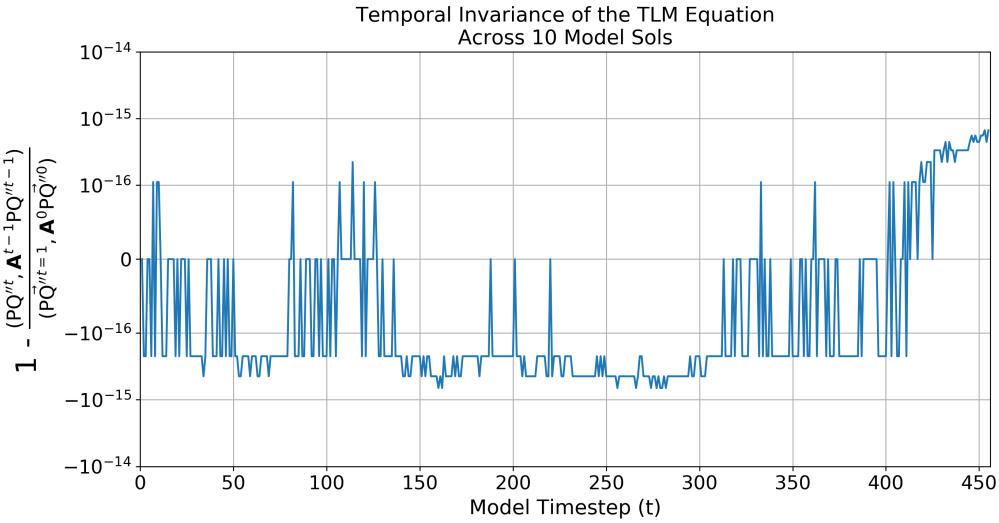


Figure 5.4: Temporal invariance of Equation 5.14 displayed by calculating the change in H_2O_2 column vmr caused by a 10% increase to the initial H_2O column using TLM calculated perturbation vectors and adjoint sensitivity vectors at every model timestep for a period of 10 sols (480 timesteps).

5.5 Sensitivity of H_2O_2 and O_3 to Inorganic Chemistry

In the following section, I demonstrate the ability of the adjoint of the 1-D photochemistry model as a form of sensitivity analysis. I limit the scope of this section to inorganic chemistry, due to the very low yields of oxidised organic products produced by the 20 ppt CH_4 upper limits discussed earlier. Changes to these already tiny abundances, < 10^{-3} ppt, are inconsequential to the surrounding atmospheric chemistry, and will only serve to increase the computational expense of the adjoint. Heterogeneous uptake of OH and HO_2 on ice is included. I choose to study the sensitivity of H_2O_2 and O_3, as these species are well studied on Mars, but discrepancies still exist between 3-D GCM models and the observational data.

I operate the TLM over 10 sols, which allows any perturbations to the initial atmospheric composition become mixed within the atmosphere and is the time for O_3 and H_2O_2 column abundances in the 1-D model to reach roughly constant values at noon. I perform the TLM calculations across 9 discrete latitudes between -60° and 60°, across 9 discrete L_S points across the full Martian year. I then find the sensitivities of H_2O_2 and O_3 columns to the initial model abundances of CO, O_2, O_3, H_2, H_2O vapour and ice, H_2O_2, and CH_4. I then perform Equation 5.11, calculating the expected change to the H_2O_2 or O_3 column caused by a 10% increase to these tracers at all layers in the 1-D model. The model itself is initialised with CO_2, CO, O_2, H_2 and H_2O vapour and ice profiles from the MCDv5.3.

Figure 5.5 presents the sensitivities of the model H_2O_2 columns in terms of the percentage change to the column expected from a 10% increase to the model's initial tracer abundances. The adjoint approach finds that the H_2O_2 column vmrs are positively sensitive to CO abundances throughout the year. A 10% increase in CO in the southern hemisphere between 0–180° L_S is capable of elevating H_2O_2 column vmrs by between 3–7.2%, whereas elsewhere the increases are small (<1.6%) until the northern hemisphere's winter period (270–360° L_S) sees a stronger sensitivity close to the poles, with H_2O_2 column increases of 2.4–3.2%. The addition of CO into the model causes the OH abundances to fall due to the reaction of CO with OH to reform CO_2 (e_1 of Table 3.2), whilst not affecting the summed abundance of HO_x due to the release of an H atom. This causes the partition function of HO_x, detailed earlier in Chapter 3, to be weighted more in favour with HO_2 radicals, which are the primary source of Mars' atmospheric H_2O_2. The additional H atoms produced from this reaction are also capable of increasing the rate of reaction c_{11} of Table 3.2, the three-body reaction with O_2 to form HO_2. The net effect of perturbations to CO in Mars photochemical models is therefore a small but non-negligible increase to the H_2O_2 content, which becomes much more pronounced in the southern hemisphere during the northern spring–summer. The effects are more pronounced during the north and south polar winters due to the significant reduction in daylight, providing more time for HO_2 to develop in nocturnal conditions prior to H_2O_2 being stripped away from UV photolysis.

There is little sensitivity of H_2O_2 to O_2, with an exception at the south pole during the northern spring–summer (0–180° L_S) where strong positive sensitivities appear. This is also the case with O_3 and H_2. For O_2, O_3, and H_2 in the southern polar regions (< -45° latitude), 10% increases to their columns can result in 20–30%, 3–5%, and 20–30% increases to the H_2O_2 column respectively. Perturbations to O_2 in photochemical Mars models here increase the production of HO_2 from reactions with H (c_{11}), especially effective at raising H_2O_2 in the long nights of the polar winters. O_3 perturbations in the southern pole can produce HO_2 directly via reactions with OH molecules (c_{14}), and H_2 is able to convert OH to H via reaction c_{10} to increase the photochemical equilibrium concentration of HO_2. All of these H_2O_2 sensitivities are significantly lower outside of the southern hemisphere due to the production of H_2O_2 occurring mainly at night. Outside of the polar regions, UV photolysis of H_2O_2 for longer periods of time suppress the changes it experiences at night.

The adjoint model finds positive changes to the H_2O_2 as a result of 10% increases to H_2O vapour throughout the year at all latitudes, with some temporal and spatial variance. H_2O vapour regulates the HO_x content of the atmosphere through its UV photolytic breakdown to H and OH (j_h2o of Table 3.3). The impacts are more pronounced in the polar regions,

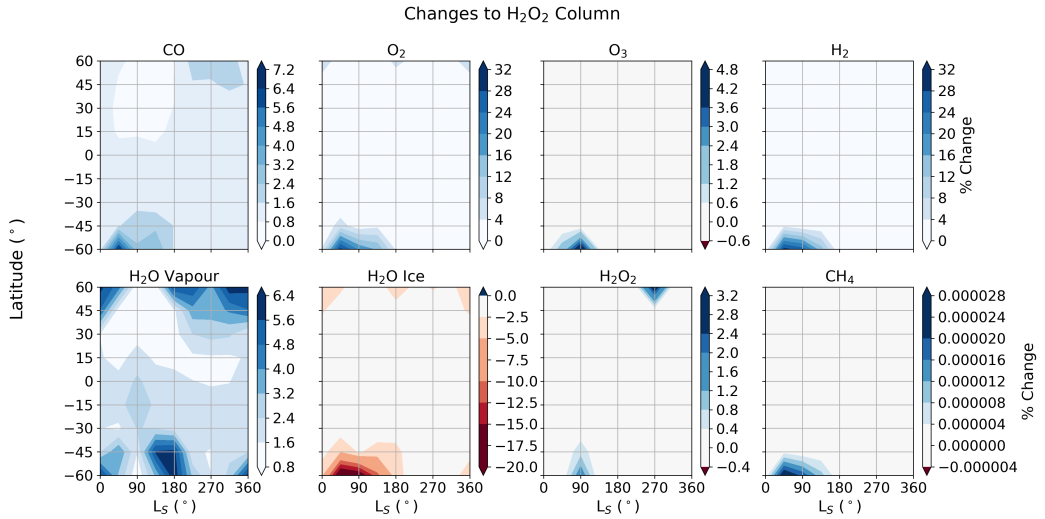


Figure 5.5: Percentage change in H_2O_2 column vmrs produced by a 10% increase to the column of inorganic trace gas species in the 1-D model, allowing for a 10 sol model spin up.

with 10% changes to the H_2O vapour column capable of producing 4.8–6.4% increases to the H_2O_2 column vmr. In the equatorial region, between -30–30°, H_2O_2 columns only experience changes ranging from 1.6–3.2%. This again is due to the production of H_2O_2 primarily occuring at night, and its instability under UV conditions.

The adjoint also finds strong negative sensitivities of the H_2O_2 column to the ice content in the 1-D model in the south polar regions between 0–180° L_S, where a 10% increase to the ice content can decrease H_2O_2 column vmrs by 10–20%, and significantly weaker impacts in the north, and < 2.5% changes in the equator. The absorption of HO_2 onto ice greatly lowers the nocturnal production rates of H_2O_2 via reactions of HO_2 with other HO_2 molecules, again more pronounced in effect in the polar regions due to longer nights. The northern polar regions fall–winter ice contents have less of an effect on H_2O_2 due to the lower H_2O vapour content, which results in fewer HO_x species existing there than in the south. Perturbations to H_2O_2 at the start of the model have next to no impact on the final H_2O_2 column, as they are immediately stripped away via photolysis and condensation at night. Changes of 3% are experienced in the poles during each hemispheres winter however, due to the longer nights resulting in a more stable atmospheric H_2O_2 column. Likewise for CH_4, inconsequential changes to H_2O_2 are made from a 10% increase due to the very slow reaction of OH with CH_4 (cab_1 of Table 4.2).

Figure 5.6 presents a study of the O_3 column vmr, this time at midnight, using the same methods as those used for Figure 5.5. The adjoint calculates that 10% increases to CO in the model result in small negative changes to the H_2O_2 vmrs across the Martian year. The H_2O_2 columns lower by 1.6–2.8% across all latitudes in the northern sprint (0–90° L_S), but

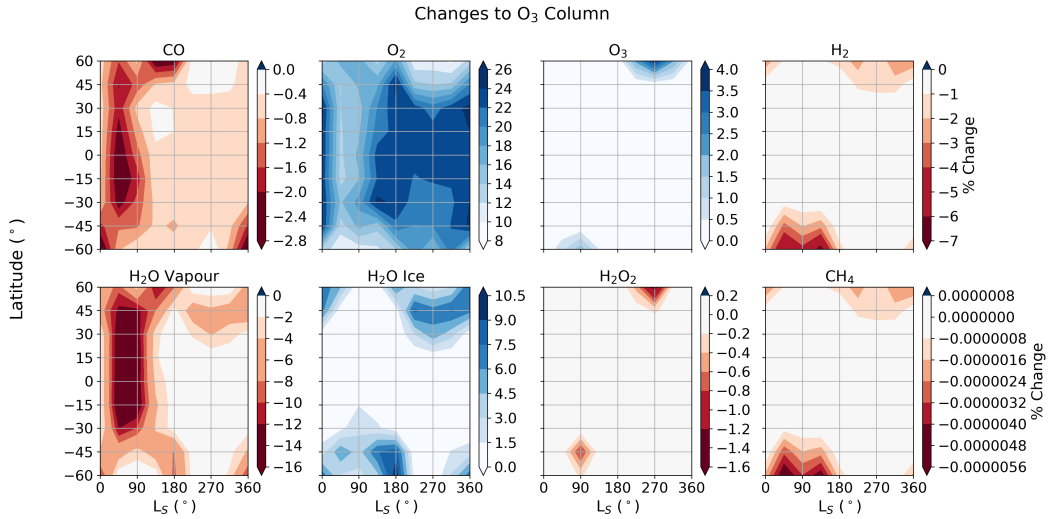


Figure 5.6: Percentage change in O_3 column vmrs produced by a 10% increase to the column of inorganic trace gas species in the 1-D model, allowing for a 10 sol model spin up.

fall to 0.4–0.8% as the year progresses. Although CO removes OH (e_1) from the atmosphere in the conversion of CO to CO_2, the additional H atom from the reaction is found to have a stronger impact on O_3 than the loss of OH. The reaction rate of O_3 with H atoms (c_3) at a temperature of 298 K is approximately 10^3 times greater than that of the O_3 reaction with OH molecules (c_{14}). Perturbations to the CO column therefore increase the sink strength for O_3 in Mars atmosphere. Beyond 90° L_S, the northern pole H_2O surface ice begins to sublimate and increase the H_2O vapour content of the equatorial regions, greatly lowering the O_3 content due to the increased HO_x source. Decreases to the O_3 columns in the equator are less pronounced due to the already small O_3 content in the model at this point.

Very strong O_3 column sensitivities to O_2 are calculated via the adjoint model throughout the Martian year, due to it being the primary source of O_3 through the three-body reactions with O atoms (a_1 of Table 3.2). 10% changes to the O_2 column throughout the northern summer–winter (90–360°) can cause O_3 column increases of 16–26%, and 10–16% in the northern spring. The O_3 columns of the polar regions, however, are calculated to be less sensitive to O_2 abundances than elsewhere by the adjoint, with 10% O_2 increases yielding 8–10% O_3 column increases. The polar regions in the winters experience less sunlight, lowering the abundance of O from photolysed CO_2 available for the three-body formation of O_3 from the additional O_2 molecules. As a result, polar region O_3 abundances tend to rely slightly less on O_2 than the equatorial regions. Between 30° south and 30° north however the additional O_2 molecules provide an additional source for O_3 production via three-body reactions with $O(^3P)$ (reaction a_1 of Table 3.2). The additional O_2 molecules also react with H atoms to produce HO_2 via reaction c_{11}. HO_2 molecules are reactive with O_3, but at temperatures of 298 K H

atoms (c_3) are more efficient as an O_3 sink than HO_2 (c_{15}) by a factor of roughly 14,400. The additional source for production for O_3, and the decrease in the sink strength of the highly reactive hydrogen atoms, combine to make O_3 highly sensitive to the O_2 abundances in my Mars photochemistry model.

A 10% perturbation to O_3 itself at the start of the model is also found to be inconsequential to the final O_3 column, due to the rapid photolysis O_3 experiences on Mars. 3–4% of the additional O_3 at the start of the model remains in the polar regions during their winter periods however, due to the lack of sunlight. O_3 columns are negatively sensitive to H_2, but likewise these sensitivities are restricted to the polar regions during the winter periods. In the dry regions of Mars' atmosphere, the lack of H_2O vapour allows $O(^1D)$ atoms to develop in greater abundances. This excess of $O(^1D)$ proceeds in the polar regions during their respective winters is a major source of HO_x species, produced by the reaction of $O(^1D)$ with H_2 atoms to produce OH and H (reaction b_3 of Table 3.2). An increase in H_2 in the north and south pole during their winter periods therefore increases the chemical sink of O_3 with the increase in OH and H, producing the stronger negative sensitivities displayed in Figure 5.6.

H_2O vapour is calculated to have a very strong and negative impact on O_3 columns as should be expected. The spatial variability is also very similar to that of the sensitivities to CO in Figure 5.6. O_3 column vmrs can lower by 10–16% in the northern spring with an increase of 10% in the H_2O column due to the consequent increase in HO_x that removes O_3 from the atmosphere. Like CO, the effects are less pronounced beyond 90° L_S due to lower O_3 abundances that develop here due to the elevated H_2O vapour levels from the sublimation of the polar caps. The adjoint also finds ice to have a much stronger impact on O_3 column abundances in the northern hemisphere than H_2O_2 (Figure 5.5). The removal of OH and HO_2 via adsorption onto ice particles lowers the chemical sink strength for O_3 in the model, enabling O_3 to be produced in greater quantities. This is especially beneficial when the abundances of O are low in regions with little daylight, i.e. in the polar regions. Ice also develops in greater quantities in these regions due to the lower atmospheric temperatures, so changes to the ice column in the polar winters have much stronger impacts than elsewhere where ice abundances are low.

O_3 columns are also found to be unaffected by the H_2O_2 content in the model's initial conditions, owing to the highly unstable nature of H_2O_2. An increase of 10% to H_2O_2 is stripped away too quickly to produce a consequential impact on O_3 columns. Small changes in the polar nights, with less daylight and a more stable H_2O_2 column, are seen however, with O_3 column vmrs able to lower by 1–1.6% when a 10% increase to H_2O_2 is made to the model input. Finally, the changes from an increase in CH_4 are calculated to be vanishingly small with current photochemistry models as the reaction rate of cab_1 is very inefficient.

5.6 Conclusion

In this chapter I have outlined the development of a 1-D tangent linear and adjoint model of the Martian atmosphere, the first to be made for any non-Earth planet. By comparing the perturbations made to a 1-D model run as calculated by the full non-linear model and those approximated via the TLM approach across four case studies including inorganic, organic, gas-phase, and heterogeneous chemistry (Figure 5.3 and Table 5.1) I have proven that the linearisation of the highly non-linear photochemistry and transport equations in the full 1-D model is possible and also highly accurate. The greatest inaccuracies appear for tracer perturbations that are < 0.01% of the control run values, which are incredibly small and imperceptible to observing equipment. The accuracy of the TLM stays high for perturbations of up to 100% of the control run, making the TLM a very important tool for future analysis of Mars' atmospheric composition. I have also proven that the adjoint produced from the transpose of the TLM matrix abides to the requirement of producing temporally invariant results within machine precision (Figure 5.4) over a period of at least 10 Mars sols.

I have also demonstrated the adjoint model's capabilities as a tool for sensitivity analysis by using the adjoint to calculate changes in H_2O_2 and O_3 columns across Mars over the course of a Martian year that result from 10% increases to various initial inorganic tracer columns in the model. I find that H_2O_2 is very sensitive to CO, O_2, and H_2 in the southern polar regions during the southern hemisphere's winter period, but much less so in the equatorial regions. The impact of H_2O ice on H_2O_2 is similarly very strong, causing steep decreases to H_2O_2 in the south during the southern hemispheres winter, but little impacts elsewhere. H_2O vapour has the most significant impact on H_2O_2, with stronger sensitivities appearing in the polar regions. Discrepancies between H_2O_2 observations and models [Encrenaz et al., 2019], assuming our photochemistry models are complete, will be most effected by errors in the H_2O vapour and CO profiles used to produce the photochemistry model H_2O_2 values.

I performed the same study for O_3 column vmrs also (Figure 5.6). My adjoint sensitivity analysis found that O_3 columns are very negatively sensitive to both H_2O vapour and CO abundances during the northern spring (0–90° L_S). Significant positive sensitivities to O_2 are experienced in the equatorial regions during the remainder of the year, but O_2 is less impactful on O_3 abundances in the polar region during the winter periods. I also find O_3 columns in the south pole during the northern spring, and the northern pole during the northern winter (270–360° L_S) to have a strong negative sensitivity to H_2, which is not experienced elsewhere. The adjoint also finds O_3 to be much more sensitive to the atmospheric ice content than H_2O_2, which is especially effective at increasing O_3 column abundances at the poles during each hemispheres respective winter. Neither H_2O_2 or O_3 is found to exhibit any consequential change from perturbations to CH_4. The photochemistry of O_3 on Mars is still incomplete, with the most modern GCMs under-estimating the maximum O_3 columns experienced in the equatorial latitudes by a factor of roughly 2 [Lefèvre et al., 2021]. The adjoint of the 1-D

photochemical model predicts that errors or miscalculations of CO would be most impactful to O_3 here, but the strongest sensitivities of O_3 are with respect to O_2 and H_2O vapour. O_3 in the polar regions, however, are significantly more sensitive to H_2 and H_2O ice than either H_2O vapour or O_2 - discrepancies between model polar ozone columns and those observed could be explained via mishandling of H_2 and the formation of ice in photochemistry models.

The photochemical adjoint for Mars that I have developed is a tool that I have demonstrated can be used to study the sensitivity of tracer abundances to the initial model state, which in turn can be used to assess what may be the cause of discrepancies between the non-linear photochemistry model and observations and identify errors or missing processes that would serve to increase model-observation coincidence. The adjoint can also be used as a valuable tool for inverse modelling, a process not covered in this work. The sensitivity vector, the output of Equation 5.16, can be used to produce a gradient for a cost-function in inverse modelling methods such as the limited memory BFGS scheme [Liu and Nocedal, 1989]. The inverse modelling method would calculate the difference between an observation and the output of the 1-D model, and use the sensitivity vector produced by the adjoint to assess what tracer species at the model input should be perturbed, within acceptable bounds, to bring the 1-D model output into better coincidence with the observation. This method would further highlight what chemical species GCM models of Mars are under or over estimating, and should be considered for further development and study in the future.

Chapter 6

Atmospheric Hydrogen Chloride on Mars

6.1 Search and Detection of Martian HCl

One of the most exciting discoveries made by the ExoMars TGO is the presence of hydrogen chloride (HCl) in the atmosphere, the first confirmed detection of a halogen gas on the planet. The first detection of HCl was reported by Korablev et al. [2021], followed closely by Olsen et al. [2021], using the ACS-MIR channel, which measured vertical profiles of the gas using solar occultation techniques during the 2018 global dust storm. HCl was observed by ACS-MIR in a layer centred between 10–30 km from the surface in abundances ranging between 0.1–4 ppb, which declined shortly after the dust storm ended. Figure 6.1 A–C highlights the layered structure of the observed HCl profiles by the ACS' NIR channel, and Figure 6.1 D displays the coincidences with the 2018 global dust storm during Mars' perihelion (180–300° L_S) approach. The ACS-MIR observations have also been corroborated by measurements from the NOMAD spectrometer by Aoki et al. [2021]. The observations of HCl made by NOMAD were performed over MY34–35, and found that the increase of atmospheric HCl in the southern hemisphere during its summer period (L_S 240–320°) is an annual occurrence that does not require the presence of a dust storm event.

The detection of HCl on Mars presents a new area of Martian atmospheric photochemistry that is vital to understand, due to the highly reactive and impactful nature of atmospheric chlorine species. O_3 abundances on Earth are very sensitive to small quantities of chlorine compounds [Douglass et al., 2006], where HCl is the principle atmospheric reservoir, to such a degree that an international agreement was developed in 1987 to phase out the production of man-made chlorfluorocarbons (CFCs) to prevent the depletion of Earth's ozone layer [Protocol, 1987] which has recently been shown to protect the functioning of terrestrial ecosystems [Young et al., 2021]. Chlorine chemistry is also vital for the stability of Venus' CO_2 based atmosphere, where HCl exists in abundances that range from 0.1–0.7 ppm [Iwagami et al., 2008].

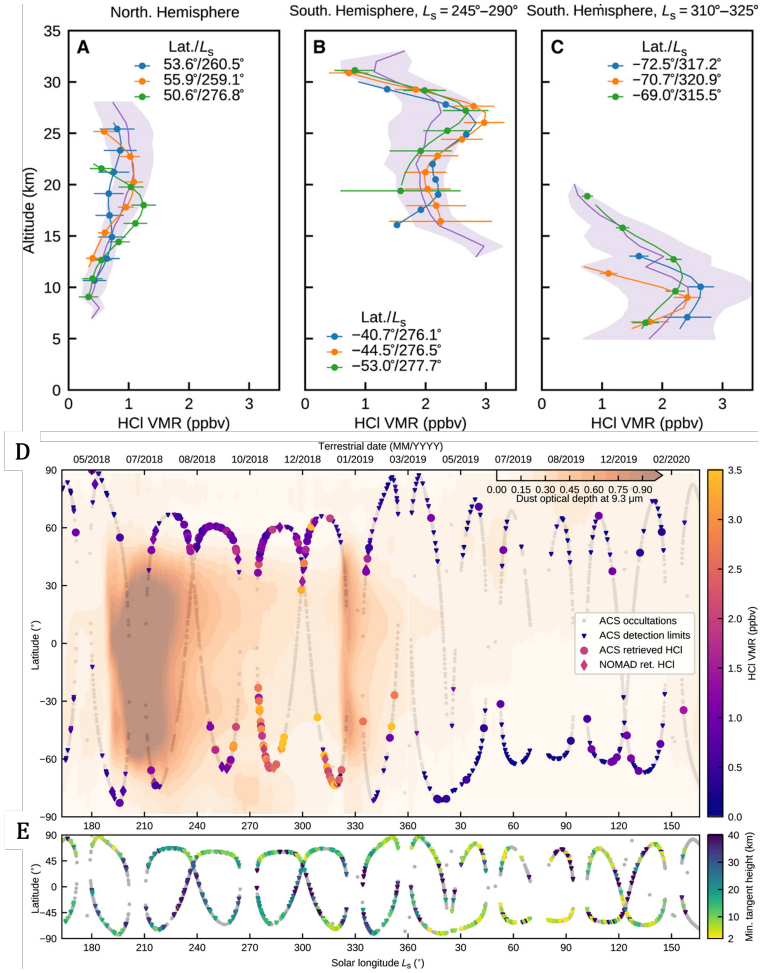


Figure 6.1: Observations of HCl on Mars made by ACS-MIR during the 2018 global dust storm. A) Northern hemisphere observations between L_S 210–330°, B) Southern hemisphere observations between L_S 245–290°, C) Southern hemisphere observations between L_S 310–325°. The purple line and shading indicates the mean of the profiles and their standard deviations in each subfigure. D) All ACS-MIR occultations are shown with gray dots. Triangles indicate lower limits of HCl only, whereas detections of HCl are circles with the maximum vmr of the profile indicated by the colorbar. NOMAD-SO retrievals are indicated by diamonds. The mean dust opacity is presented in the background of the figure. E) The lowest height (tangent height) in km above the surface of the ACS-MIR solar occultation observations. Figures from Korablev et al. [2021].

Like H_2O vapour on Mars, Venus' HCl photolyzes to produce highly reactive Cl atoms that result in the catalytic oxidation of CO that comes from the photolysis of CO_2 [Yung and Demore, 1982]. The presence of HCl on Mars will likewise result in highly reactive Cl-bearing gases that will strongly influence Mars' O_χ and HO_χ chemistry, that could lead to strong discrepancies between GCM models and observations if not accounted for.

Prior astronomical searches for an active chlorine cycle on Mars were only able to infer upper limits for HCl. Krasnopolsky et al. [1997] used the Goddard Space Flight Center (GSFC) postdisperser and the Kitt Peak National Observatory's fourier transform spectrometer to infer a 2-σ HCl upper limit of $<$ 2 ppb, implying that no significant chlorine chemistry existed on Mars. Hartogh et al. [2010] used the Herschell Space Observatory to search for HCl at sub-millimeter wavelengths from an Earth-orbit and determined a very low upper limit of 200 ppt, suggesting that Cl-chemistry on Mars is negligible to non-existent. Another ground-based search made by Villanueva et al. [2013] over a four-year observing period looked for HCl as well as chloromethane (CH_3Cl), a bi-product of chlorine reactions with CH_4 and non-methane VOC's. CH_3Cl was chosen as a target by Villanueva et al. [2013] due to it having a strong spectral feature within the 2.8–3.7 μm spectral range of the study. This search also failed to detect HCl as well as CH_3Cl, and yielded sensitive upper limits of $<$0.6 ppb for HCl and $<$ 14.3 ppb for CH_3Cl, once again an implication that no significant chlorine chemistry is occuring on Mars. The present-day detections of HCl by ACS and NOMAD show just how important advancements in spectroscopic measuring equipment are to our studies of planetary science.

The TGO selected HCl as one of its target compounds for observations due to its strong relationship with volcanic processes on Earth [Timmreck, 2012]. Volcanic activity however is also coupled with strong seismic activity, which has not been observed on Mars by NASA's InSight lander since it touched down in November 2018 [Banerdt et al., 2020], which has found Mars' seismic noise to be roughly 500 times lower than that found on Earth [Lognonné et al., 2020]. Volcanism also emits strong levels of sulfur-based compounds and CH_4 [von Glasow, 2010]. A search for Martian SO_2 performed by Krasnopolsky [2005] using ground-based spectroscopy methods placed an upper-limit of $<$1 ppb on the compound. Ground-based measurements made by Khayat et al. [2017] extended the search for volcanic gases to carbonyl sulfide (OCS) as well as SO_2, and dedicated their observations to Tharsis (home to the shield volcanoes Pavosis Mons, Arsia Mons, and Ascraeus Mons) and Syrtis Major (a shield volcano originally thought to be a plain until analysis of MGS data [Hiesinger and Head III, 2004]), volcanic districts active in Mars' long-distant past. These areas, prime candidates for remnants of volcanic activity, were only assigned upper limits of 1.8 ppb for OCS and 3.1 ppb for SO_2. A prior search of the same region, performed by Khayat et al. [2015], also included sulfur monoxide (SO) and hydrogen sulfide (H_2S) and only inferred upper limits of 0.7 ppb, 1.1 ppb, and 1.3 ppb for SO, SO_2, and H_2S. The lack of significant seismic activity and an absence of sulfur containing atmospheric species strongly implies that volcanism is not the source of HCl observed by the ACS and NOMAD.

6.2 Chlorine Photochemistry Scheme

The chlorine tracers I have included in the 1-D photochemistry model for Mars are presented in Table 6.1, and the full list of chemical reactions and their reaction rate coefficients included in the 1-D photochemistry submodule chlorine scheme is presented in Table 6.2. The primary source of the reactions is the CAABA/MECCA v4.0 box model [Sander et al., 2019], with additional reactions involving perchlorate production ($HClO_4$) taken from the modelling study performed by Catling et al. [2010]. These were chosen for inclusion as their work found that the atmospheric gas-phase production of $HClO_4$ and its subsequent deposition on the surface of the Atacama desert, which has perchlorate (ClO_4^-) in the soil at abundances closest to those observed at the landing sites of the Phoenix lander [Hecht et al., 2009a] on Earth, is a potentially feasible origin for the Atacama deserts ClO_4^- content in the soil, and may have similar potential for an explanation of Mars' ClO_4^- soil content. These additional gas-phase reactions included for the atmospheric production of $HClO_4$ are cl_{44}, cl_{45}, cl_{46}, cl_{47}, cl_{48}, cl_{49} and cl_{50} in Table 6.2.

Table 6.1: Chlorine species included in my 1-D photochemistry model.

Chlorine Tracers	
Chemical Formula	Name
Cl	Chlorine (atomic)
ClO	Chlorine Monoxide
Cl_2	Chlorine (molecular)
OClO	Chlorine Dioxide
Cl_2O_2	Chlorine Peroxide
HCl	Hydrogen Chloride
HOCl	Hypochlorous Acid
ClOO	Chlorine Superoxide
CH_3OCl	Methyl Hypochlorite
ClCO	-
ClO_3	Chlorate
$HClO_4$	Perchloric Acid
ClO_4	Perchlorate

As Cl and ClO are two very reactive compounds with atmospheric lifetimes significantly shorter than the 1-D model chemistry time-step of 600 s, these two species are grouped together and named the ClO_x (Odd-Chlorine) family and treated in the same way as HO_x in the chemistry routine by assuming ClO exists in photochemical equilibrium. ClO has atmospheric lifetimes shorter than the chemistry timestep throughout the model's altitude grid, whereas Cl has a long lifetime ($<$ 2 hours) above 60 km. Grouped together, the equations handling the individual components Cl and ClO can be made as follows:

$$[ClO_\chi]^t = [Cl]^t + [ClO]^t \tag{6.1}$$

$$= [Cl]^t \times (1 + \frac{[ClO]^t}{[Cl]^t}) \tag{6.2}$$

$$[Cl]^t = [ClO_\chi]^t \times (1 + \frac{[ClO]^t}{[Cl]^t})^{-1} \tag{6.3}$$

$$[ClO]^t = [Cl]^t \times [ClO]^t/[Cl]^t \quad , \tag{6.4}$$

where the ratio $[ClO]^t/[Cl]^t$ is the partition function of the ClO_χ system. To find this value, the rate of change of ClO is assumed to be 0, enabling the photochemical equations to be rearranged to produce the partition functions as follows:

$$\frac{d[ClO]^t}{dt} = 0 \tag{6.5}$$

$$P_{ClO} - L_{ClO}[ClO]^t = 0 \tag{6.6}$$

$$\frac{[ClO]^t}{[Cl]^t} = \frac{P_{ClO}}{[Cl]^t} \times \frac{1}{L_{ClO}} \tag{6.7}$$

Table 6.2: Reactions involving chlorine species used in my 1-D photochemistry submodule. All rate coefficients calculated at T = 298 K are given in units of cm^3 $molec.^{-1}$ s^{-1}, with exceptions denoted with ^{a} that are first-order and in units of s^{-1}. Termolecular rate coefficients are calculated for an atmospheric temperature of 298 K and pressure of 660 Pa.

Key	Reaction	Rate Equation	Rate at T=298 K	Reference
cl_1	$Cl + O_3 \longrightarrow ClO + O_2$	2.8E-11exp(-250/T)	1.21E-11	Sander et al. [2019]
cl_2	$ClO + O \longrightarrow Cl + O_2$	2.5E-11exp(110/T)	3.62E-11	Sander et al. [2019]
cl_3	$ClO + ClO \longrightarrow Cl_2 + O_2$	3.0E-11exp(-1590/T)	1.45E-13	Sander et al. [2019]
cl_4	$ClO + ClO \longrightarrow Cl + Cl + O_2$	3.0E-11exp(-2450/T)	8.07E-15	Sander et al. [2019]
cl_5	$ClO + ClO \longrightarrow Cl + OClO$	3.5E-13exp(-1370/T)	3.52E-15	Sander et al. [2019]
cl_6	$ClO + ClO \longrightarrow Cl_2O_2$	$2.5\times$2.0E-32 $(300/T)^4$	8.24E-15	Sander et al. [2019]
cl_7	$Cl_2O_2 \longrightarrow ClO + ClO$	Cl_6/(2.16E-27exp(8537/T))	1.38E-10	Sander et al. [2019]
cl_8	$Cl + H_2 \longrightarrow HCl + H$	3.9E-11exp(-2310/T)	1.68E-14	Sander et al. [2019]
cl_9	$Cl + HO_2 \longrightarrow HCl + O_2$	4.4e-11 - 7.5E-11exp(-620/T)	3.46E-11	Sander et al. [2019]
cl_{10}	$Cl + HO_2 \longrightarrow ClO + OH$	7.5E-11exp(-620/T)	9.37E-12	Sander et al. [2019]
cl_{11}	$Cl + H_2O_2 \longrightarrow HCl + HO_2$	1.1E-11exp(-980/T)	4.10E-13	Sander et al. [2019]
cl_{12}	$ClO + OH \longrightarrow 0.94\ Cl + 0.94\ HO_2 + 0.06\ HCl + 0.06\ O_2$	7.3E-12exp(300/T)	2.00E-11	Sander et al. [2019]
cl_{13}	$ClO + HO_2 \longrightarrow HOCl + O_2$	2.2E-12exp(340/T)	6.89E-12	Sander et al. [2019]
cl_{14}	$HCl + OH \longrightarrow Cl + H_2O$	1.7E-12exp(-230/T)	7.86E-13	Sander et al. [2019]
cl_{15}	$HOCl + OH \longrightarrow ClO + H_2O$	3.0E-12exp(-500/T)	5.60E-13	Sander et al. [2019]
cl_{16}	$Cl + CH_4 \longrightarrow HCl + CH_3$	6.6E-12exp(-1240/T)	1.03E-13	Sander et al. [2019]
cl_{17}	$Cl + HCHO \longrightarrow HCl + HCO$	8.2E-11exp(-34/T)	7.32E-11	Sander et al. [2019]
cl_{18}	$Cl + CH_3OOH \longrightarrow HCHO + HCl + OH$	5.9E-11	5.90E-11	Sander et al. [2019]
cl_{19}	$ClO + CH_3O_2 \longrightarrow CH_3O + ClOO$	4.92E-12exp(-261.5/T)	2.05E-12	Sander et al. [2019]

cl_{20}	$ClO + CH_3O_2 \longrightarrow CH_3OCl + O_2$	2.6E-13exp(260/T)	6.22E-13	Sander et al. [2019]
cl_{21}	$ClO + CH_3O_2 \longrightarrow CH_3O + OClO$	1.E-15	1.00E-15	Sander et al. [2019]
cl_{22}	$Cl + CH_3O_2 \longrightarrow 0.5\ ClO + 0.5\ CH_3O + 0.5\ HCl + 0.5\ CH_2OO$	1.6E-10	1.60E-10	Sander et al. [2019]
cl_{23}	$CO + Cl + M \longrightarrow COCl + M$	$2.5\times1.33E\text{-}33(298/T)^{3.8}$	5.34E-16	Sander et al. [2019]
cl_{24}	$ClOO + Cl \longrightarrow ClO + ClO$	1.2E-11	1.20E-11	Sander et al. [2019]
cl_{25}	$ClOO + Cl \longrightarrow O_2 + Cl_2$	2.31E-10	2.31E-10	Sander et al. [2019]
cl_{26}	$ClOO \longrightarrow O_2 + Cl$	$2.8E\text{-}10exp(-1820/T)\times\rho$	1.00E+4[a]	Sander et al. [2019]
cl_{27}	$HClO_4 + OH \longrightarrow ClO_4 + H_2O$	$1.24E\text{-}8exp(-1664/T)\ T^{-2.9}$	3.11E-18	
cl_{28}	$Cl + O_2 + M \longrightarrow ClOO + M$	$2.5\times1.44E\text{-}33(298/T)^{3.9}$	5.78E-16	Sander et al. [2019]
cl_{29}	$Cl + CH_3OCl \longrightarrow Cl_2 + CH_3O$	5.2E-11	5.20E-11	Sander et al. [2019]
cl_{30}	$Cl + Cl_2O_2 \longrightarrow Cl_2 + ClOO$	1.E-10	1.00E-10	Sander et al. [2019]
cl_{31}	$Cl + CH_3OCl \longrightarrow HCl + CH_2OCl$	9.15E-12	9.15E-12	Sander et al. [2019]
cl_{32}	$OH + CH_3OCl \longrightarrow CH_3O\ HOCl$	2.4E-12exp(-360/T)	7.17E-13	Sander et al. [2019]
cl_{33}	$ClCO \longrightarrow Cl + CO$	$4.1E\text{-}10exp(-2960/T)\times\rho$	3.21E+3[a]	Sander et al. [2019]
cl_{34}	$Cl_2 + O(^1D) \longrightarrow O + Cl_2$	$0.25\times7.2E\text{-}10$	1.80E-10	Sander et al. [2019]
cl_{35}	$Cl_2 + O(^1D) \longrightarrow Cl + ClO$	$0.75\times7.2E\text{-}10$	5.40E-10	Sander et al. [2019]
cl_{36}	$Cl_2 + OH \longrightarrow HOCl + Cl$	2.6E-12exp(-1100/T)	6.49E-14	Sander et al. [2019]
cl_{37}	$Cl_2 + H \longrightarrow HCl + Cl$	8.0E-11exp(-417/T)	1.98E-11	Sander et al. [2019]
cl_{38}	$Cl_2 + CH_3 \longrightarrow CH_3Cl + Cl$	$1.67E\text{-}13exp(664/T)\times(T/298)^{2.52}$	1.55E-12	Sander et al. [2019]
cl_{39}	$HCl + O(^1D) \longrightarrow 0.12\ O + 0.12\ HCL + 0.22\ H + 0.22\ ClO + 0.66\ Cl + 0.66\ OH\backslash$	1.5E-10	1.50E-10	Sander et al. [2019]
cl_{40}	$HCl + O \longrightarrow OH + Cl$	1.1E-11exp(-3300/T)	3.64E-12	Sander et al. [2019]
cl_{41}	$HCl + H \longrightarrow H_2 + Cl$	2.01E-11exp(-1790/T)	4.95E-14	Sander et al. [2019]

cl_{42}	$HOCl + O \longrightarrow ClO + OH$	1.7E-13	1.70E-13	Sander et al. [2019]
cl_{43}	$HCOOH + Cl \longrightarrow HCl + Products$	2.01E-13	2.01E-13	Sander et al. [2019]
cl_{44}	$Cl + O_3 + M \longrightarrow ClO_3 + M$	2.5E-31	4.01E-14	Catling et al. [2010]
cl_{45}	$ClO + ClO_3 \longrightarrow ClOO + OClO$	1.85E-18exp(-2417/T) $T^{2.28}$	4.08E-17	Catling et al. [2010]
cl_{46}	$ClO + ClO_3 \longrightarrow OClO + OClO$	1.42E-18exp(-2870/T) $T^{2.11}$	1.55E-17	Catling et al. [2010]
cl_{47}	$ClO + ClO_3 + M \longrightarrow Cl_2O_4 + M$	k_3rd(1.43E-1exp(-1597/T), -10.19 , 1.43e-10exp(-87/T), 0.09)	1.07E-10	Catling et al. [2010]
cl_{48}	$ClO_3 + OH \longrightarrow HClO_4$	6.67E-13	6.67E-13	Catling et al. [2010]
cl_{49}	$ClO_3 + OH + M \longrightarrow HClO_4$	k_3rd(1.90E+36exp(-5542/T), -15.3, 3.20E-10exp(-25/T), 0.07)	2.94E-10	Catling et al. [2010]
cl_{50}	$ClO_3 + OH \longrightarrow OClO + HO_2$	2.1E-10exp(-18/T) $T^{0.09}$	3.31E-10	Catling et al. [2010]
cl_{51}	$OClO + O + M \longrightarrow ClO_3 + M$	k_3rd(7.25E-31, 3.1, 8.30E-12, 1)	2.34E-13	Catling et al. [2010]
cl_{52}	$OClO + O_3 \longrightarrow ClO_3 + O_2$	2.1E-12exp(-4700/T)	2.97E-19	Sander et al. [2019]
cl_{53}	$ClO_4 + Cl \longrightarrow ClO_3 + ClO$	1.98E-10exp(-49/T) $(T/298)^{0.16}$	1.68E-10	Sander et al. [2019]
cl_{54}	$ClO_4 + HOCl \longrightarrow OH + HClO_4$	2.57E-14exp(-1017/T) $(T/298)^{1.73}$	8.47E-16	Sander et al. [2019]
cl_{55}	$HOCl + Cl \longrightarrow Cl_2 + OH$	3.2E-12exp(-130/T)	2.07E-12	Sander et al. [2019]
cl_{56}	$HOCl + Cl \longrightarrow HCl + ClO$	2.04E-13exp(-130/T)	1.32E-13	Sander et al. [2019]
cl_{57}	$OClO + O \longrightarrow ClO + O_2$	2.4E-12exp(-960/T)	9.58E-14	Sander et al. [2019]
cl_{58}	$OClO + OH \longrightarrow HOCl + O_2$	1.4E-12exp(600/T)	1.05E-11	Sander et al. [2019]
cl_{59}	$OClO + Cl \longrightarrow ClO + ClO$	3.4E-11exp(160/T)	5.82E-11	

Table 6.3: Photolysis reactions of chlorine tracers used in my 1-D photochemistry model. Reactions highlighted in green indicate new additions since I started my PhD.

Key	Reaction	Rate (s^{-1}) at 4.8 km	Rate (s^{-1}) at 75.9 km
j_hcl	HCl + $h\nu \longrightarrow$ H + Cl	1.15E-7	6.49E-7
j_hocl	HOCl + $h\nu \longrightarrow$ OH + Cl	1.89E-4	1.94E-4
j_clo	ClO + $h\nu \longrightarrow$ Cl + O	2.20E-3	2.32E-3
j_cl2	Cl_2 + $h\nu \longrightarrow$ Cl + Cl	1.75E-3	1.78E-3
j_cloo	ClOO + $h\nu \longrightarrow$ ClO + O	6.44E-3	8.89E-3
j_oclo	OClO + $h\nu \longrightarrow$ ClO + O	6.50E-2	6.55E-2
j_cl2o2	Cl_2O_2 + $h\nu \longrightarrow$ Cl + ClOO	3.35E-3	4.14E-3

The production and loss terms in the above equation only consider reactions involving both Cl and ClO, and, using reaction keys denoted in Table 6.2 and 6.3, are presented below:

$$P_{ClO}/[Cl]^t = cl_1[O_3]^t + cl_{10}[HO_2]^t + 0.5\,cl_{22}[CH_3O_2]^t + 2\,cl_{24}[ClOO]^t + cl_{53}[ClO_4]^t + cl_{56}[HOCl]^t + 2\,cl_{59}[OClO]^t \tag{6.8}$$

$$L_{ClO} = cl_2[O]^t + cl_3[ClO]^t + cl_4[ClO]^t + cl_5[ClO]^t + cl_6[ClO]^t + cl_{12}[OH]^t + cl_{13}[HO_2]^t + cl_{19}[CH_3O_2]^t + cl_{20}[CH_3O_2]^t + cl_{21}[CH_3O_2]^t + cl_{45}[ClO_3]^t + cl_{46}[ClO_3]^t + cl_{47}[ClO_3]^t + j_clo. \tag{6.9}$$

The evolution of the summed ClO_χ family is handled via the SIBEM equation, and the production and loss rates of ClO_χ are the summed production and losses of Cl and ClO.

For the remaining 11 chlorine tracers, a new numerical method is applied. The chlorine species used in this work have photochemical lifetimes that strongly vary with altitude, to the point where the steady-state approximation for short-lived species can be applied in one portion of the vertical grid, and invalid in others, much like atomic oxygen and atomic hydrogen. To prevent errors arising from this, and to maintain mass conservation, I have incorporated the Quasi-Steady-State Approximation (QSSA) to model the evolution of chlorine species. Defining the photochemical lifetime as the inverse of the loss rate (L_i), if a compound has a lifetime 100 times greater than the chemistry timestep (Δt_c = 600 s) the SIBEM method is used to carry its abundance over to the next timestep. If a compound has a lifetime below 10% of the chemistry timestep, the steady-state assumption is adopted. In all other cases, the simple exponential assumption is made to solve the chemical differential equation. This is an approach originally developed by Hesstvedt et al. [1978], and Equation 6.10 displays these three methods in their discretised form alongside their conditions dependent on the species loss rate.

$$n_i^{t+1} = \frac{n_i^t + P_i^t \Delta t_c}{1 + L_i^t \Delta t_c}, \quad L_i^t \Delta t_c < 0.01 \tag{6.10}$$

$$n_i^{t+1} = n_i^t \exp\left(-\Delta t_c L_i^t\right) + \frac{P_i^t}{L_i^t}\left(1 - \exp(-\Delta t_c L_i^t)\right), \quad 0.01 \leq L_i^t \Delta t_c \leq 10 \tag{6.11}$$

$$n_i^{t+1} = \frac{P_i^t}{L_i^t}, \quad L_i^t \Delta t_c > 10. \tag{6.12}$$

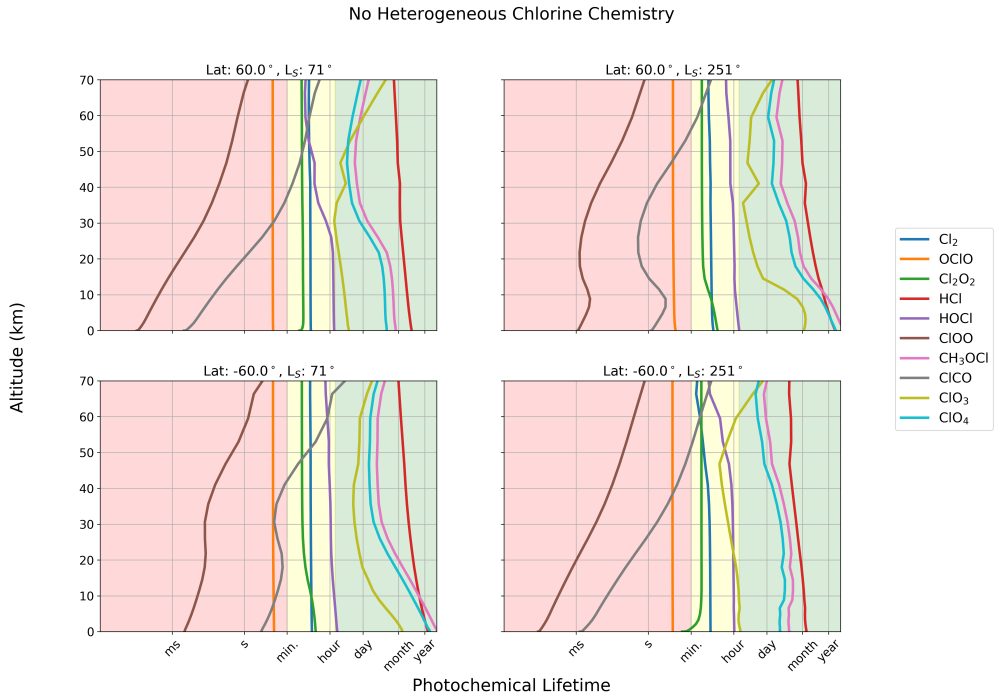


Figure 6.2: Photochemical lifetimes of chlorine-containing tracers in the 1-D photochemistry model assessed at noon (LT = 12:00 hrs) at latitudes 60° and -60° during Mars' aphelion (L_S 71°) and perihelion (L_S 251°). Red regions: steady-state approximation; Yellow regions: simple exponential solution; Green regions: semi-implicit backwards Euler method.

Figure 6.2 presents the photochemical lifetimes of the chlorine compounds in the atmosphere of Mars at 60° north and south during Mars' aphelion (L_S 71°) and perihelion (L_S 251°). The regions where the steady-state (red), simple exponential solution (yellow), and SIBEM equation (green) are used by the model are highlighted. The model was initialised with 5 ppb of HCl across all model layers and given a spin-up time of 10 sols, corresponding to the magnitude of the vertical mixing timescale of the lower $\sim$ 70 km of Mars' atmosphere, prior to the calculations of lifetimes.

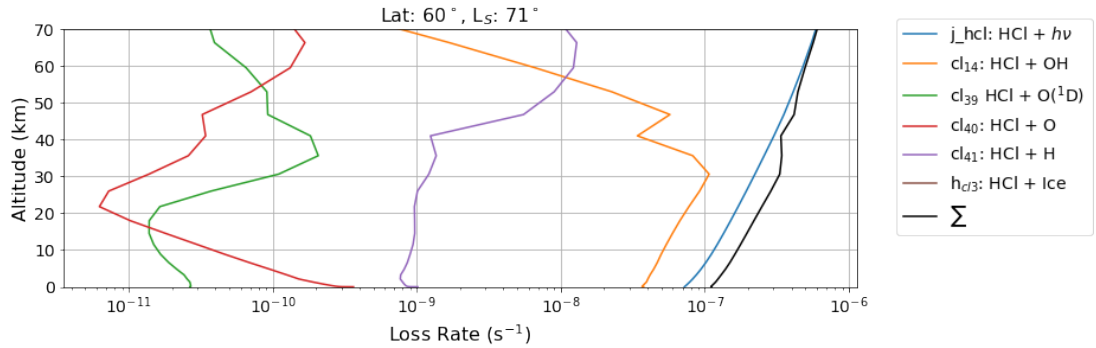


Figure 6.3: Loss rates of HCl at 60° north and L_S 71° using gas-phase chlorine chemistry only.

The photochemical lifetime of HCl, using gas-phase chlorine chemistry alone, is dominated by UV photolysis, with values of 10^{-8}–10^{-7} s^{-1} close to the surface and rising to 10^{-7}–10^{-6} s^{-1} at 70 km. Reactions with OH below the Martian hygropause, typically 10 km in the northern summer and extending to 30–40 km in the northern winter, are the second strongest photochemical sink for HCl, and are effective below the Martian hygropause where they produce loss rate magnitudes of 10^{-8} s^{-1}. The individual loss rates for a model run at latitude 60° north at L_S 71° for HCl are presented in Figure 6.3. In the northern hemisphere during the summer (L_S 90–180°), atmospheric H_2O is at a maximum as the northern polar caps exposure to sunlight results in the sublimation of water ice on the polar cap floor. This results in larger OH abundances available for the removal of HCl. The increased intensity of solar radiation in the northern hemisphere also increases the rate of photolysis of HCl, resulting in HCl lifetimes of $\sim$ 100 sols at the surface, and steadily lowering to values of $\sim$ 10 sols at 70 km. In the autumn (L_S 180–270°), atmospheric H_2O in the north begins to fall, as does the intensity of solar radiation due to the planet's obliquity. Lifetimes of HCl rise with the falling atmospheric sinks to values between 100–700 sols below the hygropause, and again decrease with altitude to $\sim$ 20 sols. The opposite effect is experienced in the southern hemisphere, where H_2O vapour reaches a maximum during the northern hemisphere's autumn and winter, and a minimum during the northern summer. These HCl lifetimes, spanning 10s to 100s of days at altitudes of 20–30 km, make the TGO observations of HCl impossible to explain through gas-phase chemistry alone, and possible heterogeneous loss processes involving either dust or water ice need to be investigated Korablev et al. [2021], Aoki et al. [2021].

6.2.1 Heterogeneous Chlorine Chemistry

Observations of HCl made by the NOMAD spectrometer aboard the TGO over MY34/35 noted a strong similiarity between the HCl profile shapes and the profile shapes of water vapour [Aoki et al., 2021]. Coupled with the observations of the Martian Cl^- soil content by the Mars Odyssey's GRS [Keller et al., 2006], I investigate the potential of water vapour related processes in the atmosphere releasing chlorine compounds trapped within dust grains that have been lofted into the atmosphere as a means of explaining the HCl observations made by TGO instrumentation [Aoki et al., 2021, Olsen et al., 2021, Korablev et al., 2021]. To do this, I have introduced three new heterogeneous reactions into the 1-D submodule that act as sources and sinks of chlorine chemistry on Mars. These reactions are creations of my own, and were chosen to study an atmospheric chemistry release mechanism discussed in Liuzzi et al. [2021] in which reactions of HO_2 may react with chloride salts such as NaCl or KCl in the lofted dust, or reactions of OH with the perchlorate oxyanion, ClO_4^{-1}. Laboratory studies of Martian soil are only possible through soil analogues [Marlow et al., 2008], and the release of chlorine and production of HCl via chlorine-containing dust has been studied for Earth's atmosphere [Sullivan et al., 2007]. I assumed the release of ClO_x from dust to roughly account for the chemical reactions that may take place within the dust grain that trigger the release of either a Cl atom or the ClO molecule, as both reactants (OH and HO_2) are capable of transferring oxygen atoms to the dust grain. As both Cl and ClO are highly reactive with very small photochemical lifetimes, I allow the 1-D model to use the partition functions to calculate their abundances upon exposure to the air. These reactions are listed in Table 6.4.

Table 6.4: Uptake coefficients for heterogeneous interactions involving chlorine species. ^{a}: A_{Des} = 1E13 s^{-1}, pre-exponential factor for the desorption of the adsorbed HCl precursor, E_{Des} = 28.0 kJ mol^{-1} HCl desorption activation energy, A_R = 1.2E4 s^{-1}, pre-exponential factor of HCl precursor reaction, ΔE = E_{Des} - E_R = 30.5 kJ mol^{-1}, energy difference between desorption and reaction of HCl on ice particle. RH denotes relative humidity (%).

Key	Reaction	Uptake Coefficient	Source
h_{cl1}	OH + Dust $\longrightarrow$ ClO_χ + Dust	$0.2\times(1 + RH^{0.36})^{-1}$	Tang et al. [2017]
h_{cl2}	HO_2 + Dust $\longrightarrow$ ClO_χ + Dust	$1.2\times(18.7 + RH^{1.1})^{-1}$	Bedjanian et al. [2013]
h_{cl3}	HCl + Ice $\longrightarrow$ Products + Ice	$0.9\times(A_{Des}/A_R)^{-1}$ $\times(\exp(-\Delta E/RT))^a$	Hynes et al. [2001]

OH and HO_2 are highly reactive species with abundances controlled by the abundance of H_2O. I hypothesise that these species are capable of reacting with the chemical composition of the airborne dust releasing chlorine-containing compounds in the process, and that HCl produced during the resultant photochemical cascade is capable of adsorbing onto water ice crystals. The oxidation of inorganic aerosols by both OH and HO_2 has been observed on Earth, with reactions with NaCl particles producing Cl_2, but the exact mechanism behind this reaction remains fairly speculative, and for NaCl particles, specifically, the reaction requires a film of water to be present on the aerosol particle for the release of Cl_2 to be remotely efficient

[George and Abbatt, 2010]. The lack of liquid H_2O on Mars makes this exact mechanism unfeasible. I chose to study the release of ClO_x species instead, where one adsorbed OH/HO_2 molecule releases one ClO_x molecule by adding the production terms ($h_{cl1}N_{OH}$ and $h_{cl2}N_{HO2}$ respectively) to the production rate of the summed ClO_x family, as these are the two chlorine radicals responsible for mediating the rest of the atmospheric Cl chemistry.

The uptake coefficients of OH and HO_2 on mineral dust have been well studied on Earth, and I have chosen values that are dependent on the relative humidity (RH) of the environment, defined as the ratio of the water vapour partial pressure (pv) and the saturation pressure (pvs). The dependence on RH is of interest due to the highly variable RH values that Mars experiences as observed by the Phoenix lander [Fischer et al., 2019]. These observations show that there are strong diurnal and seasonal variations in the RH values, shown in Figure 6.4, which provides evidence for a strong atmosphere-regolith transfer process on diurnal timescales, similar to a postulation earlier by Formisano et al. [2001] in their re-analysis of Mariner 9 data. Formisano et al. [2001] found that the observations of the Martian water vapour column were consistent with a model where H_2O adsorbs into the Martian dust and soil during the cooler nights, and is released during the hotter periods during daylight hours. Incorporating RH dependent uptake coefficients into the 1-D model will thus enable diurnal variations of heterogeneous chlorine chemistry to be better modelled.

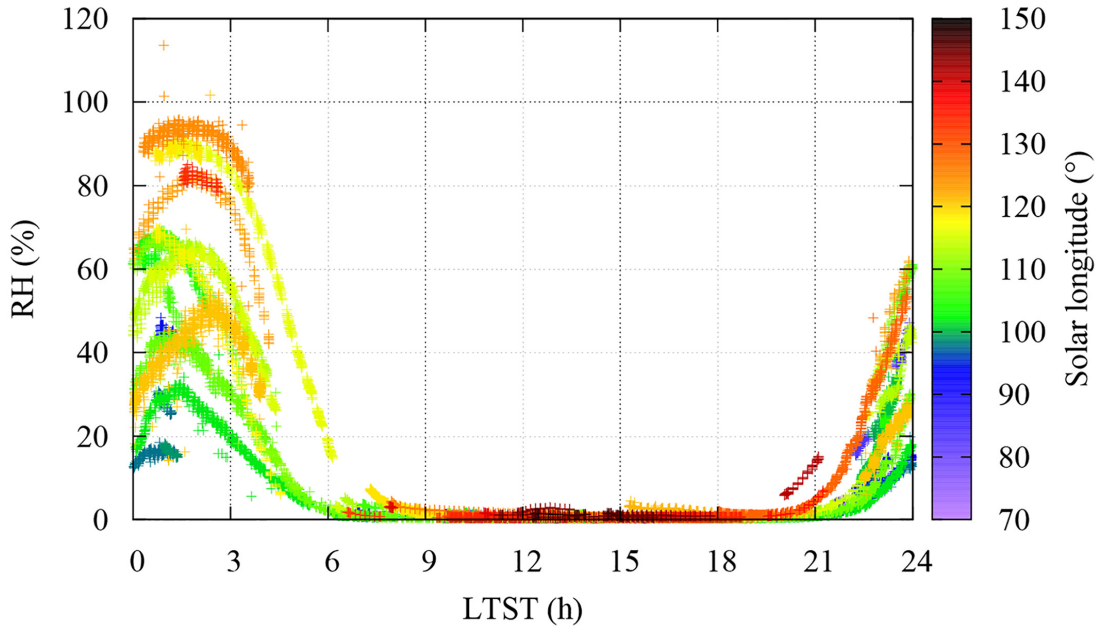


Figure 6.4: Relative humidity at the Phoenix lander's landing site . Figure from Fischer et al. [2019].

The uptake of HCl on water ice is a process common in Earth's atmosphere, and is hypothesised to be responsible for the quick disappearances of HCl on Mars [Korablev et al., 2021]. The uptake coefficient of HCl on water ice has been intensely studied in laboratories (e.g. Nagashima et al. [2018]), as adsorption onto stratospheric ice clouds is a strong regulator of the total chlorine abundance on Earth, and consequently impacts the ozone column [Liao et al., 2014, Solomon et al., 2015]. Close to the surface, Mars experiences strong diurnal variations in atmospheric temperature. At night, temperatures can drop from their noon highs of $\sim$ 300 K to 180–200 K at Gale crater [Spanovich et al., 2006], so I selected a temperature dependent uptake coefficient for HCl's adsorption onto water ice particles that was derived through laboratory measurements across tropospheric temperature (205–230 K) and pressure (220–270 Pa) ranges [Hynes et al., 2001] which are commonly experienced on Mars. Figure 6.5 presents the uptake coefficients of these three heterogeneous reactions and their variations with relative humidity and atmospheric temperature.

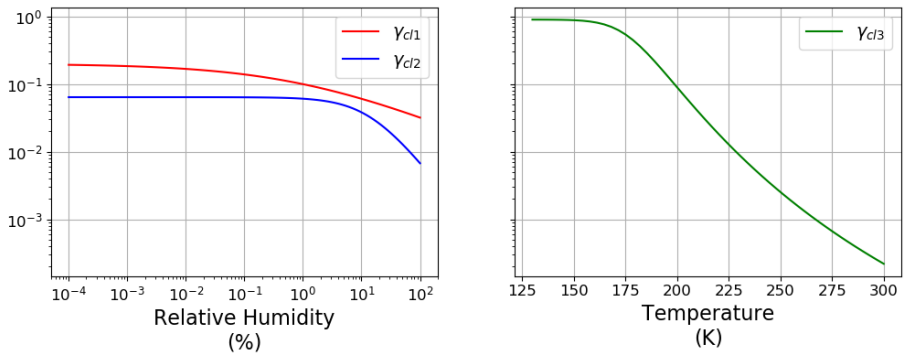


Figure 6.5: The uptake coefficients involved with chlorine species in the 1-D model and their variations with Relative Humidity (%) and temperature (K). γ_{cl1}: OH + Dust $\longrightarrow$ ClO_x + Dust, γ_{cl2}: HO_2 + Dust $\longrightarrow$ ClO_x + Dust, γ_{cl3}: HCl + Ice $\longrightarrow$ Ice + Products.

The chlorine release scheme is strictly dependent on the surface area of dust and ice in each model layer (cm^2/cm^3). As such, the rate of release for ClO_x into the atmosphere and the rate of HCl removal through H_2O ice are sensitive to the effective radii, r_{eff}, of the Martian aerosols. r_{eff} is a highly variable property subject to fluctuations between 0.1–4.0 μm for dust and 0.1–5.0 μm for ice, and are difficult properties to accurately infer from satellite observations [Luginin et al., 2020]. The aerosol radii have been found to be dependent on both horizontal and vertical transport processes, and are subject to strong local variations [Kahre et al., 2008]. The values of r_{eff} for dust and ice will be taken from the MCDv5.3 with the assumption that they are representative of the MY34 dust season.

6.2.2 Surface Deposition of HCl

I have included a dry deposition routine at the Martian surface for HCl in the 1-D model. I have included this to give the Martian soil a means of replenishing Cl lost via the heterogeneous reactions of lofted dust with OH and HO_2 radicals. The model limits the dry deposition routine to HCl as it is the focus of this study, and the only gas-phase chlorine species observed on Mars. A more complete model would include the surface deposition of other Cl-species, such as Cl_2 which has been studied on terrestrial soil [Hearn et al., 2013], and $HClO_4$ which has been investigated as a mechanism for the production of Mars' soil perchlorate content [Catling et al., 2010]. For simplicity, these have not been included in my 1-D model. Dry deposition of a compound onto a surface is a result of the gravitational settling of the gas or aerosol particle and their Brownian diffusion. Atmospheric temperature, wind speeds, pressures, and the physical and chemical properties of the surface are some of the many parameters governing the rate of a chemical species' deposition. To calculate this deposition flux for HCl, F_{HCl}, I use the equation:

$$F_{HCl} = V_{D,HCl} N_{HCl}, \tag{6.13}$$

where $V_{D,HCl}$ and N_{HCl} are the dry deposition velocity and number density of HCl at the bottom layer of the model. $V_{D,HCl}$ is calculated via the resistance method detailed in Erisman et al. [1994]. Here, three resistances (units of s cm^{-1}) are used to represent the three stages of transport for the depositing gas, and their summation via the resistance method provides the value of $V_{D,HCl}$:

$$V_{D,HCl} = (R_a + R_b + R_c)^{-1}. \tag{6.14}$$

R_a in Equation 6.14 represents the aerodynamic resistance for the turbulent layer above the surface, R_b is the aerodynamic resistance for the quasi-laminar layer, and R_c represents the resistance to deposition of the surface itself. R_a is approximated by:

$$R_a = \frac{1}{\kappa u_*} \ln \frac{z_1}{z_0}, \tag{6.15}$$

where κ is the dimensionless Von Karman constant, κ = 0.4, u_* is the frictional velocity at the surface layer (cm s^{-1}), P_1 the pressure at the lowest model layer (Pa), and z_0 is the surface roughness length (cm), assumed to be one cm in the model. z_0 depends on the local geology of Mars and is effected by the distribution in size and space of rocks and debris on the surface. As a result, its values will depend on the exact latitude and longitude of the

area being studied. A value of one cm was chosen by observing the global map of surface roughness constructed by Hébrard et al. [2012] using MGS-TES data, displayed in Figure 6.6. Although highly variable in space, values close to one cm are roughly representative of most of the Martian surface.

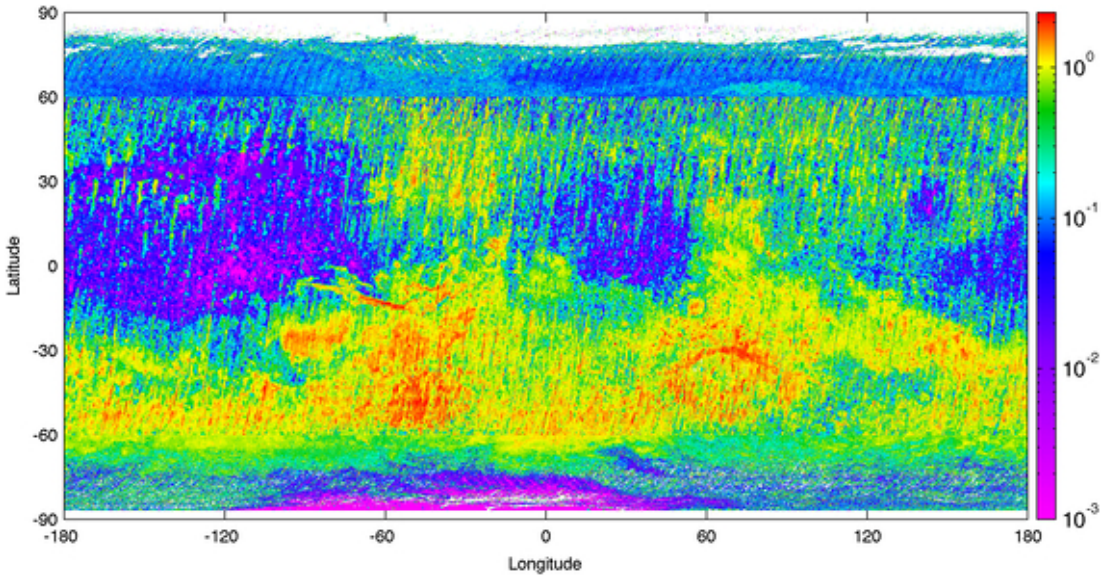


Figure 6.6: Surface roughness lengths (cm) as inferred from MGS-TES rock abundance data. Figure taken from Hébrard et al. [2012].

R_b is calculated by a method developed by Hicks et al. [1987], using the equation:

$$R_b = \frac{2}{\kappa u_*}\left(\frac{\mathrm{Sc}}{\mathrm{Pr}}\right)^{2/3}, \tag{6.16}$$

where Sc is the Schmidt number, the dimensionless ratio of the kinematic viscosity of air and the molecular diffusivity of the depositing gas species, and Pr is the Prandtl number, the dimensionless ratio of momentum and heat transport. For Mars' CO_2-based atmosphere a constant of 0.77 is used for Pr whereas Sc is calculated at each model timestep with the atmospheric physical parameters in the model. Finally, R_c for HCl is taken to be 0 for bare soil, but can rise to 100 for snow covered ground [Erisman et al., 1994].

The loss rate of HCl at the 1-D model's bottom layer due to dry deposition is then calculated through the equation:

$$L_{Dry,HCl} = \frac{V_{D,HCl}}{\Delta z}, \tag{6.17}$$

where Δz is the distance between the model's bottom layer and the surface ($\sim$ 4 m). The tendency of the HCl mmr can the be calculated as:

$$\Delta \mathrm{PQ}_{HCl,1} = \mathrm{PQ}_{HCl,1} \times \left(1 - \exp\left(-L_{Dry,HCl} \times \Delta t\right)\right). \tag{6.18}$$

I calculated R_a, R_b, $V_{D,HCl}$, and the resultant surface deposition rate of HCl across 11 discrete latitudes across the range [-75°,75°] in intervals of 15°, and across L_S values across the whole Mars year in intervals of 45° using the longitudinal mean meteorological boundary conditions of the MCDv5.3's standard climatology dataset. The results are presented in Figure 6.7. The rate of HCl deposition onto the Martian surface is greatest in the northern hemisphere during the northern autumn and winter (180–360°) L_S. Surface pressures in the northern winter in the 30–60° latitude band can reach upwards of 800 Pa, whereas southern surface pressures are lower, typically ranging between 400–600 Pa. This results in decreased wind friction velocities at the surface in the north, lowering both the turbulent and quasi-laminar layer resistances R_a and R_b, and consequently increasing the dry deposition velocity of HCl. Larger abundances below altitudes of 5 km could therefore be expected in the southern hemisphere of Mars during Mars' perihelion seasons.

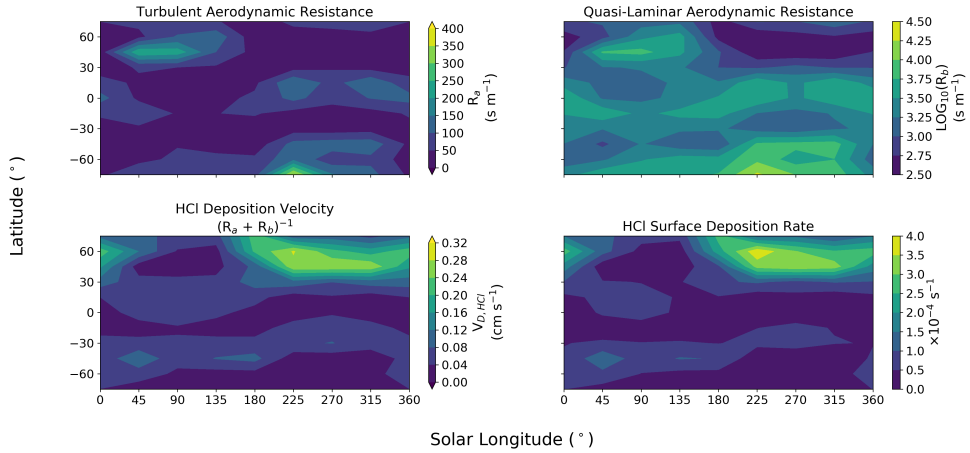


Figure 6.7: Turbulent and Quasi-Laminar layer resistances (R_a and R_b), HCl dry deposition velocities at the surface, and the resultant loss rate of HCl due to surface deposition as calculated by the 1-D model assuming a constant surface roughness of z_0 = 1 cm and bare soil (R_c = 0).

6.3 Chlorine Photochemistry from Heterogeneous Reactions

Here, I assess the photochemical products produced as a result of the new heterogeneous chlorine scheme in the 1-D model. To do this, I study the distributions of the chlorine species produced by the model at 20° north, 210° L_S. This is during peak dust-storm activity, and within the northern summer's autumn season where a small abundance of H_2O ice is present in the atmosphere. I spin the model up without any aerosols for 10 sols, at which point the aerosol profiles are inserted, and the model runs for 2 sols. I extract the profiles used to make Figure 6.8 on the second sol, allowing the model to perform photochemical calculations across one full sol.

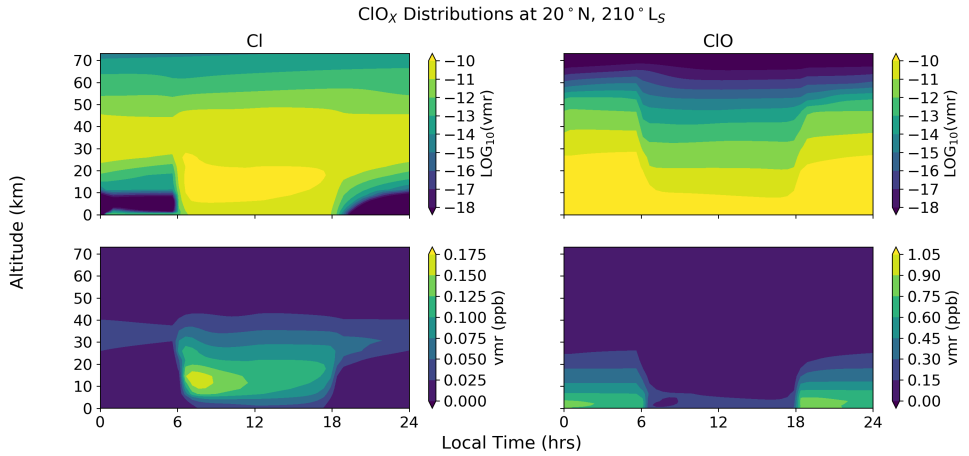


Figure 6.8: Diurnal variations of Cl and ClO at 20° north, 210° L_S, as modelled by the 1-D photochemistry model using the heterogeneous chlorine chemistry scheme. Upper row displays the vmrs in Log_{10} form, bottom row presents the vmrs with a linear colour scheme.

Figure 6.8 displays the diurnal variations of Cl and ClO that are produced by the heterogeneous chlorine scheme. ClO is an unstable compound when exposed to UV light, and photolyses to become O and Cl (reaction j_clo of Table 6.3). Below 10 km the rate of ClO photolysis decreases enough for vmrs of up to 150 ppt to develop, gradually lowering to sub-ppt levels at roughly 40 km in daylight. The conversion of ClO to Cl via UV photolysis results in Cl being the dominant ClO_x species in the day, reaching vmrs of 175 ppt between 10–30 km. At night, ClO becomes more stable and is produced at abundances between 0.75–1.05 ppb below 5 km, six times greater than Cl experiences at any time of the day. Reactions of Cl with inorganic tracers like O_3 and HO_2 typically result in the production of either ClO (reactions cl_1, cl_{10} of Table 6.2) or HCl (reaction cl_9), which are both more stable than Cl.

Figure 6.9 presents the diurnal variations of ClOO, OClO, ClCO, and Cl_2O_2 from the same model run at 20° north, 210° L_S. These were chosen together as they are typically handled via the simple exponential solution, detailed in Equation 6.11, as seen in Figure 6.2. OClO and ClOO are two unique compounds with identical chemical formulae but differing molecular

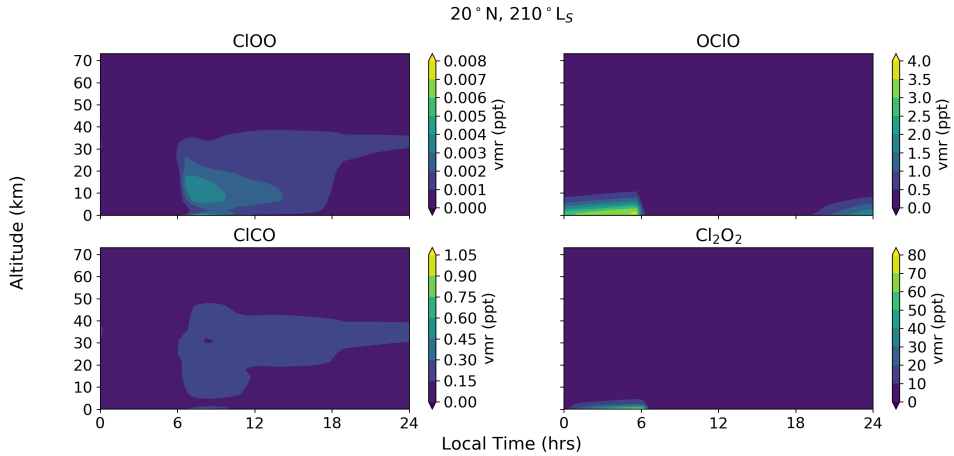


Figure 6.9: Diurnal variations of ClOO, OClO, ClCO, and Cl_2O_2 at 20° north, 210° L_S, as modelled by the 1-D photochemistry model using the heterogeneous chlorine chemistry scheme.

geometry. ClOO is primarily formed through the three-body reaction of Cl atoms with O_2 (cl_{28}, Table 6.2), whereas OClO is produced mainly through the slower self-reaction of ClO (cl_5). As such, their abundances are moderated by the distributions of Cl and ClO. As Cl atoms favour daylight, the accumulation of ClOO occurs mainly in daylight conditions. ClOO is unstable however, and can dissociate via reaction cl_{26}, as well as via UV photolysis (j_cloo of Table 6.3). The result of this is a very low abundance of ClOO on Mars, with magnitudes struggling to exceed 10^{-2} ppt. OClO does not dissociate as ClOO does, but it experiences photolysis rates an order of magnitude greater than ClOO. As it relies on ClO for formation, with minimum abundances seen during the day, it favours night time accumulation. As there is more ClO present below 10 km at night than there is Cl anywhere during the day, and the only efficient photochemical sink for OClO is reactions with O to produce ClO_3 (cl_{51}) or OH to form HOCl (cl_{58}), OClO can reach abundances below 5 km of $\sim$ 4 ppt prior to exposure to UV radiation that results in photolysis rates of 10^{-3} s^{-1} at the Martian surface that strips it down to ClO and O.

ClCO is produced via the three-body reaction of CO with Cl atoms (cl_{23}), and quickly again back to CO and Cl (cl_{33}). It therefore appears when Cl atoms are in high abundance, and favours production in the higher altitudes where CO exists in larger quantities due to the photolysis of CO_2. The relatively large quantity of CO in the Martian atmosphere allows Cl atoms formed between 10–40 km in daylight to produce ClCO at abundances between 0.15–0.30 ppt between 10–40 km. The largest ClCO abundances are found at the surface, when the ClO produced over the previous evening photolyses in the morning to produce a sharp rise in Cl atoms which can then engage reaction cl_3. When the sun drops below the horizon, the Cl converts to ClO cutting of ClCO production, and the abundances sharply drop to sub-ppt levels at night. C_2O_2 appears only very close to the surface below altitudes of 5 km. This is

unsurprising, as the production of Cl_2O_2 is only possible via the self-reactions of ClO (cl_6). It is a slow production method, only capable of yielding abundances of $\sim$ 60–80 ppt below 1 km over the course of the Martian night, before daylight comes and rapidly photolyses it back to Cl and ClOO (j_cl2o2 of Table 6.3). The resultant Cl atoms can then destroy any Cl_2O_2 that has avoided UV photolysis to produce Cl_2 and more ClOO. This formation of ClOO via the destruction of Cl_2O_2 can be seen in the plot for ClOO between 06:00–12:00 hrs at the model surface.

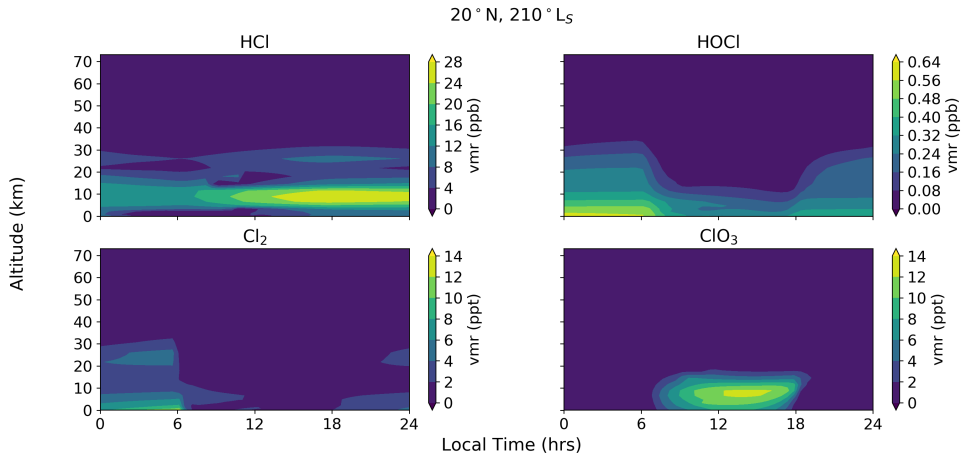


Figure 6.10: Diurnal variations of HCl, HOCl, Cl_2, and ClO_3 at 20° north, 210° L_S, as modelled by the 1-D photochemistry model using the heterogeneous chlorine chemistry scheme.

Figure 6.10 presents the diurnal variations of HCl, HOCl, Cl_2, and ClO_3, which Figure 6.2 shows are stable enough to be handled through either the SIBEM method or the simple exponential approximation. From the HCl distribution, it can be seen that the 1-D model calculates HCl to be produced with a layered vertical structure centred on altitudes between 10–20 km. This is in good agreement with the observations reported by Korablev et al. [2021] (Figure 6.1), however, the abundances are too high in the 1-D model by a factor of $\sim$ 10. This can be attributed to the hindrances that arise in 1-D models from the absence of a loss due to the neglecting of horizontal transport, as well as assumptions and simplifications made to the heterogeneous chlorine scheme. The HCl profiles of Figure 6.2 start after one full sol of calculations is performed. Over this time, no HCl loss to horizontal transport is considered, and the heterogeneous chlorine scheme does not calculate the abundance of Cl contained in dust, so that the dust profiles in the model are a constant and inexhaustible source of Cl and ClO. Further, the reaction rates h_{cl1} and h_{cl2} assume that for every OH and HO_2 atom adsorbed onto a dust grain, one ClO_x particle is released. The next step for the heterogeneous chlorine scheme prior to use in full 3-D GCM models would be to accommodate the reaction rates for the HO_x compounds chemical reactions within the mineral dust grains. The 1-D model's chlorine scheme due to these restrictions is therefore more suited for the modelling of short lived transient events, such as the traversing of aerosol clouds over a few hours, with regards

to HCl profiles. The formation of HCl over short timescales (< 6 hours) and profile comparisons to observations made by the ACS-MIR [Korablev et al., 2021] from the heterogeneous chlorine scheme using dust and ice profiles measured by the ACS-TIRVIM [Luginin et al., 2019] and H_2O vapour profiles from the ACS-MIR [Fedorova et al., 2020] will be described in more detailed in Section 6.4.

HOCl is very unstable under UV radiation, with photolysis frequencies $\sim 10^3$ times greater than HCl (Table 6.3). As a result, HOCl reaches its maximum vmr of 0.64 ppb towards the end of the evening. It is produced predominantly via reaction cl_{13} (Table 6.2), the reaction of HO_2 with ClO, and is efficiently destroyed by OH and Cl (reactions cl_{15} and cl_{55} respectively). As a result, the HOCl diurnal profiles adopt the same shape as ClO from Figure 6.8. Abundances are $\sim$ 600 ppt in the lower 5 km and steadily fall to sub-ppt levels at 30 km during the evenings, and when daylight comes the surface values fall to $\sim$ 300 ppt and reach sub-ppt levels between 10–20 km. HOCl has absorption features within the ACS-MIR's spectral range of 2.3–4.2 μm within the HITRAN spectral database, commonly used in the retrieval algorithms of the TGO equipment to infer trace gas abundances from their spectrographic records [Robert and et. al, 2016, Rothman et al., 2009]. HOCl transmission line intensities, centred on $\sim$ 2.77 μm, are significantly less than those of HCl, implying that for HOCl to be observable to the ACS-MIR channel it will need to exist in abundances greater than HCl. The caveats of the 1-D model approach addressed in the preceding paragraph will also apply to the HOCl profiles, meaning that loss to winds and the depletion of the dust's Cl content could result in even smaller abundances than 0.64 ppb from developing. With that in mind, my calculations suggest that HOCl will not be observable by either the ACS or NOMAD spectrometer suites of the TGO.

Cl_2 reaches magnitudes of 10 ppt below 5 km during the evenings. It has photolysis rates up to 10 times greater than those of HOCl (j_cl2, Table 6.3), and is almost completely removed from the atmosphere shortly after daylight appears. It is produced mainly through the self reactions of ClO (reaction cl_{13}), and the strongest chemical sinks during the day are $O(^1D)$ and OH (reactions cl_{35} and cl_{36}). The resultant diurnal variations mirror those of ClO, but the production reactions are not very efficient and struggle to yield anything greater than 14 ppt during the evening. ClO_3 displays a different trend to HOCl and Cl_2 in the sense that it favours daytime conditions. The primary source for ClO_3 in the 1-D model is the three-body combination of Cl atoms and O_3. The reaction itself (cl_{44} of Table 6.2) is slow however, and the main destructive sinks of OH and ClO molecules (cl_{48}–cl_{50} and cl_{45}–cl_{47} respectively) prevent significant quantities from developing. During daylight, OH converts ClO_3 to $HClO_4$ and suppresses ClO_3 production, whereas at night the increased abundance of ClO below 5 km converts the ClO_3 made during the day to Cl_2O_4. With the decreased quantity of Cl at night too there is a negligible production of ClO_3 during the night.

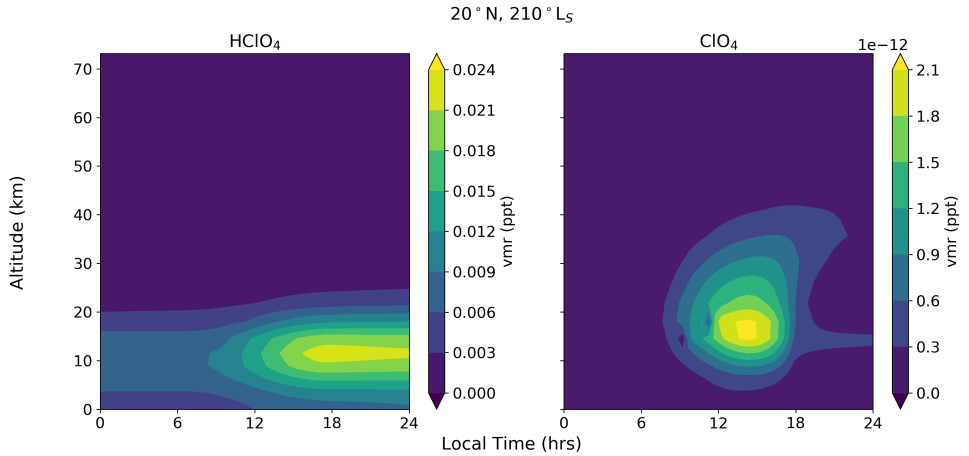


Figure 6.11: Diurnal variations of $HClO_4$ and ClO_4 at 20° north, 210° L_S, as modelled by the 1-D photochemistry model using the heterogeneous chlorine chemistry scheme.

The atmospheric production of $HClO_4$ was considered by Catling et al. [2010] as a means of explaining the ClO_4^- abundances seen in the soil of the Atacama desert on Earth, and also considered as a means for the production of the ClO_4^- observed by the Phoenix Lander on Mars [Hecht et al., 2009b]. The 1-D model developed by Catling et al. [2010], from which I extracted the ClO_4^- chemistry mechanism (i.e. reactions cl_{48}–cl_{54} of Table 6.2), found that the production and surface deposition of $HClO_4$ in the dry atmosphere of the Atacama desert was a feasible means of producing Atacama's ClO_4^- soil content. They also concluded that more work needs to be done in laboratories to constrain the rate coefficients of reactions cl_{44} and cl_{49}, specifically noting that a decrease by a factor of 30 is required for the model HCl, ClO and HOCl profiles to coincide with observations above the Atacama. My model utilises these rate coefficients, lowered by the factor of 30. Figure 6.11 presents the vmr of $HClO_4$ and ClO_4^- after 1 Mars sol with the heterogeneous chlorine scheme active. $HClO_4$ is stable under UV conditions and has no chemical sinks in the model, but despite this stability the production via atmospheric chemistry is very slow on Mars. The atmospheric production of ClO_4 itself is entirely negligible. $HClO_4$ is produced from reactions of ClO_3 with OH (cl_{48} and cl_{49}). The most efficient path is through three-body reactions with OH (cl_{49}), which is 10^3 times more efficient than the bi-molecular route (cl_{48}). The dependence of $HClO_4$ production on ClO_3 means that it is produced in daylight when ClO_3 forms its layer between 5–10 km (Figure 6.10), and would then be deposited to the surface. The maximum vmr reaches a small maximum of 2.4×10^{-2} ppt after 1 sol, and can therefore be regarded as inconsequential to the atmospheric chlorine cycle. However, future studies with 3-D GCM's should treat $HClO_4$ and include a surface deposition or aerosol adsorption routine to assess the amount of ClO_4^- deposited to the soil from these small $HClO_4$ abundances produced from the heterogeneous chlorine routine.

Tracer species such as Cl_2, HOCl, and $HClO_4$ omitted from the dry deposition schemes will tend to have larger abundances below altitudes of roughly 10 km than modelled in this study. However, as seen in Figures 6.10 and 6.11 these abundances are significantly lower than those of HCl. Ignoring their surface deposition in the 1-D model will impact the rate of chlorine being adsorbed back into the Martian soil, but can be expected to have little impact on the vertical distribution profiles of HCl itself. A proper treatment of the chlorine content in the Martian soil in 3-D GCM models will require the inclusion of the surface deposition of additional Cl-species.

6.4 HCl from Heterogeneous Interactions

To study the potential of a heterogeneous chemistry scheme being responsible for the HCl profiles observed by the TGO [Korablev et al., 2021, Olsen et al., 2021, Aoki et al., 2021] I use my model to study two scenarios in an effort to reconcile my 1-D model's HCl profile with those detailed in Korablev et al. [2021].

The first scenario uses dust and water ice mass loading profiles that were observed by the ACS-TIRVIM during MY34–35 by Luginin et al. [2019], as well as H_2O vapour profiles observed during the MY34 dust-storm by the ACS-MIR in Belyaev et al. [2021]. The observations of the TIRVIM (aerosols) and MIR (H_2O and HCl) channels do not occur simultaneously - it was therefore necessary to find aerosol profiles that roughly coincide with the observations of HCl and H_2O. To do this, I developed a simple cost-function made of the differences in the MIR and TIRVIM observations' temporal parameters, i.e. solar longitude, local time, latitude, and Mars longitude. The TIRVIM aerosol profile producing the smallest temporal cost-function, with the requirements that neither latitude nor solar longitude deviate from the MIR HCl observation by $\pm$ 5°, is used for the respective HCl observation. A total of 77 HCl profiles were found with roughly coinciding aerosol and H_2O observations, with the model situated at the latitude and L_S of the ACS-MIR HCl observation.

The aerosol mass loadings are provided in units of g/cm^{-3}, which are converted to mass mixing ratio by division with the total atmospheric density (a function of time and location in the model). The geometric radii of dust and ice particles is taken from the MCD v5.3's standard climatological run. For dust, a constant profile is assumed from the lowest observed point by the ACS-TIRVIM to the model surface, and from the highest observed point to the model ceiling ($\sim$ 75 km) the dust loading is assumed to be 0 across the chemistry timestep (600 seconds). For ice, model altitude points lying outside of the ACS-TIRVIM grid are set to 0. For H_2O vapour, model altitude points outside of the ACS-MIR grid are set to the value at the ACS-MIR altitude boundaries. The second scenario makes use of aerosol and H_2O vapour profiles from the MCDv5.3's standard climatological run. Over two Mars years, Aoki et al. [2021] noted

that the appearance of HCl is a seasonal event that is independent of dust storm activity. This scenario, representative of a standard climatological mean Mars year, will address whether or not the heterogeneous scheme is capable of producing HCl at abundances observable to TGO instrumentation ($\sim$ 1 ppb) outside of significant dust events.

Both scenarios are modelled identically. The model is initialised with 0 ppb for all chlorine tracers, and 20 ppt of CH_4 as per the most recent upper limits inferred by the TGO [Knutsen et al., 2021], with all non-methane VOC's intialised to 0 ppb. The model uses MCDv5.3 vmr profiles of CO_2, CO, O_2, and H_2 held at a constant (as is H_2O vapour in the climatological runs), as well as physical atmospheric parameters as detailed in Chapter 3, without considerations of diurnal variances - the local time the model uses is that of the HCl observation it is studying. The model is also initialised at the latitude and solar longitude of the observation made by ACS-MIR, and is allowed to spin for 10 sols without any dust or water ice to enable adequate mixing of reactive O_x and HO_x species. After 10 sols, the aerosol profiles are inserted, and HCl profiles are extracted 6 hours (12 model timesteps) later. A timescale of 6 hours was chosen as it represents a brief transient event like the passing of an aerosol cloud.

6.4.1 HCl Profile Comparisons

Figure 6.12 and 6.13 present eighteen of the studied profiles and their coincidences with the ACS-MIR HCl profiles using the ACS-TIRVIM aerosol and H_2O runs. The remaining 59 HCl profile comparisons are presented in the appendix of this work, Figures B.1–B.7, the majority of which display strong coincidences with the ACS-MIR HCl observations. Immediately, it can be seen that the heterogeneous chemistry routine in the 1-D model reproduces the observed layered structure of HCl very well. Similarly, the abundances calculated by the 1-D model are in close coincidence with those seen by the ACS-MIR in Korablev et al. [2021]. Water ice clouds in altitudes above 40–km exist in very cold regions, where the atmospheric temperatures can dip to values as low as 150 K. From Figure 6.5, the temperature dependent uptake coefficient of HCl on ice reaches a maximum in these regions, enabling the high-altitude water ice clouds to become a strong heterogeneous sink for Mars' atmospheric chlorine. Dust, however, tends to be confined below 30–km but there are sporadic appearances of high-altitude dust clouds Luginin et al. [2019]. H_2O vapour, capable of reaching higher-altitudes due to the temperature increases caused by the suspended dust during dust-storms [Maltagliati et al., 2011], increases the abundance of HO_x species available to initiate the heterogeneous reactions h_{cl1} and h_{cl2} to produce ClO_x. The vertical structure of H_2O ice and dust produces a window in the 1-D model ranging between $\sim$ 15–40 km where HCl formed via the cascade of Cl-chemistry can exist without being removed from adsorption processes. The additional HO_x in these regions produced by the elevated H_2O vapour at high altitudes is lost in the adsorption processes, easing the strength of the atmospheric chemical sink of HCl.

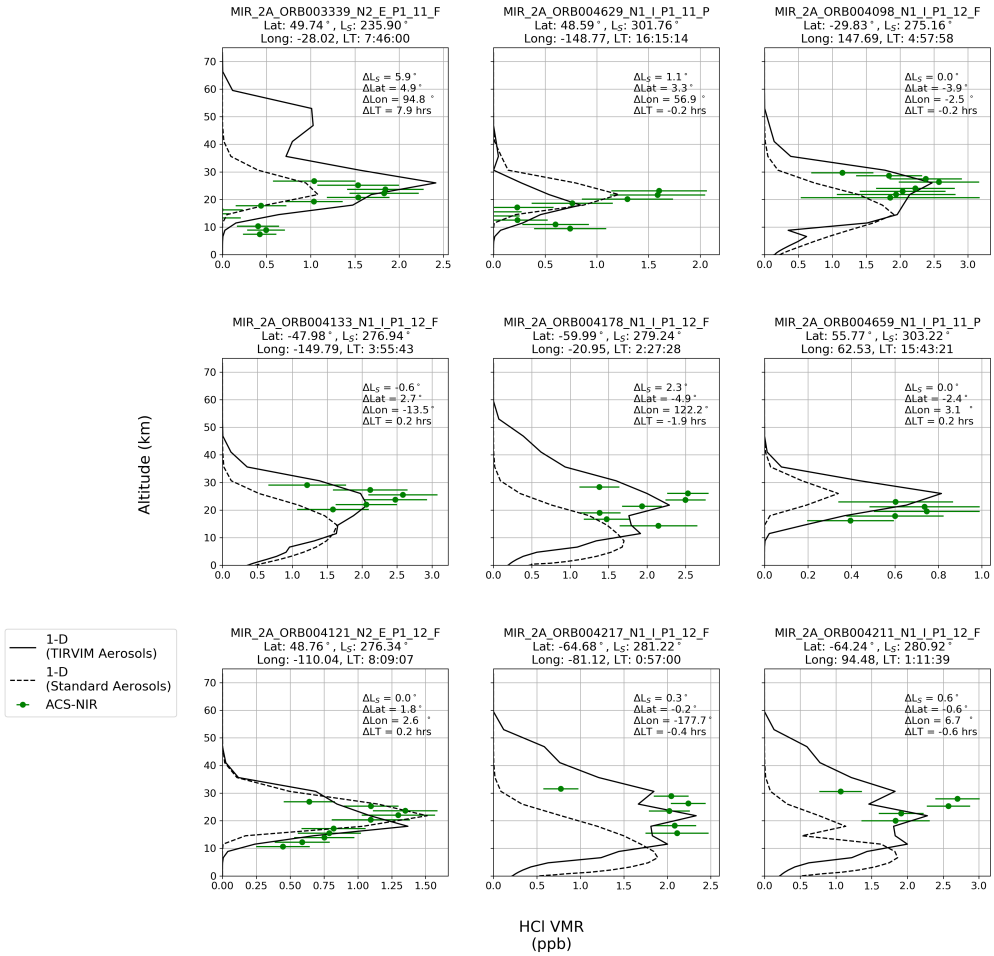


Figure 6.12: HCl profiles produced by the 1-D photochemistry model through the heterogeneous chlorine chemistry routine using standard climatological aerosol and H_2O vapour profiles (dashed lines) and ACS-TIRVIM and MIR observed aerosol mass loadings and H_2O vapour profiles (solid lines) and their coincidences with the HCl observations performed by Korablev et al. [2021]. Subplot title indicate parameters of the ACS-MIR HCl observation, and the in-plot text denotes the differences with the ACS-TIRVIM aerosol profiles solar longitude (ΔL_S), latitude (ΔLat), longitude (ΔLong), and local time (ΔLT).

To assess where the 1-D model is performing well with regards to planet latitude and solar longitude when compared to the ACS-MIR HCl profiles, I calculate the partial column abundance of HCl observed by the TGO and compare it to the column abundance calculated by the 1-D model. To construct the partial column abundances, I first interpolate the ACS-MIR profile onto the 1-D model altitude grid, and calculate the column abundance (molecules cm^{-2}) contained in the altitude region where ACS-MIR observations where made using the 1-D model pressure and temperature profiles. I then divide by the partial column density of the atmosphere in this

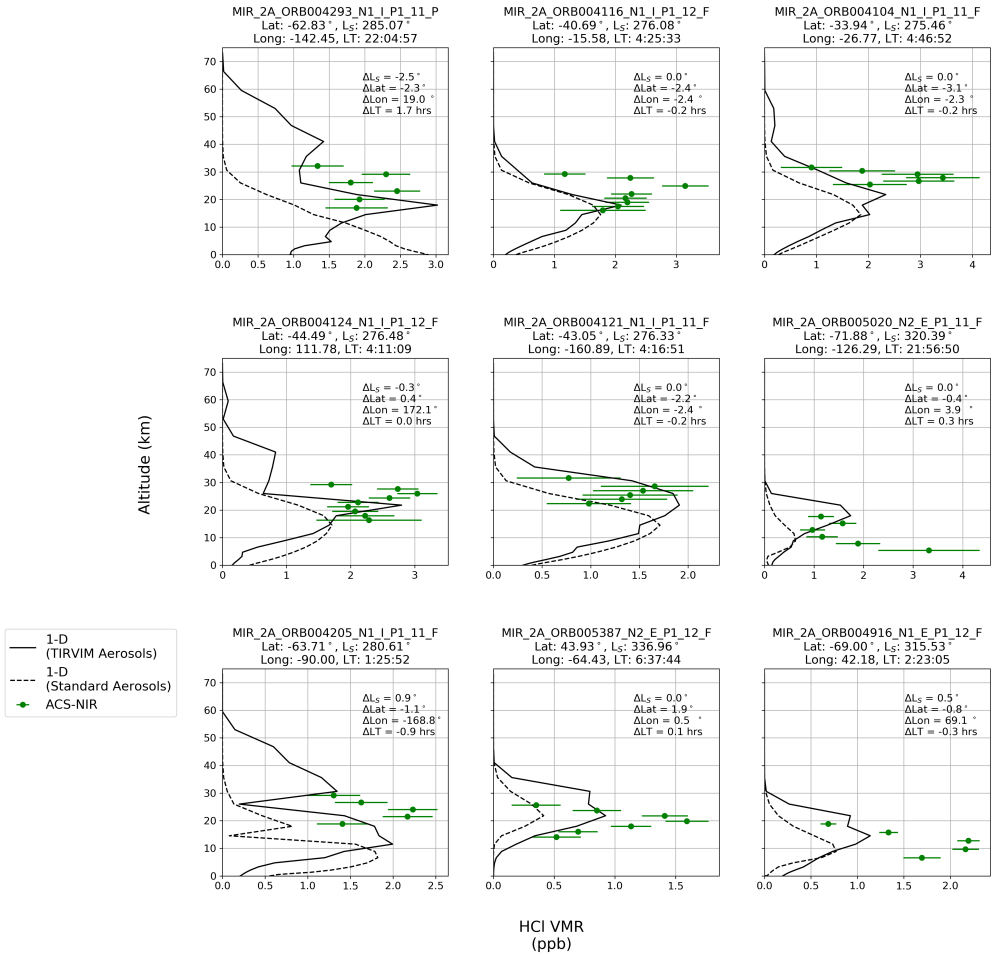


Figure 6.13: Similar to Figure 6.12.

same region to produce a vmr. I do the same for the 1-D model, calculating the HCl vmr of the region where HCl observations were made. Figure 6.14 presents these calculations. The largest differences between the 1-D model and the observations from ACS-MIR appear in the deep southern latitudes between 305–325°L_S, where the maximum values are seen to appear [Aoki et al., 2021]. The 1-D model columns are in good agreement with the observations of Korablev et al. [2021], with maximum differences of less than 3 ppb. The trend of the 1-D model also matches the trend of the observations in Figure 6.14, where observations in the high northern latitudes are typically the lowest, with slight elevations appearing just after 270°

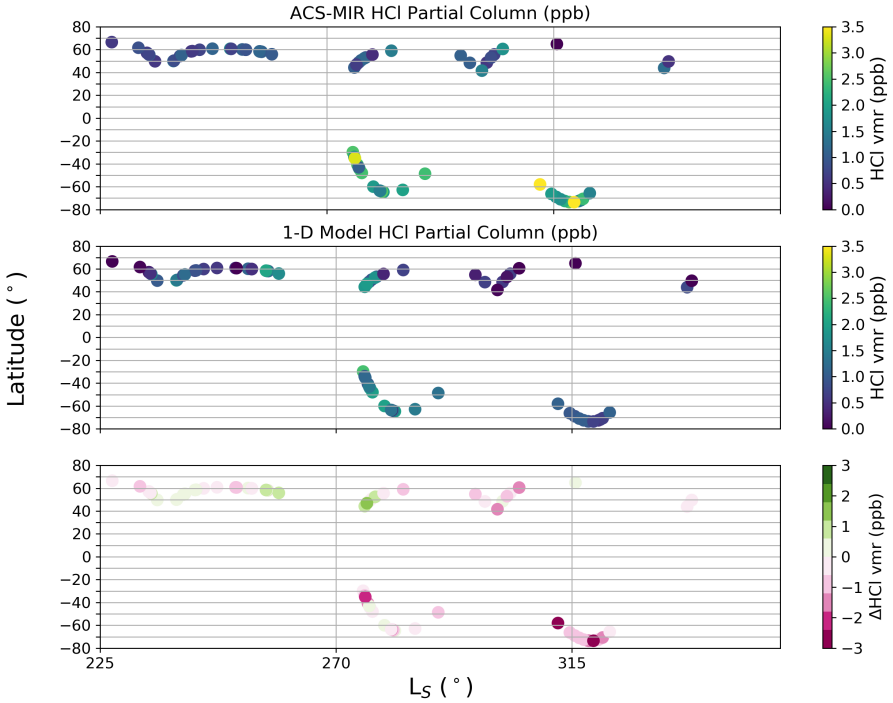


Figure 6.14: Partial column vmr of HCl observed by the ACS-MIR (top) and those modelled by the 1-D photochemistry model using the heterogeneous chlorine scheme with ACS-TIRVIM observed ice and dust profiles and ACS-MIR H_2O vapour profiles.

L_S. Values in the southern hemispere from 270°–300° also display good coincidence with the observations, but the larger spikes seen by ACS-MIR are not matched by the 1-D model. The model produces too much HCl only on occasion in the northern hemisphere, whereas the model generally has a negative bias in the southern hemisphere.

Figure 6.15 presents the rates of production and loss in molecules cm^{-3} s^{-1} for HCl in two of the 77 ACS-MIR HCl profiles reproduced by the 1-D model using ACS-TIRVIM aerosol profiles and heterogeneous chlorine chemistry. In contrast to gas-phase chemistry (Figure 6.3), the most effective HCl sink in the atmosphere is now adsorption onto H_2O ice, which can become upwards of 10^2 times more efficient at removing HCl than photolysis. This has the effect of lowering the column lifetime of HCl in the 1-D model from greater than 600 sols in the southern hemisphere to timescales of $\sim$ 20 hours. This strong uptake of HCl onto H_2O ice particles is thus a good explanation for the fast disappearance of the HCl observed by the TGO. The formation of the layer of HCl is driven by the reactions of Cl atoms with HO_2 and H_2. The abundances of Cl is controlled by the dust profile, which are in a layered structure as observed by ACS-TIRVIM centred on altitudes between 15$\sim$30 km. The water ice particles

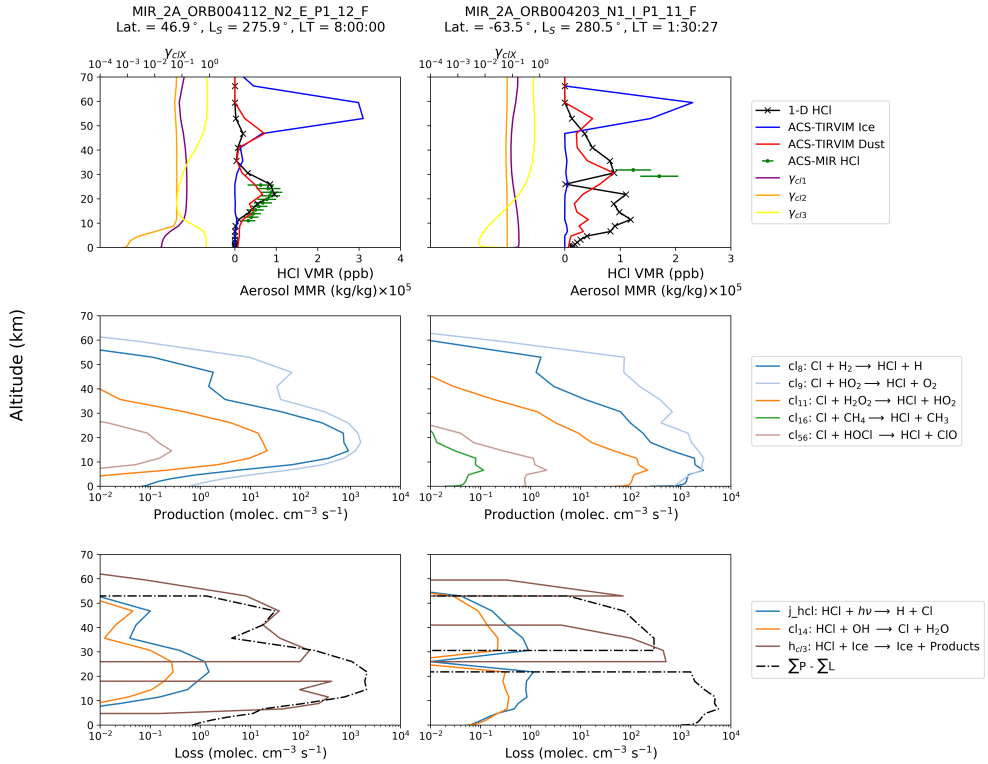


Figure 6.15: Reaction rates involving the production and loss of atmospheric HCl for two ACS-MIR observed profiles [Korablev et al., 2021] when dust and water ice profiles from ACS-TIRVIM are used in the 1-D photochemistry model. Heterogeneous reactions involved in producing ClO_x and adsorbing HCl are included. γ_{cl1} : OH + Dust $\longrightarrow$ ClO_x; γ_{cl2} : HO_2 + Dust $\longrightarrow$ ClO_x, γ_{cl3} : HCl + Ice.

are typically found at higher altitudes, from 40$\sim$60 km, which reinforces the layered structure of HCl by preventing it accumaliting at higher altitudes. The regions favouring ice growth due to the colder temperatures also results in increased temperature dependent uptake coefficients of HCl onto water ice, as per Figure 6.5.

6.4.2 HCl Adjoint Sensitivities

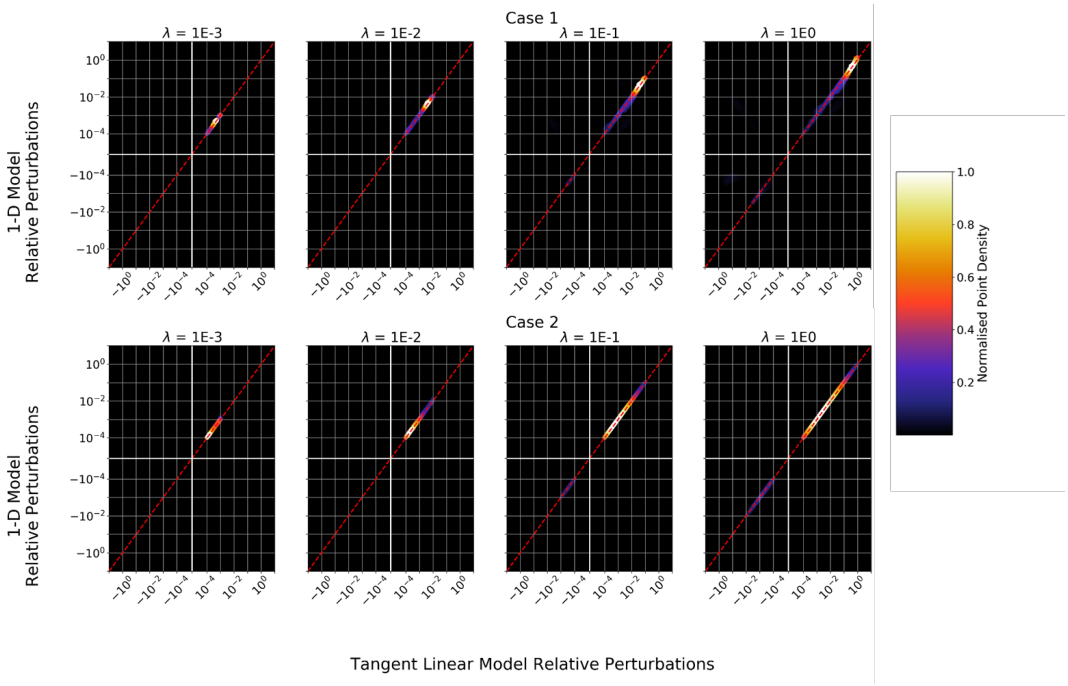


Figure 6.16: Comparisons of the relative perturbations made to a control state in the 1-D model (Equation 5.17) as calculated via the full non-linear 1-D photochemistry model and their approximations from the TLM (Equation 5.10). Both cases include chlorine chemistry, with 31 tracers in total considered, and perturbations are recorded over three sols (144 model timesteps).

I have adapted the TLM code, detailed in Chapter 5, to accommodate tracer support for chlorine compounds and dust and H_2O ice aerosols. With additional chemical species and reactions, the accuracy of the TLM needs to be reassessed performing the same method as that of Chapter 5 (Figure 5.3). I perform two case studies to assess how accurate the TLM with chlorine chemistry is at modelling perturbations, and these are displayed in Figure 6.16. The two cases studies run over three sols here to demonstrate that the TLM maintains accuracy for significant periods of time making it a valuable tool to study the sensitivities of tracers with short lifetimes. Case one has the control run operating at 0° north, 270° L_S, with no heterogeneous chemistry active and the model initialised with 1 ppb of HCl. The model spins up for 10 sols prior to the three sols studied to enable the column to be well mixed. The 1-D model then has HCl perturbed at the first output timestep by a range of magnitudes, λ in Equation 5.18, between 10^{-3}–10^{0}. Case two moves the model to 65° north at 210° L_S and includes the heterogeneous uptake of OH, HO_2, and HCl on ice particles and the release of ClO_x via OH and HO_2 uptake on dust particles. The correlation coefficient, R, the gradient of the linear line of best fit, m, and the total number of perturbations across the runs, N, of these two cases are listed in Table 6.5.

Table 6.5: Results of the comparisons of the TLM approximated and 1-D model calculated relative perturbations to a 1-D model control run with chlorine chemistry active.

Initial Pertubation Magnitude (λ)	Correlation Coefficient (R)	Gradient of Linear L.o.B.F (m)	Number of Perturbations (N)
Case 1			
0° N, 270° L_S			
HCl, Layers 7–9 (1.31–3.25 km)			
Gas Phase Chemistry Only (HCl initialised at 1 ppb)			
λ	R	m	N
10^{-3}	0.990	1.034	9144
10^{-2}	0.973	0.992	11542
10^{-1}	0.796	0.750	13956
10^{0}	0.764	0.846	16054
Case 2			
60° N, 210 L_S			
HCl, Layers 16–19 (21.79–35.61 km)			
Gas Phase + Heterogeneous Chemistry (HCl initialised at 1 ppb)			
10^{-3}	0.980	1.062	793
10^{-2}	0.926	1.006	3442
10^{-1}	0.999	0.995	7286
10^{0}	0.999	0.990	11690

It can be seen immediately that the TLM approximation is very accurate for the 1-D photochemistry submodule that includes chlorine chemistry, with and without the presence of heterogeneous interactions with dust and H_2O ice. Accuracies are better (R and m closer to 1) in the higher altitude perturbations of case 2 due to the highly non-linear turbulent transport processes below the planetary boundary layer ($\sim$ 10 km). This causes the ignored higher order terms of the Taylor expansion to become non-negligible quicker than in the higher altitudes that experience smoother laminar transport processes. The TLM also cannot account for changes in photolysis rates due to changes in O_3. This is due to the photolysis routine in the 1-D model being handled via an interpolation procedure from an offline dataset that is not possible to account for in the TLM matrix. This could be expected to greatly hinder the TLM approximation due to the highly reactive nature of Cl chemistry with O_3, the TLM I have developed remains accurate. I chose not to include CH_4 oxidation in the model in this section. This is because the initial concentration of CH_4 being used, 20 ppt in line with the most recent upper limits [Knutsen et al., 2021], yields inconsequential abundances of oxidised organic products (< 10^{-2} ppt). As the adjoint model is based upon a first-order Taylor series expansion, the model is adept at considering perturbations of magnitudes equivalent to the magnitudes of the control run. Larger perturbations however cause the ignored higher order terms to become non-negligible, greatly lowering the adjoint accuracy. Therefore, the addition of the 11 non-methane VOCs will only serve to increase the computational expense of the TLM calculations without yielding any informative data.

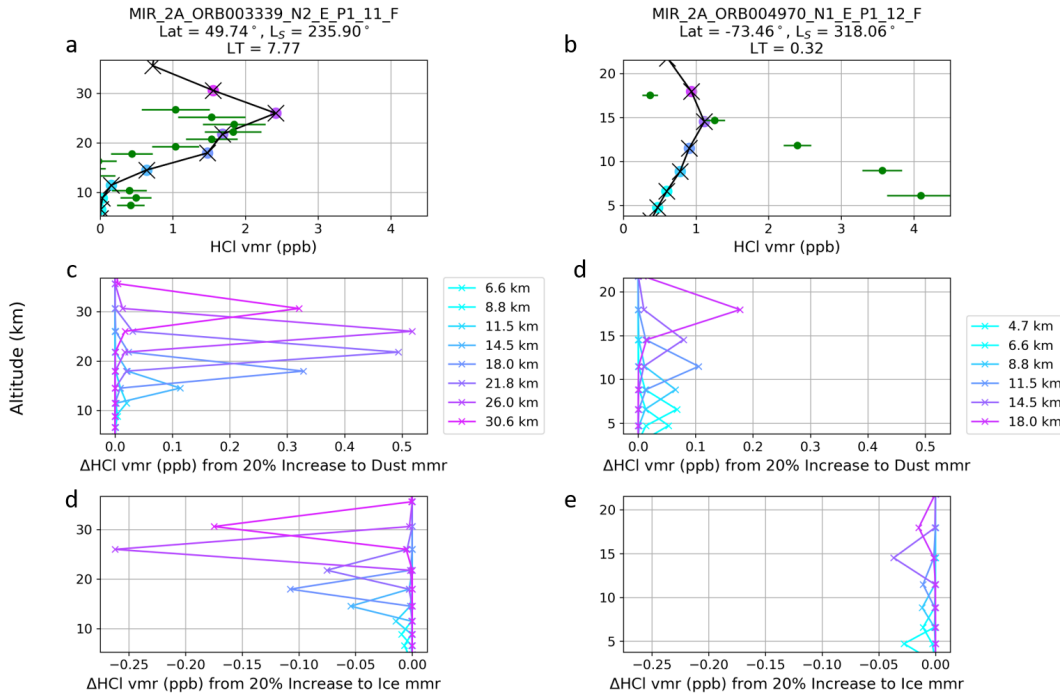


Figure 6.17: (a-b) 1-D model HCl profiles and observations made by the ACS-MIR. (c-d) Change experienced in the 1-D model HCl abundances (ppb) at each layer resulting from a 20% increase to dust mmrs 6 hours prior as calculated by the adjoint. (e-f) Change experienced in the 1-D model HCl abundances (ppb) at each layer resulting from a 20% increase to H_2O ice mmrs 6 hours prior as calculated by the adjoint

Here I use the 1-D photochemical adjoint to assess the sensitivity of the 1-D model's HCl profiles to the ACS-TIRVIM aerosol profiles. I use the adjoint to study two of the HCl observations made by the ACS-MIR, and calculated the sensitivity of the model's HCl vmr (mol/mol) in the altitude range where ACS-MIR observations were made with respect to the mmr (kg/kg) of the aerosols six hours (12 model timesteps) prior. The sensitivities are shown in Figure 6.17, with the x-axis displaying the change in HCl vmr calculated by the adjoint that would result from a 20% increase in the dust and ice mmrs observed by the ACS-TIRVIM. Two profiles include an HCl observation in the north (49.74° latitude) at 235.90° L_S, the second at higher southern latitudes (-73.46°) at 318.06° L_S. In the northern study, the adjoint finds that the HCl profiles are highly sensitive to the dust profile between 20–30 km, with 20% increases in dust mmr (kg/kg) resulting in 0.5 ppb increases in HCl vmrs (mol/mol), and less so below 20 km, with smaller changes of < 0.2 ppb occuring. The strongest dust sensitivities in the southern study are found between 15–20 km, which are weaker than those in the north with maximum changes from a 20% dust mmr elevation resulting in HCl changes of 0.18 ppb, and < 0.1 ppb below 15 km. These sensitivity differences between the north and south study are due to the

water vapour content in the model at these latitudes at different points in time. In the north, H_2O vapour is most abundant between 20–40 km, increasing the amount of OH and HO_2 available for absorption reactions with dust between 20–30 km. In the south at 318° L_S, H_2O vapour is at a maximum between the surface and $\sim$ 20 km. The dust content, observed by ACS-TIRVIM, below 20–km is larger in the northern study than that used in the southern study by a factor between 5–10. There is also no dust observed in the southern study above 20 km, whereas the northern study has a dust profile extending to 45 km. The response to a 20% elevation in dust in the south therefore has less of an impact on HCl than a 20% elevation in the northern study.

Similarly for ice, the northern hemisphere study of Figure 6.17 displays strong negative sensitivities to ice between 20–30 km, where a 20% increase in ice mmr can return a decrease in HCl of 0.26 ppb, which steadily falls to values < 0.05 ppb below 15 km. The southern hemispheres HCl profile however is much less sensitive to H_2O ice, with 20% elevations only decreasing HCl by < 0.05 ppb below 20 km. This is due to differences in the ice content of the atmosphere of the two runs. In the south, temperatures are higher as the southern hemisphere is orientated facing the sun at 318°, so less ice is available below 20 km onto which HCl could absorb. In the north however, temperatures are significantly colder as the hemisphere is in the middle of the fall season, and ice develops in larger abundances at higher altitudes. A 20% increase to ice in the north therefore impacts the HCl profile significantly more than a 20% increase to ice in the south as it represents a larger absolute amount in the north.

In Figure 6.18, I expand the sensitivity study with the photochemical adjoint to all 77 of the 1-D model/ACS-MIR HCl comparisons. I assess the maximum change to a HCl concentration caused by a 20% change to inorganic tracers and aerosols below model altitudes of 30 km as calculated via the adjoint approach. The sensitivities of HCl profile vmrs to the inorganic tracers (CO, O_2, H_2, H_2O vapour, H_2O_2, and O_3) are with respect to the initial inorganic tracer concentrations at the start of the model's two sol spin-up. Constant MCDv5.3 profiles of CO_2, CO, O_2, and H_2, and ACS-MIR profiles of H_2O vapour were used in the HCl profile calculations of Figures 6.12–6.13 and Figures B.1–B.7, causing their TLM matrices (Equation 5.9–5.10) to become the identity matrices, i.e. perturbations to the initial tracer vmrs of these species made at the start of the spin-up will remain constant throughout the spin-up. The sensitivities to dust and ice aerosols are with respect to the dust and ice mmrs observed by the ACS-TIRVIM, which are inserted after the two sol spin-up and held constant for 6 hours (12 model timesteps). The HCl profile sensitivities to dust and ice are therefore to the dust and ice mmr's 6 hours prior to the time of the HCl profiles.

From Figure 6.14, the strongest discrepancies between my model's HCl columns and those observed by ACS-MIR [Korablev et al., 2021] occur in the southern hemisphere. These discrepancies occur in two clusters, found between 270–295° L_S (which I shall refer to as cluster A here) and 310–330° L_S (referred to as cluster B). The 1-D model under-calculates the HCl

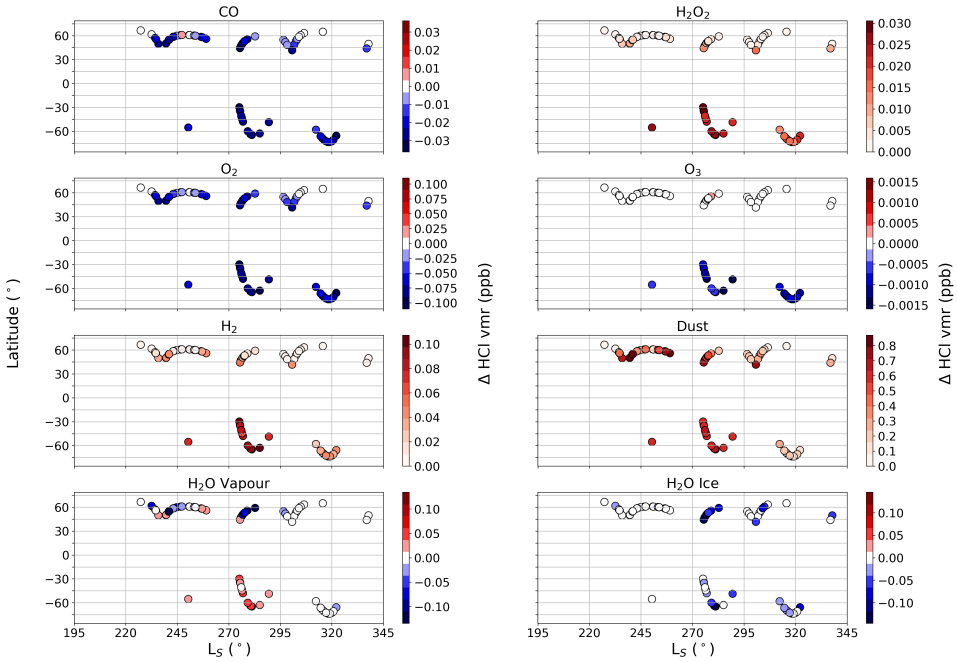


Figure 6.18: Maximum changes to the HCl profiles of Figures 6.12,6.13, and Figures B.1–B.7 (Δ ppb) caused by a 20% change to the initial inorganic tracer concentrations of the 1-D model.

abundances in both clusters, episodically in cluster A but more generally in cluster B. The HCl observations of cluster A are found, through the adjoint approach, to be significantly more positively sensitive to H_2 abundances below 30 km than elsewhere. Increase of 20% to H_2 vmrs here can elevate the HCl profiles by 0.1 ppb, whereas in observations in the northern hemisphere, and in southern cluster B, these impacts lower to values < 0.04 ppb. H_2O_2 displays a similar effect, but with smaller impacts on HCl than H_2, with maximum increases of HCl from a 20% increase in H_2O_2 only reaching 0.03 ppb in south cluster A, < 0.002 in south cluster B, and < 0.005 across the northern hemisphere. HCl sensitivities to the ACS-TIRVIM observed H_2O vmr profiles display a unique behaviour. Large positive sensitivities (20% changes to H_2O vmrs below 30 km increasing HCl by 0.15 ppb) are experienced in south cluster A observations, but almost no sensitivity to the profile in south cluster B. This can be explained by the seasonal sublimation of the south pole's water ice. The sublimation from the south reaches a maximum between 270–295°, causing large increases in the H_2O vapour content below 30 km. After 295°, the H_2O vapour sublimation in the southern pole starts to

weaken, and the H_2O vapour in the south is dispersed across the equatorial latitudes, lowering the content below 30 km in the south. H_2, H_2O vapour, and H_2O_2 supply the atmosphere with HO_2 and OH that proceed to adsorb onto dust and release ClO_x in the model, explaining the tendency of their sensitivities to be positive.

The model HCl profiles are negatively sensitive to H_2O vapour in the northern hemisphere in the 1-D model. This is not intuitive as we would expect the provider of HO_x to the atmosphere to increase the rate of ClO_x release from OH/HO_2 absorption. Increases of 20% of H_2O here however tend to lower the HCl abundances by 0.05–0.15 ppb. Interestingly, these negative sensitivities appear only for HCl observations taken in daylight conditions. The exposure of H_2O to sunlight increases the production of OH radicals, which increases the loss rate of HCl (reaction cl_{14}), and also provides an increase in $O(^1D)$ content, further increasing HCl's chemical sink strength (reaction cl_{39}). These two loss processes in the northern hemisphere during daylight in summation are greater than the increased production of HCl coming from the absorption of OH onto dust releasing ClO_x.

HCl sensitivities to O_3 in Figure 6.18 are low throughout the dataset I have studied, with maximum changes to HCl from a 20% O_3 increase below 30 km occuring in the southern hemisphere (-Δ1.5 ppt). These are very low, and we can expect O_3 to have very little impact on the HCl observations made by the ACS-MIR. HCl is calculated to have much larger, and almost entirely negative, sensitivities to O_2 across all latitudes throughout the dust-storm period. 20% increases to O_2 commonly result in 0.1 ppb decreases to HCl vmrs in the 1-D model. Increasing the O_2 content below 30 km has the net effect of increasing the O_3 abundances due to the three-body recombination reaction of a_1 in Table 3.2. 20% elevations to O_2 can result in large increases in O_3. These O_3 increases react with HO_x compounds, decreasing the rate at which heterogeneous rates h_{cl1} and h_{cl2} can release ClO_x, thus lowering the HCl profiles at the time of observation. 20% increases in CO can also lower HCl abundances below 30 km, with maximum HCl decreases reaching only -0.03 ppb. These decreases arise from the consequent decrease in OH from reactions with the excess CO (reaction e_1 of Table 3.2), again lowering the rate of ClO_x release from dust, and decreasing the HCl abundances at the point of observation.

HCl sensitivities to dust are very high and positive, with a seasonal variance similar to the seasonal dust cycle. Maximum dust content observed by the ACS-TIRVIM occurs prior to 295°, and slowly decreases throughout the remainder of the year. When dust content is high, HCl is capable of increasing by 0.8–0.9 ppb for a 20% increase in dust mmr just 6 hours prior to the time of observation. When dust content starts to fall, HCl impacts lower to increases of < 0.2 ppb. South cluster A HCl is significantly more sensitive to dust than cluster B because

of this difference in dust content. HCl displays strong negative sensitivities to ice below 30 km in Figure 6.18 in regions where ice is abundant in the atmosphere. These are often in the northern hemisphere's observations between 270–315° L_S, with episodic spikes in cluster A and B in the south.

These results from Figure 6.18 can be used to assess what may be causing discrepancies made in Figure 6.14 when comparing the total HCl content observed by ACS-MIR with that calculated by the 1-D model using ACS-TIRVIM aerosols and ACS-MIR H_2O vapour profiles. The larger discrepancy found in southern cluster A, a lack of -2 ppb of HCl in the 1-D model compared to the ACS-MIR observation, could be explained by a larger H_2 content below 30 km than what is in the model, and an increased dust content below 30 km than what was observed by ACS-TIRVIM. The dust-loading profiles (g/cm^3) from Luginin et al. [2019] below 30 km typically have uncertainties ranging between $\pm$ 30–40%, with some rising to > 90% below 15 km. Furthermore, due to atmospheric conditions such as the atmospheric optical opacity of dust the closest ACS-TIRVIM observations get to the Martian surface range between 5–10 km. The 1-D model uses profiles that assume a constant dust distribution from the lowest altitude observed by ACS-TIRVIM to the surface. Perturbations to the dust content by 30–40%, with possible larger abundances below 5–10 km, could potentially increase the HCl content in the model to match that observed by the ACS-MIR. Similarly, H_2O from the ACS-MIR channel [Belyaev et al., 2021] is subject to viewing limitations, with profiles in the southern hemisphere reaching altitudes of $\sim$ 20 km due to the atmospheric dust content. The 1-D also assumes a constant distribution from the model surface to the lowest ACS-MIR altitude point. Big differences between my model's assumed H_2O distributions below 20 km and the true H_2O vmrs on Mars would have the potential to also increase the HCl content to match the ACS-MIR HCl observations.

The first *in-situ* observations of O_2 on Mars were performed at the Gale crater by the Curiosity rover [Trainer et al., 2019], which discovered O_2 at the surface of Mars exhibits a seasonal variation that is not replicated by current photochemical models. Between 270–360°, Trainer et al. [2019] found that the LMD MGCM cannot replicate the interannual variations to O_2 observed by SAM, postulating the existance of an unknown chemical or physical sink for O_2. Errors in the O_2 content below 30 km in photochemical models could also contribute to model HCl and ACS-MIR observation discrepancies in the southern hemisphere, where 20% decreases to O_2 at points below 30 km can cause increases of 0.1 ppb to HCl in both clusters of southern observations. A missing chemical or physical process impacting O_2 variability in GCM models will therefore have a significant impact on our chemical model to describe HCl accurately on Mars.

The ice loading profiles from Luginin et al. [2019] also come with uncertainties of similar magnitudes to the dust loading profiles, ranging between 30–40% in altitudes below 30 km with some exceeding 90%. The ice content below the lowest altitude point observed by ACS-TIRVIM is also assumed to be 0 in my model runs. Errors in the retrieved aerosols in south cluster B can be expected to have strong impacts on the HCl content produced by model calculations, and be a driving force behind the discrepancies between my model's HCl profiles and those seen by ACS-MIR.

6.4.3 Dust-Bound Chlorine Lifetime

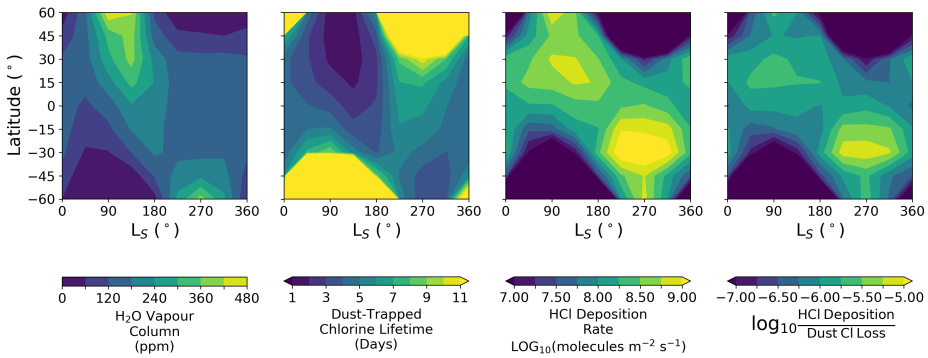


Figure 6.19: H_2O vapour column vmr in ppm and the lifetime of chlorine trapped within dust grains when the heterogeneous chlorine chemistry routine is active (h_{cl1} and h_{cl2}. The rate of HCl dry deposition to the Martian surface is also shown in molecules m^{-2} per Mars sol.

The feasibility of this dust-to-atmosphere chlorine release mechanism can be assessed by calculating the lifetime of the chlorine trapped within the dust column, which I refer to as the dust-trapped chlorine lifetime, when absorption of OH and HO_2 removes one Cl atom (h_{cl1} and h_{cl2}). Assuming a weight-percentage of 0.6% for Cl within the dust, in the middle of the range of the weight-percentages within the Martian top-soil reported by Keller et al. [2006] using the Mars Odyssey's GRS, the lifetime of Cl in the dust can be calculated by dividing the total number of Cl atoms contained in dust (molecules cm^{-2}) in the model column by the summed column loss rates of h_{cl1} and h_{cl2} (molecules cm^{-2} s^{-1}). I perform these calculations over a range of latitudes and solar longitudes, the results of which are given in Figure 6.19. MCDv5.3 standard climatological tracer and aerosol profiles and meteorological boundary conditions were used in these model runs. The column vmr of H_2O vapour that moderates the abundances of HO_2 and OH radicals needed to extract Cl from the dust grains and the number of HCl molecules deposited to the surface per Mars sol are also shown.

Immediately we can see the anti-correlation between the H_2O column and the lifetime for the Cl trapped in the dust grains, caused by the resultant increase in OH and HO_2 formed via H_2O photolysis. It is important to note that the results of Figure 6.19 assume that there is no method for Cl re-entering the dust grains once released to the atmosphere via OH and HO_2 absorption. HCl deposited to the surface, and other chlorine species such as Cl_2 and $HClO_4$ which do not yet have deposition routines in the model, could act as a means of replenishment when dust from the surface is lofted back into the atmosphere. Further, terrestrial mineral dust has been found in *in-situ* experiments in Asia to efficiently absorb gas-phase HCl [Ooki and Uematsu, 2005], another mechanism that could reintroduce Cl atoms back into the dust-grains to prevent the total exhaustion of chlorine trapped in the dust grains. Kahre et al. [2006] used the NASA Ames Mars GCM to model dust lifted via dust devils and wind stress, finding that both methods between -60° and 60° latitudes typically lift dust at a rate of $\sim 10^{-10}$ kg m^{-2} s^{-1}. Assuming a weight percentage of 0.6% for chlorine within the dust, $\sim 10^{12}$ Cl atoms m^{-2} s^{-1} are resupplied to the atmosphere inside the lofted dust grains. The total number of Cl atoms in the model column released through reactions h_{cl1} and h_{cl2} range between 10^{11}–10^{14} m^{-2} s^{-1}, which is comparable with the resupply rate from wind stress and dust devil activity. The rates of HCl deposition, in molecules m^{-2} s^{-1}, are also presented in Figure 6.19. The deposition of HCl in the 1-D model is highest in the same regions where the dust-trapped chlorine lifetimes are lowest, but are orders of magnitude too low to be the main candidate for replenishment of chlorine in the Martian soil. Future studies should investigate means of balancing the chlorine content in the soil through the surface deposition of other chlorine species, like $HClO_4$, Cl_2 or Cl atoms themselves, and absorption onto the dust grains themselves. The release rate of ClO_x from the dust grains in the model also assume an instantaneous production, whereas in reality there will be chemical kinetics occurring within the dust grain that will be dependent on factors such as the dust composition, the atmospheric temperature, and the dust grain surface topology. All of these factors will combine to increase the true lifetime of Cl trapped in the dust grains with respect to the simplified model results of Figure 6.19, which makes the heterogeneous chlorine chemistry routine I have used in this work a feasible instigator of Mars' atmospheric chlorine chemistry. This is outside of the scope of the study performed here however, and the continued development of the routine would benefit greatly from laboratory studies of Mars soil analogues [Allen et al., 1997] and further parameterisation of the Martian soils composition from *in-situ* equipment [Meslin et al., 2013, Berger et al., 2016] and orbiters [Keller et al., 2006].

6.4.4 HCl Atmospheric Lifetime with Ice Uptake

The uptake of HCl on water ice causes strong decreases to the atmospheric lifetime of HCl, as demonstrated in Figure 6.20. Here, the lifetime of HCl is calculated at 60° S throughout the Martian year for model runs with no uptake on ice and with an uptake on ice. As previously seen in Figure 6.2, when gas-phase chemistry alone is considered HCl is expected to have an atmospheric lifetime spanning close to a year ($\sim 10^7$ s) in the lower 70 km of the atmosphere. When the heterogeneous uptake of HCl onto ice is active however, these lifetimes can drop by a magnitude of 10^4 s below altitudes of 30 km to values ranging between 1–10 hours. The abundances of ice in the atmosphere is seasonally variable and strongly dependent on atmospheric temperature, which is why at 60° south the 1-D model sees the shortest HCl lifetimes in the northern summer (when the southern hemisphere is experiencing its winter period), and larger ones appearing in the northern autumn–winter when the increased solar irradiation causes temperatures to rise and ice levels to fall. HCl observations made during the 2018 dust-storm typically lie in the altitude region of 5–30 km [Korablev et al., 2021, Olsen et al., 2021, Aoki et al., 2021]. With HCl uptake on water ice active, the lifetimes of HCl here range between 10^2–10^5 seconds (or tens of minutes to roughly one day). These lifetimes would be capable of causing the quick disappearances of HCl observed by the ACS [Korablev et al., 2021] that gas-phase-only chemistry models cannot.

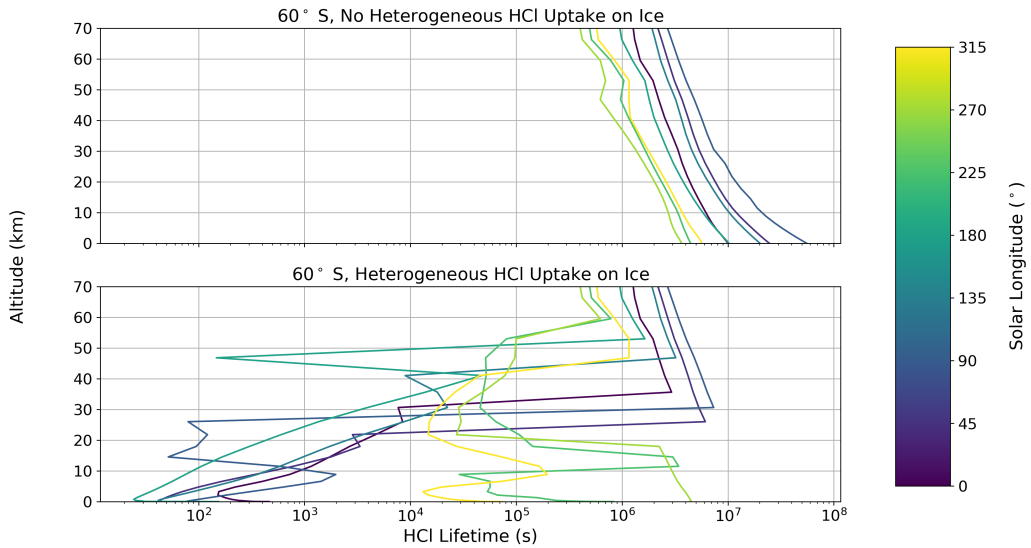


Figure 6.20: The photochemical lifetime of HCl with altitude at 60° S and solar longitude as calculated by the 1-D model excluding then including heterogeneous uptake of HCl on H_2O ice.

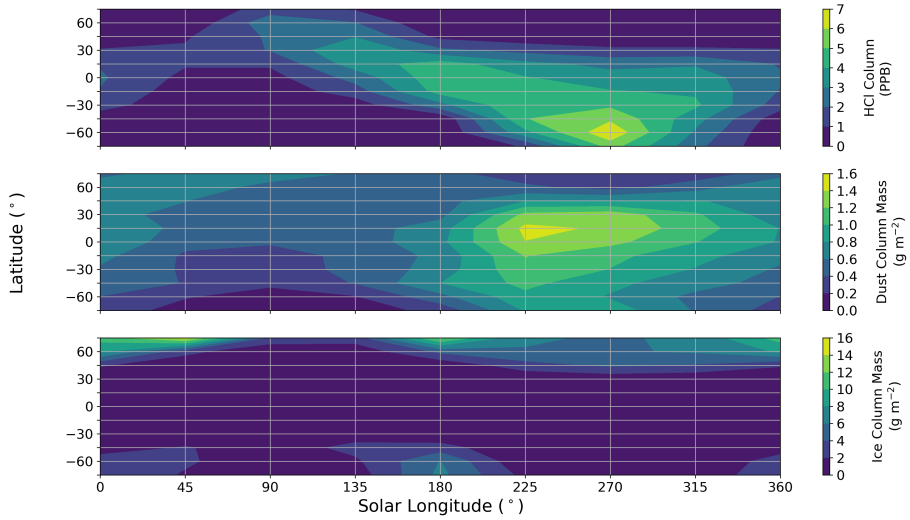


Figure 6.21: HCl column abundance (ppb) variations with latitude and solar longitude, using longitudinal mean meteorological boundary conditions, long-lived inorganic tracers (CO, O_2, H_2, CO_2, and H_2O vapour), and aerosol profiles as calculated by the 1-D photochemistry model using the heterogeneous chlorine chemistry scheme. The column mass of dust, the source of Cl and ClO molecules, and H_2O ice, the heterogeneous sink for HCl, are presented also.

6.4.5 HCl Column Abundances

Figure 6.21 presents a study of the variation in the column abundance of HCl on Mars with respect to latitude and solar longitude when the new heterogeneous chlorine chemistry scheme is applied. To perform this study, the 1-D model performs calculations across 11 latitude points across the range -70°–70° and 8 solar longitude points across the span of the entire Martian year. In each run, the model is initialised with 0 ppb of HCl, and 20 ppt of CH_4. Diurnal calculations are performed over a 10 sol spin-up to enable adequate mixing of HO_x and O_x, and meteorological boundary conditions from the MCD v5.3 are used, as well as tracer volume mixing ratios of the long-lived inorganic compounds (CO_2, CO, O_2, H_2, and H_2O vapour). In these interpolation procedures, longitudinal mean values are used in the 1-D model calculations. After the 10 sol spin-up, ice and dust mixing ratio profiles are interpolated from the MCD v5.3, as well as effective particle radii, and 1-D model calculations are performed over half of one Mars sol , at which point the column abundances of HCl are calculated at noon, LT = 12:00 hrs (24 model timesteps).

An anti-correlation between HCl and H_2O ice columns and a correlation between the HCl and dust columns are noticeable immediately. HCl production in the 1-D model favours the southern hemisphere during the dust storm period (135–315° L_S), with maximum column vmrs reaching 7 ppb at 60° south at 270° L_S. Here, H_2O vapour columns are at a maximum

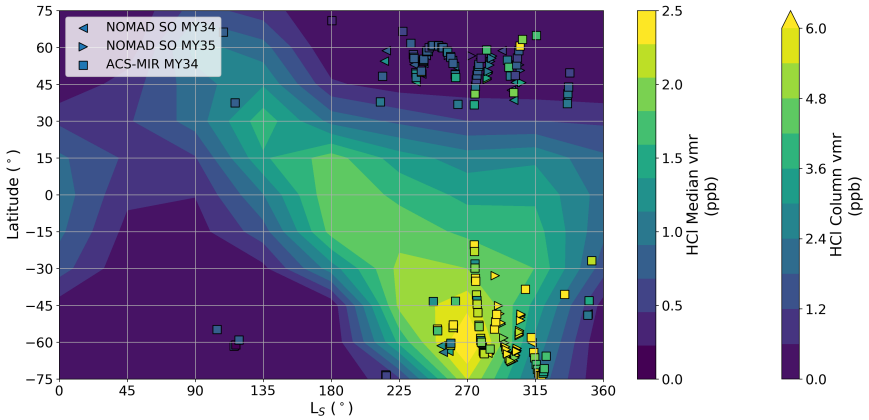


Figure 6.22: HCl column vmrs (ppb) calculated by the 1-D model from Figure 6.21 (colour saturated at 6 ppb) with the median HCl vmrs observed by the TGO NOMAD throughout MY34–35 [Aoki et al., 2021] and the median HCl vmrs observed by the ACS-MIR throughout MY34 [Korablev et al., 2021] superimposed. Left hand colour bar displays ACS-MIR/NOMAD median HCl vmr, right hand colour bar displays the 1-D model HCl column vmr.

in the high southern latitudes due to the sublimation of the southern cap's water ice. The atmosphere is also quite dusty, with between 0.8–1.0 g m^{-2} in the column. The exposure of the atmosphere in the south to solar radiation also suppresses the formation of atmospheric water ice, which also results in a greater rate of photolysis of H_2O vapour to HO_x radical species. The larger abundance of OH and HO_2 from this increase in H_2O photolysis enables a greater release rate of Cl and ClO from dust grains in the reactive heterogeneous chemistry scheme, and the decreased ice abundances allow larger quantities of HCl to form. The location in both time and space of this maximum in the model coincides very well with the point of the maximum HCl vmr observed by the NOMAD spectrometer in MY34 [Aoki et al., 2021], which detected vmrs of 4 ppb at altitudes below 30 km.

Figure 6.22 takes the seasonal distribution of HCl from the 1-D model in Figure 6.21 and superimposes the median HCl vmrs observed by the ACS-MIR [Korablev et al., 2021] and the NOMAD SO [Aoki et al., 2021] over MY34–35. Despite the 1-D model lacking a means of balancing the source of ClO_x within the dust grains, resulting in a constant source of production of atmospheric chlorine, the 1-D model's seasonal HCl output produces a cycle close to that observed by the ACS and NOMAD spectrometers. The lowest HCl abundances are found in both hemispheres during the northern summer (90–180 L_S) when dust content is low. Both plots also show an increase in the northern hemisphere during the dust-storm season (180–315° L_S), but the 1-D model, using climatological dust and ice profiles, cannot reproduce the episodic spikes ACS-MIR observed here. The largest median HCl profile values observed by the ACS and NOMAD are located in the southern hemisphere around the point

of Mars' perihelion (271° L_S), which is reproduced by the 1-D model. These figures show that chlorine chemistry initiated by heterogeneous reactions between H_2O and dust, and HCl and H_2O ice, have the capacity to explain the seasonal HCl cycle that the ExoMars TGO has observed on Mars.

6.5 Heterogeneous Chlorine Impacts on H_2O_2

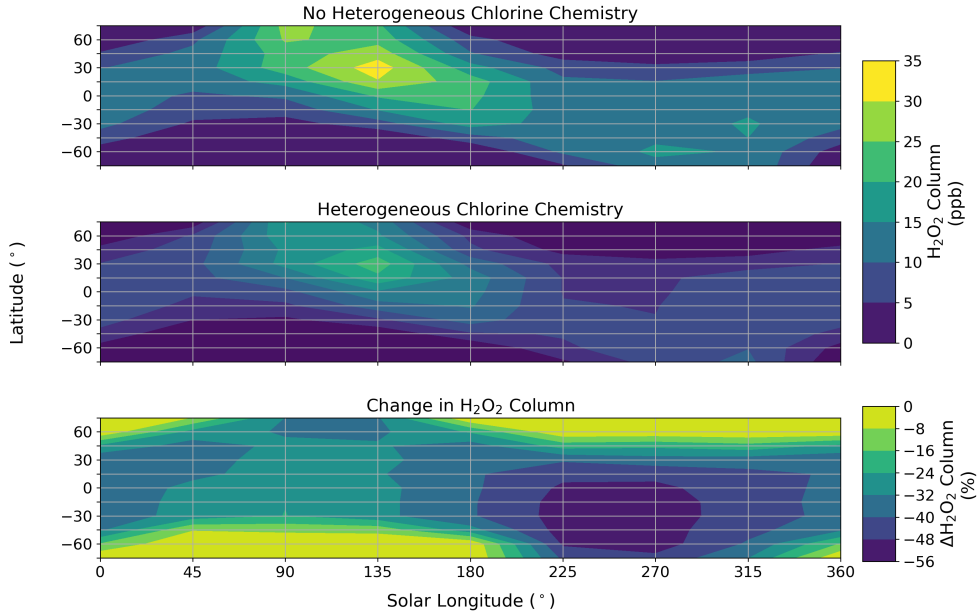


Figure 6.23: H_2O_2 column abundances and their variations with latitude and solar longitude as calculated by the 1-D model using model runs with no heterogeneous chemistry (top), and with the heterogeneous chlorine chemistry scheme active (middle). The bottom heatmap presents the resultant change (in percentage with respect to the chlorine-absent run) to the H_2O_2 column due to chlorine chemistry.

After studying the production and loss of HCl and the coincidences between the 1-D model and the ACS-MIR on Mars, I now look at the impact that this new heterogeneous chlorine scheme has on inorganic trace gas chemistry. First, I shall assess the impacts of the resultant chlorine chemistry on H_2O_2. H_2O_2 acts as a source of OH through its UV photolysis, and also acts to moderate the abundance of O_2 (Figure 2.7), making it an important tracer in Mars' atmosphere. The reanalysis of H_2O_2 observations made by the ground-based TEXES spectographic telescope [Encrenaz et al., 2019] found that significant differences in H_2O_2 absorbtion feature strengths in the GEISA spectroscopic databases existed between the versions released in years 2003 and 2015, and as a result the previous observations of H_2O_2 made by Encrenaz et al. [2004b] needed to be reduced by a factor of $\sim$ 1.75 accordingly.

This resulted in GCM models producing inaccurate column vmrs when compared to the observations, especially across the 150–230° L_S period, finding that current GCM models overestimate the amount of H_2O_2 on Mars. Figure 6.23 presents the H_2O_2 column vmr and its variance with latitude and solar longitude when no heterogeneous chlorine chemistry is active, and when heterogeneous chlorine chemistry is active. In both instances, uptake of OH and HO_2 on ice particles is active. The runs are performed with the same methodology as the experiments performed in Section 6.4.5 to produce Figure 6.21, using longitudinal mean meteorological boundary conditions and long-lived inorganic vmr profiles.

From Figure 6.23, between 150–230° L_S the H_2O_2 column in the southern hemisphere experiences decreases of 20–56% when the heterogeneous chlorine scheme is active. These large decreases extend throughout the perihelion season when dust is most abundant, especially within the southern hemisphere where the lower H_2O ice content enables greater amounts of Cl-chemistry to develop. Figure 6.24a examines the column abundances of H_2O_2 calculated by the 1-D photochemistry model, with and without the heterogeneous chlorine chemistry scheme active, across the latitude band of 0–30° north through 0–180° L_S, and 0–30° south through 180–360° L_S. The plotted results are the mean values across this latitude band, and the error bars correspond to the standard deviation of this mean. This configuration corresponds to the geometry of the observations performed by Encrenaz et al. [2004b] and Encrenaz et al. [2019], where Mars' northern hemisphere was orientated towards Earth during the northern spring and summer, and the southern hemisphere faced Earth during the northern autumn and winter. Figure 6.24b shows the same results, but using the full 3-D LMD-MGCM and the GEM-Mars GCM [Neary and Daerden, 2018], taken from Encrenaz et al. [2019].

Differences between the results from the 1-D model and the 3-D LMD-MGCM, the 1-D model's parent, arise from a number of sources. The 1-D model takes longitudinal mean meteorological boundary conditions and tracer profiles of CO_2, CO, O_2, H_2 and H_2O vapour from the MCD v5.3 database, whereas the full 3-D GCM calculates these dynamically. The 1-D model results are also produced by running the model across discrete L_S steps, whereas the 3-D GCM results are from a continuous annual run. Each point for the 1-D model is the mean H_2O_2 column of three runs at the discrete L_S point, performed at latitudes 0, 15, and 30°. The 3-D GCM results are the mean H_2O_2 column across the 20° latitude band. Despite these differences, the 1-D model displays the ability to accurately model the seasonal cycle of H_2O_2 as calculated by the 3-D LMD-MGCM, while producing abundances closer to those of the GEM-Mars run.

The first improvement in the 1-D model results when heterogeneous chlorine chemistry is active is seen between 80–100° L_S. From both Figures 6.24a and b, the 1-D model and the 3-D models slightly over estimate the H_2O_2 column. With the chlorine scheme active, H_2O_2 vmrs lower by between 8–10 ppb, which could bring about a better coincidence between the 3-D models and the reanalysed TEXES datasets here. Between 150–230° L_S, a very strong

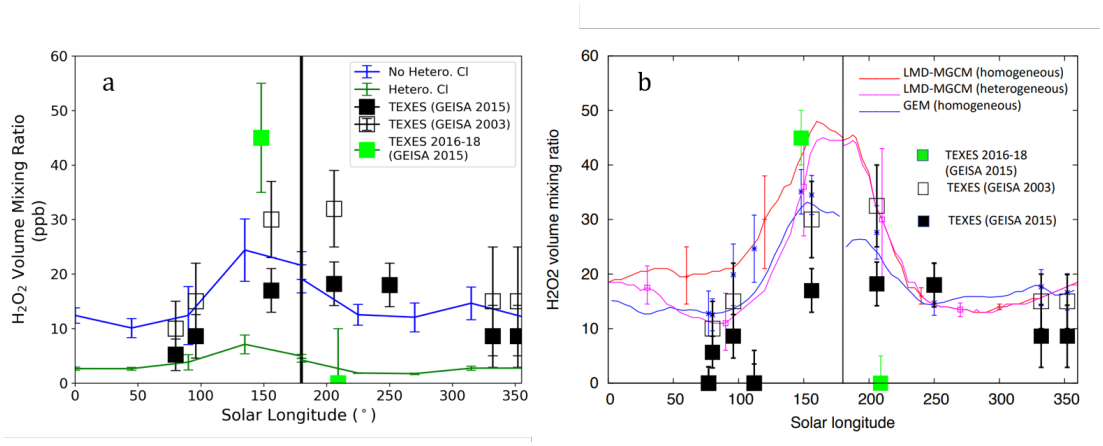


Figure 6.24: (a) Column mixing ratios of H_2O_2 as calculated by the 1-D photochemistry model with and without the heterogeneous chlorine chemistry routine active and (b) the 3-D General Circulation Models with and without heterogeneous uptake of OH and HO_2 on ice. Figure a does not include the upper limits of H_2O_2 produced by Encrenaz et al. [2019]. The original observations of Mars' H_2O_2 column by Encrenaz et al. [2004b], and the reanalysed values using the updated GEISA 2015 spectrographic records performed by Encrenaz et al. [2019] are presented in each plot. Figure b has been taken directly from Encrenaz et al. [2019].

decrease appears between the two 1-D model runs, with H_2O_2 falling by 10–20 ppb with the heterogeneous chlorine scheme active. A drop in H_2O_2 by this amount in the 3-D LMG-MGCM runs would bring the models into much better coincidence with the reanalysed TEXES datasets. The 3-D model results at 250° L_S are in good coincidence with the observed H_2O_2 abundances already, and the 1-D model here calculates a decrease of $\sim$ 10 ppb here. We can hypothesise that this would result in 3-D model coincidences decreasing here when the chlorine scheme is included in 3-D GCMs. Finally, between 320–360° L_S it can be seen that both the 1-D model, without chlorine chemistry, and the 3-D GCMs, with and without uptake of OH and HO_2 on ice, produce too large an abundance of H_2O_2 when compared to the TEXES dataset. When heterogeneous chlorine chemistry is active in the 1-D model however, decreases of 8–12 ppb occur across this period, which are large enough to bring the 3-D GCM results into better coincidence with the TEXES reanalysed dataset.

Encrenaz et al. [2019] were only able to infer an upper limit of 10 ppb for H_2O_2 during MY34 at 209° L_S, seen in Figure 6.24b. This measurement was taken at the peak of the MY34 dust storm, and H_2O columns during global dust storm events are known to fall in the equatorial latitudes [Smith et al., 2018]. This is hypothesised to be due to more heat being trapped by the lofted dust, resulting in a greater global circulation of air from equatorial latitudes to higher latitudes. As H_2O_2 is produced by HO_2 molecules reacting with one another, themselves products of H_2O photolysis, there is a strong correlation between H_2O_2 and H_2O inferred from photochemical models [Clancy and Nair, 1996]. The greater dust content at these times will

also increase the amount of chlorine released in the atmosphere through the heterogeneous chlorine scheme, increasing the rate of reaction cl_{11} (Table 6.2) which involves Cl atoms breaking down H_2O_2. The combination of a decreased source of H_2O_2, and an increased sink in the form of Cl atoms, could explain the lack of a proper detection here.

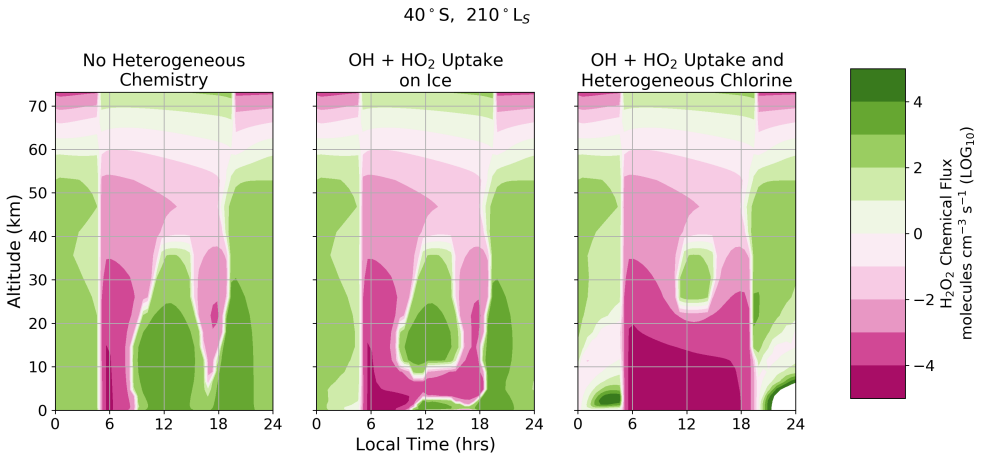


Figure 6.25: Net photochemical flux of H_2O_2 at 40°S, 210° L_S across one Mars sol with (left) no heterogeneous chemistry considered, (middle) OH and HO_2 uptake on H_2O ice particles, and (right) OH, HO_2 uptake on ice and the heterogeneous chlorine chemistry routine active.

Figure 6.25 shows the net flux of H_2O_2 due to photochemistry in molecules cm^{-3} s^{-1} as calculated by the 1-D model for three scenarios at 40° south and 210°, and the variance with altitude and local time. The first scenario (left) has no heterogeneous chemistry involved, the second (middle) has OH and HO_2 uptake on ice included, and the third (right) includes both OH and HO_2 uptake on ice and the heterogeneous chlorine scheme. During the day, HO_2 molecules are broken apart by reactions with Cl (cl_9), and are also adsorbed onto dust grains to release ClO_x (h_{cl2}). The adsorbtion onto dust continues into the night, but ClO becomes the dominant ClO_x tracer and suppresses HO_2 abundances through reaction cl_{13}, which is just below 10 times less effective at 298 K than cl_9. The net rate of production in the night for H_2O_2 below 20 km is lowered by up to 90% in when the heterogeneous chlorine scheme is active, and during the day a net loss is experienced.

In summary, the introduction of chlorine chemistry into the atmosphere of Mars results in the suppression of H_2O_2 production by decreasing the amount of HO_2 available to produce it, and also makes H_2O_2 less stable during daylight in the presence of the $\sim$ 100 ppt of Cl atoms.

6.6 Heterogeneous Chlorine and Organic Chemistry

The presence of Cl atoms in the Martian atmosphere adds an additional and potentially very powerful sink for atmospheric CH_4. Cl reacts with CH_4 to break the organic molecule down to CH_3 and HCl, a reaction that at 298 K has a rate coefficient equal to 1.03×10^{-13} cm^3 molecule^{-1} s^{-1} (reaction cl_{16} of Table 6.2). This is $\sim$ 100 times larger than the rate coefficient for the reaction of OH with CH_4, which was originally thought to be the biggest atmospheric sink available of CH_4. From Figure 6.8, we can expect the $\sim$ 100–200 ppt of Cl atoms that accumulate in the Martian daytime to produce a significant effect on CH_4's rate of chemical loss. To assess these impacts, I use the 1-D model to calculate the photochemical lifetime of CH_4 across the latitude range [-60°,60°] over nine discrete solar longitude points across the Martian year. Figure 6.26 presents the resultant CH_4 column lifetimes for runs with no chlorine chemistry present, runs with the heterogeneous chlorine scheme active, and the ratio of the two that provides a measure of how much more destructive the atmospheric column is to CH_4 when chlorine chemistry is active.

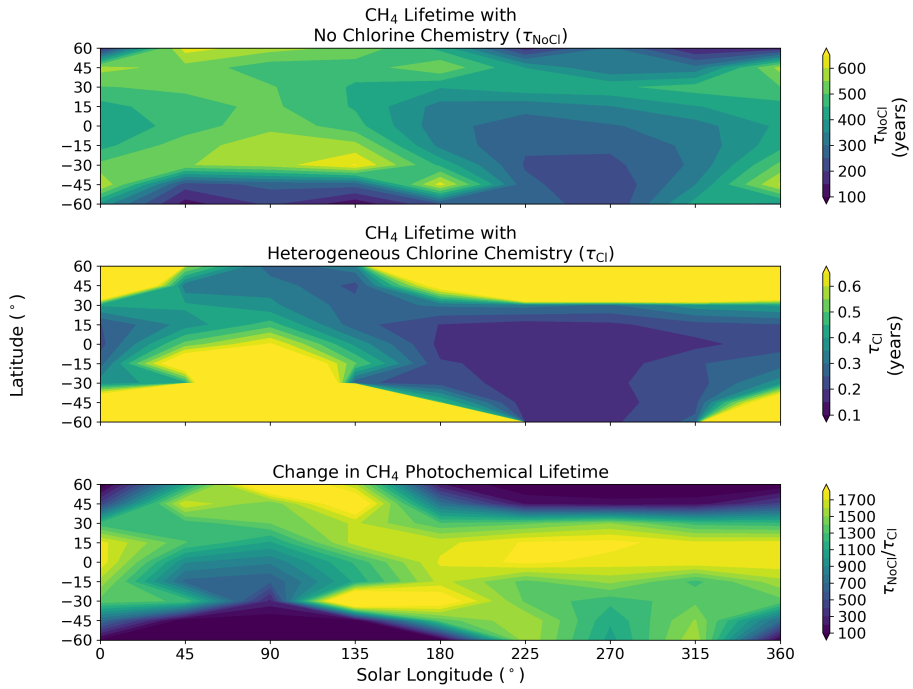


Figure 6.26: Photochemical lifetime of CH_4 in terrestrial years and the variance across latitude and solar longitude on Mars without chlorine chemistry, and with the heterogeneous chlorine scheme active.

The photochemical lifetime of CH_4 after one sol of exposure to the heterogeneous chlorine scheme falls by very large amounts, with the strongest changes appearing in the mid-latitude range of -30°–30° during the northern spring–summer (0°–180°), then extending into the southern hemisphere during the autumn-winter, matching the behaviour of the dust-cycle on Mars. Calculations performed by Lefèvre and Forget [2009] found that the atmospheric sink for CH_4 needs to be roughly 600 times more powerful than what is currently in our photochemical models. Here, my model predicts that my new heterogeneous chlorine routine is capable of increasing the atmospheric sink strength by factors greater than 1000. The original dominating sink of CH_4 was the OH radical, as detailed earlier in Chapter 4. The presence of $\sim$ 100 ppt of Cl atoms in the lowest 30–km greatly increases the loss rate of CH_4 in comparison to runs where no chlorine chemistry is active. Figure 6.27 displays the CH_4 loss rate calculated by the 1-D model at 0° north at 270° L_S, at which point the change due to chlorine interactions is the largest (Figure 6.26). As ClO_x molecules originate from dust interactions, their abundances are confined to the top of the dust layer ($\sim$ 40 km). Below 20 km, where dust mmrs are highest, the CH_4 lifetime (the inverse of the loss rate) can drop to below one year. Below 5 km, dust abundances can become high enough to create Cl abundances that lower this further to tens of days. As Cl abundances fall at higher altitudes ($>$ 40 km) O(^{1}D) takes over as the dominant chemical, and photolysis only becomes effective at altitudes above 60 km.

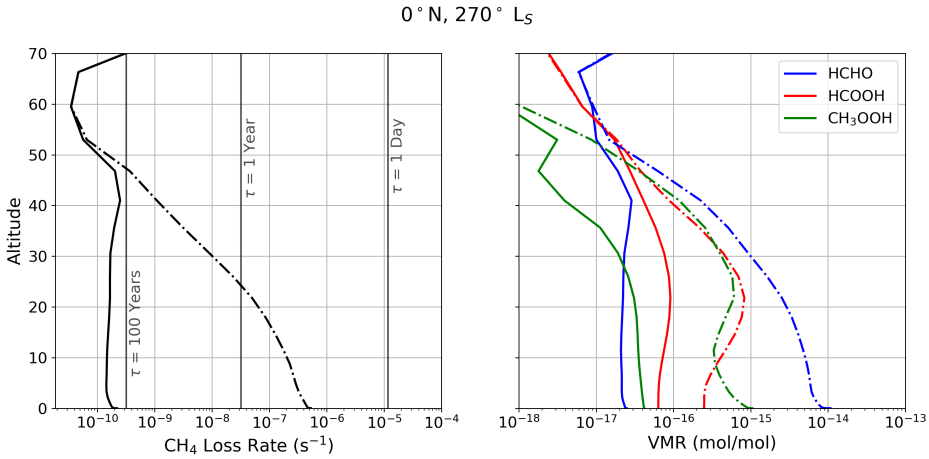


Figure 6.27: Photochemical loss rates of CH_4 for a chlorine-free model run (solid) and a run producing chlorine via the heterogeneous chlorine routine (dashed), and the vmr profiles of HCHO, HCOOH, and CH_3OOH at LT = 12:00 hrs after one sol of chlorine chemistry.

Figure 6.27 also shows the vmr profiles of three important non-methane VOCs, HCHO, HCOOH, and CH_3OOH at noon one sol after chlorine chemistry is active in the model. HCHO is the only non-methane VOC observable to TGO spectrometers [Vandaele and Rodriguez-Gomez, 2013, Korablev et al., 2018], so evaluating the abundance produced with a significantly more powerful CH_4 photochemical sink is important. There have been no successful observations of CH_4 or HCHO to date, so the presence of large amounts of HCHO in the model will be

a cause for concern. From Figure 6.27, we see that HCHO is increased in magnitude of by a factor of almost 10^3 but still fails to reach quantities greater than 0.01 ppt, far below the NOMAD spectrometers lower sensitivity limit of 40 ppt [Vandaele and Rodriguez-Gomez, 2013]. The layered structure of HCHO described in Chapter 4 disappears as Cl atoms are also an effective chemical sink for HCHO (cl_{17} of Table 6.2, which hinders the increased production of HCHO from the larger flux of CH_3 from the increased destruction of CH_4.

6.7 Conclusion

The work performed in this chapter demonstrates that chlorine compounds within the soil and their release via heterogeneous absorption of OH and HO_2, and the highly efficient uptake of HCl on H_2O ice, has significant potential for explaining a number of photochemical phenomena on Mars that current GCMs fail to replicate. The absence of strong seismic activity and any observations of sulfur species effectively rules out the recent observations of HCl [Korablev et al., 2021, Olsen et al., 2021, Aoki et al., 2021] arising from volcanic activity. Using ACS-TIRVIM observed dust and ice profiles [Luginin et al., 2019] and ACS-MIR observations of H_2O vapour [Belyaev et al., 2021] that roughly coincide with the ACS-MIR observations of HCl over MY34 [Korablev et al., 2021] in my 1-D model using my heterogeneous chlorine scheme (h_{cl1}, h_{cl2}, and h_{cl3}) produces transient HCl profiles that are in very close coincidence with those seen by the TGO equipment (Figures 6.12–6.13 and Figures B.1–B.7).

These 1-D model profiles match the seasonal and spatial variances seen by Korablev et al. [2021] (Figure 6.14), and sensitivity studies of the observations using the TLM and adjoint method with chlorine chemistry equipped shows that uncertainties in the ACS-TIRVIM aerosol profiles and ACS-MIR H_2O vapour distributions below 30 km are capable of being the sources of the 1-D model and ACS-MIR HCl profile discrepancies (Figure 6.18). Furthermore, HCl observed by ACS-MIR is found to have a strong positive sensitivity to H_2 in the south during high dust-storm activity, and strong negative sensitivities to O_2 across all latitudes. We do not have observations of the vertical structure of H_2 on Mars, and rely on column abundances and models to infer its distribution [Krasnopolsky and Feldman, 2001, Chaufray et al., 2015]. O_2 has only recently been observed *in-situ* on Mars [Trainer et al., 2019], and has revealed to us that the LMD-GCM cannot fully account for its seasonal and inter-annual behaviour. The adjoint finds the 1-D model very sensitive to these two species with respect to the HCl produced below 30 km, implying that errors in the H_2 and O_2 profiles used below 30 km, taken from the MCDv5.3 (itself a dataset of model runs performed by the 3-D LMD-GCM), will cause discrepancies between the model's HCl profiles and those observed by TGO instrumentation. As well as addressing where Cl chemistry comes from, my model's heterogeneous uptake of HCl onto water ice lowers HCl lifetimes (Figure 6.20) from values of $\sim$ 1 year to timescales of a few hours below 30 km, which enables HCl to produce the distinct layered profile shapes observed by ACS-MIR and NOMAD.

Furthermore, the 1-D model finds HCl profiles being produced at observable abundances outside of dust-storm events. Using MCDv5.3 aerosol and H_2O profiles that are climatological means, representative of a 'typical' Mars year, produce profiles that coincide significantly less with ACS-MIR observations than those made using ACS-TIRVIM and MIR aerosols and H_2O, but of comparable magnitudes (0.1–4 ppb). The appearance of HCl being independent of dust-storm events is a feature observed by the NOMAD spectrometer in Aoki et al. [2021], which my model replicates in Figures 6.12–6.13 and Figures B.1–B.7. The maximum HCl vmr observed by NOMAD also coincides very well with the maximum 1-D model column in Figure 6.21.

The heterogeneous chlorine routine is incomplete however, and requires a means of re-uptake of chlorine into the dust and surface to balance the loss of chlorine occuring from reactions h_{cl1} and h_{cl2}. This limits my model to studying the effects of heterogeneous chlorine over one Martian sol, which is a timescale less than the lifetime of the chlorine trapped within dust in the model column in the most reactive regions (Figure 6.19). Using MCDv5.3 climatological aerosols and stable tracer profiles over a period of one sol produces HCl column abundances that match the seasonal behaviour of HCl observed by Korablev et al. [2021] and Aoki et al. [2021], which see maximum HCl vmrs appearing almost exactly where the 1-D model anticipates maximum column vmrs to occur (Figure 6.21). The column vmrs in my model after one sol do however exceed upper limits inferred from previous non-detections of HCl. Krasnopolsky et al. [1997] found an upper limit of 2 ppb at 351° L_S using ground-based telescopes pointing towards Mars southern hemisphere. The 1-D model finds this to be the point where HCl from dust activity starts to lower in column abundance to values < 3 ppb. Hartogh et al. [2010] found a much more stringent upper limit of 200 ppt using ground-based equipment, this time at 77° L_S. The northern hemisphere is in view here, where the 1-D model calculates < 3 ppb of HCl to form as this, typically, is not a dust period. Finally, Villanueva et al. [2013] make three measurements of HCl at 12°, 324°, and 352° to infer upper limits of 0.6, 1.5, and 2.1 ppb respectively. These are exceeded by the 1-D model in Figure 6.19, but are also points at which the model columns are at a seasonal minimum. Incorporating a mechanism for chlorine reuptake into the soil, and balancing the chlorine content of the lofted dust, would suppress these model HCl columns and enable extend runs to be performed and the mechanism to be constrained and better parameterised. The uptake of chlorine species onto mineral dust grains is known to be an effective atmospheric sink for chlorine species on Earth [Sullivan et al., 2007], a process that should be considered in future improvements to this heterogeneous chlorine routine in my 1-D model. Despite these caveats, the seasonal behaviour of HCl in the 1-D model is in very strong agreement with that seen by observations and prior non-detections.

The heterogeneous chlorine routine also strongly influences H_2O_2 in the 1-D model (Figure 6.23), where values can dip by > 50% in the dusty season in the equator and southern latitudes. This enables the 1-D photochemistry model to improve H_2O_2 column coincidences with observations made by Encrenaz et al. [2019] between 300–100° L_S, but decreases coincidence when larger H_2O_2 abundances are seen between 150–250°. The 1-D model here experiences a decrease in H_2O_2 of $\sim$ 20 ppb (Figure 6.24a), which, if also experienced by the LMD-GCM, would bring the 3-D GCM results into better coincidence with observations (Figure 6.24b).

Finally, the heterogeneous chlorine scheme has a very strong impact for organic chemistry on Mars. Including the heterogeneous routine for one sol increases the CH_4 atmospheric sink in the Martian atmosphere by factors ranging between 500–1700 (Figure 6.26), much higher than the factor of 600 calculated by Lefèvre and Forget [2009]. The Cl atoms produced during the daytime by the interactions of OH and HO_2 with dust are much more efficient at breaking CH_4 down below 30 km than either OH, O(^{1}D), or UV photolysis. The resultant oxidised organic products, namely HCHO, HCOOH and CH_3OOH however remain at undetectable levels despite increasing by factors greater than 100 in comparison to chlorine-free chemistry models. The introduction of chlorine chemistry into Mars photochemistry models is therefore crucial in helping explain the observations of CH_4 being made by Curiosity [Webster et al., 2015, Webster et al., 2018] and some orbiters [Giuranna et al., 2019] and the non-detections being made by the ExoMars TGO [Korablev et al., 2019]. Constraining the heterogeneous chlorine routine by balancing the loss of chlorine in the dust with re-uptake of chlorine compounds will enable longer model runs to be performed to assess the long term feasibility of this new photochemistry scheme, and definitively address whether or not chlorine chemistry is capable of solving the mystery of Mars' CH_4. These initial findings with the 1-D model, however, show that it is a feasible and very promising mechanism and should be the focus of future studies for Martian atmospheric photochemistry.

Chapter 7

Conclusions and Future Work

The goal of this thesis was to expand the 1-D photochemistry submodule of the LMD-OU 3-D Mars General Circulation Model to include a larger range of trace gas species to be used to improve upon our understanding of Mars' atmospheric photochemistry, and to aid interpreting data ariving from the ExoMars Trace Gas Orbiter (TGO). My model's updated photochemistry routine is now capable of modelling the oxidation of CH_4 and 11 of its oxidised products, as well as the oxidation of C_2H_6 and 29 of its resultant photochemical products. I have included 37 additional gas-phase reaction rates covering the oxidation of CH_4, and 70 gas-phase and 20 new photolysis reactions to model the oxidation of C_2H_6. My work makes my 1-D photochemistry model one of the most expansive organic chemistry routines available for Martian atmospheric science and a powerful tool for the study of potential biosignatures. As well as an expansive organic chemistry routine, I have included tracer support for chlorine chemistry on Mars. This consists of an additional 13 tracers, with 59 gas-phase and 4 photolysis reactions added to the model code, and 3 new heterogeneous reactions involving the uptake of OH and HO_2 on dust releasing of ClO_x species and the uptake of HCl on H_2O ice particles. These new chlorine chemistry routines will be able to provide new insights into the nature of the atmospheric HCl, and the subsequent chlorine cycle on Mars, that has just recently been observed by the TGO when reintroduced into the 3-D parent GCM.

These new routines were then used to address the following three research questions defined in Chapter 1:

1. What are the bounds on the atmospheric lifetimes of methane and non-methane volatile organic compounds on Mars, given our current knowledge of its atmospheric photochemistry?
2. Does a more detailed one dimensional photochemistry submodule improve model agreements with observations of trace gas species?
3. Can a photochemical adjoint for Mars' atmosphere provide information regarding the sensitivity of inorganic and chlorine-containing trace gas species on Mars to the abundances of other trace gas species?

7.1 Atmospheric Lifetimes of Organic Compounds

The additional 107 gas-phase reactions and 20 photolysis reactions involving CH_4 and non-CH_4 VOCs I have included into the 1-D model in Chapter 4 enabled me to calculate the bounds of organic trace gas species that have spectographic absorption features within the ExoMars TGOs spectral range, and how these vary across time and space. I found that CH_4, with our current knowledge of Mars' atmospheric photochemistry, is in agreement with previous modelling studies on Mars [Wong et al., 2003, Summers et al., 2002], with photochemical lifetimes spanning between 200–600 years. These are subject to seasonal variations in the higher latitudes of each hemisphere due to the sublimation of H_2O ice at the polar caps during each hemisphere's summer, where the elevated H_2O vapour in the atmosphere increases the abundance of OH molecules which are theorised to be CH_4's dominant atmospheric sink. I also assess how the atmospheric chemical sink of CH_4 varies with altitude throughout the Martian year (Figure 4.3), finding that a photochemically inert region exists for CH_4 between 50–60 km across equatorial latitudes where CH_4 molecules experience photochemical lifetimes between 1000–1750 terrestrial years. Above this inert altitude pocket, UV photolysis becomes effective at destroying CH_4, and below the primary sinks are OH molecules below the H_2O vapour hygropause (seasonally varying between $\sim$ 5–40 km and $O(^1D)$ atoms above that lower lifetimes, as a function of altitude, to 150–600 years.

My 1-D model's CH_4 oxidation routine is also used to assess the variance of HCHO's atmospheric lifetime (Figure 4.7), a species capable of being detected by the NOMAD spectrometer aboard the ExoMars TGO with abundances larger than 40 ppt [Vandaele and Rodriguez-Gomez, 2013]. My 1-D model produces values in agreement with prior modelling studies[Wong et al., 2003, Summers et al., 2002], finding short photochemical lifetimes that range between 1.5–6 hours across equatorial latitudes throughout the Martian year. UV photolysis is the primary sink for HCHO on Mars, effectively penetrating the atmosphere to the surface, followed by destructive reactions with OH. Its lifetime is therefore dependent on the solar radiation available to the surface, and the height and abundance of H_2O within the hygropause. Slightly larger atmospheric lifetimes are found in layers centred between 25–50 km during the northern spring (0–90° L_S), which results in HCHO being produced in a layered structure from the oxidation of a low and continuous homogeneous CH_4 background of 50 ppt. These abundances fail to come close to the 40 ppt estimated to be necessary for a detection by NOMAD (Figure 4.4).

The photochemistry of HCOOH on Mars has also been studied in this work for the first time. It is a stable compound under UV radiation on Mars, and the only chemical sink within the model is the destructive reaction with OH. At the top of the hygropause (varying between 5–40 km seasonally) the OH abundances result in HCOOH lifetimes of < 20 sols, which gradually rise

to values of 100–200 sols close to the surface (Figure 4.9). The relative stability of HCOOH compared to HCHO makes a detection after an initial release of an organic precursor such as CH_4 or C_2H_6 more feasible, however the rates at which it is produced are very low and abundances of < 10^3 ppt are produced from low CH_4 backgrounds of 50 ppt (Figure 4.4).

C_2H_6 was found to have a photochemical lifetime that displays strong spatial and temporal variability on Mars (Figure 4.12). The updated chemistry routine finds C_2H_6 lifetimes range between 2–5 years below the Martian hygropause due to its destruction being dominated by reactions with OH. Above the hygropause, the C_2H_6 lifetime drops sharply to values ranging between 70–180 days due to reactions with O(^{3}P) atoms which accrue in larger quantities above the hygropause. The vertically integrated lifetimes of C_2H_6 range between 0.5–1.5 years, displaying an anti-correlation to the atmospheres H_2O content in contrast to CH_4.

In Chapter 6, I performed the first study of the impact of chlorine chemistry on Mars, produced via dust and HO_x interactions, on the atmospheric lifetime of CH_4 (Figure 6.26). The introduction of chlorine chemistry from dust interactions can only be studied over short time periods due to the inexhaustible chlorine content in the soil in the model (discussed in Chapter 6), however the preliminary findings see strong impacts on CH_4 in the Martian atmosphere. To corroborate past observations and non-detections of CH_4, the destructive sink on Mars is expected to be approximately 600 times more powerful than what current photochemistry models predict [Lefèvre and Forget, 2009]. With a HCl content roughly similar to the abundances observed by the ACS and NOMAD (0$\sim$10 ppb), my updated 1-D model finds that the photochemical lifetime of CH_4 can lower by factors between 100–1700. This strongly implies that the 'missing sink' for CH_4 on Mars, that could help explain the difficulties experienced detecting it by the TGO [Korablev et al., 2019, Knutsen et al., 2021], could be the introduction of chlorine chemistry into our photochemical models of Mars.

7.2 Model Improvements

The introduction of organic chemistry routines in my 1-D model have revealed that the detection of non-methane VOCs on Mars resulting from the oxidation of organic precursors will not be possible without a powerful additional chemical sink. HCHO and HCOOH are oxidised organic products of both CH_4 and C_2H_6, with greater yields of both producable via C_2H_6, and CH_3CHO and CH_3COOH are unique to the oxidation of C_2H_6. None of these species have been observed on Mars to date, in line with my model predictions. This is unfortunate, as there are no comparisons between my model and observational data to be made in regards to abundances or profile shapes of organic species on Mars.

However the heterogeneous chlorine chemistry scheme, detailed in Chapter 6, accurately reproduces the HCl profiles observed by the ACS in Korablev et al. [2021] during the MY34 dust-storm when using dust and ice profiles observed by the ACS-TIRVIM and H_2O vapour profiles observed by ACS-MIR that roughly coincide in time and space with the HCl observations (Figure 6.12–6.13 and Figures B.1–B.7). Without the uptake onto H_2O ice that I have included in the 1-D model, HCl is too stable a compound to be formed in the layered structures seen by ACS and NOMAD [Aoki et al., 2021, Korablev et al., 2021, Olsen et al., 2021]. Furthermore, I find that the appearance of HCl via the heterogeneous chemistry routine is not dependent on a global dust-storm. This is in agreement with Aoki et al. [2021], who used the NOMAD spectrometer to observe HCl during the MY34 dust-storm, and during MY35 that did not experience a global dust-storm. Superimposing the median HCl values observed over MY34–35 by Aoki et al. [2021] and those of MY34 by Korablev et al. [2021] onto a contour map of the HCl columns calculated by my 1-D model (Figure 6.22) further demonstrates the 1-D model's ability to replicate the seasonal cycle of HCl that is being observed on Mars.

Including my chlorine chemistry scheme also introduces a new loss process for CH_4 on Mars. The reactions of Cl atoms with CH_4 molecules are over 1000 times more efficient at 298 K than the reactions of OH atoms. I found that the abundances of Cl produced by the heterogeneous chlorine chemistry routine, which is capable of replicating the HCl observations made by the ACS-MIR [Korablev et al., 2021], can destroy CH_4 at a rate 100–1700 times faster than previous models. Previous photochemical models of Mars require a physical or chemical sink for CH_4 600 times larger than what they calculate, which is achieved by the 1-D model. Further work and investigations need to be performed to enable the heterogeneous chlorine scheme to work over long periods of time, but my model results greatly improve upon the model estimates of CH_4's photochemical lifetime when HCl lies in abundances between $0\sim10$ ppb as seen by ACS-MIR and NOMAD.

Comparing my 1-D model H_2O_2 columns with and without the effects of chlorine chemistry (Figure 6.24) also demonstrates some improvements resulting from the updated photochemistry scheme when compared to H_2O_2 observations performed by Encrenaz et al. [2019]. The original 1-D model, and the 3-D LMD-GCM, produce too large an H_2O_2 column throughout the Martian year. The introduction of chlorine from dust greatly reduces the abundance of H_2O_2 at all points in the Martian year, bringing model outputs into better coincidence during the periods 0–150° and 300–360° L_S. During the middle of the year (150–300° L_S), the 1-D model lowers the H_2O_2 column by too large an amount, lowering model coincidence here. This period however requires the largest decrease to H_2O_2 (a drop of $\sim$ 30 ppb) in the 3-D LMD-GCM to bring their results into better agreement with the observed columns. The

introduction of chlorine chemistry into the 3-D LMD-GCM would have the potential to cause similar decreases, and a more accurate and better studied heterogeneous chlorine chemistry scheme in the model will likely yield to better agreement between our model H_2O_2 results and the observations of H_2O_2 from ground-based equipment.

7.3 Martian Photochemical Adjoint Sensitivity Analysis

In Chapter 5 I explained the concepts of the Tangent Linear Model and its resultant adjoint, and demonstrated the accuracy of the 1-D photochemical TLM/adjoint that I developed for Mars' atmosphere. The TLM I have developed was demonstrated to be accurate for tracer perturbations of up to $\sim$ 100% in magnitude, and is capable of working at any time and location on Mars for gas-phase and heterogeneous chemistry schemes, and for the study of inorganic, organic, and chlorine-containing tracers (Figure 5.3 and Figure 6.16). The resultant adjoint to be used in future sensitivity analysis experiments is very accurate, and can operate for periods of over 10 days whilst maintaining accuracy (Figure 5.4).

I demonstrate the 1-D photochemical adjoint, the first to be made for a non-Earth atmosphere, in Chapter 5 by using it to study the sensitivity of the H_2O_2 and O_3 columns to the initial model profiles of CO, O_2, H_2, and H_2O vapour and ice over time and space (Figure 5.5 and Figure 5.6). H_2O_2 is found to be driven primarily by H_2O vapour throughout the year, slightly more sensitive to the model H_2O abundances in the high north and south than in the equator. H_2O_2 is found to be negatively sensitive to H_2O ice, in agreement with prior modelling studies [Encrenaz et al., 2019]. Using profiles from the MCDv5.3 climatological datasets, my adjoint finds the strongest negative sensitivities to exist in the high southern latitudes during the northern spring, the period where Mars is furthest from the Sun and the south experiences long nights enabling higher atmospheric ice content to develop. In the equator the adjoint finds ice, when considering uptake of OH and HO_2, to have little impact on the overal H_2O_2 column.

My 1-D adjoint also demonstrates the sensitivity of O_3 to changes in the inorganic chemistry of Mars. Strong negative sensitivities to CO and H_2O vapour are seen during the northern spring (0–90° L_S), which become significantly smaller during the rest of the year in the equatorial regions. During this period where sensitivities to CO and H_2O vapour fall, the adjoint finds O_3 becoming signficantly more sensitive to the O_2 content of the atmosphere. O_3 is also calculated to be much more sensitive to the H_2O ice content in the atmosphere than H_2O_2, experiencing increases of 7–11% from 10% increases to the ice content in the high north and south during the polar winters. These studies enable us to see where errors or miscalculations may be appearing when comparing model outputs to satellite, ground-based, or *in-situ* observations.

In Chapter 6 I also perform adjoint sensitivity analysis of HCl profiles produced by my 1-D model to the dust and H_2O ice profiles measured by the ACS-TIRVIM that are used in the heterogeneous chlorine chemistry routines (Figure 6.17), and the initial abundances of inorganic compounds in the model runs 6.18). This method revealed that HCl is positively sensitive to H_2, H_2O vapour, and dust in the south during 270–300° L_S, the location and period over which the largest HCl observations occur. Discrepancies between model output and observations could be attributed to miscalculated abundances of these tracer gas species. Strong negative sensitivities to O_2 are experienced throughout the year, exceptions being in the northern hemisphere during the northern winter. Low coincidences between model HCl and ACS-MIR observations in the northern hemisphere are therefore not likely to be due to errors in O_2 in photochemical models, but these will have strong impacts on the HCl results elsewhere.

7.4 Future Work

Organic Oxidation Routine

The organic chemistry routine I adopted comes from the CAABA/MECCA v4.0 box model [Sander et al., 2019], and includes a simplified approach for the handling of R-O_2 permutation reactions. The simplifications involve assuming that CH_3O_2 is the most common co-reactant in the R-O_2 reactions [Jenkin et al., 1997], and also disregards reactions of OH that have very low branching ratios, often calculated in laboratories under Earth-atmosphere settings. The impacts on the CH_4 oxidation scheme for Mars in my model will be very low due to only two R-O_2 species being handled (CH_3O_2 and $HOCH_2O_2$) and the routine being significantly simpler. The addition of C_2H_6 however introduces 7 more R-O_2 species which increases the risk of errors impacting results. As demonstrated in Chapter 4, the abundances at which these are produced are very small (< 10^{-4} ppt), and the resultant profiles of gases such as HCHO and HCOOH are similarly very small - errors that do appear here from the permutation scheme will have very little real world impact. However, including Cl-chemistry greatly increases the rate of CH_4 loss, and can be expected to have a similar impact on C_2H_6. A greater study of the permutation reaction and its sources of error will need to be performed prior to studying the effects of chlorine on C_2H_6 on Mars.

Investigate a New Astrobiological Pathway for CH_4 Production

A new atmospheric source of CH_4 included in my model is the photolysis of CH_3CHO which is found to be efficient all the way down to the Martian surface (Figure 4.15) with photolysis rates of 10^{-6} s^{-1}. The presence of 50 ppt of C_2H_6 is capable of producing enough CH_3CHO to produce CH_4 at a rate of 10–100 molecules cm^{-3} s^{-1} in the equatorial latitudes of Mars, which could open up new investigations into biological activity on Mars. Acetalyne hydratase is an enzyme capable of catalysing the conversion of acetylene (C_2H_2) to CH_3CHO using liquid H_2O [Liao et al., 2010]. Instead of CH_4 produced via methanotrophic bacteria [Seto et al., 2019] diffusing through the regolith, this mechanism would see CH_3CHO seeping through the regolith to produce CH_4 upon exposure to UV radiation. The feasibility of a biological source such as sub-surface acetalyne hydratase on Mars could be investigated in laboratory experiments by assessing the abundances of C_2H_2 and H_2O required under Mars sub-surface conditions to produce sufficient CH_3CHO to be observed by Curiosity, and more modelling work should be perfomed to assess the CH_3CHO abundances at the surface needed to produce the prior observations of Mumma et al. [2009] and Giuranna et al. [2019].

Make Improvements to the TLM and Adjoint

The TLM I developed only considered the rates of change due to trace gas transport and photochemical interactions. This prevents the TLM, and the consequent adjoint, from dynamically calculating the evolution of H_2O ice from condensation and sublimation and dust from dust-devils and wind-stress lifting. Unfortunately, the H_2O ice condensation and sublimation routines cannot be effectively linearised by the TLM code due to the conditional nature of the routines involved in the non-linear model. However, efforts should be made to include the lifting of dust via wind-stress and its deposition onto the surface into the TLM code to enable adjoint sensitivity analysis to include support for dust transport. This would provide a powerful tool for use in dust-storm studies, and coupled with the linearised photochemistry routines it could be used to aid in interpreting the loss of hydrogen to space due to dust-storm activity recently observed by MAVEN [Stone et al., 2020]. As I have demonstrated in Chapter 6, HCl observations on Mars could be attributed to heterogeneous reactions between dust and OH and HO_2 molecules. To enable an accurate study of this mechanism via adjoint analysis in a 3-D model, the inclusion of a linearised dust transport scheme would be a high priority.

Perform Data Assimilation with the Photochemical Adjoint

Due to time constraints, I was unable to perform an assimilation study using the 1-D model's photochemical adjoint. The product of the adjoint model is a sensitivity vector that can be used in inverse modelling methods to produce the best initial conditions within the model responsible for producing an observational measurement by acting as the gradient of a cost-function that the routine aims to minimise, i.e. the difference in HCl from the model and the ACS-MIR observations. To assess where my 1-D model is going wrong when comparing HCl observations to the 1-D model output, an inverse modelling approach should be performed. This will show whether or not the heterogeneous chlorine scheme results can be improved by adjusting the aerosol profiles within their measurement errors, or whether increases or decreases to various inorganic compounds can improve 1-D model coincidences whilst keeping within the bounds of the inorganic abundances made by prior observations.

The recent work of Lefèvre et al. [2021] used the 3-D LMD-GCM to study the relationship of O_3 and H_2O vapour from SPICAM measurements, and found that the photochemistry scheme produces a deficit in the LMD-GCM's O_3 column when compared to those seen by SPICAM. The 1-D adjoint should be employed over key regions of this study, and used to assess what species in the model may be causing the O_3 deficit and how they can be amended. Performing an assimilation routine with the adjoint sensitivity vector as the cost-function gradient, using ACS and NOMAD observations of ice, dust, and H_2O vapour could then be used to assess whether alterations to these species within measurement errors can explain the lack of O_3 in the LMD-GCM model.

The production of a 3-D photochemical adjoint for use within the LMD-OU GCM would be a great asset to Martian atmospheric science, enabling powerful forms of data assimilation to be performed. To do this, I would first have to create a linearised horizontal transport scheme. Issues regarding computational efficiency will arise though, due to the increasing size of the TLM and the number of calculations it needs to perform. Prior to attempting this, it would be advised to go over the TLM code again and assess ways of increasing its computational efficiency. This could be done by removing the considerations of inert tracers like Ar and N_2 from the TLM considerations, and looking for areas where negligible values are being calculated in the linearised routines and removing them. A 3-D adjoint would be able to provide insights into the O_3 deficit in our models [Lefèvre et al., 2021], the hemispheric asymmetry of CO [Smith et al., 2018], and the recently discovered Martian atmospheric chlorine cycle [Aoki et al., 2021].

Improve the Heterogeneous Chlorine Routine

The heterogeneous chemistry scheme I created and studied in Chapter 6 is in need of refinement prior to extended model runs. There is no consideration of chlorine content trapped within the soil and airborne dust grains, which needs to be considered to prevent an infinite supply of chlorine being released over time to the Martian atmosphere. I included a dynamic surface deposition routine for HCl onto the surface, calculating the laminar and turbulent layer resistances R_a and R_b, which should be extended to other chlorine-containing tracers such as HOCl, Cl_2, and $HClO_4$ as a means of reintroducing chlorine to the surface. Reaction rates in the dust grains themselves, where OH and HO_2 react with the mineral structure of the dust to release Cl or ClO, should also be studied, because the model currently assumes that dust grains release 1 ClO_x compound per OH and HO_2 molecule adsorbed onto their surface. This would greatly increase the lifetime of the Cl trapped in the dust, and contribute to keeping the total mass of Cl trapped in the dust constant. Including a tracer within my 1-D model that represents Cl abundances remaining in dust grains is a possibility that would require only small adjustments to the code, but including the change to trapped chlorine from dust transport would be much more of a challenge.

More laboratory studies are also needed to assess the feasibility of the heterogeneous chlorine scheme. The release of ClO_x is assumed by me, and is loosely drawn from the work of George and Abbatt [2010] who observed the release of Cl_2 from mineral dust when the dust is coated in a thin film of H_2O. Wang et al. [2020] found similar results using Mars soil analogues studying the impacts of electrostatic discharges on Cl^- released from dust grains. The mechanism behind George and Abbatt [2010] chlorine findings is unconfirmed and also relies on the presence of liquid water making it unfeasible for Mars, and the dependency on large electric fields for Cl release in the work of Wang et al. [2020] implies that Mars would not be capable of producing sufficient chlorine for HCl production outside of dust-storms. A detailed laboratory study of HO_x species and their heterogeneous interactions with chlorine-containing dust grains is therefore crucial to understanding the exact mechanism driving the HCl cycle on Mars.

Study NO_x Heterogeneous Reactions with Dust

As Mars' dust has the potential to greatly impact the photochemistry of Mars via the release of ClO_x compounds, further studies of the NO_x chemistry in the lower atmosphere should also be conducted. NO_x species are capable of adsorbing onto dust grains on Earth [Ndour et al., 2008, Schuttlefield et al., 2008] and engaging in chemical reactions with the minerals trapped inside the grains [Wang et al., 2003]. These reactions could have pronounced effects on the oxygen chemistry of Mars' lower atmosphere by converting NO_2 molecules to NO via dust grain reactions [Underwood et al., 2001], effectively lowering the lifetime of O_2 in Mars' atmosphere below 70 km. Decreases in model O_2 abundances where shown in Figure 6.18 to

have strong impacts on the HCl profiles produced by the 1-D model's heterogeneous chemistry scheme, and also on H_2O_2 columns in the high polar latitudes. We know that current GCM models under-calculate the seasonal variations of O_2 at the Gale Crater from measurements made by Curiosity [Trainer et al., 2019], and the addition of NO_x heterogeneous chemistry on dust grains could provide significant improvements to our GCM model O_2 cycles.

Perform Long-term Chlorine Modelling Studies

When the chlorine content of the Martian dust and surface is balanced by some re-uptake mechanisms, the heterogeneous chlorine scheme should be used to study the long term impacts of chlorine chemistry on Mars. The presence of perchlorate in the Martian soil has been hypothesised to be the result of the atmospheric producion and subsequent surface deposition of $HClO_4$ [Catling et al., 2010]. I have included the atmospheric production of $HClO_4$ into the 1-D photochemistry model, but due to the restrictions of the length of the model runs I have not had the opportunity to study it over large enough periods of time. Figure 6.11 shows the $HClO_4$ diurnal variation calculated by my 1-D model after one sol of active chlorine chemistry, with vmrs reaching maximum values of 0.02 ppt. The short-term production of Mars' perchlorate is negligible, but a deposition routine like the one I developed for HCl should be produced and studied over long timescales, with an appropriately modified heterogeneous chlorine scheme, to assess the feasibility of Mars' surface perchlorate originating from atmospheric chemistry.

The long-term effects of Mars' atmospheric chlorine on stable tracers such as CO, H_2, and O_2 should be investigated. Introducing a source of chlorine dependent on the atmospheres dust content could have significant consequences on the production and loss rates of each of these species that can only be assessed with long model runs. Reactions of Cl with HO_2 and H_2 are the primary drivers of the HCl profiles in the 1-D model, so a source of chlorine in the model not previously considered will have the potential to greatly lower the lifetimes of O_2 and H_2. The decrease in OH and HO_2 below 70 km due to the adsorption onto dust will possibly have long term impacts on the rate of CO recycling back to CO_2 via reactions with OH. Hemispheric asymmetry in dust content and chlorine abundances could help to emphasise the hemispheric asymmetry that CO is seen to exhibit in our current photochemical models, but this again would only be achievable by longer model runs using a 3-D GCM equipped with a modified form of my heterogeneous chlorine chemistry scheme.

7.5 Summary

The work in this thesis has demonstrated that an expanded photochemistry model is of crucial importance for future General Circulation Models of Mars' atmosphere. HCHO and HCOOH are photochemical products of both CH_4 and C_2H_6 oxidation, whereas CH_3CHO and CH_3COOH are unique to C_2H_6. CH_4 is expected to have a photochemical lifetime of 100–600 years with current photochemistry schemes, but I find that the addition of a chlorine chemistry routine that can reproduce HCl profiles observed by the ACS-MIR can increase the photochemical sink strength of CH_4 by factors between 100–1700. HCHO and HCOOH are short-lived on Mars, with lifetimes ranging between 1–6 hours and 20–200 sols respectively.

I developed a photochemical adjoint that performs at a high level of accuracy for a large range of photochemistry schemes, which can provide powerful insights into the sensitivity of trace gas species on Mars to one another backwards in time. I used this adjoint model to demonstrate the seasonal variability of H_2O_2 and O_3's sensitivity on H_2O, CO, H_2O ice, and O_2, which could be taken further by using the adjoint model in assimilation processes to find the best initial model conditions for the reproduction of observational data.

The profiles of HCl observed by ACS-MIR and NOMAD aboard the ExoMars TGO were successfully reproduced by my 1-D model after I included relative humidity dependent uptake coefficients of OH and HO_2 onto dust grains, with a subsequent release of ClO_x species, and a temperature dependent uptake coefficient for HCl on H_2O ice. The 1-D model profiles coincide best with ACS-MIR observations of MY34 when using ACS-TIRVIM observed dust and ice profiles and ACS-MIR H_2O vapour profiles that roughly coincide with the HCl measurement. Using climatological dust and ice still produces observable (> 0.1 ppb) abundances of HCl, agreeing with the later observations during MY35 made by NOMAD [Aoki et al., 2021]. The heterogeneous chlorine chemistry routine releases too much ClO_x for extended runs however, but accurately models when and where the maximum and minimum HCl abundances observed by ACS-MIR and NOMAD occur on Mars.

Appendix A

Appendix

A.1 Equations Involved in the Tangent Linear Model

To construct the TLM of the 1-D photochemistry model, I rewrite the time-discretised form of the non-linear model equation in a form containing two fluxes - the flux of tracer species i at model layer l from vertical transport ($\Delta \mathrm{PQ}_{i,l}^{\mathrm{Trans}}$), and the flux from photochemical interactions ($\Delta \mathrm{PQ}_{i,l}^{\mathrm{Chem}}$), such that the non-linear equation is written as:

$$\frac{\Delta \mathrm{PQ}_{i,l}^{t}}{\Delta t} = \frac{\Delta \mathrm{PQ}_{i,l}^{\mathrm{Trans}}(\vec{\mathrm{PQ}}^{t}) + \Delta \mathrm{PQ}_{i,l}^{\mathrm{Chem}}(\vec{\mathrm{PQ}}^{t})}{\Delta t}, \tag{A.1}$$

where $\vec{\mathrm{PQ}}^{t}$ is a vector holding the mmr's of all tracer species i across all model layers l at model timestep t. This is simply the descretized format of Equation 5.2. Equation A.1 can be rewritten in vector form, as it applies to all tracer species across all model layers, and substituted into the equation for the TLM matrix (Equation 5.10) to give:

$$\mathbf{A}^{t} = \mathbf{I} + \Big(\frac{\partial}{\partial \vec{\mathrm{PQ}}^{t}} \frac{\Delta \mathrm{PQ}_{i,l}^{t}}{\Delta t} \Big) \Delta t \tag{A.2}$$

$$= \mathbf{I} + \frac{\partial}{\partial \vec{\mathrm{PQ}}^{t}} \Delta \vec{\mathrm{PQ}}^{\mathrm{Trans}} + \frac{\partial}{\partial \vec{\mathrm{PQ}}^{t}} \Delta \vec{\mathrm{PQ}}^{\mathrm{Chem}}. \tag{A.3}$$

The photochemistry model works by calculating the tendency of the tracers due to transport first, and then calculates the tendencies due to photochemical interactions using the updated values from the transport calculations. As the TLM runs parallel to the full non-linear model, the linearised transport flux is calculated first, followed by the linearised photochemistry flux.

A.1.1 Linearised Vertical Transport

The end equation that calculates the vertical flux for tracer i at layer l is simply:

$$\Delta \mathrm{PQ}_{i,l}^{\mathrm{Trans}} = \mathrm{PQ}_{i,l}^{t1} - \mathrm{PQ}_{i,l}^{t}, \tag{A.4}$$

in which $\mathrm{PQ}_{i,l}^{t1}$ is the tracer mmr value after it is updated for vertical transport. As my model interpolates physical atmospheric parameters relevant to vertical diffusion, e.g. temperature and pressure, the change in vertical flux of tracer i will only be effected by changes in tracer i itself. Linearising with respect to tracers j at layer m results in:

$$\frac{\partial}{\partial \mathrm{PQ}_{j,m}^{t}} \Delta \mathrm{PQ}_{i,l}^{\mathrm{Trans}} = \begin{cases} 0 & j \neq i \\ \frac{\partial}{\partial \mathrm{PQ}_{i,m}^{t}} \mathrm{PQ}_{i,l}^{t1} & i = j \quad \text{and} \quad m \neq l \\ \frac{\partial}{\partial \mathrm{PQ}_{i,m}^{t}} \mathrm{PQ}_{i,l}^{t1} - 1 & i = j \quad \text{and} \quad m = l\,. \end{cases} \tag{A.5}$$

The values of $\mathrm{PQ}_{i,l}^{t1}$ are calculated seperately at the top of the model, layer L, at the bottom of the model, l = 1, and in between, $2 \leq \mathrm{l} < L$. The transport tendencies are found using a series of mmr dependent and independent coefficients, and the model calculates these from the top of the model down. These coefficients are presented below:

$$\mathrm{z1}_l = \begin{cases} \Big(\mathrm{za}_L + \mathrm{zb}_L\Big)^{-1} & l = L \\ \Big(\mathrm{za}_l + \mathrm{zb}_l + \mathrm{zb}_{l+1} \times (1 - \mathrm{zd}_{l+1})\Big)^{-1} & 2 \leq l < L \\ \Big(\mathrm{za}_1 + \mathrm{zb}_1 + \mathrm{zb}_2 \times (1 - \mathrm{zd}_2)\Big) & l = 1 \end{cases} \tag{A.6}$$

$$\mathrm{zc}_{i,l} = \begin{cases} \mathrm{za}_L \times \mathrm{z1}_L \times \mathrm{PQ}_{i,L}^{t} & l = L \\ \Big(\mathrm{za}_l \mathrm{PQ}_{i,l}^{t} + \mathrm{zb}_{l+1} \mathrm{zc}_{i,l+1}\Big)\mathrm{z1}_l & 2 \leq l < L \\ \Big(\mathrm{za}_l \mathrm{PQ}_{i,l}^{t} + \mathrm{zb}_2 \mathrm{zc}_{i,2}\Big)\mathrm{z1}_l & l = 1 \end{cases} \tag{A.7}$$

$$\mathrm{zd}_{i,l} = \begin{cases} \mathrm{zb}_L \times \mathrm{z1}_L & l = L \\ \mathrm{zb}_l \mathrm{z1}_l & 2 \leq l < L \end{cases} \tag{A.8}$$

where za and zb are coefficients dependent only on pressure and temperature calculated by the non-linear code. These coefficients are used to find the updated mmr, $\mathrm{PQ}_{i,l}^{t1}$, through the equations:

$$\mathrm{PQ}_{i,l}^{t1} = \begin{cases} \mathrm{zc}_l + zd_l \times \mathrm{PQ}_{i,l-1}^{t} & 2 \leq l \leq \mathrm{L} \\ \mathrm{zc}_l & l = 1 \end{cases}, \tag{A.9}$$

iterating from the top of the model down to the surface. Noting that the only coefficient dependent on mmr, Equation A.9 can be differentiated with respect to tracer i at some model layer m:

$$\frac{\partial}{\partial \mathrm{PQ}^t_{i,m}} \mathrm{PQ}^{t1}_{i,l} = \begin{cases} \frac{\partial}{\partial \mathrm{PQ}^t_{i,m}} \mathrm{zc}_{i,l} & 2 \leq l \leq \mathrm{L} \quad \text{and} \quad m \neq l-1 \\ \frac{\partial}{\partial \mathrm{PQ}^t_{i,m}} \mathrm{zc}_{i,l} + \mathrm{zd}_l & 2 \leq l \leq \mathrm{L} \quad \text{and} \quad m = l-1 \\ \frac{\partial}{\partial \mathrm{PQ}^t_{i,m}} \mathrm{zc}_{i,l} & l = \mathrm{L} \quad \forall m \end{cases} . \tag{A.10}$$

The partial derivative of coefficient $\mathrm{zc}_{i,l}$ (Equation A.7) with respect to the mmr of tracer i at layer m can be found by noting that the partial derivative of $\mathrm{PQ}^t_{i,l}$ by $\mathrm{PQ}^t_{i,m}$ is equal to 1 for l = m and 0 for all others. This yields the following set of calculations for the differentiation of the top layer, L, the middle layers, $2 \leq l < L$, and the surface layer, $l = 1$ respectively:

$$\frac{\partial}{\partial \mathrm{PQ}_{i,m}} \mathrm{zc}_{i,L} = \begin{cases} \mathrm{za}_L \times \mathrm{z1}_L & m = L \\ 0 & m < L \end{cases} \tag{A.11}$$

$$\frac{\partial}{\partial \mathrm{PQ}_{i,m}} \mathrm{zc}_{i,l} = \begin{cases} \mathrm{za}_l \times \mathrm{z1}_l + \mathrm{zb}_{l+1} \frac{\partial}{\partial \mathrm{PQ}_{i,l}} \mathrm{zc}_{i,l+1} & m = l \\ \mathrm{zb}_{l+1} \frac{\partial}{\partial \mathrm{PQ}_{i,m}} \mathrm{zc}_{i,l+1} & m \neq l \end{cases} \tag{A.12}$$

$$\frac{\partial}{\partial \mathrm{PQ}_{i,m}} \mathrm{zc}_{i,1} = \begin{cases} \mathrm{za}_1 \mathrm{z1}_1 + \mathrm{zb}_2 \mathrm{z1}_1 \frac{\partial}{\partial \mathrm{PQ}_{i,1}} \mathrm{zc}_{i,2} & m = 1 \\ \mathrm{zb}_2 \mathrm{z1}_1 \frac{\partial}{\partial \mathrm{PQ}_{i,m}} \mathrm{zc}_{i,2} & m > 1 \end{cases} \tag{A.13}$$

Iterating from L down to $l = 1$ enables the successive calculations of zc's partial derivative at each layer l with respect to all model layers m. These values can then be substituted into Equation A.10, which enables the calculation of Equation A.5 to be performed. Performing Equation A.5 across all tracers and model layers yields the second term of the right hand side of Equation A.3.

A.1.2 Linearised Photochemistry Equations

The flux due to photochemical reactions is calculated in the 1-D model using units of number density (molecules cm^{-3}) as opposed to mmr (kg/kg). Tracer i at model layer l will have a number density denoted here as $\mathrm{N}_{i,l}$. The conversion of tracer mmr to number density is performed via:

$$\mathrm{N}^t_{i,l} = \frac{M^t_{\mathrm{mol,air},l} N^t_{\mathrm{air},l}}{M_{\mathrm{mol},i}} \times \mathrm{PQ}^t_{i,l}, \tag{A.14}$$

with $M^t_{\mathrm{mol,air},l}$ being the mean molar mass of dry air ($\sim$ 43.34 on Mars), $M_{\mathrm{mol},i}$ being the molar mass of tracer i (g mol^{-1}), and $N^t_{\mathrm{air},l}$ being the total atmospheric number density. $M^t_{\mathrm{mol,air},l}$ is calculated by the 1-D model at each timestep. It's dominated by the contributions from CO_2 ($\sim$ 95%), N_2 ($\sim$ 2.8%) and Ar ($\sim$ 2%) - as the 1-D model in this work operates with a fixed CO_2 profile, and N_2 and Ar are chemically inert and not included in the sensitivity analysis of this work, $M^t_{\mathrm{mol,air},l}$ is taken as a mmr-independent value supplied by the 1-D control run. The partial derivative of Equation A.14 with respect to some tracer j at layer m is thus:

$$\frac{\partial}{\partial \mathrm{PQ}_{j,m}} N^t_{i,l} = \frac{M^t_{\mathrm{mol,air},l} N^t_{\mathrm{air},l}}{M_{\mathrm{mol},i}} \times \frac{\partial}{\partial \mathrm{PQ}_{j,m}} \mathrm{PQ}^t_{i,l} \tag{A.15}$$

$$= \mathrm{V}^t_{i,l} \times \frac{\partial}{\partial \mathrm{PQ}_{j,m}} \mathrm{PQ}^t_{i,l}, \tag{A.16}$$

where $\mathrm{V}^t_{i,l}$ is the number density conversion factor of tracer i's mmr at model layer l.

The photochemistry routine comes after the vertical diffusion routines, and uses tracer abundances that have been updated with their vertical diffusion fluxes. The chemistry routine then iterates over 3 smaller chemistry timesteps, Δ t$_C$, of magnitude $\sim$ 600 s within one physical timestep, Δt. The tracer abundances upon entering this timeloop, updated with diffusion fluxes, will be referenced with the superscript t0, and are equal to:

$$\vec{\mathrm{PQ}}^{t0} = \vec{\mathrm{PQ}}^{t} + \Delta\vec{\mathrm{PQ}}^{\mathrm{Trans}}. \tag{A.17}$$

The three sub-chemistry timesteps will be denoted with the tc superscript. For tracer i at layer l linearised with respect to tracer j at layer m:

$$\frac{\partial}{\partial \mathrm{PQ}_{j,m}} \mathrm{PQ}^{t0}_{i,l} = \begin{cases} 0 \quad \forall\, j \neq i \\ 1 + \frac{\partial}{\partial \mathrm{PQ}_{i,l}} \Delta\mathrm{PQ}^{\mathrm{Trans}}_{i,l} \quad j = i,\, l = m \\ \frac{\partial}{\partial \mathrm{PQ}_{i,m}} \Delta\mathrm{PQ}^{\mathrm{Trans}}_{i,l} \quad j = i,\, l \neq m \end{cases} \tag{A.18}$$

The chemistry loop begins first by calculating and updating the number densities NO and NO_2, then proceeds to do the same for odd-hydrogen species (H, OH, HO_2) via the methods detailed in Chapter 2. Then, if the solar zenith angle in the model is greater than 95°, odd-oxygen (O, O_3) is updated. If chlorine chemistry is operational, the odd-chlorine (Cl, ClO) routine is then performed, updating Cl and ClO. Finally, the remainder of the tracers are handled. The TLM needs to work in parallel to the 1-D model, so I will detail the linearisation routines in this order.

Linearised Odd-Nitrogen

The summed NO_X family number density is assumed to be 0.6 ppb, and therefore a constant throughout the chemistry routine. A partition function, rno2_no is produced to determine the individual abundances of NO and NO_2. The non-linear equations are:

$$N_{NOx,l} = 6 \times 10^{-10} N_{\text{air},l} \tag{A.19}$$

$$\text{rno2_no} = \frac{d_2 N_{O3,l}^{tc-1} + d_3 N_{HO2,l}^{tc-1}}{j_no2 + d_1 N_{O,l}^{tc-1}} \tag{A.20}$$

$$N_{NO,l}^{tc} = \frac{N_{NOx,l}}{1 + \text{rno2_no}} \tag{A.21}$$

$$N_{NO2,l}^{tc} = N_{NO,l}^{tc} \times \text{rno2_no}. \tag{A.22}$$

The partial derivative of these with respect to the mmr vector $\vec{\text{PQ}}^t$ becomes:

$$\frac{\partial N_{NOx,l}}{\partial \vec{\text{PQ}}^t} = 0 \tag{A.23}$$

$$\frac{\partial \text{rno2_no2}}{\partial \vec{\text{PQ}}^t} = A_{rno2} \frac{\partial}{\partial \vec{\text{PQ}}^t} N_{O3,l}^{tc-1} + B_{rno2} \frac{\partial}{\partial \vec{\text{PQ}}^t} N_{HO2,l}^{tc-1} - C_{rno2} \frac{\partial}{\partial \vec{\text{PQ}}^t} N_{O,l}^{tc-1} \tag{A.24}$$

$$\frac{\partial N_{NO,l}}{\partial \vec{\text{PQ}}^t} = -A_{NO} \frac{\partial \text{rno2_no2}}{\partial \vec{\text{PQ}}^t} \tag{A.25}$$

$$\frac{\partial N_{NO2,l}}{\partial \vec{\text{PQ}}^t} = A_{NO2} \frac{\partial N_{NO,l}}{\partial \vec{\text{PQ}}^t} + B_{NO2} \frac{\partial \text{rno2_no2}}{\partial \vec{\text{PQ}}^t}, \tag{A.26}$$

with the coefficients detailed in Table A.1.

Table A.1: Coefficients used in the linearisation of NO and NO_2 number densities.

	A	B	C
rno2_no	$\frac{d_2}{j_no2 + d_1 N_{O,l}^{tc-1}}$	$\frac{d003}{j_no2 d_1 N_{O,l}^{tc-1}}$	$\frac{d_1 \text{rno2_no}}{j_no2 + d_1 N_{O,l}^{tc-1}}$
NO	$\frac{N_{NOx,l}}{(\text{rno2_no}+1)^2}$	-	-
NO2	rno2_no	$N_{NO,l}^{tc-1}$	-

Linearised Odd-Hydrogen

The non-linear equations for H, OH, and HO_2 are:

$$N^{t0}_{HOx,l} = N^{t0}_{H,l} + N^{t0}_{OH,l} + N^{t0}_{HO2,l} \tag{A.27}$$

$$N^{tc}_{H,l} = N^{tc-1}_{HOx} \times \left(1 + \frac{1 + \text{roh_ho2}^{-1}}{\text{rh_ho2}}\right) \tag{A.28}$$

$$N^{tc}_{OH,l} = N^{tc}_{H,l} \times \text{rh_ho2}^{-1} \tag{A.29}$$

$$N^{tc}_{HO2,l} = N^{tc}_{OH,l} \times \text{roh_ho2}, \tag{A.30}$$

where rh_ho2 and roh_ho2 are the partition functions described in Chapter 2. The number density of the summed HO_X family is calculated and advanced towards the end of the time loop, and will be detailed in Section A.1.2. The partial derivatives of these equations with respect to all tracer species across all models in the vector $\vec{\text{PQ}}^{\,t}$ are:

$$\frac{\partial}{\partial \vec{\text{PQ}}^{\,t}} N^{t0}_{HOx,l} = V^{t}_{H,l} \frac{\partial \text{PQ}^{t0}_{H,l}}{\partial \vec{\text{PQ}}^{\,t}} + V^{t}_{OH,l} \frac{\partial \text{PQ}^{t0}_{OH,l}}{\partial \vec{\text{PQ}}^{\,t}} + V^{t}_{HO2,l} \frac{\partial \text{PQ}^{t0}_{HO2,l}}{\partial \vec{\text{PQ}}^{\,t}} \tag{A.31}$$

$$\frac{\partial}{\partial \vec{\text{PQ}}^{\,t}} N^{tc}_{H,l} = A_H \frac{\partial N^{tc-1}_{HOx,l}}{\partial \vec{\text{PQ}}^{\,t}} - B_H \frac{\partial \text{roh_ho2}}{\partial \vec{\text{PQ}}^{\,t}} + C_H \frac{\partial \text{rh_ho2}}{\partial \vec{\text{PQ}}^{\,t}} \tag{A.32}$$

$$\frac{\partial}{\partial \vec{\text{PQ}}^{\,t}} N^{tc}_{HO2,l} = A_{HO2} \frac{\partial}{\partial \vec{\text{PQ}}^{\,t}} N^{tc}_{H,l} - B_{HO2} \frac{\partial \text{rh_ho2}}{\partial \vec{\text{PQ}}^{\,t}} \tag{A.33}$$

$$\frac{\partial}{\partial \vec{\text{PQ}}^{\,t}} N^{tc}_{OH,l} = A_{OH} \frac{\partial}{\partial \vec{\text{PQ}}^{\,t}} N^{tc}_{HO2,l} + B_{OH} \frac{\partial \text{roh_ho2}}{\partial \vec{\text{PQ}}^{\,t}}, \tag{A.34}$$

with coefficients displayed in Table A.2.

Table A.2: Coefficients used in Equation A.32–A.34 constructed of non-linear model control run values.

	A	B	C
H	$(1 + \frac{1+\text{roh_ho2}}{\text{rh_ho2}})^{-1}$	$\frac{A_H^2 \times N^{tc-1}_{HOx,l}}{\text{rh_ho2}}$	$\frac{B_H(1+\text{roh_ho2})}{\text{rh_ho2}}$
HO2	rh_ho2^{-1}	$\frac{N^{tc-1}_{H,l}}{\text{rh_ho2}^2}$	-
OH	roh_ho2	$N^{tc-1}_{HO2,l}$	-

Linearised Odd-Oxygen

The non-linear equations for odd-oxygen during daylight are:

$$N^{t0}_{Ox,l} = N^{t0}_{O,l} + N^{t0}_{O3,l} \tag{A.35}$$

$$N^{tc}_{O1D,l} = \frac{P_{O1D,l}}{L_{O1D,l}} \tag{A.36}$$

$$N^{tc}_{O3,l} = \frac{N^{tc-1}_{Ox,l}}{1 + \mathrm{ro_o3}} \tag{A.37}$$

$$N^{tc}_{O,l} = N^{tc}_{O3,l} \times \mathrm{ro_o3} \tag{A.38}$$

$$N^{tc}_{Ox,l} = \frac{N^{t0}_{Ox,l} + P_{Ox,l}\Delta t_C}{1 + (N^{tc-1}_{Ox,l})^{-1} L_{Ox,l}\Delta t_c}, \tag{A.39}$$

and the partial derivatives with respect to mmr vector $\vec{\mathrm{PQ}}^{\,t}$ are:

$$\frac{\partial}{\partial \vec{\mathrm{PQ}}^{\,t}} N^{t0}_{Ox,l} = V^t_{O,l} \frac{\partial \mathrm{PQ}^{t0}_{O,l}}{\partial \vec{\mathrm{PQ}}^{\,t}} + V^t_{O3,l} \frac{\partial \mathrm{PQ}^{t0}_{O3,l}}{\partial \vec{\mathrm{PQ}}^{\,t}} \tag{A.40}$$

$$\frac{\partial}{\partial \vec{\mathrm{PQ}}^{\,t}} N^{tc}_{O1D,l} = A_{O1D} \frac{\partial}{\partial \vec{\mathrm{PQ}}^{\,t}} P_{O1D,l} - B_{O1D} \frac{\partial}{\partial \vec{\mathrm{PQ}}^{\,t}} L_{O1D,l} \tag{A.41}$$

$$\frac{\partial}{\partial \vec{\mathrm{PQ}}^{\,t}} N^{tc}_{O3,l} = A_{O3} \frac{\partial}{\partial \vec{\mathrm{PQ}}^{\,t}} N^{tc-1}_{Ox,l} + B_{O3} \frac{\partial}{\partial \vec{\mathrm{PQ}}^{\,t}} \mathrm{ro_o3} \tag{A.42}$$

$$\frac{\partial}{\partial \vec{\mathrm{PQ}}^{\,t}} N^{tc}_{O,l} = A_{O} \frac{\partial}{\partial \vec{\mathrm{PQ}}^{\,t}} N^{tc}_{O3,l} + B_{O3} \frac{\partial}{\partial \vec{\mathrm{PQ}}^{\,t}} \mathrm{ro_o3} \tag{A.43}$$

$$\begin{aligned} \frac{\partial}{\partial \vec{\mathrm{PQ}}^{\,t}} N^{tc}_{Ox,l} = {} & A_{Ox} \frac{\partial}{\partial \vec{\mathrm{PQ}}^{\,t}} N^{t0}_{Ox,l} + B_{Ox} \frac{\partial}{\partial \vec{\mathrm{PQ}}^{\,t}} P_{Ox,l} \\ & - C_{Ox} \frac{\partial}{\partial \vec{\mathrm{PQ}}^{\,t}} L_{Ox,l} + D_{Ox} \frac{\partial}{\partial \vec{\mathrm{PQ}}^{\,t}} N^{tc-1}_{Ox,l}, \end{aligned} \tag{A.44}$$

and the coefficients are displayed in Table A.3.

Table A.3: Coefficients used in the linearisation of odd-oxygen species (Equations A.40–A.44.

	A	B	C	D
O1D	$\frac{1}{L_{O1D,l}}$	$\frac{P_{O1D,l}}{L^2_{O1D,l}}$	-	-
O3	$\frac{1}{1+\mathrm{ro_o3}}$	$A^2_{O3} N^{tc-1}_{Ox,l}$	-	-
O	ro_o3	$N^{tc}_{O3,l}$	-	-
Ox	$\frac{1}{1+(N^{tc-1}_{Ox,l})^{-1} L_{Ox,l}\Delta t_c}$	$A_{Ox}\Delta t_c$	$N^{tc}_{Ox,l} \frac{\Delta t_C}{N^{tc-1}_{Ox,l}}$	$C_{Ox} \times \frac{L_{Ox,l}}{N^{tc-1}_{Ox,l}}$

Linearised Odd-Chlorine

The non-linear equations for modelling Cl and ClO in the 1-D photochemistry model are:

$$N^{t0}_{ClOx,l} = N^{t0}_{Cl,l} + N^{t0}_{ClO,l} \tag{A.45}$$

$$N^{tc}_{Cl,l} = \frac{N^{tc-1}_{ClOx,l}}{1 + \mathrm{rclo_cl}} \tag{A.46}$$

$$N^{tc}_{ClO,l} = N^{tc}_{Cl,l} \times \mathrm{rclo_cl}, \tag{A.47}$$

the partial derivatives with respect to mmr vector $\vec{\mathrm{PQ}}^{t}$ become:

$$\frac{\partial}{\partial \vec{\mathrm{PQ}}^{t}} N^{t0}_{ClOx,l} = \mathrm{V}_{Cl,l} \vec{\mathrm{PQ}}^{t} PQ^{t0}_{Cl,l} + \mathrm{V}_{ClO,l} \vec{\mathrm{PQ}}^{t} PQ^{t0}_{ClO,l} \tag{A.48}$$

$$\frac{\partial}{\partial \vec{\mathrm{PQ}}^{t}} N^{tc}_{Cl,l} = A_{Cl} \frac{\partial}{\partial \vec{\mathrm{PQ}}^{t}} N^{tc-1}_{ClOx} - B_{Cl} \frac{\partial}{\partial \vec{\mathrm{PQ}}^{t}} \mathrm{rclo_cl} \tag{A.49}$$

$$\frac{\partial}{\partial \vec{\mathrm{PQ}}^{t}} N^{tc}_{ClO,l} = A_{ClO} \frac{\partial}{\partial \vec{\mathrm{PQ}}^{t}} N^{tc}_{Cl,l} + B_{ClO} \frac{\partial}{\partial \vec{\mathrm{PQ}}^{t}} \mathrm{rclo_cl}. \tag{A.50}$$

The advancement of the summed ClO_X number density is handled later, and will be detailed in Section A.1.2 alongside the summed HO_X number density.

Table A.4: Coefficients used in the linearisation of odd-chlorine species (Equations A.48–A.50).

	A	B
Cl	$\frac{1}{1+\mathrm{rclo_cl}}$	$A_{Cl} N^{tc}_{Cl}$
ClO	rclo_cl	$N^{tc}_{Cl,l}$

Remaining Chemistry

This section covers the linearisation of the chemical species not handled via the NO_X, HO_X, or ClO_X routines, as well as O and O_3 during the night (when the solar zenith angle is greater than 95°). As detailed in Chapter 6, the chlorine species excluding Cl and ClO are uniquely handled via the QSSA approach. The remaining inorganic and organic tracers however are handled either through SIBEM equation, or the steady-state approximation. I shall begin by detailing the linearisation of the SIBEM approach, followed by the steady-state approximation, and finally the QSSA scheme.

The non-linear SIBEM equation discretised by time is:

$$N_{i,l}^{tc} = \frac{N_{i,l}^{t0} + P_{i,l}\Delta t_C}{1 + L_{i,l}\Delta t_c}, \tag{A.51}$$

the partial derivative with respect to $\vec{\mathrm{PQ}}^t$ becomes:

$$\frac{\partial}{\partial \vec{\mathrm{PQ}}^t} N_{i,l}^{tc} = A_{SIBEM} \frac{\partial}{\partial \vec{\mathrm{PQ}}^t} N_{i,l}^{t0} + B_{SIBEM} \frac{\partial}{\partial \vec{\mathrm{PQ}}^t} P_{i,l} - C_{SIBEM} \frac{\partial}{\partial \vec{\mathrm{PQ}}^t} L_{i,l}. \tag{A.52}$$

The summed ClO_X and HO_X species are handled in this section of the model also, having a slightly altered form to the standard SIBEM equation. The loss terms, $L_{HOx,l}$ and $L_{ClOx,l}$, are in units of molec. cm^{-3} s^{-1} as opposed to s^{-1}, and thus requires normalisation by the summed family number density. Their advancements, and subsequent linearisations, are identical those done for O_X in Equation A.39, with the substitution of ClO_X and HO_X for the O_X subscripts.

For a species i with photochemical lifetime consistently less than the chemistry timestep $\Delta\,\mathrm{t}_C$, the non-linear Steady-State equation is:

$$N_{i,l}^{tc} = \frac{P_{i,l}}{L_{i,l}}, \tag{A.53}$$

the partial derivative with respect to $\vec{\mathrm{PQ}}^t$ becoming:

$$\frac{\partial}{\partial \vec{\mathrm{PQ}}^t} N_{i,l}^{tc} = A_{SS} \frac{\partial}{\partial \vec{\mathrm{PQ}}^t} P_{i,l} - B_{SS} \frac{\partial}{\partial \vec{\mathrm{PQ}}^t} L_{i,l}. \tag{A.54}$$

For chlorine compounds, as described in Chapter 6, the number densities are advanced in accordance to their atmospheric lifetimes at the model grid point l. If the lifetime ($\tau_{i,l} = \mathrm{L}_{i,l}^{-1}$) is greater than $10\times$ the chemistry timestep then the SIBEM equation is used, and Equation A.52 is the linearised form. If $\tau_{i,l}$ is less than 10% of the chemistry timestep, the Steady-State approximation is used and Equation A.53 is the linearised form. If $\tau_{i,l}$ lies within these two bounds, the simple exponential solution is adopted. It has the non-linear form:

$$N_{i,l}^{tc} = N_{i,l}^{t0} \exp\left(-L_{i,l}\Delta t_C\right) + \frac{P_{i,l}}{L_{i,l}}\left(1 - \exp\left(-L_{i,l}\Delta t_C\right)\right), \tag{A.55}$$

that has a partial derivative with respect to the mmr vector equal to:

$$\frac{\partial}{\partial \vec{\mathrm{PQ}}^t} N_{i,l}^{tc} = A_{QSSA} \frac{\partial}{\partial \vec{\mathrm{PQ}}^t} N_{i,l}^{t0} + B_{QSSA} \frac{\partial}{\partial \vec{\mathrm{PQ}}^t} P_{i,l} - C_{QSSA} \frac{\partial}{\partial \vec{\mathrm{PQ}}^t} L_{i,l}. \tag{A.56}$$

The coefficients of Equations A.52, A.53, and A.56 are presented in Table A.5.

Table A.5

	A	B	C
SIBEM	$\frac{1}{1+L_{i,l}\Delta t_C}$	$A_{SIBEM} \times \Delta t_C$	$B_{SIBEM} \times N_{i,l}^{tc}$
SS	$\frac{1}{L_{i,l}}$	$A_{SS} \times N_{i,l}^{tc}$	-
QSSA	$\exp(-L_{i,l}\Delta t_C)$	$\frac{1-A_{QSSA}}{L_{i,l}}$	$N_{i,l}^{t0}\Delta t_C + \frac{P_{i,l}}{L_{i,l}} B_{QSSA}$ - $\frac{P_{i,l}}{L_{i,l}} \Delta t_c A_{QSSA}$

Linearised Number Density to Mass Mixing Ratios

Upon exit of the chemistry time-loop, the linearised photochemistry scheme returns a $IL \times IL$ matrix (for I total tracer species and L total model layers), $\partial \vec{N}^{t2} / \partial \vec{\mathrm{PQ}}^t$, in which the superscript $t2$ indicates the values upon exiting the chemistry routine after the three chemistry sub-timesteps. The value of the chemistry flux in Equation A.1 for tracer species i at layer l is:

$$\Delta \mathrm{PQ}_{i,l}^{\mathrm{Chem}} = PQ_{i,l}^{t2} - PQ_{i,l}^{t0} \tag{A.57}$$

$$= \frac{1}{V_{i,l}^t N_{\mathrm{air},l}} \times N_{i,l}^{t2} - PQ_{i,l}^{t0}. \tag{A.58}$$

The partial derivative of this with respect to the mmr vector returns the third term on the right hand side of Equation A.3, which can be found by substituting in Equation A.18 into it. With linearised transport and photochemistry matrices, Equation A.3 can be performed by adding the two together along with the identity matrix **I**.

Appendix B

Appendix

B.1 ACS-MIR HCl and 1-D Model Comparisons

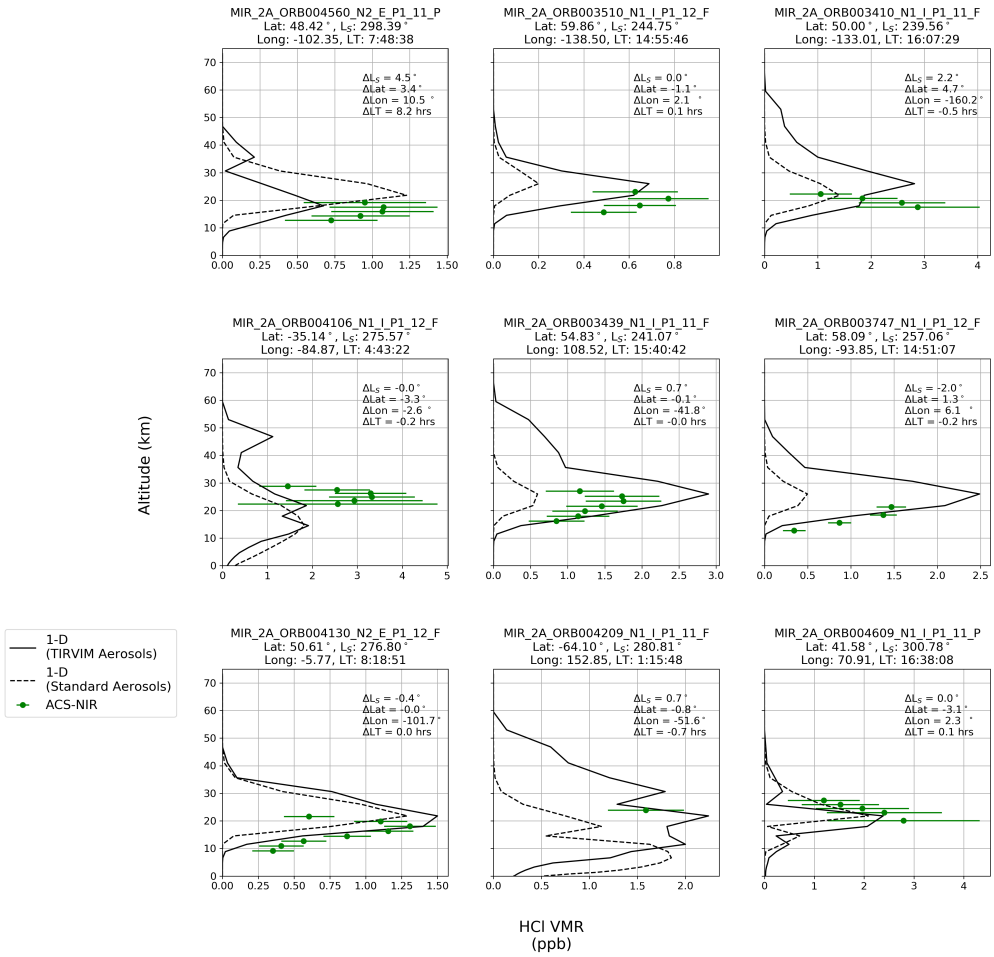


Figure B.1: Observations of HCl via the ACS-MIR during MY34 and HCl profiles produced by the 1-D model using the heterogeneous chlorine chemistry routine with ACS-TIRVIM dust and ice profiles and ACS-MIR H_2O vapour profiles, and aerosol and H_2O profiles from the MCDv5.3 databases Standard Climatological dataset.

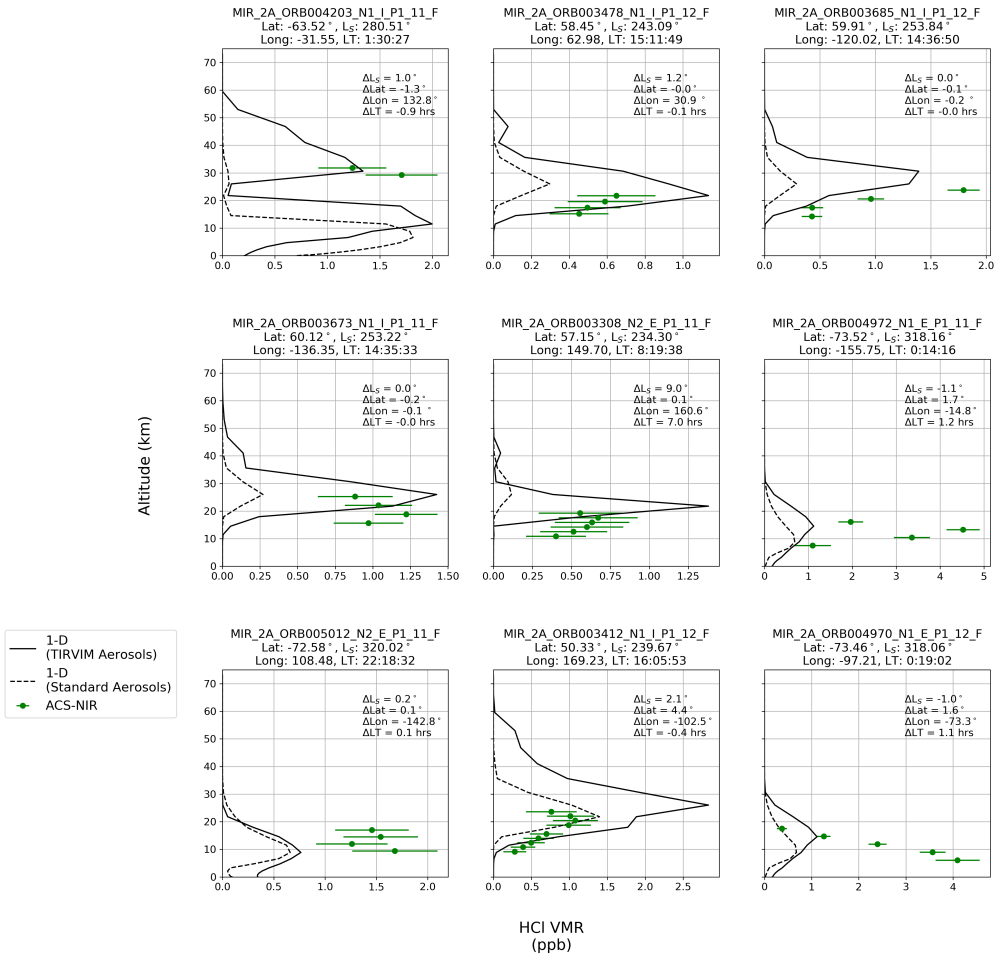


Figure B.2: Same as Figure B.1.

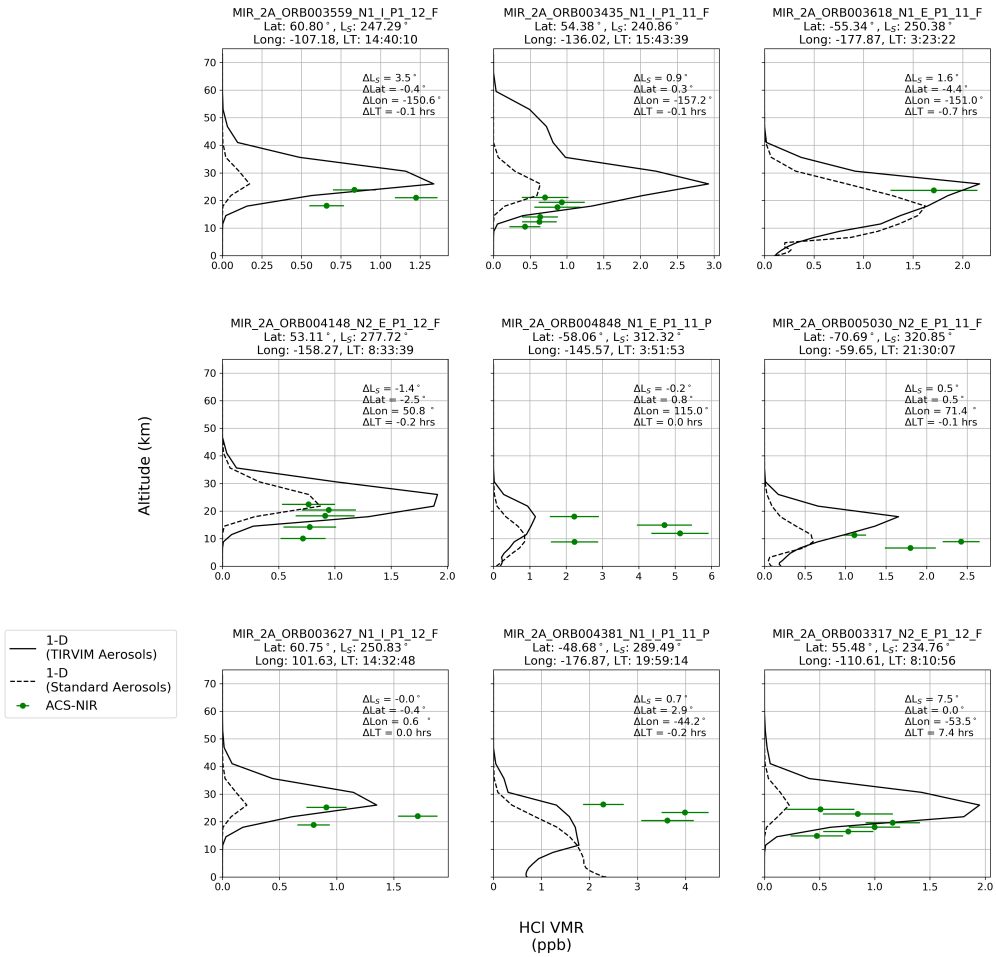


Figure B.3: Same as Figure B.1.

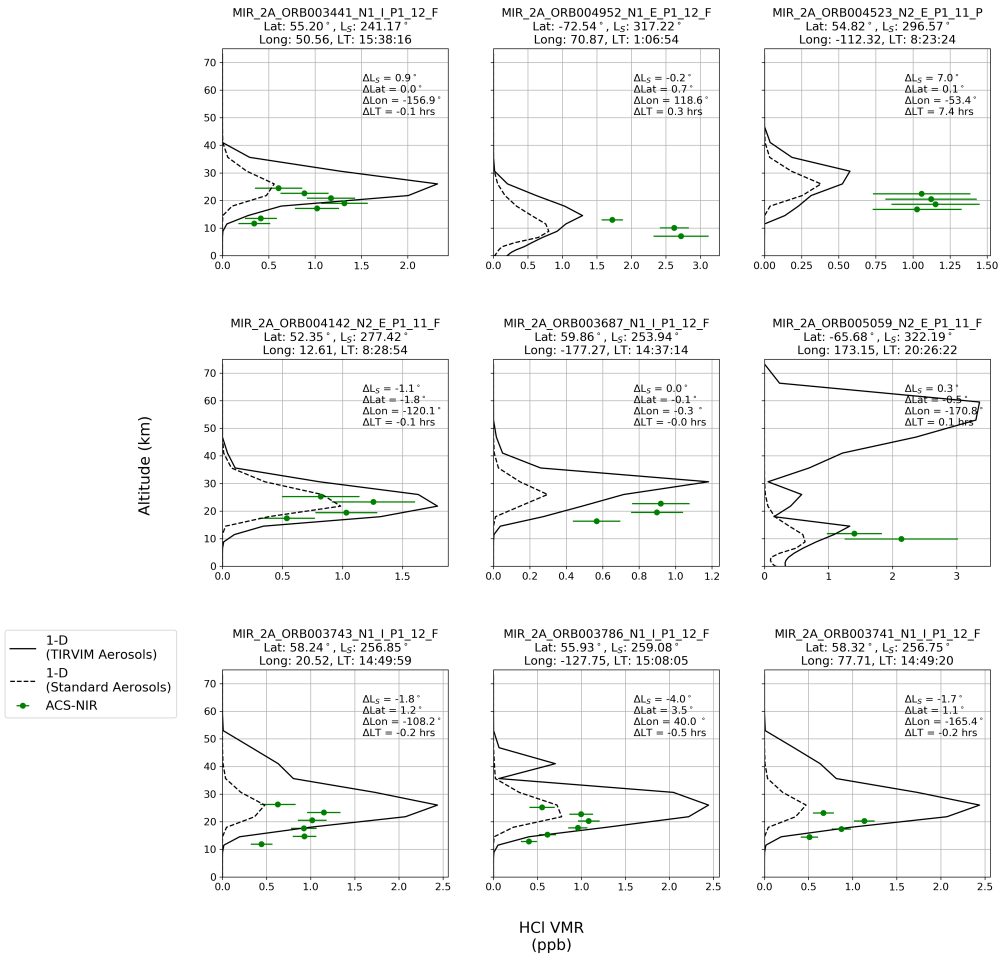


Figure B.4: Same as Figure B.1.

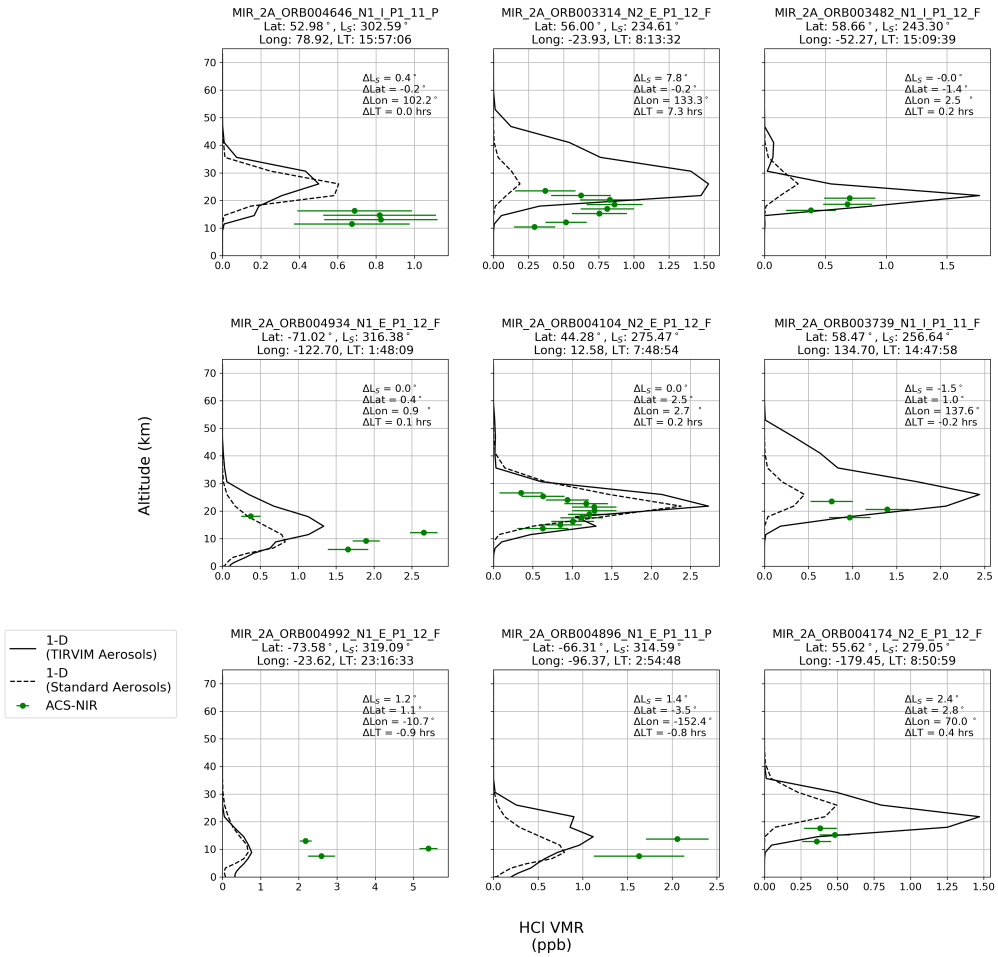


Figure B.5: Same as Figure B.1.

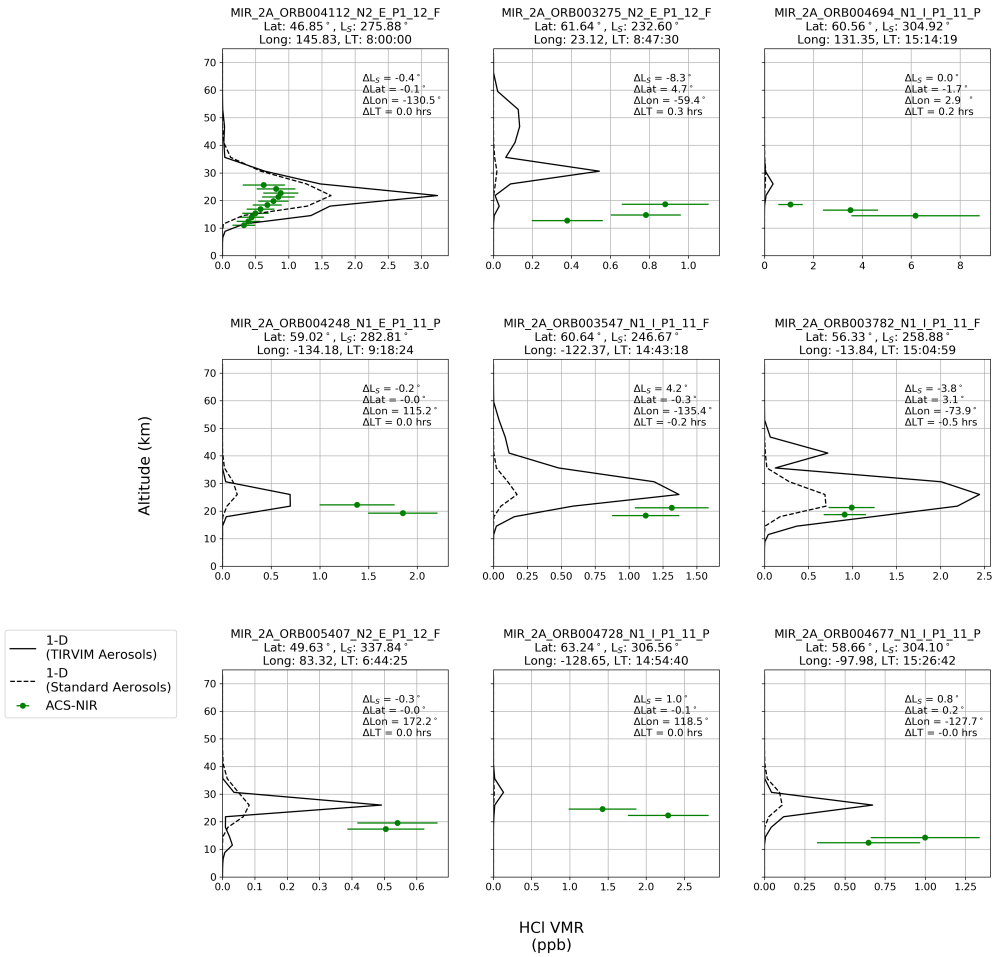


Figure B.6: Same as Figure B.1.

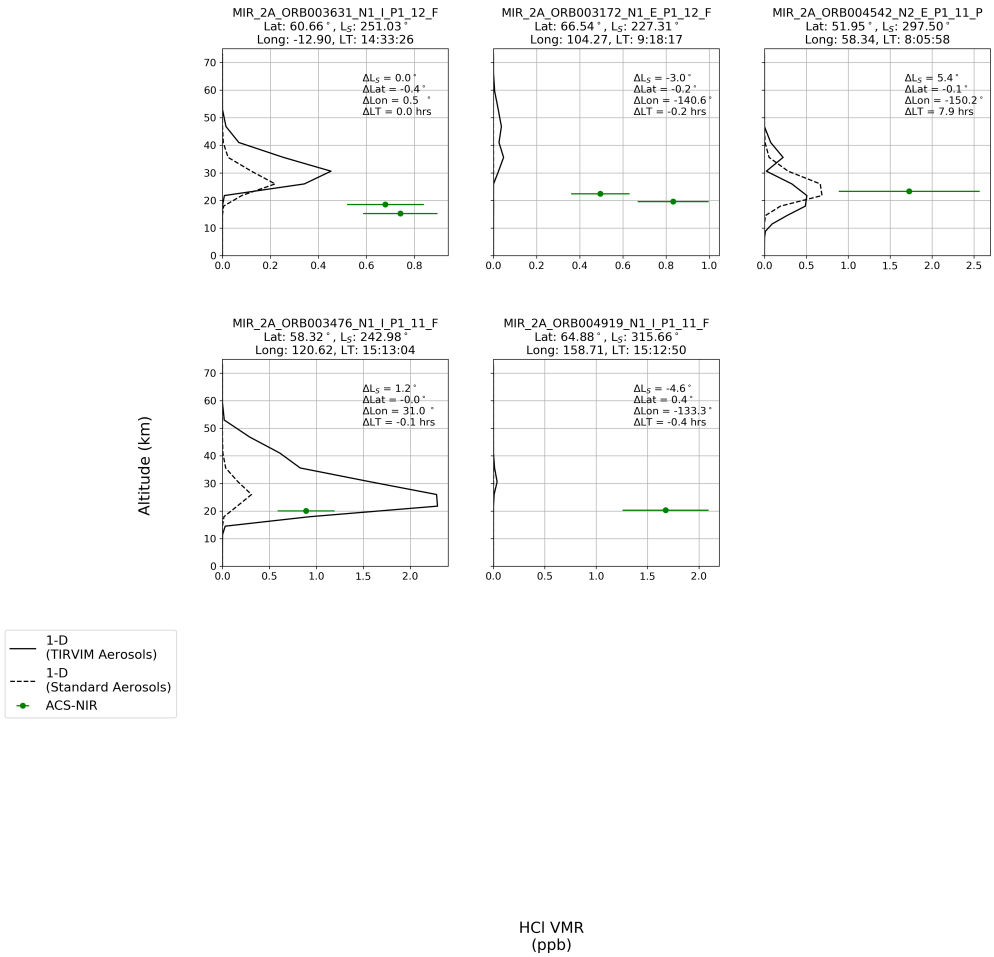


Figure B.7: Same as Figure B.1.

Bibliography

J. Alday, C. F. Wilson, P. G. J. Irwin, K. S. Olsen, L. Baggio, F. Montmessin, A. Trokhimovskiy, O. Korablev, A. A. Fedorova, D. A. Belyaev, A. Grigoriev, A. Patrakeev, and A. Shakun. Oxygen isotopic ratios in Martian water vapour observed by ACS MIR on board the ExoMars Trace Gas Orbiter. *Astronomy and Astrophysics*, 630:A91, October 2019a. doi: 10.1051/0004-6361/201936234.

J. Alday, C. F. Wilson, P. G. J. Irwin, K. S. Olsen, L. Baggio, F. Montmessin, A. Trokhimovskiy, O. Korablev, A. A. Fedorova, D. A. Belyaev, A. Grigoriev, A. Patrakeev, and A. Shakun. Oxygen isotopic ratios in Martian water vapour observed by ACS MIR on board the ExoMars Trace Gas Orbiter. *Astronomy and Astrophysics*, 630:A91, October 2019b. doi: 10.1051/0004-6361/201936234.

Carlton C Allen, Richard V Morris, David J Lindstrom, MM Lindstrom, and JP Lockwood. Jsc mars-1-martian regolith simulant. In *Lunar and Planetary Science Conference*, volume 28, 1997.

AD Anbar, M-T Leu, HA Nair, and YL Yung. Adsorption of ho x on aerosol surfaces: Implications for the atmosphere of mars. *Journal of Geophysical Research: Planets*, 98 (E6):10933–10940, 1993.

S Aoki, MJ Richter, C DeWitt, A Boogert, T Encrenaz, H Sagawa, H Nakagawa, AC Vandaele, MARCO Giuranna, and TK Greathouse. Stringent upper limit of ch4 on mars based on sofia/exes observations. *Astronomy & Astrophysics*, 610:A78, 2018.

S. Aoki, A. C. Vandaele, F. Daerden, G. L. Villanueva, G. Liuzzi, I. R. Thomas, J. T. Erwin, L. Trompet, S. Robert, L. Neary, S. Viscardy, R. T. Clancy, M. D. Smith, M. A. Lopez-Valverde, B. Hill, B. Ristic, M. R. Patel, G. Bellucci, J.-J. Lopez-Moreno, and the NOMAD team. Water vapor vertical profiles on mars in dust storms observed by tgo/nomad. *Journal of Geophysical Research: Planets*, 124(12):3482–3497, 2019. doi: https://doi.org/10.1029/2019JE006109. URL `https://agupubs.onlinelibrary.wiley.com/doi/abs/10.1029/2019JE006109`.

S Aoki, F Daerden, S Viscardy, IR Thomas, JT Erwin, S Robert, L Trompet, L Neary, GL Villanueva, and G Liuzzi. Annual appearance of hydrogen chloride on mars and a striking similarity with the water vapor vertical distribution observed by tgo/nomad. *Geophysical Research Letters*, 48(11):e2021GL092506, 2021.

R. Atkinson, D. L. Baulch, R. A. Cox, J. N. Crowley, R. F. Hampson, R. G. Hynes, M. E. Jenkin, M. J. Rossi, J. Troe, and IUPAC Subcommittee. Evaluated kinetic and photochemical data for atmospheric chemistry: Volume ii; gas phase reactions of organic species. *Atmospheric Chemistry and Physics*, 6(11):3625–4055, 2006. doi: 10.5194/acp-6-3625-2006. URL https://www.atmos-chem-phys.net/6/3625/2006/.

SK Atreya and ZG Gu. Photochemistry and stability of the atmosphere of mars. *Advances in Space Research*, 16(6):57–68, 1995.

Sushil K. Atreya, Ah-San Wong, Nilton O. Renno, William M. Farrell, Gregory T. Delory, Davis D. Sentman, Steven A. Cummer, John R. Marshall, Scot C.R. Rafkin, and David C. Catling. Oxidant enhancement in martian dust devils and storms: Implications for life and habitability. *Astrobiology*, 6(3):439–450, 2006. doi: 10.1089/ast.2006.6.439. URL https://doi.org/10.1089/ast.2006.6.439. PMID: 16805700.

Sushil K Atreya, Paul R Mahaffy, and Ah-San Wong. Methane and related trace species on mars: Origin, loss, implications for life, and habitability. *Planetary and Space Science*, 55 (3):358–369, 2007.

W Bruce Banerdt, Suzanne E Smrekar, Don Banfield, Domenico Giardini, Matthew Golombek, Catherine L Johnson, Philippe Lognonné, Aymeric Spiga, Tilman Spohn, Clément Perrin, et al. Initial results from the insight mission on mars. *Nature Geoscience*, 13(3):183–189, 2020.

Jeffrey R Barnes, Thomas D Walsh, and James R Murphy. Transport timescales in the martian atmosphere: General circulation model simulations. *Journal of Geophysical Research: Planets*, 101(E7):16881–16889, 1996.

Charles A. Barth, Charles W. Hord, A. Ian Stewart, Arthur L. Lane, Mary L. Dick, and Gail P. Anderson. Mariner 9 ultraviolet spectrometer experiment: Seasonal variation of ozone on mars. *Science*, 179(4075):795–796, 1973. ISSN 0036-8075. doi: 10.1126/science.179.4075.795. URL https://science.sciencemag.org/content/179/4075/795.

D. L. Baulch, C. J. Cobos, R. A. Cox, C. Esser, P. Frank, Th. Just, J. A. Kerr, M. J. Pilling, J. Troe, R. W. Walker, and J. Warnatz. Evaluated kinetic data for combustion modelling. *Journal of Physical and Chemical Reference Data*, 21(3):411–734, 1992. doi: 10.1063/1.555908. URL https://doi.org/10.1063/1.555908.

D. L. Baulch, C. T. Bowman, C. J. Cobos, R. A. Cox, Th. Just, J. A. Kerr, M. J. Pilling, D. Stocker, J. Troe, W. Tsang, R. W. Walker, and J. Warnatz. Evaluated kinetic data for combustion modeling: Supplement ii. *Journal of Physical and Chemical Reference Data*, 34(3):757–1397, 2005. doi: 10.1063/1.1748524.

Y. Bedjanian, M. N. Romanias, and A. El Zein. Uptake of ho_2 radicals on arizona test dust. *Atmospheric Chemistry and Physics*, 13(13):6461–6471, 2013. doi: 10.5194/acp-13-6461-2013. URL https://acp.copernicus.org/articles/13/6461/2013/.

Michael JS Belton and Donald M Hunten. The abundance and temperature of co_ $\{2\}$ in the martian atmosphere. *The Astrophysical Journal*, 145:454, 1966.

Michael JS Belton and Donald M Hunten. A search for o2 on mars and venus: A possible detection of oxygen in the atmosphere of mars. *The Astrophysical Journal*, 153:963, 1968.

Denis A Belyaev, Anna A Fedorova, Alexander Trokhimovskiy, Juan Alday, Franck Montmessin, Oleg I Korablev, Franck Lefèvre, Andrey S Patrakeev, Kevin S Olsen, and Alexey V Shakun. Revealing a high water abundance in the upper mesosphere of mars with acs onboard tgo. *Geophysical Research Letters*, 48(10):e2021GL093411, 2021.

Jeff A Berger, Mariek E Schmidt, Ralf Gellert, John L Campbell, Penelope L King, Roberta L Flemming, Douglas W Ming, Benton C Clark, Irina Pradler, and Scott JV VanBommel. A global mars dust composition refined by the alpha-particle x-ray spectrometer in gale crater. *Geophysical Research Letters*, 43(1):67–75, 2016.

Jean-Loup Bertaux, François Leblanc, Séverine Perrier, Eric Quémerais, Oleg Korablev, Emmanuel Dimarellis, Aurélie Reberac, François Forget, PC Simon, SA Stern, et al. Nightglow in the upper atmosphere of mars and implications for atmospheric transport. *Science*, 307(5709):566–569, 2005.

Jean-Loup Bertaux, Oleg Korablev, Séverine Perrier, Eric Quémerais, Franck Montmessin, F. Leblanc, S. Lebonnois, P. Rannou, F. Lefèvre, F. Forget, A. Fedorova, E. Dimarellis, A. Reberac, D. Fonteyn, J. Y. Chaufray, and S. Guibert. Spicam on mars express: Observing modes and overview of uv spectrometer data and scientific results. *Journal of Geophysical Research: Planets*, 111(E10), 2006. doi: https://doi.org/10.1029/2006JE002690. URL https://agupubs.onlinelibrary.wiley.com/doi/abs/10.1029/2006JE002690.

Jean-Pierre Bibring, Yves Langevin, John F. Mustard, François Poulet, Raymond Arvidson, Aline Gendrin, Brigitte Gondet, Nicolas Mangold, P. Pinet, F. Forget, Michel Berthé, Jean-Pierre Bibring, Aline Gendrin, Cécile Gomez, Brigitte Gondet, Denis Jouglet, François Poulet, Alain Soufflot, Mathieu Vincendon, Michel Combes, Pierre Drossart, Thérèse Encrenaz, Thierry Fouchet, Riccardo Merchiorri, GianCarlo Belluci, Francesca Altieri, Vittorio Formisano, Fabricio Capaccioni, Pricilla Cerroni, Angioletta Coradini, Sergio Fonti, Oleg Korablev, Volodia Kottsov, Nikolai Ignatiev, Vassili Moroz, Dimitri Titov, Ludmilla Zasova, Damien Loiseau, Nicolas Mangold, Patrick Pinet, Sylvain Douté, Bernard Schmitt, Christophe Sotin, Ernst Hauber, Harald Hoffmann, Ralf Jaumann, Uwe Keller, Ray Arvid-

son, John F. Mustard, Tom Duxbury, François Forget, and G. Neukum. Global mineralogical and aqueous mars history derived from omega/mars express data. *Science*, 312(5772): 400–404, 2006. ISSN 0036-8075. doi: 10.1126/science.1122659. URL https://science.sciencemag.org/content/312/5772/400.

K Biemann, John Oro, P Toulmin, Leslie E Orgel, AO Nier, DM Anderson, PG Simmonds, D Flory, AV Diaz, and DR Rushneck. Search for organic and volatile inorganic compounds in two surface samples from the chryse planitia region of mars. *Science*, 194(4260):72–76, 1976.

JE Blamont and E Chassefiere. First detection of ozone in the middle atmosphere of mars from solar occultation measurements. *Icarus*, 104(2):324–336, 1993.

Mark A Bullock, Carol R Stoker, Christopher P McKay, and Aaron P Zent. A coupled soil-atmosphere model of h2o2 on mars. *Icarus*, 107(1):142–154, 1994.

J. B. Burkholder, S. P. Sander, J. Abbatt, J. R. Barker, R. E. Huie, Jr. Kolb, C. E., III Kurylo, M. J., V. L. Orkin, D. M. Wilmouth, and P. H. Wine. NASA Data Evaluation (2015): Chemical Kinetics and Photochemical Data for Use in Atmospheric Studies. In *AGU Fall Meeting Abstracts*, volume 2015, pages A21B–0130, December 2015.

J. B. Burkholder, S. P. Sander, J. Abbatt, J. R. Barker, C. Cappa, J. D. Crounse, T. S. Dibble, R. E. Huie, C. E. Kolb, M. J. Kurylo, V. L. Orkin, C. J. Percival, D. M. Wilmouth, and P.H. Wine. Chemical kinetics and photochemical data for use in atmospheric studies, evaluation no. 19. *JPL Publication 19-5, Jet Propulsion Laboratory, Pasadena*, 2019.

I.M. Campbell and C.N. Gray. Rate constants for o(3p) recombination and association with n(4s). *Chemical Physics Letters*, 18(4):607 – 609, 1973. doi: https://doi.org/10.1016/0009-2614(73)80479-8.

Bruce A. Cantor. Moc observations of the 2001 mars planet-encircling dust storm. *Icarus*, 186 (1):60–96, 2007. ISSN 0019-1035. doi: https://doi.org/10.1016/j.icarus.2006.08.019. URL https://www.sciencedirect.com/science/article/pii/S0019103506002855.

Bruce A. Cantor, Philip B. James, and Wendy M. Calvin. Marci and moc observations of the atmosphere and surface cap in the north polar region of mars. *Icarus*, 208(1):61–81, 2010. ISSN 0019-1035. doi: https://doi.org/10.1016/j.icarus.2010.01.032. URL https://www.sciencedirect.com/science/article/pii/S0019103510000515.

Michael H. Carr and James W. Head III. Oceans on mars: An assessment of the observational evidence and possible fate. *Journal of Geophysical Research: Planets*, 108(E5), 2003. doi: https://doi.org/10.1029/2002JE001963. URL https://agupubs.onlinelibrary.wiley.com/doi/abs/10.1029/2002JE001963.

D. C. Catling, M. W. Claire, K. J. Zahnle, R. C. Quinn, B. C. Clark, M. H. Hecht, and S. Kounaves. Atmospheric origins of perchlorate on mars and in the atacama. *Journal of Geophysical Research: Planets*, 115(E1), 2010. doi: https://doi.org/10.1029/2009JE003425. URL https://agupubs.onlinelibrary.wiley.com/doi/abs/10.1029/2009JE003425.

MS Chaffin, J Deighan, NM Schneider, and AIF Stewart. Elevated atmospheric escape of atomic hydrogen from mars induced by high-altitude water. *Nature geoscience*, 10(3):174–178, 2017.

Brendon K. Chastain and Vincent Chevrier. Methane clathrate hydrates as a potential source for martian atmospheric methane. *Planetary and Space Science*, 55(10):1246–1256, 2007. ISSN 0032-0633. doi: https://doi.org/10.1016/j.pss.2007.02.003. URL https://www.sciencedirect.com/science/article/pii/S003206330700061X.

J-Y Chaufray, Francisco Gonzalez-Galindo, François Forget, Miguel A Lopez-Valverde, François Leblanc, Ronan Modolo, and Sebastien Hess. Variability of the hydrogen in the martian upper atmosphere as simulated by a 3d atmosphere–exosphere coupling. *Icarus*, 245:282–294, 2015.

Jean-Yves Chaufray, François Leblanc, Eric Quémerais, and Jean-Loup Bertaux. Martian oxygen density at the exobase deduced from oi 130.4-nm observations by spectroscopy for the investigation of the characteristics of the atmosphere of mars on mars express. *Journal of Geophysical Research: Planets*, 114(E2), 2009.

J.Y. Chaufray, J.L. Bertaux, F. Leblanc, and E. Quémerais. Observation of the hydrogen corona with spicam on mars express. *Icarus*, 195(2):598–613, 2008. ISSN 0019-1035. doi: https://doi.org/10.1016/j.icarus.2008.01.009. URL https://www.sciencedirect.com/science/article/pii/S0019103508000584.

L. E. Christensen, M. Okumura, S. P. Sander, R. J. Salawitch, G. C. Toon, B. Sen, J.-F. Blavier, and K. W. Jucks. Kinetics of ho2 + ho2 $\rightarrow$ h2o2 + o2: Implications for stratospheric h2o2. *Geophysical Research Letters*, 29(9):13–1–13–4, 2002. doi: 10.1029/2001GL014525.

Philip R. Christensen. Water at the Poles and in Permafrost Regions of Mars. *Elements*, 2 (3):151–155, 06 2006. ISSN 1811-5209. doi: 10.2113/gselements.2.3.151. URL https://doi.org/10.2113/gselements.2.3.151.

Philip R Christensen, Donald L Anderson, Stillman C Chase, Roger N Clark, Hugh H Kieffer, Michael C Malin, John C Pearl, James Carpenter, Nuno Bandiera, and F Gerald Brown. Thermal emission spectrometer experiment: Mars observer mission. *Journal of Geophysical Research: Planets*, 97(E5):7719–7734, 1992.

R. T. Clancy and H. Nair. Annual (perihelion-aphelion) cycles in the photochemical behavior of the global mars atmosphere. *Journal of Geophysical Research*, 101:12785–12790, 1996. doi: 10.1029/96JE00836.

R. T. Clancy, B. J. Sandor, M. J. Wolff, P. R. Christensen, M. D. Smith, J. C. Pearl, B. J. Conrath, and R. J. Wilson. An intercomparison of ground-based millimeter, MGS TES, and Viking atmospheric temperature measurements: Seasonal and interannual variability of temperatures and dust loading in the global Mars atmosphere. *Journal of Geophysical Research*, 105(E4):9553–9572, April 2000. doi: 10.1029/1999JE001089.

R. Todd Clancy and Brad J. Sandor. CO_2 ice clouds in the upper atmosphere of Mars. *Geophysical Research Letters*, 25(4):489–492, January 1998. doi: 10.1029/98GL00114.

R Todd Clancy, Michael J Wolff, and Philip B James. Minimal aerosol loading and global increases in atmospheric ozone during the 1996–1997 martian northern spring season. *Icarus*, 138(1):49–63, 1999.

R. Todd Clancy, Michael J. Wolff, and Philip R. Christensen. Mars aerosol studies with the MGS TES emission phase function observations: Optical depths, particle sizes, and ice cloud types versus latitude and solar longitude. *Journal of Geophysical Research (Planets)*, 108(E9):5098, September 2003. doi: 10.1029/2003JE002058.

R. Todd Clancy, Michael J. Wolff, Barbara A. Whitney, Bruce A. Cantor, and Michael D. Smith. Mars equatorial mesospheric clouds: Global occurrence and physical properties from Mars Global Surveyor Thermal Emission Spectrometer and Mars Orbiter Camera limb observations. *Journal of Geophysical Research (Planets)*, 112(E4):E04004, April 2007. doi: 10.1029/2006JE002805.

RT Clancy, BJ Sandor, and GH Moriarty-Schieven. A measurement of the 362 ghz absorption line of mars atmospheric h2o2. *Icarus*, 168(1):116–121, 2004.

Regina J. Cody, Paul N. Romani, Fred L. Nesbitt, Mark A. Iannone, Dwight C. Tardy, and Louis J. Stief. Rate constant for the reaction ch3 + ch3 $\rightarrow$ c2h6 at t = 155 k and model calculation of the ch3 abundance in the atmospheres of saturn and neptune. *Journal of Geophysical Research: Planets*, 108(E11), 2003. doi: https://doi.org/10.1029/2002JE002037. URL `https://agupubs.onlinelibrary.wiley.com/doi/abs/10.1029/2002JE002037`.

N. Cohen and K. R. Westberg. Chemical kinetic data sheets for high-temperature reactions. part ii. *Journal of Physical and Chemical Reference Data*, 20(6):1211–1311, 1991. doi: 10.1063/1.555901. URL `https://doi.org/10.1063/1.555901`.

Ralf Conrad. The global methane cycle: recent advances in understanding the microbial processes involved. *Environmental Microbiology Reports*, 1(5):285–292, 2009. doi: https://doi.org/10.1111/j.1758-2229.2009.00038.x. URL `https://sfamjournals.onlinelibrary.wiley.com/doi/abs/10.1111/j.1758-2229.2009.00038.x`.

Robert R Conway. Spectroscopy of the cameron bands in the mars airglow. *Journal of Geophysical Research: Space Physics*, 86(A6):4767–4775, 1981.

PL Cooper and JPD Abbatt. Heterogeneous interactions of oh and ho2 radicals with surfaces characteristic of atmospheric particulate matter. *The Journal of Physical Chemistry*, 100 (6):2249–2254, 1996.

F. Daerden, L. Neary, S. Viscardy, A. García Muñoz, R.T. Clancy, M.D. Smith, T. Encrenaz, and A. Fedorova. Mars atmospheric chemistry simulations with the gem-mars general circulation model. *Icarus*, 326:197–224, 2019. ISSN 0019-1035. doi: https://doi.org/10.1016/j.icarus.2019.02.030. URL https://www.sciencedirect.com/science/article/pii/S0019103518304883.

O. Dobis and S. W. Benson. Temperature coefficients of the rates of chlorine atom reactions with c2h6, c2h5, and c2h4. the rates of disproportionation and recombination of ethyl radicals. *Journal of the American Chemical Society*, 113(17):6377–6386, 1991. doi: 10.1021/ja00017a004. URL https://doi.org/10.1021/ja00017a004.

A. R. Douglass, R. S. Stolarski, S. E. Strahan, and B. C. Polansky. Sensitivity of arctic ozone loss to polar stratospheric cloud volume and chlorine and bromine loading in a chemistry and transport model. *Geophysical Research Letters*, 33(17), 2006. doi: https://doi.org/10.1029/2006GL026492. URL https://agupubs.onlinelibrary.wiley.com/doi/abs/10.1029/2006GL026492.

Jennifer L Eigenbrode, Roger E Summons, Andrew Steele, Caroline Freissinet, Maëva Millan, Rafael Navarro-González, Brad Sutter, Amy C McAdam, Heather B Franz, and Daniel P Glavin. Organic matter preserved in 3-billion-year-old mudstones at gale crater, mars. *Science*, 360(6393):1096–1101, 2018.

T Encrenaz, B Bezard, T Greathouse, S Holmes, M Richter, D Nuccitelli, J Lacy, S Lebonnois, F Lefeevre, and S Atreya. Ground-based high-resolution ir spectroscopy of mars: H2o and h2o2 mapping, search for ch4, and determination of co2 isotopic ratios. In *MAMO Workshop, Granada*. Citeseer, 2006.

T. Encrenaz, T.K. Greathouse, M.J. Richter, B. Bézard, T. Fouchet, F. Lefèvre, F. Montmessin, F. Forget, S. Lebonnois, and S.K. Atreya. Simultaneous mapping of h2o and h2o2 on mars from infrared high-resolution imaging spectroscopy. *Icarus*, 195(2):547–556, 2008. ISSN 0019-1035. doi: https://doi.org/10.1016/j.icarus.2008.01.022. URL https://www.sciencedirect.com/science/article/pii/S0019103508000390.

Th Encrenaz, Bruno Bézard, Thomas K Greathouse, MJ Richter, JH Lacy, SK Atreya, AS Wong, Sébastien Lebonnois, Franck Lefèvre, and François Forget. Hydrogen peroxide on mars: evidence for spatial and seasonal variations. *Icarus*, 170(2):424–429, 2004a.

Th Encrenaz, B Bézard, T.K Greathouse, M.J Richter, J.H Lacy, S.K Atreya, A.S Wong, S Lebonnois, F Lefèvre, and F Forget. Hydrogen peroxide on mars: evidence for spatial and seasonal variations. *Icarus*, 170(2):424–429, 2004b. ISSN 0019-1035. doi: https://doi.org/10.1016/j.icarus.2004.05.008. URL https://www.sciencedirect.com/science/article/pii/S0019103504001654.

Therese Encrenaz. Search for methane on mars: Observations, interpretation and future work. *Advances in Space Research*, 42(1):1–5, 2008.

Thérèse Encrenaz, Thomas K Greathouse, Shohei Aoki, Frank Daerden, Marco Giuranna, François Forget, Franck Lefèvre, Franck Montmessin, Thierry Fouchet, Bruno Bézard, et al. Ground-based infrared mapping of h2o2 on mars near opposition. *Astronomy & Astrophysics*, 627:A60, 2019.

Jan Willem Erisman, Addo Van Pul, and Paul Wyers. Parametrization of surface resistance for the quantification of atmospheric deposition of acidifying pollutants and ozone. *Atmospheric Environment*, 28(16):2595–2607, 1994.

G Etiope. Understanding the origin of methane on mars through isotopic and molecular data from nomad (exomars): will there be more answers or questions. In *Scientific workshop:'From Mars Express to ExoMars*, pages 27–28, 2018.

Giuseppe Etiope and Ronald W. Klusman. Geologic emissions of methane to the atmosphere. *Chemosphere*, 49(8):777–789, 2002. ISSN 0045-6535. doi: https://doi.org/10.1016/S0045-6535(02)00380-6. URL https://www.sciencedirect.com/science/article/pii/S0045653502003806.

Giuseppe Etiope, Akper Feyzullayev, and Calin L Baciu. Terrestrial methane seeps and mud volcanoes: A global perspective of gas origin. *Marine and Petroleum Geology*, 26(3):333–344, 2009.

Giuseppe Etiope, Bethany L Ehlmann, and Martin Schoell. Low temperature production and exhalation of methane from serpentinized rocks on earth: a potential analog for methane production on mars. *Icarus*, 224(2):276–285, 2013.

Kjell Fagerström, Anders Lund, Gharib Mahmoud, Jerzy T. Jodkowski, and Emil Ratajczak. Pressure and temperature dependence of the gas-phase reaction between methyl and hydroxyl radicals. *Chemical Physics Letters*, 224(1):43 – 50, 1994. ISSN 0009-2614. doi: https://doi.org/10.1016/0009-2614(94)00513-3. URL http://www.sciencedirect.com/science/article/pii/0009261494005133.

WM Farrell, GT Delory, and SK Atreya. Martian dust storms as a possible sink of atmospheric methane. *Geophysical research letters*, 33(21), 2006.

Kelly Fast, Theodor Kostiuk, Fred Espenak, John Annen, David Buhl, Tilak Hewagama, Michael F A'Hearn, David Zipoy, Timothy A Livengood, and Guido Sonnabend. Ozone abundance on mars from infrared heterodyne spectra: I. acquisition, retrieval, and anticorrelation with water vapor. *Icarus*, 181(2):419–431, 2006.

A.A. Fedorova, O.I. Korablev, J.-L. Bertaux, A.V. Rodin, F. Montmessin, D.A. Belyaev, and A. Reberac. Solar infrared occultation observations by spicam experiment on mars-express: Simultaneous measurements of the vertical distributions of h2o, co2 and aerosol. *Icarus*, 200(1):96–117, 2009. ISSN 0019-1035. doi: https://doi.org/10.1016/j.icarus.2008.11.006. URL https://www.sciencedirect.com/science/article/pii/S001910350800393X.

Anna Fedorova, Oleg Korablev, Severine Perrier, Jean-Loup Bertaux, Frank Lefevre, and Alexander Rodin. Observation of o2 1.27 μm dayglow by spicam ir: Seasonal distribution for the first martian year of mars express. *Journal of Geophysical Research: Planets*, 111 (E9), 2006.

Anna Fedorova, Alexander Trokhimovskiy, Oleg Korablev, Franck Montmessin, Karim Gizatullin, Daria Betsis, Alexander Lomakin, Andrey Patrakeev, Nikita Kokonkov, Alexey Shakun, and Jean-Loup Bertaux. Performance of the ACS NIR channel and O2 profiles. In *European Planetary Science Congress*, pages EPSC2018–490, September 2018.

Anna Fedorova, Franck Lefèvre, Alexander Trokhimovskiy, Oleg Korablev, Franck Montmessin, Francois Forget, Kevin Olsen, Mikhail Luginin, Alexander Lomakin, and Nikolay Ignatiev. Co and o2 in the martian atmosphere with acs nir onboard tgo. Technical report, Copernicus Meetings, 2021.

Anna A. Fedorova, Franck Montmessin, Oleg Korablev, Mikhail Luginin, Alexander Trokhimovskiy, Denis A. Belyaev, Nikolay I. Ignatiev, Franck Lefèvre, Juan Alday, Patrick G. J. Irwin, Kevin S. Olsen, Jean-Loup Bertaux, Ehouarn Millour, Anni Määttänen, Alexey Shakun, Alexey V. Grigoriev, Andrey Patrakeev, Svyatoslav Korsa, Nikita Kokonkov, Lucio Baggio, Francois Forget, and Colin F. Wilson. Stormy water on mars: The distribution and saturation of atmospheric water during the dusty season. *Science*, 367(6475):297–300, 2020. ISSN 0036-8075. doi: 10.1126/science.aay9522. URL https://science.sciencemag.org/content/367/6475/297.

E Fischer, Germán M Martínez, NO Rennó, LK Tamppari, and AP Zent. Relative humidity on mars: new results from the phoenix tecp sensor. *Journal of Geophysical Research: Planets*, 124(11):2780–2792, 2019.

S. Fonti and G. A. Marzo. Mapping the methane on Mars. *Astronomy & Astrophysics*, 512: A51, March 2010. doi: 10.1051/0004-6361/200913178.

S. Fonti, F. Mancarella, G. Liuzzi, T. L. Roush, M. Chizek Frouard, J. Murphy, and A. Blanco. Revisiting the identification of methane on Mars using TES data. *Astronomy and Astrophysics*, 581:A136, September 2015. doi: 10.1051/0004-6361/201526235.

F. Forget, F. Hourdin, and O. Talagrand. CO $_2$Snowfall on Mars: Simulation with a General Circulation Model. *Icarus*, 131:302–316, February 1998. doi: 10.1006/icar.1997.5874.

François Forget, Frédéric Hourdin, Richard Fournier, Christophe Hourdin, Olivier Talagrand, Matthew Collins, Stephen R Lewis, Peter L Read, and Jean-Paul Huot. Improved general circulation models of the martian atmosphere from the surface to above 80 km. *Journal of Geophysical Research: Planets*, 104(E10):24155–24175, 1999.

V Formisano, D Grassi, NI Ignatiev, and L Zasova. Iris mariner 9 data revisited: water and dust daily cycles. *Planetary and Space Science*, 49(13):1331–1346, 2001.

V. Formisano, S. Atreya, T. Encrenaz, N. Ignatiev, and M. Giuranna. Detection of Methane in the Atmosphere of Mars. *Science*, 306:1758–1761, December 2004. doi: 10.1126/science.1101732.

V Formisano, F Angrilli, G Arnold, S Atreya, G Bianchini, D Biondi, A Blanco, MI Blecka, A Coradini, and L Colangeli. The planetary fourier spectrometer (pfs) onboard the european mars express mission. *Planetary and Space Science*, 53(10):963–974, 2005.

T. Fouchet, E. Lellouch, N.I. Ignatiev, F. Forget, D.V. Titov, M. Tschimmel, F. Montmessin, V. Formisano, M. Giuranna, A. Maturilli, and T. Encrenaz. Martian water vapor: Mars express pfs/lw observations. *Icarus*, 190(1):32–49, 2007. ISSN 0019-1035. doi: https://doi.org/10.1016/j.icarus.2007.03.003. URL https://www.sciencedirect.com/science/article/pii/S0019103507001042.

I. A. Franchi, I. P. Wright, A. S. Sexton, and C. T. Pillinger. The oxygen-isotopic composition of Earth and Mars. *Meteoritics and Planetary Science*, 34(4):657–661, July 1999. doi: 10.1111/j.1945-5100.1999.tb01371.x.

G. Friedrichs, J. T. Herbon, D. F. Davidson, and R. K. Hanson. Quantitative detection of hco behind shock waves: The thermal decomposition of hco. *Phys. Chem. Chem. Phys.*, 4:5778–5788, 2002. doi: 10.1039/B205692E. URL http://dx.doi.org/10.1039/B205692E.

Jiajian Gao, Yingli Wang, Yuan Ping, Dacheng Hu, Guangwen Xu, Fangna Gu, and Fabing Su. A thermodynamic analysis of methanation reactions of carbon oxides for the production of synthetic natural gas. *RSC Advances*, 2:2358–2368, 2012. doi: 10.1039/C2RA00632D. URL http://dx.doi.org/10.1039/C2RA00632D.

A. Geminale, V. Formisano, and M. Giuranna. Methane in martian atmosphere: Average spatial, diurnal, and seasonal behaviour. *Planetary and Space Science*, 56(9):1194–1203, 2008. ISSN 0032-0633. doi: https://doi.org/10.1016/j.pss.2008.03.004. URL https://www.sciencedirect.com/science/article/pii/S0032063308000743.

A. Geminale, V. Formisano, and G. Sindoni. Mapping methane in martian atmosphere with pfs-mex data. *Planetary and Space Science*, 59(2):137–148, 2011. ISSN 0032-0633. doi: https://doi.org/10.1016/j.pss.2010.07.011. URL https://www.sciencedirect.com/science/article/pii/S0032063310002138. Methane on Mars: Current Observations, Interpretation and Future Plans.

I. J. George and J. P. D. Abbatt. Heterogeneous oxidation of atmospheric aerosol particles by gas-phase radicals. *Nature Chemistry*, 2(9):713–722, September 2010. doi: 10.1038/nchem.806.

J-C Gérard, Shohei Aoki, Leonardos Gkouvelis, Yannick Willame, Cédric Depiesse, Ian R Thomas, Bojan Risctic, AC Vandaele, Frank Daerden, and Benoît Hubert. Martian visible and ultraviolet dayglow: altitude, latitudinal and seasonal variations observed with nomad/tgo. 2020.

EL Gibb, MJ Mumma, N Dello Russo, MA DiSanti, and K Magee-Sauer. Methane in oort cloud comets. *Icarus*, 165(2):391–406, 2003.

Edward Gillen, Paul B Rimmer, and David C Catling. Statistical analysis of curiosity data shows no evidence for a strong seasonal cycle of martian methane. *Icarus*, 336:113407, 2020.

Marco Giuranna, Sébastien Viscardy, Frank Daerden, Lori Neary, Giuseppe Etiope, Dorothy Oehler, Vittorio Formisano, Alessandro Aronica, Paulina Wolkenberg, and Shohei Aoki. Independent confirmation of a methane spike on mars and a source region east of gale crater. *Nature Geoscience*, 12(5):326–332, 2019.

Elodie Gloesener, Özgür Karatekin, and Véronique Dehant. Stability and composition of ch4-rich clathrate hydrates in the present martian subsurface. *Icarus*, 353:114099, 2021. ISSN 0019-1035. doi: https://doi.org/10.1016/j.icarus.2020.114099. URL https://www.sciencedirect.com/science/article/pii/S0019103520304450. From Mars Express to Exomars.

I.E. Gordon, L.S. Rothman, C. Hill, R.V. Kochanov, Y. Tan, P.F. Bernath, M. Birk, V. Boudon, A. Campargue, K.V. Chance, B.J. Drouin, J.-M. Flaud, R.R. Gamache, J.T. Hodges, D. Jacquemart, V.I. Perevalov, A. Perrin, K.P. Shine, M.-A.H. Smith, J. Tennyson, G.C. Toon, H. Tran, V.G. Tyuterev, A. Barbe, A.G. Császár, V.M. Devi, T. Furtenbacher, J.J. Harrison, J.-M. Hartmann, A. Jolly, T.J. Johnson, T. Karman, I. Kleiner, A.A. Kyuberis,

J. Loos, O.M. Lyulin, S.T. Massie, S.N. Mikhailenko, N. Moazzen-Ahmadi, H.S.P. Müller, O.V. Naumenko, A.V. Nikitin, O.L. Polyansky, M. Rey, M. Rotger, S.W. Sharpe, K. Sung, E. Starikova, S.A. Tashkun, J. Vander Auwera, G. Wagner, J. Wilzewski, P. Wcisło, S. Yu, and E.J. Zak. The hitran2016 molecular spectroscopic database. *Journal of Quantitative Spectroscopy and Radiative Transfer*, 203:3 – 69, 2017. ISSN 0022-4073. doi: https://doi.org/10.1016/j.jqsrt.2017.06.038. URL http://www.sciencedirect.com/science/article/pii/S0022407317301073. HITRAN2016 Special Issue.

Raina V Gough, Margaret A Tolbert, Christopher P McKay, and Owen B Toon. Methane adsorption on a martian soil analog: An abiogenic explanation for methane variability in the martian atmosphere. *Icarus*, 207(1):165–174, 2010.

Raina V Gough, JJ Turley, GR Ferrell, KE Cordova, SE Wood, David O DeHaan, CP McKay, OB Toon, and MA Tolbert. Can rapid loss and high variability of martian methane be explained by surface h2o2? *Planetary and Space Science*, 59(2-3):238–246, 2011.

C. B. M. Groß, T. J. Dillon, G. Schuster, J. Lelieveld, and J. N. Crowley. Direct kinetic study of oh and o3 formation in the reaction of ch3c(o)o2 with ho2. *The Journal of Physical Chemistry A*, 118(6):974–985, 2014. doi: 10.1021/jp412380z. URL https://doi.org/10.1021/jp412380z. PMID: 24491030.

John P Grotzinger, Joy Crisp, Ashwin R Vasavada, Robert C Anderson, Charles J Baker, Robert Barry, David F Blake, Pamela Conrad, Kenneth S Edgett, Bobak Ferdowski, et al. Mars science laboratory mission and science investigation. *Space science reviews*, 170(1):5–56, 2012.

Alex Guenther, Chris Geron, Tom Pierce, Brian Lamb, Peter Harley, and Ray Fall. Natural emissions of non-methane volatile organic compounds, carbon monoxide, and oxides of nitrogen from north america. *Atmospheric Environment*, 34(12):2205 – 2230, 2000. ISSN 1352-2310. doi: https://doi.org/10.1016/S1352-2310(99)00465-3. URL http://www.sciencedirect.com/science/article/pii/S1352231099004653.

Sandrine Guerlet, Nikolay Ignatiev, François Forget, Thierry Fouchet, Alexey Shakun, Ehouarn Millour, Luca Montabone, Roland Young, Alexey Grigoriev, Alexander Trokhimovskiy, Franck Montmessin, and Oleg Korablev. Thermal structure and aerosol content in the martian atmosphere from ACS-TIRVIM on board ExoMars/TGO. In *EGU General Assembly 2019*, Vienne, Austria, April 2019. URL https://hal.archives-ouvertes.fr/hal-02409201.

Xin Guo, W Gregory Lawson, Mark I Richardson, and Anthony Toigo. Fitting the viking lander surface pressure cycle with a mars general circulation model. *Journal of Geophysical Research: Planets*, 114(E7), 2009.

Robert M Haberle, Francois Forget, Anthony Colaprete, James Schaeffer, William V Boynton, Nora J Kelly, and Matthew A Chamberlain. The effect of ground ice on the martian seasonal co2 cycle. *Planetary and Space Science*, 56(2):251–255, 2008.

Victoria E. Hamilton and Philip R. Christensen. Evidence for extensive, olivine-rich bedrock on Mars. *Geology*, 33(6):433, June 2005. doi: 10.1130/G21258.1.

R. Hanel, B. Conrath, W. Hovis, V. Kunde, P. Lowman, W. Maguire, J. Pearl, J. Pirraglia, C. Prabhakara, B. Schlachman, G. Levin, P. Straat, and T. Burke. Investigation of the martian environment by infrared spectroscopy on mariner 9. *Icarus*, 17(2):423–442, 1972. ISSN 0019-1035. doi: https://doi.org/10.1016/0019-1035(72)90009-7. URL https://www.sciencedirect.com/science/article/pii/0019103572900097.

P. Hartogh, C. Jarchow, E. Lellouch, M. de Val-Borro, M. Rengel, R. Moreno, A. S. Medvedev, H. Sagawa, B. M. Swinyard, T. Cavalié, D. C. Lis, M. I. Błęcka, M. Banaszkiewicz, D. Bockelée-Morvan, J. Crovisier, T. Encrenaz, M. Küppers, L. M. Lara, S. Szutowicz, B. Vandenbussche, F. Bensch, E. A. Bergin, F. Billebaud, N. Biver, G. A. Blake, J. A. D. L. Blommaert, J. Cernicharo, L. Decin, P. Encrenaz, H. Feuchtgruber, T. Fulton, T. de Graauw, E. Jehin, M. Kidger, R. Lorente, D. A. Naylor, G. Portyankina, M. Sánchez-Portal, R. Schieder, S. Sidher, N. Thomas, E. Verdugo, C. Waelkens, N. Whyborn, D. Teyssier, F. Helmich, P. Roelfsema, J. Stutzki, H. G. Leduc, and J. A. Stern. Herschel/HIFI observations of Mars: First detection of O_2 at submillimetre wavelengths and upper limits on HCl and H_2O_2. *Astronomy and Astrophysics*, 521:L49, October 2010. doi: 10.1051/0004-6361/201015160.

John D Hearn, Richard Weber, Robert Nichols, Michael V Henley, and Shannon Fox. Deposition of cl2 on soils during outdoor releases. *Journal of hazardous materials*, 252: 107–114, 2013.

M. H. Hecht, S. P. Kounaves, R. C. Quinn, S. J. West, S. M. M. Young, D. W. Ming, D. C. Catling, B. C. Clark, W. V. Boynton, J. Hoffman, L. P. DeFlores, K. Gospodinova, J. Kapit, and P. H. Smith. Detection of perchlorate and the soluble chemistry of martian soil at the phoenix lander site. *Science*, 325(5936):64–67, 2009a. doi: 10.1126/science.1172466.

MH Hecht, SP Kounaves, RC Quinn, SJ West, SMM Young, DW Ming, DC Catling, BC Clark, WV Boynton, and J Hoffman. Detection of perchlorate and the soluble chemistry of martian soil at the phoenix lander site. *Science*, 325(5936):64–67, 2009b.

Daven K Henze, Amir Hakami, and John H Seinfeld. Development of the adjoint of geos-chem. *Atmospheric Chemistry and Physics*, 7(9):2413–2433, 2007.

Kenneth C. Herr and George C. Pimentel. Infrared absorptions near three microns recorded over the polar cap of mars. *Science*, 166(3904):496–499, 1969. ISSN 0036-8075. doi: 10.1126/science.166.3904.496. URL https://science.sciencemag.org/content/166/3904/496.

Kenneth C. Herr and George C. Pimentel. Evidence for Solid Carbon Dioxide in the Upper Atmosphere of Mars. *Science*, 167(3914):47–49, January 1970. doi: 10.1126/science.167.3914.47.

J. T. Herron. Evaluated chemical kinetic data for the reactions of atomic oxygen o(3p) with saturated organic compounds in the gas phase. *Journal of Physical and Chemical Reference Data*, 17(3):967–1026, 1988. doi: 10.1063/1.555810. URL https://doi.org/10.1063/1.555810.

Eigil Hesstvedt, Öystein Hov, and Ivar SA Isaksen. Quasi-steady-state approximations in air pollution modeling: Comparison of two numerical schemes for oxidant prediction. *International Journal of Chemical Kinetics*, 10(9):971–994, 1978.

BB Hicks, DD Baldocchi, TP Meyers, RP Hosker, and DR Matt. A preliminary multiple resistance routine for deriving dry deposition velocities from measured quantities. *Water, Air, and Soil Pollution*, 36(3):311–330, 1987.

H. Hiesinger and J. W. Head III. The syrtis major volcanic province, mars: Synthesis from mars global surveyor data. *Journal of Geophysical Research: Planets*, 109(E1), 2004. doi: https://doi.org/10.1029/2003JE002143. URL https://agupubs.onlinelibrary.wiley.com/doi/abs/10.1029/2003JE002143.

J. Horita and M. E. Berndt. Abiogenic methane formation and isotopic fractionation under hydrothermal conditions. *Science*, 285(5430):1055–1057, 1999. ISSN 0036-8075. doi: 10.1126/science.285.5430.1055. URL https://science.sciencemag.org/content/285/5430/1055.

David G. Horvath, Pranabendu Moitra, Christopher W. Hamilton, Robert A. Craddock, and Jeffrey C. Andrews-Hanna. Evidence for geologically recent explosive volcanism in elysium planitia, mars. *Icarus*, 365:114499, 2021. ISSN 0019-1035. doi: https://doi.org/10.1016/j.icarus.2021.114499. URL https://www.sciencedirect.com/science/article/pii/S0019103521001779.

BJ Hoskins. Stability of the rossby-haurwitz wave. *Quarterly Journal of the Royal Meteorological Society*, 99(422):723–745, 1973.

H Houben. Assimilation of mars global surveyor meteorological data. *Advances in Space Research*, 23(11):1899–1902, 1999.

F Hourdin and A Armengaud. Test of a hierarchy of finite-volume schemes for transport of trace species in an atmospheric general circulation model. *Mon. Weather Rev*, 127:822–837, 1999.

Frédéric Hourdin, Phu Le Van, François Forget, and Olivier Talagrand. Meteorological variability and the annual surface pressure cycle on mars. *Journal of the atmospheric sciences*, 50(21):3625–3640, 1993.

HST. Seasonal changes in mars' north polar ice cap. URL https://www.jpl.nasa.gov/images/seasonal-changes-in-mars-north-polar-ice-cap.

Robert G. Hynes, Juliane C. Mössinger, and R. Anthony Cox. The interaction of hcl with water-ice at tropospheric temperatures. *Geophysical Research Letters*, 28(14):2827–2830, 2001. doi: https://doi.org/10.1029/2000GL012706. URL https://agupubs.onlinelibrary.wiley.com/doi/abs/10.1029/2000GL012706.

E. Hébrard, C. Listowski, P. Coll, B. Marticorena, G. Bergametti, A. Määttänen, F. Montmessin, and F. Forget. An aerodynamic roughness length map derived from extended martian rock abundance data. *Journal of Geophysical Research: Planets*, 117(E4), 2012. doi: https://doi.org/10.1029/2011JE003942. URL https://agupubs.onlinelibrary.wiley.com/doi/abs/10.1029/2011JE003942.

N. Iwagami, S. Ohtsuki, K. Tokuda, N. Ohira, Y. Kasaba, T. Imamura, H. Sagawa, G.L. Hashimoto, S. Takeuchi, M. Ueno, and S. Okumura. Hemispheric distributions of hcl above and below the venus' clouds by ground-based 1.7μm spectroscopy. *Planetary and Space Science*, 56(10):1424–1434, 2008. ISSN 0032-0633. doi: https://doi.org/10.1016/j.pss.2008.05.009. URL https://www.sciencedirect.com/science/article/pii/S0032063308001402. Ground-based and Venus Express Coordinated Campaign.

Telana L Jackson, William M Farrell, Gregory T Delory, and Jeyasingh Nithianandam. Martian dust devil electron avalanche process and associated electrochemistry. *Journal of Geophysical Research: Planets*, 115(E5), 2010.

B. M. Jakosky, M. Slipski, M. Benna, P. Mahaffy, M. Elrod, R. Yelle, S. Stone, and N. Alsaeed. Mars' atmospheric history derived from upper-atmosphere measurements of 38ar/36ar. *Science*, 355(6332):1408–1410, 2017. ISSN 0036-8075. doi: 10.1126/science.aai7721. URL https://science.sciencemag.org/content/355/6332/1408.

B.M. Jakosky, D. Brain, M. Chaffin, S. Curry, J. Deighan, J. Grebowsky, J. Halekas, F. Leblanc, R. Lillis, J.G. Luhmann, L. Andersson, N. Andre, D. Andrews, D. Baird, D. Baker, J. Bell, M. Benna, D. Bhattacharyya, S. Bougher, C. Bowers, P. Chamberlin, J.-Y. Chaufray, J. Clarke, G. Collinson, M. Combi, J. Connerney, K. Connour, J. Correira, K. Crabb, F. Crary, T. Cravens, M. Crismani, G. Delory, R. Dewey, G. DiBraccio, C. Dong, Y. Dong, P. Dunn, H. Egan, M. Elrod, S. England, F. Eparvier, R. Ergun, A. Eriksson, T. Esman, J. Espley, S. Evans, K. Fallows, X. Fang, M. Fillingim, C. Flynn, A. Fogle, C. Fowler, J. Fox, M. Fujimoto, P. Garnier, Z. Girazian, H. Groeller, J. Gruesbeck, O. Hamil, K.G. Hanley, T. Hara, Y. Harada, J. Hermann, M. Holmberg, G. Holsclaw, S. Houston, S. Inui, S. Jain,

R. Jolitz, A. Kotova, T. Kuroda, D. Larson, Y. Lee, C. Lee, F. Lefevre, C. Lentz, D. Lo, R. Lugo, Y.-J. Ma, P. Mahaffy, M.L. Marquette, Y. Matsumoto, M. Mayyasi, C. Mazelle, W. McClintock, J. McFadden, A. Medvedev, M. Mendillo, K. Meziane, Z. Milby, D. Mitchell, R. Modolo, F. Montmessin, A. Nagy, H. Nakagawa, C. Narvaez, K. Olsen, D. Pawlowski, W. Peterson, A. Rahmati, K. Roeten, N. Romanelli, S. Ruhunusiri, C. Russell, S. Sakai, N. Schneider, K. Seki, R. Sharrar, S. Shaver, D.E. Siskind, M. Slipski, Y. Soobiah, M. Steckiewicz, M.H. Stevens, I. Stewart, A. Stiepen, S. Stone, V. Tenishev, N. Terada, K. Terada, E. Thiemann, R. Tolson, G. Toth, J. Trovato, M. Vogt, T. Weber, P. Withers, S. Xu, R. Yelle, E. Yiğit, and R. Zurek. Loss of the martian atmosphere to space: Present-day loss rates determined from maven observations and integrated loss through time. *Icarus*, 315:146–157, 2018. ISSN 0019-1035. doi: https://doi.org/10.1016/j.icarus.2018.05.030. URL `https://www.sciencedirect.com/science/article/pii/S0019103517306917`.

Bruce M Jakosky. Atmospheric loss to space and the history of water on mars. *Annual Review of Earth and Planetary Sciences*, 49:71–93, 2021.

Michael E Jenkin, Sandra M Saunders, and Michael J Pilling. The tropospheric degradation of volatile organic compounds: a protocol for mechanism development. *Atmospheric Environment*, 31(1):81–104, 1997.

Eriita G Jones, Charles H Lineweaver, and Jonathan D Clarke. An extensive phase space for the potential martian biosphere. *Astrobiology*, 11(10):1017–1033, 2011.

A. V. Joshi and H. Wang. Master equation modeling of wide range temperature and pressure dependence of co + oh $\rightarrow$ products. *International Journal of Chemical Kinetics*, 38(1): 57–73, 2006.

KW Jucks, DG Johnson, KV Chance, WA Traub, JJ Margitan, GB Osterman, RJ Salawitch, and Y Sasano. Observations of oh, ho2, h2o, and o3 in the upper stratosphere: Implications for hox photochemistry. *Geophysical research letters*, 25(21):3935–3938, 1998.

Ralph Kahn. Ice haze, snow, and the mars water cycle. *Journal of Geophysical Research: Solid Earth*, 95(B9):14677–14693, 1990. doi: https://doi.org/10.1029/JB095iB09p14677. URL `https://agupubs.onlinelibrary.wiley.com/doi/abs/10.1029/JB095iB09p14677`.

Melinda A Kahre, James R Murphy, and Robert M Haberle. Modeling the martian dust cycle and surface dust reservoirs with the nasa ames general circulation model. *Journal of Geophysical Research: Planets*, 111(E6), 2006.

Melinda A Kahre, Jeffery L Hollingsworth, Robert M Haberle, and James R Murphy. Investigations of the variability of dust particle sizes in the martian atmosphere using the nasa ames general circulation model. *Icarus*, 195(2):576–597, 2008.

D. M. Kass, A. Kleinböhl, D. J. McCleese, J. T. Schofield, and M. D. Smith. Interannual similarity in the martian atmosphere during the dust storm season. *Geophysical Research Letters*, 43(12):6111–6118, 2016. doi: https://doi.org/10.1002/2016GL068978. URL https://agupubs.onlinelibrary.wiley.com/doi/abs/10.1002/2016GL068978.

D. M. Kass, J. T. Schofield, A. Kleinböhl, D. J. McCleese, N. G. Heavens, J. H. Shirley, and L. J. Steele. Mars climate sounder observation of mars' 2018 global dust storm. *Geophysical Research Letters*, 47(23):e2019GL083931, 2020. doi: https://doi.org/10.1029/2019GL083931. URL https://agupubs.onlinelibrary.wiley.com/doi/abs/10.1029/2019GL083931. e2019GL083931 2019GL083931.

Frederick Kaufman and John R. Kelso. M effect in the gas-phase recombination of o with o2. *The Journal of Chemical Physics*, 46(11):4541–4543, 1967. doi: 10.1063/1.1840589. URL https://doi.org/10.1063/1.1840589.

J. M. Keller, W. V. Boynton, S. Karunatillake, V. R. Baker, J. M. Dohm, L. G. Evans, M. J. Finch, B. C. Hahn, D. K. Hamara, D. M. Janes, K. E. Kerry, H. E. Newsom, R. C. Reedy, A. L. Sprague, S. W. Squyres, R. D. Starr, G. J. Taylor, and R. M. S. Williams. Equatorial and midlatitude distribution of chlorine measured by mars odyssey grs. *Journal of Geophysical Research: Planets*, 111(E3), 2006. doi: https://doi.org/10.1029/2006JE002679. URL https://agupubs.onlinelibrary.wiley.com/doi/abs/10.1029/2006JE002679.

Richard A Kerr. Question of martian methane is still up in the air, 2012.

A.S. Khayat, G.L. Villanueva, M.J. Mumma, and A.T. Tokunaga. A search for so2, h2s and so above tharsis and syrtis volcanic districts on mars using ground-based high-resolution submillimeter spectroscopy. *Icarus*, 253:130–141, 2015. ISSN 0019-1035. doi: https://doi.org/10.1016/j.icarus.2015.02.028. URL https://www.sciencedirect.com/science/article/pii/S0019103515000809.

A.SJ. Khayat, G.L. Villanueva, M.J. Mumma, and A.T. Tokunaga. A deep search for the release of volcanic gases on mars using ground-based high-resolution infrared and submillimeter spectroscopy: Sensitive upper limits for ocs and so2. *Icarus*, 296:1–14, 2017. ISSN 0019-1035. doi: https://doi.org/10.1016/j.icarus.2017.05.014. URL https://www.sciencedirect.com/science/article/pii/S0019103517300301.

Armin Kleinböhl, John T. Schofield, David M. Kass, Wedad A. Abdou, Charles R. Backus, Bhaswar Sen, James H. Shirley, W. Gregory Lawson, Mark I. Richardson, Fredric W. Taylor, Nicholas A. Teanby, and Daniel J. McCleese. Mars climate sounder limb profile retrieval of atmospheric temperature, pressure, and dust and water ice opacity. *Journal of Geophysical Research: Planets*, 114(E10), 2009. doi: https://doi.org/10.1029/2009JE003358. URL https://agupubs.onlinelibrary.wiley.com/doi/abs/10.1029/2009JE003358.

Arvydas Kliore, Dan L. Cain, Gerald S. Levy, Von R. Eshleman, Gunnar Fjeldbo, and Frank D. Drake. Occultation experiment: Results of the first direct measurement of mars's atmosphere and ionosphere. *Science*, 149(3689):1243–1248, 1965. ISSN 0036-8075. doi: 10.1126/science.149.3689.1243. URL https://science.sciencemag.org/content/149/3689/1243.

S. J. Knak Jensen, J. Skibsted, H. J. Jakobsen, I. L. ten Kate, H. P. Gunnlaugsson, J. P. Merrison, K. Finster, E. Bak, J. J. Iversen, J. C. Kondrup, and P. Nørnberg. A sink for methane on Mars? The answer is blowing in the wind. *Icarus*, 236:24–27, July 2014. doi: 10.1016/j.icarus.2014.03.036.

Elise W Knutsen, Geronimo L Villanueva, Giuliano Liuzzi, Matteo MJ Crismani, Michael J Mumma, Michael D Smith, Ann Carine Vandaele, Shohei Aoki, Ian R Thomas, and Frank Daerden. Comprehensive investigation of mars methane and organics with exomars/nomad. *Icarus*, 357:114266, 2021.

Jasper F Kok and Nilton O Renno. Electrification of wind-blown sand on mars and its implications for atmospheric chemistry. *Geophysical research letters*, 36(5), 2009.

O. Korablev, F. Montmessin, and A. Trokhimovskiy. The Atmospheric Chemistry Suite (ACS) of Three Spectrometers for the ExoMars 2016 Trace Gas Orbiter. *Space Science Reviews*, 214, February 2018. doi: 10.1007/s11214-017-0437-6.

O.I. Korablev, M. Ackerman, V.A. Krasnopolsky, V.I. Moroz, C. Muller, A.V. Rodin, and S.K. Atreya. Tentative identification of formaldehyde in the martian atmosphere. *Planetary and Space Science*, 41(6):441–451, 1993. ISSN 0032-0633. doi: https://doi.org/10.1016/0032-0633(93)90004-L. URL https://www.sciencedirect.com/science/article/pii/003206339390004L.

Oleg Korablev, Ann Carine Avandaele, Franck Montmessin, Anna A. Fedorova, Alexander Trokhimovskiy, François Forget, Franck Lefèvre, Frank Daerden, Ian R. Thomas, Loïc Trompet, Justin T. Erwin, Shohei Aoki, Séverine Robert, Lori Neary, Sébastien Viscardy, Alexey V. Grigoriev, Nikolay I. Ignatiev, Alexey Shakun, Andrey Patrakeev, Denis A. Belyaev, Jean-Loup Bertaux, Kevin S. Olsen, Lucio Baggio, Juan Alday, Yuriy S. Ivanov, Bojan Ristic, Jon Mason, Yannick Willame, Cédric Depiesse, Laszlo Hetey, Sophie Berkenbosch, Roland Clairquin, Claudio Queirolo, Bram Beeckman, Eddy Neefs, Manish R. Patel, Giancarlo Bellucci, Jose-Juan López-Moreno, Colin F. Wilson, Giuseppe Etiope, Lev Zelenyi, Håkan Svedhem, Jorge L. Vago, ACS Science Team, NOMAD Science Team, Gustavo Alonso-Rodrigo, Francesca Altieri, Konstantin Anufreychik, Gabriele Arnold, Sophie Bauduin, David Bolsée, Giacomo Carrozzo, R. Todd Clancy, Edward Cloutis, Matteo Crismani, Fabiana da Pieve, Emiliano D'Aversa, Natalia Duxbury, Therese Encrenaz, Thierry Fouchet, Bernd Funke, Didier Fussen, Maia Garcia-Comas, Jean-Claude Gérard, Marco Giuranna, Leo

Gkouvelis, Francisco Gonzalez-Galindo, Davide Grassi, Sandrine Guerlet, Paul Hartogh, James Holmes, Benoît Hubert, Jacek Kaminski, Ozgur Karatekin, Yasumasa Kasaba, David Kass, Igor Khatuntsev, Armin Kleinböhl, Nikita Kokonkov, Vladimir Krasnopolsky, Ruslan Kuzmin, Gaétan Lacombe, Orietta Lanciano, Emmanuel Lellouch, Stephen Lewis, Mikhail Luginin, Giuliano Liuzzi, Manuel López-Puertas, Miguel López-Valverde, Anni Määttänen, Arnaud Mahieux, Emmanuel Marcq, Javier Martin-Torres, Igor Maslov, Alexander Medvedev, Ehouarn Millour, Boris Moshkin, Michael J. Mumma, Hiromu Nakagawa, Robert E. Novak, Fabrizio Oliva, Dmitry Patsaev, Arianna Piccialli, Cathy Quantin-Nataf, Etienne Renotte, Birgit Ritter, Alexander Rodin, Frédéric Schmidt, Nick Schneider, Valery Shematovich, Michael D. Smith, Nicholas A. Teanby, Ed Thiemann, Nicolas Thomas, Jean Vander Auwera, Luis Vazquez, Geronimo Villanueva, Matthieu Vincendon, James Whiteway, Valérie Wilquet, Michael J. Wolff, Paulina Wolkenberg, Roger Yelle, Roland Young, Ludmila Zasova, and Maria Paz Zorzano. No detection of methane on Mars from early ExoMars Trace Gas Orbiter observations. *Nature*, 568(7753):517–520, April 2019. doi: 10.1038/s41586-019-1096-4.

Oleg Korablev, Kevin S. Olsen, Alexander Trokhimovskiy, Franck Lefèvre, Franck Montmessin, Anna A. Fedorova, Michael J. Toplis, Juan Alday, Denis A. Belyaev, Andrey Patrakeev, Nikolay I. Ignatiev, Alexey V. Shakun, Alexey V. Grigoriev, Lucio Baggio, Irbah Abdenour, Gaetan Lacombe, Yury S. Ivanov, Shohei Aoki, Ian R. Thomas, Frank Daerden, Bojan Ristic, Justin T. Erwin, Manish Patel, Giancarlo Bellucci, Jose-Juan Lopez-Moreno, and Ann C. Vandaele. Transient hcl in the atmosphere of mars. *Science Advances*, 7(7), 2021. doi: 10.1126/sciadv.abe4386. URL `https://advances.sciencemag.org/content/7/7/eabe4386`.

Timothy A Kral, Curtis R Bekkum, and Christopher P McKay. Growth of methanogens on a mars soil simulant. *Origins of Life and Evolution of the Biosphere*, 34(6):615–626, 2004.

Timothy A Kral, Timothy H Goodhart, Joshua D Harpool, Christopher E Hearnsberger, Graham L McCracken, and Stanley W McSpadden. Sensitivity and adaptability of methanogens to perchlorates: Implications for life on mars. *Planetary and Space Science*, 120:87–95, 2016.

V. A. Krasnopolsky. Photochemistry of the martian atmosphere (mean conditions). *Icarus*, 101(2):313–332, 1993.

V. A. Krasnopolsky. Solar activity variations of thermospheric temperatures on mars and a problem of co in the lower atmosphere. *Icarus*, 207(2):638–647, 2010.

V. A. Krasnopolsky. Annual mean mixing ratios of n2, ar, o2, and co in the martian atmosphere. *Planetary and Space Science*, 144:71–73, 2017.

V. A. Krasnopolsky and Paul D Feldman. Detection of molecular hydrogen in the atmosphere of mars. *Science*, 294(5548):1914–1917, 2001.

V. A. Krasnopolsky, G. L. Bjoraker, M. J. Mumma, and D. E. Jennings. High-resolution spectroscopy of mars at 3.7 and 8 μm: A sensitive search for h2o2, h2co, hcl, and ch4, and detection of hdo. *Journal of Geophysical Research: Planets*, 102(E3):6525–6534, 1997. doi: https://doi.org/10.1029/96JE03766. URL https://agupubs.onlinelibrary.wiley.com/doi/abs/10.1029/96JE03766.

V.A. Krasnopolsky. Uniqueness of a solution of a steady state photochemical problem: Applications to mars. *J. Geophys. Res.*, 100(E2):3263–3276, 1995. cited By 48.

Vladimir A Krasnopolsky. A sensitive search for so2 in the martian atmosphere: implications for seepage and origin of methane. *Icarus*, 178(2):487–492, 2005.

Vladimir A. Krasnopolsky. Photochemistry of the martian atmosphere: Seasonal, latitudinal, and diurnal variations. *Icarus*, 185(1):153–170, 2006a. ISSN 0019-1035. doi: https://doi.org/10.1016/j.icarus.2006.06.003. URL https://www.sciencedirect.com/science/article/pii/S0019103506002041.

Vladimir A Krasnopolsky. Some problems related to the origin of methane on mars. *Icarus*, 180(2):359–367, 2006b.

Vladimir A Krasnopolsky. Long-term spectroscopic observations of mars using irtf/cshell: Mapping of o2 dayglow, co, and search for ch4. *Icarus*, 190(1):93–102, 2007.

Vladimir A Krasnopolsky. Seasonal variations of photochemical tracers at low and middle latitudes on mars: Observations and models. *Icarus*, 201(2):564–569, 2009.

Vladimir A. Krasnopolsky. Search for methane and upper limits to ethane and so2 on mars. *Icarus*, 217(1):144–152, 2012. ISSN 0019-1035. doi: https://doi.org/10.1016/j.icarus.2011.10.019. URL https://www.sciencedirect.com/science/article/pii/S001910351100412X.

Vladimir A Krasnopolsky and Franck Lefèvre. Chemistry of the atmospheres of mars, venus, and titan. *Comparative Climatology of Terrestrial Planets*, 1:231–275, 2013.

Vladimir A Krasnopolsky, Jean Pierre Maillard, and Tobias C Owen. Detection of methane in the martian atmosphere: evidence for life? *Icarus*, 172(2):537–547, 2004.

Monika E Kress and Christopher P McKay. Formation of methane in comet impacts: implications for earth, mars, and titan. *Icarus*, 168(2):475–483, 2004. ISSN 0019-1035. doi: https://doi.org/10.1016/j.icarus.2003.10.013. URL https://www.sciencedirect.com/science/article/pii/S0019103503003609.

R. Kuhlmann, M. Lawrence, P. Crutzen, and P. Rasch. A model for studies of tropospheric ozone and nonmethane hydrocarbons: Model description and ozone results. *Journal of Geophysical Research, v.108 (2003)*, 108, 05 2003. doi: 10.1029/2002JD002893.

Gerard P Kuiper. Visual observations of mars, 1956. *The Astrophysical Journal*, 125:307, 1957.

T. I. Laura, D. P. Bruce, M. S. Bradley, and C. Anthony. Water ice cloud formation on mars is more difficult than presumed: Laboratory studies of ice nucleation on surrogate materials. *Icarus*, 210(2):985 – 991, 2010. ISSN 0019-1035. doi: https://doi.org/10.1016/j.icarus.2010.07.020.

S. Lebonnois, E. Quémerais, F. Montmessin, F. Lefèvre, S. Perrier, J.-L. Bertaux, and F. Forget. Vertical distribution of ozone on Mars as measured by SPICAM/Mars Express using stellar occultations. *Journal of Geophysical Research (Planets)*, 111:E09S05, September 2006. doi: 10.1029/2005JE002643.

F. Lefèvre and F. Forget. Observed variations of methane on Mars unexplained by known atmospheric chemistry and physics. *Nature*, 460:720–723, August 2009. doi: 10.1038/nature08228.

F. Lefèvre and V. A. Krasnopolsky. *Atmospheric Photochemistry*, pages 374–404. March 2017. doi: 10.1017/9781139060172.013.

F. Lefèvre, S. Lebonnois, F. Montmessin, and F. Forget. Three-dimensional modeling of ozone on mars. *Journal of Geophysical Research (Planets)*, 109:E07004, July 2004a. doi: 10.1029/2004JE002268.

F. Lefèvre, S. Lebonnois, F. Montmessin, and F. Forget. Three-dimensional modeling of ozone on mars. *Journal of Geophysical Research (Planets)*, 109:E07004, July 2004b. doi: 10.1029/2004JE002268.

F. Lefèvre, J.-L. Bertaux, S. Perrier, S. Lebonnois, O. Korablev, A. Fedorova, F. Montmessin, and F. Forget. The Martian Ozone Layer as Seen by SPICAM/Mars-Express. In *Seventh International Conference on Mars*, volume 1353 of *LPI Contributions*, page 3137, July 2007.

F. Lefèvre, J.-L. Bertaux, R. T. Clancy, T. Encrenaz, K. Fast, F. Forget, S. Lebonnois, F. Montmessin, and S. Perrier. Heterogeneous chemistry in the atmosphere of Mars. *Nature*, 454:971–975, aug 2008. doi: 10.1038/nature07116.

Franck Lefevre, GP Brasseur, I Folkins, AK Smith, and Paul Simon. Chemistry of the 1991–1992 stratospheric winter: Three-dimensional model simulations. *Journal of Geophysical Research: Atmospheres*, 99(D4):8183–8195, 1994.

Franck Lefèvre, A Trokhimovskiy, A Fedorova, Lucio Baggio, Gaetan Lacombe, Anni Määttänen, J-L Bertaux, F Forget, E Millour, O Venot, et al. Relationship between the ozone and water vapor columns on mars as observed by spicam and calculated by a global climate model. *Journal of Geophysical Research: Planets*, 126(4):e2021JE006838, 2021.

E Lellouch, T Encrenaz, T de Graauw, S Erard, P Morris, J Crovisier, H Feuchtgruber, T Girard, and M Burgdorf. The 2.4–45μm spectrum of mars observed with the infrared space observatory. *Planetary and Space Science*, 48(12):1393–1405, 2000. ISSN 0032-0633. doi: https://doi.org/10.1016/S0032-0633(00)00118-5. URL `https://www.sciencedirect.com/science/article/pii/S0032063300001185`. Mars Exploration Program.

G. V. Levin and P. A. Straat. Methane and life on Mars. In *Instruments and Methods for Astrobiology and Planetary Missions XII*, volume 7441, page 74410D, August 2009. doi: 10.1117/12.829183.

Stephen R Lewis, Matthew Collins, Peter L Read, François Forget, Frédéric Hourdin, Richard Fournier, Christophe Hourdin, Olivier Talagrand, and Jean-Paul Huot. A climate database for mars. *Journal of Geophysical Research: Planets*, 104(E10):24177–24194, 1999.

Jin Liao, L Gregory Huey, Zhen Liu, David J Tanner, Chris A Cantrell, John J Orlando, Frank M Flocke, Paul B Shepson, Andrew J Weinheimer, Samuel R Hall, et al. High levels of molecular chlorine in the arctic atmosphere. *Nature Geoscience*, 7(2):91–94, 2014.

Rong-Zhen Liao, Jian-Guo Yu, and Fahmi Himo. Mechanism of tungsten-dependent acetylene hydratase from quantum chemical calculations. *Proceedings of the National Academy of Sciences*, 107(52):22523–22527, 2010.

Rebecca Lindsey, Michon Scott, and R Simmon. What are phytoplankton. *NASA's Earth Observatory. Available on http://earthobservatory. nasa. gov/Librar y/phytoplankton*, 2010.

Dong C Liu and Jorge Nocedal. On the limited memory bfgs method for large scale optimization. *Mathematical programming*, 45(1):503–528, 1989.

Giuliano Liuzzi, Geronimo L. Villanueva, Michael J. Mumma, Michael D. Smith, Frank Daerden, Bojan Ristic, Ian Thomas, Ann Carine Vandaele, Manish R. Patel, José-Juan Lopez-Moreno, and Giancarlo Bellucci. Methane on mars: New insights into the sensitivity of ch4 with the nomad/exomars spectrometer through its first in-flight calibration. *Icarus*, 321: 671–690, 2019. ISSN 0019-1035. doi: https://doi.org/10.1016/j.icarus.2018.09.021. URL `https://www.sciencedirect.com/science/article/pii/S0019103518302112`.

Giuliano Liuzzi, Geronimo L Villanueva, Sebastien Viscardy, Daniel Mège, Matteo MJ Crismani, Shohei Aoki, Joanna Gurgurewicz, Pierre-Antoine Tesson, Michael J Mumma, Michael D Smith, et al. Probing the atmospheric cl isotopic ratio on mars: Implications for planetary evolution and atmospheric chemistry. *Geophysical Research Letters*, 48(9): e2021GL092650, 2021.

Philippe Lognonné, WB Banerdt, WT Pike, Domenico Giardini, U Christensen, Raphaël F Garcia, T Kawamura, S Kedar, B Knapmeyer-Endrun, L Margerin, et al. Constraints on the shallow elastic and anelastic structure of mars from insight seismic data. *Nature Geoscience*, 13(3):213–220, 2020.

Mikhail Luginin, Anna Fedorova, Nikolay Ignatiev, Alexey Grigoriev, Alexander Trokhimovskiy, Alexey Shakun, Franck Montmessin, and Oleg Korablev. Vertical distribution of dust and water ice during 2018 dust storm from tirvim and nir solar occultations onboard exomars/tgo. *Geophysical Research Abstracts*, 21:1, 2019. ISSN 10297006. URL http://search.ebscohost.com/login.aspx?direct=true&db=a9h&AN=140492739&site=ehost-live.

Mikhail Luginin, A Fedorova, N Ignatiev, A Trokhimovskiy, A Shakun, A Grigoriev, A Patrakeev, Franck Montmessin, and O Korablev. Properties of water ice and dust particles in the atmosphere of mars during the 2018 global dust storm as inferred from the atmospheric chemistry suite. *Journal of Geophysical Research: Planets*, 125(11):e2020JE006419, 2020.

Mikhail Luginin, Nikolay Ignatiev, Anna Fedorova, Alexander Trokhimovskiy, Alexey Grigoriev, Alexey Shakun, Franck Montmessin, and Oleg Korablev. Observations of CO2 clouds on Mars from TIRVIM and NIR solar occultation measurements onboard TGO. In *EGU General Assembly 2021*, pages EGU21–12721, Online Meeting, Germany, April 2021. doi: 10.5194/egusphere-egu21-12721. URL https://hal-insu.archives-ouvertes.fr/insu-03196491.

S Madronich, S Flocke, J Zeng, I Petropavlovskikh, and J Lee-Taylor. Tropospheric ultraviolet and visible (tuv) radiation model. *National Center for Atmospheric Research (NCAR), Boulder, CO. Home page at: http://www. acd. ucar. edu/TUV*, 2002.

Sasha Madronich and Jack G. Calvert. Permutation reactions of organic peroxy radicals in the troposphere. *Journal of Geophysical Research: Atmospheres*, 95(D5):5697–5715, 1990. doi: https://doi.org/10.1029/JD095iD05p05697. URL https://agupubs.onlinelibrary.wiley.com/doi/abs/10.1029/JD095iD05p05697.

William C. Maguire. Martian isotopic ratios and upper limits for possible minor constituents as derived from mariner 9 infrared spectrometer data. *Icarus*, 32(1):85–97, 1977. ISSN 0019-1035. doi: https://doi.org/10.1016/0019-1035(77)90051-3. URL https://www.sciencedirect.com/science/article/pii/0019103577900513.

Paul R. Mahaffy, Christopher R. Webster, Sushil K. Atreya, Heather Franz, Michael Wong, Pamela G. Conrad, Dan Harpold, John J. Jones, Laurie A. Leshin, Heidi Manning, Tobias Owen, Robert O. Pepin, Steven Squyres, and Melissa Trainer. Abundance and isotopic composition of gases in the martian atmosphere from the curiosity rover. *Science*, 341 (6143):263–266, 2013. ISSN 0036-8075. doi: 10.1126/science.1237966. URL https://science.sciencemag.org/content/341/6143/263.

L. Maltagliati, F. Montmessin, A. Fedorova, O. Korablev, F. Forget, and J.-L. Bertaux. Evidence of water vapor in excess of saturation in the atmosphere of mars. *Science*, 333(6051):1868–1871, 2011. ISSN 0036-8075. doi: 10.1126/science.1207957. URL https://science.sciencemag.org/content/333/6051/1868.

L. Maltagliati, F. Montmessin, O. Korablev, A. Fedorova, F. Forget, A. Määttänen, F. Lefèvre, and J.-L. Bertaux. Annual survey of water vapor vertical distribution and water-aerosol coupling in the martian atmosphere observed by spicam/mex solar occultations. *Icarus*, 223:942–962, April 2013.

J. A. Manion, R. E. Huie, R. D. Levin, D. R. Burgess Jr., V. L. Orkin, W. Tsang, W. S McGivern, J. W Hudgens, V. D Knyazev, D. B Atkinson, E. Chai, A. M Tereza, C. Y. Lin, T. C Allison, W. G Mallard, F. Westley, J. T. Herron, R. F. Hampson, and D. H. Frizzell. Nist chemical kinetics database, nist standard reference database 17, version 7.0 (web version), release 1.6.8. *National Institute of Standards and Technology, Gaithersburg, Maryland, 20899-8320.*, 2015.

Jeffrey J Marlow, Zita Martins, and Mark A Sephton. Mars on earth: soil analogues for future mars missions. *Astronomy & Geophysics*, 49(2):2–20, 2008.

Terry Z Martin. Mass of dust in the martian atmosphere. *Journal of Geophysical Research: Planets*, 100(E4):7509–7512, 1995.

David C McCabe, Tomasz Gierczak, Ranajit K Talukdar, and AR Ravishankara. Kinetics of the reaction oh+ co under atmospheric conditions. *Geophysical research letters*, 28(16): 3135–3138, 2001.

D. J. McCleese, J. T. Schofield, F. W. Taylor, S. B. Calcutt, M. C. Foote, D. M. Kass, C. B. Leovy, D. A. Paige, P. L. Read, and R. W. Zurek. Mars climate sounder: An investigation of thermal and water vapor structure, dust and condensate distributions in the atmosphere, and energy balance of the polar regions. *Journal of Geophysical Research: Planets*, 112(E5), 2007. doi: https://doi.org/10.1029/2006JE002790. URL https://agupubs.onlinelibrary.wiley.com/doi/abs/10.1029/2006JE002790.

D. J. McCleese, N. G. Heavens, J. T. Schofield, W. A. Abdou, J. L. Bandfield, S. B. Calcutt, P. G. J. Irwin, D. M. Kass, A. Kleinböhl, S. R. Lewis, D. A. Paige, P. L. Read, M. I. Richardson, J. H. Shirley, F. W. Taylor, N. Teanby, and R. W. Zurek. Structure and dynamics of the martian lower and middle atmosphere as observed by the mars climate sounder: Seasonal variations in zonal mean temperature, dust, and water ice aerosols. *Journal of Geophysical Research: Planets*, 115(E12), 2010. doi: https://doi.org/10.1029/2010JE003677. URL `https://agupubs.onlinelibrary.wiley.com/doi/abs/10.1029/2010JE003677`.

Michael B. McElroy and Thomas M. Donahue. Stability of the martian atmosphere. *Science*, 177(4053):986–988, 1972. doi: 10.1126/science.177.4053.986.

ESA/ATG Medialab. Trace gas orbiter instruments, Nov 2015. URL `http://www.esa.int/ESA_Multimedia/Images/2015/11/Trace_Gas_Orbiter_instruments`.

L. Menut, R. Vautard, M. Beekmann, and C. Honoré. Sensitivity of photochemical pollution using the adjoint of a simplified chemistry-transport model. *Journal of Geophysical Research: Atmospheres*, 105(D12):15379–15402, 2000. doi: https://doi.org/10.1029/1999JD900953. URL `https://agupubs.onlinelibrary.wiley.com/doi/abs/10.1029/1999JD900953`.

P-Y Meslin, R Gough, Franck Lefèvre, and F Forget. Little variability of methane on mars induced by adsorption in the regolith. *Planetary and Space Science*, 59(2-3):247–258, 2011.

P-Y Meslin, O Gasnault, O Forni, S Schröder, A Cousin, G Berger, SM Clegg, J Lasue, S Maurice, V Sautter, et al. Soil diversity and hydration as observed by chemcam at gale crater, mars. *Science*, 341(6153), 2013.

RE Milliken, JF Mustard, F Poulet, J-P Bibring, Y Langevin, B Gondet, and S Pelkey. The h2o content of the martian surface as seen by mars express omega. In *37th Annual Lunar and Planetary Science Conference*, page 1987, 2006.

E. Millour, F. Forget, A. Spiga, T. Navarro, J. B. Madeleine, L. Montabone, A. Pottier, F. Lefevre, F. Montmessin, J. Y. Chaufray, M. A. Lopez-Valverde, F. Gonzalez-Galindo, S. R. Lewis, P. L. Read, J. P. Huot, M. C. Desjean, and MCD/GCM development Team. The Mars Climate Database (MCD version 5.2). In *European Planetary Science Congress*, pages EPSC2015–438, October 2015.

E. Millour, F. Forget, A. Spiga, M. Vals, V. Zakharov, T. Navarro, L. Montabone, F. Lefèvre, F. Montmessin, J.-Y. Chaufray, M. Lopez-Valverde, F. Gonzalez-Galindo, S. Lewis, P. Read, M.-C. Desjean, and MCD/GCM Development Team. The Mars Climate Database (MCD version 5.3). In *EGU General Assembly Conference Abstracts*, volume 19 of *EGU General Assembly Conference Abstracts*, page 12247, April 2017.

A. Mittelholz, C. L. Johnson, J. M. Feinberg, B. Langlais, and R. J. Phillips. Timing of the martian dynamo: New constraints for a core field 4.5 and 3.7 ga ago. *Science Advances*, 6(18), 2020. doi: 10.1126/sciadv.aba0513. URL https://advances.sciencemag.org/content/6/18/eaba0513.

F. Montmessin, B. Gondet, J. P. Bibring, Y. Langevin, P. Drossart, F. Forget, and T. Fouchet. Hyperspectral imaging of convective CO_2 ice clouds in the equatorial mesosphere of Mars. *Journal of Geophysical Research (Planets)*, 112(E11):E11S90, November 2007. doi: 10.1029/2007JE002944.

Franck Montmessin, Jean-Loup Bertaux, Eric Quémerais, Oleg Korablev, Pascal Rannou, François Forget, Séverine Perrier, Didier Fussen, Sébastien Lebonnois, Aurélie Rébérac, and Emmanuel Dimarellis. Subvisible co2 ice clouds detected in the mesosphere of mars. *Icarus*, 183(2):403–410, 2006. ISSN 0019-1035. doi: https://doi.org/10.1016/j.icarus.2006.03.015. URL https://www.sciencedirect.com/science/article/pii/S0019103506001205.

John E Moores, Raina V Gough, German M Martinez, Pierre-Yves Meslin, Christina L Smith, Sushil K Atreya, Paul R Mahaffy, Claire E Newman, and Christopher R Webster. Methane seasonal cycle at gale crater on mars consistent with regolith adsorption and diffusion. *Nature Geoscience*, 12(5):321–325, 2019a.

John E Moores, Penelope L King, Christina L Smith, German M Martinez, Claire E Newman, Scott D Guzewich, Pierre-Yves Meslin, Christopher R Webster, Paul R Mahaffy, Sushil K Atreya, et al. The methane diurnal variation and microseepage flux at gale crater, mars as constrained by the exomars trace gas orbiter and curiosity observations. *Geophysical Research Letters*, 46(16):9430–9438, 2019b.

Youssef Moudden. Simulated seasonal variations of hydrogen peroxide in the atmosphere of mars. *Planetary and Space Science*, 55(14):2137–2143, 2007.

Brian K. Muirhead, Austin K. Nicholas, Jeffrey Umland, Orson Sutherland, and Sanjay Vijendran. Mars sample return campaign concept status. *Acta Astronautica*, 176:131–138, 2020. ISSN 0094-5765. doi: https://doi.org/10.1016/j.actaastro.2020.06.026. URL https://www.sciencedirect.com/science/article/pii/S0094576520303933.

S. A. Mulenko. Investigation of the recombination of the hco radical in an atmosphere of argon and helium by the method of internal resonator laser spectroscopy. *Journal of Applied Spectroscopy*, 33:688–694, 1980.

S.A. Mulenko. The application of an intracavity laser spectroscopy method for elementary processes study in gas-phase reactions. *Revue Roumaine de Physique*, 1987.

M. J. Mumma, G. L. Villanueva, R. E. Novak, T. Hewagama, B. P. Bonev, M. A. DiSanti, A. M. Mandell, and M. D. Smith. Strong Release of Methane on Mars in Northern Summer 2003. *Science*, 323:1041, February 2009. doi: 10.1126/science.1165243.

M. Nachbar, D. Duft, T. P. Mangan, J. C. Martin, J. M. Plane, and T. Leisner. Laboratory measurements of heterogeneous co2 ice nucleation on nanoparticles under conditions relevant to the martian mesosphere. *Journal of Geophysical Research: Planets*, 121(5): 753–769, 2016. doi: 10.1002/2015JE004978.

Ken Nagashima, Gen Sazaki, Tetsuya Hama, Ken-ichiro Murata, and Yoshinori Furukawa. Uptake mechanism of atmospheric hydrogen chloride gas in ice crystals via hydrochloric acid droplets. *Crystal Growth & Design*, 18(7):4117–4122, 2018.

Hari Nair, Mark Allen, Ariel D Anbar, Yuk L Yung, and R Todd Clancy. A photochemical model of the martian atmosphere. *Icarus*, 111(1):124–150, 1994.

NASA. Possible methane sources and sinks. https://www.nasa.gov/jpl/msl/pia19088, 2018. Accessed: 2018-03-28.

Rafael Navarro-González, Edgar Vargas, Jose de La Rosa, Alejandro C Raga, and Christopher P McKay. Reanalysis of the viking results suggests perchlorate and organics at midlatitudes on mars. *Journal of Geophysical Research: Planets*, 115(E12), 2010.

Marieme Ndour, Barbara D'Anna, Christian George, Oumar Ka, Yves Balkanski, Jörg Kleffmann, Konrad Stemmler, and Markus Ammann. Photoenhanced uptake of no2 on mineral dust: Laboratory experiments and model simulations. *Geophysical Research Letters*, 35(5), 2008.

L. Neary and F. Daerden. The gem-mars general circulation model for mars: Description and evaluation. *Icarus*, 300:458–476, 2018. ISSN 0019-1035. doi: https://doi.org/10.1016/j.icarus.2017.09.028. URL https://www.sciencedirect.com/science/article/pii/S0019103517302270.

L. Neary, F. Daerden, S. Aoki, J. Whiteway, R. T. Clancy, M. Smith, S. Viscardy, J.T. Erwin, I. R. Thomas, G. Villanueva, G. Liuzzi, M. Crismani, M. Wolff, S. R. Lewis, J. A. Holmes, M. R. Patel, M. Giuranna, C. Depiesse, A. Piccialli, S. Robert, L. Trompet, Y. Willame, B. Ristic, and A. C. Vandaele. Explanation for the increase in high-altitude water on mars observed by nomad during the 2018 global dust storm. *Geophysical Research Letters*, 47(7):e2019GL084354, 2020. doi: https://doi.org/10.1029/2019GL084354. URL https://agupubs.onlinelibrary.wiley.com/doi/abs/10.1029/2019GL084354. e2019GL084354 2019GL084354.

Claire E Newman, Stephen R Lewis, Peter L Read, and François Forget. Modeling the martian dust cycle, 1. representations of dust transport processes. *Journal of Geophysical Research: Planets*, 107(E12):6–1, 2002a.

Claire E Newman, Stephen R Lewis, Peter L Read, and François Forget. Modeling the martian dust cycle 2. multiannual radiatively active dust transport simulations. *Journal of Geophysical Research: Planets*, 107(E12):7–1, 2002b.

Jonathan O'Callaghan. Water on mars: Discovery of three buried lakes intrigues scientists. *Nature. https://doi. org/10.1038/d41586-020-02751-1*, 2020.

K. S. Olsen, F. Lefèvre, F. Montmessin, A. Trokhimovskiy, L. Baggio, A. Fedorova, J. Alday, A. Lomakin, D. A. Belyaev, A. Patrakeev, A. Shakun, and O. Korablev. First detection of ozone in the mid-infrared at Mars: implications for methane detection. *Astronomy and Astrophysics*, 639:A141, July 2020. doi: 10.1051/0004-6361/202038125.

K. S. Olsen, A. Trokhimovskiy, L. Montabone, A. A. Fedorova, M. Luginin, F. Lefèvre, O. I. Korablev, F. Montmessin, F. Forget, E. Millour, A. Bierjon, L. Baggio, J. Alday, C. F. Wilson, P. G. J. Irwin, D. A. Belyaev, A. Patrakeev, and A. Shakun. Seasonal reappearance of HCl in the atmosphere of Mars during the Mars year 35 dusty season. *Astronomy and Astrophysics*, 647:A161, March 2021. doi: 10.1051/0004-6361/202140329.

Atsushi Ooki and Mitsuo Uematsu. Chemical interactions between mineral dust particles and acid gases during asian dust events. *Journal of Geophysical Research: Atmospheres*, 110 (D3), 2005.

J. J. Orlando and G. S. Tyndall. The atmospheric chemistry of the hc(o)co radical. *International Journal of Chemical Kinetics*, 33(3):149–156, 2001. doi: 10.1002/1097-4601(200103)33:3<149::AID-KIN1008>3.0.CO;2-1. URL https://onlinelibrary.wiley.com/doi/abs/10.1002/1097-4601%28200103%2933%3A3%3C149%3A%3AAID-KIN1008%3E3.0.CO%3B2-1.

Tobias Owen, K. Biemann, D. R. Rushneck, J. E. Biller, D. W. Howarth, and A. L. Lafleur. The composition of the atmosphere at the surface of mars. *Journal of Geophysical Research (1896-1977)*, 82(28):4635–4639, 1977. doi: https://doi.org/10.1029/JS082i028p04635. URL https://agupubs.onlinelibrary.wiley.com/doi/abs/10.1029/JS082i028p04635.

Vance I Oyama and Bonnie J Berdahl. The viking gas exchange experiment results from chryse and utopia surface samples. *Journal of Geophysical Research*, 82(28):4669–4676, 1977.

Christopher Oze and Mukul Sharma. Have olivine, will gas: Serpentinization and the abiogenic production of methane on mars. *Geophysical Research Letters*, 32(10), 2005. doi: https://doi.org/10.1029/2005GL022691. URL https://agupubs.onlinelibrary.wiley.com/doi/abs/10.1029/2005GL022691.

Christopher Oze, L Camille Jones, Jonas I Goldsmith, and Robert J Rosenbauer. Differentiating biotic from abiotic methane genesis in hydrothermally active planetary surfaces. *Proceedings of the National Academy of Sciences*, 109(25):9750–9754, 2012.

B. P'al, 'A. Kereszturi, F. Forget, and M. Smith. Global seasonal variations of the near-surface relative humidity levels on present-day mars. *Icarus*, 333:481–495, 2019.

TD Parkinson and DM Hunten. Spectroscopy and acronomy of o2 on mars. *Journal of Atmospheric Sciences*, 29(7):1380–1390, 1972.

Manish R Patel, Graham Sellers, J. Mason, James Andrew Holmes, Megan Brown, Stephen Lewis, Kylash Rajendran, Paul Michael Streeter, Charlotte Marriner, and Brijen Hathi. The vertical distribution of ozone in mars years 34-35 from exomars tgo/nomad-uvis observations. *Earth and Space Science Open Archive*, page 35, 2021. doi: 10.1002/essoar.10505984.1. URL https://doi.org/10.1002/essoar.10505984.1.

Nildeep Patel, Richard Slade, and Jim Clemmet. The exomars rover locomotion subsystem. *Journal of Terramechanics*, 47(4):227–242, 2010. ISSN 0022-4898. doi: https://doi.org/10.1016/j.jterra.2010.02.004. URL https://www.sciencedirect.com/science/article/pii/S0022489810000182.

F. Paulot, D. K. Henze, and P. O. Wennberg. Impact of the isoprene photochemical cascade on tropical ozone. *Atmospheric Chemistry and Physics*, 12(3):1307–1325, 2012. doi: 10.5194/acp-12-1307-2012. URL https://acp.copernicus.org/articles/12/1307/2012/.

John C. Pearl, Michael D. Smith, Barney J. Conrath, Joshua L. Bandfield, and Philip R. Christensen. Observations of martian ice clouds by the mars global surveyor thermal emission spectrometer: The first martian year. *Journal of Geophysical Research: Planets*, 106(E6):12325–12338, 2001. doi: https://doi.org/10.1029/1999JE001233. URL https://agupubs.onlinelibrary.wiley.com/doi/abs/10.1029/1999JE001233.

Howard Perko, John Nelson, and Jacklyn Green. Mars soil mechanical properties and suitability of mars soil simulants. *Journal of Aerospace Engineering - J AEROSP ENG*, 19, 07 2006. doi: 10.1061/(ASCE)0893-1321(2006)19:3(169).

Séverine Perrier, Jean-Loup Bertaux, Franck Lefèvre, Sébastien Lebonnois, Oleg Korablev, Anna Fedorova, and Franck Montmessin. Global distribution of total ozone on mars from spicam/mex uv measurements. *Journal of Geophysical Research: Planets*, 111(E9), 2006.

Roger J. Phillips, Brian J. Davis, Kenneth L. Tanaka, Shane Byrne, Michael T. Mellon, Nathaniel E. Putzig, Robert M. Haberle, Melinda A. Kahre, Bruce A. Campbell, Lynn M. Carter, Isaac B. Smith, John W. Holt, Suzanne E. Smrekar, Daniel C. Nunes, Jeffrey J. Plaut, Anthony F. Egan, Timothy N. Titus, and Roberto Seu. Massive co2 ice deposits sequestered in the south polar layered deposits of mars. *Science*, 332(6031):838–841, 2011. ISSN 0036-8075. doi: 10.1126/science.1203091. URL https://science.sciencemag.org/content/332/6031/838.

Jeffrey J. Plaut, Giovanni Picardi, Ali Safaeinili, Anton B. Ivanov, Sarah M. Milkovich, Andrea Cicchetti, Wlodek Kofman, Jérémie Mouginot, William M. Farrell, Roger J. Phillips, Stephen M. Clifford, Alessandro Frigeri, Roberto Orosei, Costanzo Federico, Iwan P. Williams, Donald A. Gurnett, Erling Nielsen, Tor Hagfors, Essam Heggy, Ellen R. Stofan, Dirk Plettemeier, Thomas R. Watters, Carlton J. Leuschen, and Peter Edenhofer. Subsurface radar sounding of the south polar layered deposits of mars. *Science*, 316(5821):92–95, 2007. doi: 10.1126/science.1139672.

James B Pollack, Robert M Haberle, James Schaeffer, and Hilda Lee. Simulations of the general circulation of the martian atmosphere: 1. polar processes. *Journal of Geophysical Research: Solid Earth*, 95(B2):1447–1473, 1990.

James B Pollack, Robert M Haberle, James R Murphy, James Schaeffer, and Hilda Lee. Simulations of the general circulation of the martian atmosphere: 2. seasonal pressure variations. *Journal of Geophysical Research: Planets*, 98(E2):3149–3181, 1993.

G. L. Pratt and S. W. Wood. Kinetics of the reaction of methyl radicals with oxygen. *J. Chem. Soc., Faraday Trans. 1*, 80:3419–3427, 1984. doi: 10.1039/F19848003419. URL `http://dx.doi.org/10.1039/F19848003419`.

Montreal Protocol. Montreal protocol on substances that deplete the ozone layer. *Washington, DC: US Government Printing Office*, 26:128–136, 1987.

Jianqi Qin. Mars upper atmospheric temperature and atomic oxygen density derived from the o i 130.4 nm emission observed by NASA's MAVEN mission. *The Astronomical Journal*, 159(5):206, apr 2020. doi: 10.3847/1538-3881/ab7fae. URL `https://doi.org/10.3847/1538-3881/ab7fae`.

B. Ritter, J.-C. Gérard, L. Gkouvelis, B. Hubert, S.K. Jain, and N.M. Schneider. Characteristics of mars uv dayglow emissions from atomic oxygen at 130.4 and 135.6 nm: Maven/iuvs limb observations and modeling. *Journal of Geophysical Research: Space Physics*, 124(6): 4809–4832, 2019. doi: https://doi.org/10.1029/2019JA026669. URL `https://agupubs.onlinelibrary.wiley.com/doi/abs/10.1029/2019JA026669`.

S. Robert and Vandaele et. al. Expected performances of the NOMAD/ExoMars instrument. 124:94–104, May 2016. doi: 10.1016/j.pss.2016.03.003.

R Rodrigo, E García Álvarez, MJ López González, and MA López Valverde. Estimates of eddy diffusion coefficient in the mars' atmosphere. *Atmosfera*, 3(1), 2009.

B. M. Rosner and B. Schink. Purification and characterization of acetylene hydratase of pelobacter acetylenicus, a tungsten iron-sulfur protein. *Journal of bacteriology*, 177:5767–72, 11 1995. doi: 10.1128/jb.177.20.5767-5772.1995.

Laurence S Rothman, Iouli E Gordon, Alain Barbe, D Chris Benner, Peter F Bernath, Manfred Birk, Vincent Boudon, Linda R Brown, Alain Campargue, and J-P Champion. The hitran 2008 molecular spectroscopic database. *Journal of Quantitative Spectroscopy and Radiative Transfer*, 110(9-10):533–572, 2009.

Ronald Saltinski. Biologists look at the planet mars. *The American Biology Teacher*, 33 (9):521–525, 1971. ISSN 00027685, 19384211. URL http://www.jstor.org/stable/4443690.

B.R. Sandel, H. Gröller, R.V. Yelle, T. Koskinen, N.K. Lewis, J.-L. Bertaux, F. Montmessin, and E. Quémerais. Altitude profiles of o2 on mars from spicam stellar occultations. *Icarus*, 252: 154–160, 2015. ISSN 0019-1035. doi: https://doi.org/10.1016/j.icarus.2015.01.004. URL https://www.sciencedirect.com/science/article/pii/S001910351500010X.

R. Sander, P. Jöckel, O. Kirner, A. Kunert, J. Landgraf, A. Pozzer, and O. Kirner. The photolysis module jval-14, compatible with the messy standard, and the jval preprocessor (jvpp). *Geoscientific Model Development*, 7:2653–2662, 11 2014. doi: 10.5194/gmd-7-2653-2014.

R. Sander, A. Baumgaertner, D. Cabrera-Perez, F. Frank, S. Gromov, J.-U. Grooß, H. Harder, V. Huijnen, P. Jöckel, V. A. Karydis, K. E. Niemeyer, A. Pozzer, H. Riede, M. G. Schultz, D. Taraborrelli, and S. Tauer. The community atmospheric chemistry box model caaba/mecca-4.0. *Geoscientific Model Development*, 12(4):1365–1385, 2019. doi: 10.5194/gmd-12-1365-2019. URL https://gmd.copernicus.org/articles/12/1365/2019/.

S. P. Sander, R. R. Friedl, A. R. Ravishankara, D. M. Golden, C. E. Kolb, M. J. Kurylo, M. J. Molina, G. K. Moortgat, H. Keller-Rudek, B. J.Finlayson-Pitts, P. H. Wine, R. E. Huie, and V. L. Orkin. Chemical kinetics and photochemical data for use in atmospheric studies, evaluation number 17. *NASA JPL Publication*, 2011.

S. P. Sander, R. R. Friedl, A. R. Ravishankara, D. M. Golden, C. E. Kolb, M. J. Kurylo, M. J. Molina, G. K. Moortgat, H. Keller-Rudek, B. J.Finlayson-Pitts, P. H. Wine, R. E. Huie, and V. L. Orkin. Chemical kinetics and photochemical data for use in atmospheric studies, evaluation number 18. *NASA JPL Publication*, 2015.

Michelle L Santee and David Crisp. Diagnostic calculations of the circulation in the martian atmosphere. *Journal of Geophysical Research: Planets*, 100(E3):5465–5484, 1995.

Marielle Saunois, Ann R. Stavert, Ben Poulter, Philippe Bousquet, Josep G. Canadell, Robert B. Jackson, Peter A. Raymond, Edward J. Dlugokencky, Sander Houweling, Prabir K. Patra, Philippe Ciais, Vivek K. Arora, David Bastviken, Peter Bergamaschi, Donald R. Blake, Gordon Brailsford, Lori Bruhwiler, Kimberly M. Carlson, Mark Carrol, Simona Castaldi, Naveen Chandra, Cyril Crevoisier, Patrick M. Crill, Kristofer Covey,

Charles L. Curry, Giuseppe Etiope, Christian Frankenberg, Nicola Gedney, Michaela I. Hegglin, Lena Höglund-Isaksson, Gustaf Hugelius, Misa Ishizawa, Akihiko Ito, Greet Janssens-Maenhout, Katherine M. Jensen, Fortunat Joos, Thomas Kleinen, Paul B. Krummel, Ray L. Langenfelds, Goulven G. Laruelle, Licheng Liu, Toshinobu Machida, Shamil Maksyutov, Kyle C. McDonald, Joe McNorton, Paul A. Miller, Joe R. Melton, Isamu Morino, Jurek Müller, Fabiola Murguia-Flores, Vaishali Naik, Yosuke Niwa, Sergio Noce, Simon O'Doherty, Robert J. Parker, Changhui Peng, Shushi Peng, Glen P. Peters, Catherine Prigent, Ronald Prinn, Michel Ramonet, Pierre Regnier, William J. Riley, Judith A. Rosentreter, Arjo Segers, Isobel J. Simpson, Hao Shi, Steven J. Smith, L. Paul Steele, Brett F. Thornton, Hanqin Tian, Yasunori Tohjima, Francesco N. Tubiello, Aki Tsuruta, Nicolas Viovy, Apostolos Voulgarakis, Thomas S. Weber, Michiel van Weele, Guido R. van der Werf, Ray F. Weiss, Doug Worthy, Debra Wunch, Yi Yin, Yukio Yoshida, Wenxin Zhang, Zhen Zhang, Yuanhong Zhao, Bo Zheng, Qing Zhu, Qiuan Zhu, and Qianlai Zhuang. The Global Methane Budget 2000-2017. *Earth System Science Data*, 12(3):1561–1623, July 2020. doi: 10.5194/essd-12-1561-2020.

Hauke Schmidt and Daniel Martin. Adjoint sensitivity of episodic ozone in the paris area to emissions on the continental scale. *Journal of Geophysical Research: Atmospheres*, 108(D17), 2003. doi: https://doi.org/10.1029/2001JD001583. URL `https://agupubs.onlinelibrary.wiley.com/doi/abs/10.1029/2001JD001583`.

Jennifer Schuttlefield, Gayan Rubasinghege, Mohamed El-Maazawi, Jason Bone, and Vicki H Grassian. Photochemistry of adsorbed nitrate. *Journal of the American Chemical Society*, 130(37):12210–12211, 2008.

Jens Sehested, Ole John Nielsen, Helge Egsgaard, Niels Wessel Larsen, Thorvald Pedersen, Lene Krogh Christensen, and Mette Wiegell. First direct kinetic study of isotopic enrichment of ozone. *Journal of Geophysical Research: Atmospheres*, 100(D10):20979–20982, 1995.

Mayumi Seto, Katsuyuki Noguchi, and Philippe Van Cappellen. Potential for aerobic methanotrophic metabolism on mars. *Astrobiology*, 19(10):1187–1195, 2019.

Tatsuo Shimazaki. A model of temporal variations in ozone density in the martian atmosphere. *Planetary and Space Science*, 29(1):21–33, 1981.

Tatsuo Shimazaki and Mikio Shimizu. The seasonal variation of ozone density in the martian atmosphere. *Journal of Geophysical Research: Space Physics*, 84(A4):1269–1276, 1979.

Steven F Sholes, Joshua Krissansen-Totton, and David C Catling. A maximum subsurface biomass on mars from untapped free energy: Co and h2 as potential antibiosignatures. *Astrobiology*, 19(5):655–668, 2019.

G Sindoni, V Formisano, and A Geminale. Observations of water vapour and carbon monoxide in the martian atmosphere with the swc of pfs/mex. *Planetary and Space Science*, 59(2-3): 149–162, 2011.

Navita Sinha, Sudip Nepal, Timothy Kral, and Pradeep Kumar. Survivability and growth kinetics of methanogenic archaea at various phs and pressures: Implications for deep subsurface life on mars. *Planetary and Space Science*, 136:15–24, 2017. ISSN 0032-0633. doi: https://doi.org/10.1016/j.pss.2016.11.012. URL https://www.sciencedirect.com/science/article/pii/S003206331630441X.

David E. Smith, Maria T. Zuber, Herbert V. Frey, James B. Garvin, James W. Head, Duane O. Muhleman, Gordon H. Pettengill, Roger J. Phillips, Sean C. Solomon, H. Jay Zwally, W. Bruce Banerdt, Thomas C. Duxbury, Matthew P. Golombek, Frank G. Lemoine, Gregory A. Neumann, David D. Rowlands, Oded Aharonson, Peter G. Ford, Anton B. Ivanov, Catherine L. Johnson, Patrick J. McGovern, James B. Abshire, Robert S. Afzal, and Xiaoli Sun. Mars Orbiter Laser Altimeter: Experiment summary after the first year of global mapping of Mars. *Journal of Geophysical Research*, 106(E10):23689–23722, October 2001. doi: 10.1029/2000JE001364.

M. D. Smith, M. J. Wolff, R. T. Clancy, and S. L. Murchie. Compact Reconnaissance Imaging Spectrometer observations of water vapor and carbon monoxide. *Journal of Geophysical Research (Planets)*, 114:E00D03, June 2009. doi: 10.1029/2008JE003288.

Michael D. Smith. The annual cycle of water vapor on mars as observed by the thermal emission spectrometer. *Journal of Geophysical Research: Planets*, 107(E11):25–1–25–19, 2002. doi: https://doi.org/10.1029/2001JE001522. URL https://agupubs.onlinelibrary.wiley.com/doi/abs/10.1029/2001JE001522.

Michael D Smith. Interannual variability in tes atmospheric observations of mars during 1999–2003. *Icarus*, 167(1):148–165, 2004.

Michael D. Smith, Frank Daerden, Lori Neary, and Alain Khayat. The climatology of carbon monoxide and water vapor on mars as observed by crism and modeled by the gem-mars general circulation model. *Icarus*, 301:117–131, 2018. ISSN 0019-1035. doi: https://doi.org/10.1016/j.icarus.2017.09.027. URL https://www.sciencedirect.com/science/article/pii/S0019103517303500.

Michael D. Smith, Frank Daerden, Lori Neary, Alain S.J. Khayat, James A. Holmes, Manish R. Patel, Geronimo Villanueva, Giuliano Liuzzi, Ian R. Thomas, Bojan Ristic, Giancarlo Bellucci, Jose Juan Lopez-Moreno, and Ann Carine Vandaele. The climatology of carbon monoxide on mars as observed by nomad nadir-geometry observations. *Icarus*, 362: 114404, 2021. ISSN 0019-1035. doi: https://doi.org/10.1016/j.icarus.2021.114404. URL https://www.sciencedirect.com/science/article/pii/S0019103521000919.

P. H. Smith, III Bell, J. F., N. T. Bridges, D. T. Britt, L. Gaddis, R. Greeley, H. U. Keller, K. E. Herkenhoff, R. Jaumann, J. R. Johnson, R. L. Kirk, M. Lemmon, J. N. Maki, M. C. Malin, S. L. Murchie, J. Oberst, T. J. Parker, R. J. Reid, R. Sablotny, L. A. Soderblom, C. Stoker, R. Sullivan, N. Thomas, M. G. Tomasko, W. Ward, and E. Wegryn. Results from the Mars Pathfinder Camera. *Science*, 278:1758, December 1997. doi: 10.1126/science.278.5344.1758.

Susan Solomon, Doug Kinnison, Justin Bandoro, Rolando Garcia, et al. Simulation of polar ozone depletion: An update. *Journal of Geophysical Research: Atmospheres*, 120(15): 7958–7974, 2015. doi: https://doi.org/10.1002/2015JD023365. URL `https://agupubs.onlinelibrary.wiley.com/doi/abs/10.1002/2015JD023365`.

N. Spanovich, M.D. Smith, P.H. Smith, M.J. Wolff, P.R. Christensen, and S.W. Squyres. Surface and near-surface atmospheric temperatures for the mars exploration rover landing sites. *Icarus*, 180(2):314–320, 2006. ISSN 0019-1035. doi: https://doi.org/10.1016/j.icarus.2005.09.014. URL `https://www.sciencedirect.com/science/article/pii/S0019103505003313`.

A. Stcherbinine, M. Vincendon, F. Montmessin, M. J. Wolff, O. Korablev, A. Fedorova, A. Trokhimovskiy, A. Patrakeev, G. Lacombe, L. Baggio, and A. Shakun. Martian water ice clouds during the 2018 global dust storm as observed by the acs-mir channel onboard the trace gas orbiter. *Journal of Geophysical Research: Planets*, 125(3):e2019JE006300, 2020. doi: https://doi.org/10.1029/2019JE006300. URL `https://agupubs.onlinelibrary.wiley.com/doi/abs/10.1029/2019JE006300`. e2019JE006300 10.1029/2019JE006300.

Liam J Steele, Stephen R Lewis, Manish R Patel, Franck Montmessin, François Forget, and Michael D Smith. The seasonal cycle of water vapour on mars from assimilation of thermal emission spectrometer data. *Icarus*, 237:97–115, 2014.

Adam H Stevens, Manish R Patel, and Stephen R Lewis. Modelled isotopic fractionation and transient diffusive release of methane from potential subsurface sources on mars. *Icarus*, 281:240–247, 2017.

Shane W Stone, Roger V Yelle, Mehdi Benna, Daniel Y Lo, Meredith K Elrod, and Paul R Mahaffy. Hydrogen escape from mars is driven by seasonal and dust storm transport of water. *Science*, 370(6518):824–831, 2020.

RC Sullivan, SA Guazzotti, DA Sodeman, and KA Prather. Direct observations of the atmospheric processing of asian mineral dust. *Atmospheric Chemistry and Physics*, 7(5): 1213–1236, 2007.

Ryan C. Sullivan, Sergio A. Guazzotti, David A. Sodeman, Youhua Tang, Gregory R. Carmichael, and Kimberly A. Prather. Mineral dust is a sink for chlorine in the marine boundary layer. *Atmospheric Environment*, 41(34):7166–7179, January 2007. doi: 10.1016/j.atmosenv.2007.05.047.

Walter Sullivan. 2 gases associated with life found on mars near polar cap; 2 gases associated with life are found on mars. *The New York Times*, page 1–1, Aug 1969. URL https://www.nytimes.com/1969/08/08/archives/2-gases-associated-with-life-found-on-mars-near-polar-cap-2-gases.html.

Michael E Summers, B Joseph Lieb, Emily Chapman, and Yuk L Yung. Atmospheric biomarkers of subsurface life on mars. *Geophysical Research Letters*, 29(24):24–1, 2002.

A. Sánchez-Lavega, T. del Río-Gaztelurrutia, J. Hernández-Bernal, and M. Delcroix. The onset and growth of the 2018 martian global dust storm. *Geophysical Research Letters*, 46(11):6101–6108, 2019. doi: https://doi.org/10.1029/2019GL083207. URL https://agupubs.onlinelibrary.wiley.com/doi/abs/10.1029/2019GL083207.

Mingjin Tang, Xin Huang, Keding Lu, Maofa Ge, Yongjie Li, Peng Cheng, Tong Zhu, Aijun Ding, Yuanhang Zhang, Sasho Gligorovski, et al. Heterogeneous reactions of mineral dust aerosol: implications for tropospheric oxidation capacity. *Atmospheric Chemistry and Physics*, 17(19):11727–11777, 2017.

D. Taraborrelli. *Isoprene oxidation and its impacts on the atmospheric composition*. PhD thesis, Johannes Gutenberg-Universität, Mainz, Germany, 2010. URL http://d-nb.info/1003538770/34.

Benjamin M. Taysum and Paul I. Palmer. Photochemistry of methane and ethane in the martian atmosphere. *Journal of Geophysical Research: Planets*, 125 (6):e2020JE006491, 2020. doi: https://doi.org/10.1029/2020JE006491. URL https://agupubs.onlinelibrary.wiley.com/doi/abs/10.1029/2020JE006491. e2020JE006491 10.1029/2020JE006491.

I. R. Thomas, A. C. Vandaele, and et. al Neefs. The ExoMars 2016 Trace Gas Orbiter NOMAD Spectrometer Suite for Nadir, Limb and Solar Occultation Measurements of Mars' Atmosphere. *AGU Fall Meeting Abstracts*, December 2016.

Xiaoxu Tian and Xiaolei Zou. Development of the tangent linear and adjoint models of the mpas-atmosphere dynamic core and applications in adjoint relative sensitivity studies. *Tellus A: Dynamic Meteorology and Oceanography*, 72(1):1–17, 2020.

Claudia Timmreck. Modeling the climatic effects of large explosive volcanic eruptions. *Wiley Interdisciplinary Reviews: Climate Change*, 3(6):545–564, 2012.

R. Todd Clancy, Brad J. Sandor, Antonio García-Muñoz, Franck Lefèvre, Michael D. Smith, Michael J. Wolff, Franck Montmessin, Scott L. Murchie, and Hari Nair. First detection of mars atmospheric hydroxyl: Crism near-ir measurement versus lmd gcm simulation of oh meinel band emission in the mars polar winter atmosphere. *Icarus*, 226(1):272–281, 2013. ISSN 0019-1035. doi: https://doi.org/10.1016/j.icarus.2013.05.035. URL https://www.sciencedirect.com/science/article/pii/S0019103513002352.

Melissa G Trainer, Michael H Wong, Timothy H McConnochie, Heather B Franz, Sushil K Atreya, Pamela G Conrad, Franck Lefèvre, Paul R Mahaffy, Charles A Malespin, and Heidi LK Manning. Seasonal variations in atmospheric composition as measured in gale crater, mars. *Journal of Geophysical Research: Planets*, 124(11):3000–3024, 2019.

JT Trauger and JI Lunine. Spectroscopy of molecular oxygen in the atmospheres of venus and mars. *Icarus*, 55(2):272–281, 1983.

A. Trokhimovskiy and O. et al. Korablev. Atmospheric Chemistry Suite (ACS): a set of Infrared Spectrometers for Atmospheric Measurements on Board ExoMars Trace Gas Orbiter. In F. Forget and M. Millour, editors, *Mars Atmosphere: Modelling and Observation, 5th International Workshop*, page 4402, January 2014.

Alexander Trokhimovskiy, Anna Fedorova, Oleg Korablev, Franck Montmessin, Jean-Loup Bertaux, Alexander Rodin, and Michael D. Smith. Mars' water vapor mapping by the spicam ir spectrometer: Five martian years of observations. *Icarus*, 251:50–64, 2015a. ISSN 0019-1035. doi: https://doi.org/10.1016/j.icarus.2014.10.007. URL https://www.sciencedirect.com/science/article/pii/S0019103514005466. Dynamic Mars.

Alexander Trokhimovskiy, Oleg Korablev, Yurii K. Kalinnikov, Anna Fedorova, Alexander V. Stepanov, Andrei Yu. Titov, Ilia Dziuban, Andrei Patrakeev, and Franck Montmessin. Near-infrared echelle-AOTF spectrometer ACS-NIR for the ExoMars Trace Gas Orbiter. In Marija Strojnik Scholl and Gonzalo Páez, editors, *Infrared Remote Sensing and Instrumentation XXIII*, volume 9608, pages 62 – 70. International Society for Optics and Photonics, SPIE, 2015b. doi: 10.1117/12.2190369. URL https://doi.org/10.1117/12.2190369.

W. Tsang and R. F. Hampson. Chemical kinetic data base for combustion chemistry. part i. methane and related compounds. *Journal of Physical and Chemical Reference Data*, 15 (3):1087–1279, 1986.

M Tschimmel, NI Ignatiev, DV Titov, E Lellouch, T Fouchet, M Giuranna, and V Formisano. Investigation of water vapor on mars with pfs/sw of mars express. *Icarus*, 195(2):557–575, 2008.

GM Underwood, CH Song, M Phadnis, GR Carmichael, and VH Grassian. Heterogeneous reactions of no2 and hno3 on oxides and mineral dust: A combined laboratory and modeling study. *Journal of Geophysical Research: Atmospheres*, 106(D16):18055–18066, 2001.

J Vago, O Witasse, H Svedhem, P Baglioni, A Haldemann, G Gianfiglio, T Blancquaert, D McCoy, and R de Groot. Esa exomars program: the next step in exploring mars. *Solar System Research*, 49(7):518–528, 2015.

Jorge Vago, Bruno Gardini, Gerhard Kminek, Pietro Baglioni, Giacinto Gianfiglio, Andrea Santovincenzo, Silvia Bayón, and Michel van Winnendael. ExoMars - searching for life on the Red Planet. *ESA Bulletin*, 126:16–23, May 2006.

A. C. Vandaele, M. De Mazière, R. Drummond, A. Mahieux, E. Neefs, V. Wilquet, O. Korablev, A. Fedorova, D. Belyaev, F. Montmessin, and J.-L. Bertaux. Composition of the venus mesosphere measured by solar occultation at infrared on board venus express. *Journal of Geophysical Research: Planets*, 113(E5), 2008. doi: https://doi.org/10.1029/2008JE003140. URL https://agupubs.onlinelibrary.wiley.com/doi/abs/10.1029/2008JE003140.

A. C. R. Vandaele and J. Rodriguez-Gomez. NOMAD, a spectrometer suite for nadir and solar occultation observations on the ExoMars Trace Gas Orbiter. *European Planetary Science Congress*, 8:EPSC2013-175, September 2013.

A.C. Vandaele, E. Neefs, R. Drummond, I.R. Thomas, F. Daerden, J.-J. Lopez-Moreno, J. Rodriguez, M.R. Patel, G. Bellucci, M. Allen, F. Altieri, D. Bolsée, T. Clancy, S. Delanoye, C. Depiesse, E. Cloutis, A. Fedorova, V. Formisano, B. Funke, D. Fussen, A. Geminale, J.-C. Gérard, M. Giuranna, N. Ignatiev, J. Kaminski, O. Karatekin, F. Lefèvre, M. López-Puertas, M. López-Valverde, A. Mahieux, J. McConnell, M. Mumma, L. Neary, E. Renotte, B. Ristic, S. Robert, M. Smith, S. Trokhimovsky, J. Vander Auwera, G. Villanueva, J. Whiteway, V. Wilquet, and M. Wolff. Science objectives and performances of nomad, a spectrometer suite for the exomars tgo mission. *Planetary and Space Science*, 119:233–249, 2015. ISSN 0032-0633. doi: https://doi.org/10.1016/j.pss.2015.10.003. URL https://www.sciencedirect.com/science/article/pii/S0032063315003025.

Ann Carine Vandaele, J-J Lopez-Moreno, Manish R Patel, Giancarlo Bellucci, F Daerden, B Ristic, Séverine Robert, IR Thomas, Valérie Wilquet, M Allen, et al. Nomad, an integrated suite of three spectrometers for the exomars trace gas mission: Technical description, science objectives and expected performance. *Space Science Reviews*, 214(5):1–47, 2018.

Ann Carine Vandaele, Oleg Korablev, Frank Daerden, Shohei Aoki, Ian R Thomas, Francesca Altieri, Miguel López-Valverde, Geronimo Villanueva, Giuliano Liuzzi, Michael D Smith, et al. Martian dust storm impact on atmospheric h 2 o and d/h observed by exomars trace gas orbiter. *Nature*, 568(7753):521–525, 2019.

Geronimo L. Villanueva, Giuliano Liuzzi, Matteo J. Crismani, Shohei Aoki, Ann-Carine Vandaele, Michael J. Mumma, Michael D. Smith, Frank Daerden, Lori Neary, Sebastien Viscardy, Ian R. Thomas, Miguel Angel Lopez-Valderde, Bojan Ristic, Manish R. Patel, James H. Holmes, Giancarlo Bellucci, and Juan Lopez-Moreno. Strong seasonal and diurnal variability of water D/H on Mars as revealed with ExoMars/NOMAD. In *EPSC-DPS Joint Meeting 2019*, volume 2019, pages EPSC–DPS2019–725, September 2019.

Geronimo L. Villanueva, Giuliano Liuzzi, Matteo M. J. Crismani, Shohei Aoki, Ann Carine Vandaele, Frank Daerden, Michael D. Smith, Michael J. Mumma, Elise W. Knutsen, Lori Neary, Sebastien Viscardy, Ian R. Thomas, Miguel Angel Lopez-Valverde, Bojan Ristic, Manish R. Patel, James A. Holmes, Giancarlo Bellucci, and Jose Juan Lopez-Moreno. Water heavily fractionated as it ascends on mars as revealed by exomars/nomad. *Science Advances*, 7(7), 2021. doi: 10.1126/sciadv.abc8843. URL https://advances.sciencemag.org/content/7/7/eabc8843.

G.L. Villanueva, M.J. Mumma, R.E. Novak, Y.L. Radeva, H.U. Käufl, A. Smette, A. Tokunaga, A. Khayat, T. Encrenaz, and P. Hartogh. A sensitive search for organics (ch4, ch3oh, h2co, c2h6, c2h2, c2h4), hydroperoxyl (ho2), nitrogen compounds (n2o, nh3, hcn) and chlorine species (hcl, ch3cl) on mars using ground-based high-resolution infrared spectroscopy. *Icarus*, 223(1):11–27, 2013. ISSN 0019-1035. doi: https://doi.org/10.1016/j.icarus.2012.11.013. URL https://www.sciencedirect.com/science/article/pii/S0019103512004599.

Roland von Glasow. Atmospheric chemistry in volcanic plumes. *Proceedings of the National Academy of Sciences*, 107(15):6594–6599, 2010.

M. Wall. Methane-sniffing orbiter finishes 'aerobraking' dives through mars' atmosphere. *Space.com*, 2018.

Alian Wang, Yuanchao Yan, Bradley L Jolliff, Scott M McLennan, Kun Wang, Erbin Shi, and William M Farrell. Chlorine release from common chlorides by martian dust activity. *Journal of Geophysical Research: Planets*, 125(6):e2019JE006283, 2020.

Shuhui Wang, Ralf Ackermann, Chester W Spicer, Jerome D Fast, Martina Schmeling, and Jochen Stutz. Atmospheric observations of enhanced no2-hono conversion on mineral dust particles. *Geophysical research letters*, 30(11), 2003.

C. R. Webster, P. R. Mahaffy, S. K. Atreya, and G. Flesch. Mars Methane Detection and Variability at Gale Crater Measured by the TLS instrument in SAM on the Curiosity Rover. *AGU Fall Meeting Abstracts*, December 2015.

Chris R. Webster, Paul R. Mahaffy, Gregory J. Flesch, Paul B. Niles, John H. Jones, Laurie A. Leshin, Sushil K. Atreya, Jennifer C. Stern, Lance E. Christensen, Tobias Owen, Heather Franz, Robert O. Pepin, and Andrew Steele. Isotope Ratios of H, C, and O in CO_2 and H_2O of the Martian Atmosphere. *Science*, 341(6143):260–263, July 2013. doi: 10.1126/science.1237961.

Christopher R Webster, Paul R Mahaffy, Sushil K Atreya, Gregory J Flesch, and Kenneth A Farley. Low upper limit to methane abundance on mars. *Science*, 342(6156):355–357, 2013.

Christopher R Webster, Paul R Mahaffy, Sushil K Atreya, John E Moores, Gregory J Flesch, Charles Malespin, Christopher P McKay, German Martinez, Christina L Smith, and Javier Martin-Torres. Background levels of methane in mars' atmosphere show strong seasonal variations. *Science*, 360(6393):1093–1096, 2018.

Benjamin P Weiss, Yuk L Yung, and Kenneth H Nealson. Atmospheric energy for subsurface life on mars? *Proceedings of the National Academy of Sciences*, 97(4):1395–1399, 2000.

J. A. Whiteway, L. Komguem, C. Dickinson, C. Cook, M. Illnicki, J. Seabrook, V. Popovici, T. J. Duck, R. Davy, P. A. Taylor, J. Pathak, D. Fisher, A. I. Carswell, M. Daly, V. Hipkin, A. P. Zent, M. H. Hecht, S. E. Wood, L. K. Tamppari, N. Renno, J. E. Moores, M. T. Lemmon, F. Daerden, and P. H. Smith. Mars water-ice clouds and precipitation. *Science*, 325(5936):68–70, 2009. ISSN 0036-8075. doi: 10.1126/science.1172344. URL https://science.sciencemag.org/content/325/5936/68.

Y Willame, AC Vandaele, C Depiesse, Franck Lefèvre, V Letocart, D Gillotay, and Franck Montmessin. Retrieving cloud, dust and ozone abundances in the martian atmosphere using spicam/uv nadir spectra. *Planetary and space science*, 142:9–25, 2017.

R. John Wilson, Stephen R. Lewis, Luca Montabone, and Michael D. Smith. Influence of water ice clouds on martian tropical atmospheric temperatures. *Geophysical Research Letters*, 35(7), 2008. doi: https://doi.org/10.1029/2007GL032405. URL https://agupubs.onlinelibrary.wiley.com/doi/abs/10.1029/2007GL032405.

Paulina Wolkenberg, Michael D Smith, Vittorio Formisano, and Giuseppe Sindoni. Comparison of pfs and tes observations of temperature and water vapor in the martian atmosphere. *Icarus*, 215(2):628–638, 2011.

A. S. Wong and S. K. Atreya. Atmospheric photochemistry above possible martian hot spots. *Advances in Space Research*, 33(12):2236 – 2239, 2004. ISSN 0273-1177. doi: https://doi.org/10.1016/S0273-1177(03)00524-6. URL http://www.sciencedirect.com/science/article/pii/S0273117703005246. Mercury, Mars and Saturn.

Ah-San Wong, Sushil K Atreya, and Thérèse Encrenaz. Chemical markers of possible hot spots on mars. *Journal of Geophysical Research: Planets*, 108(E4), 2003.

Stephen E Wood and David A Paige. Modeling the martian seasonal co2 cycle 1. fitting the viking lander pressure curves. *Icarus*, 99(1):1–14, 1992.

Weiyu Yang and Ionel Michael Navon. *Documentation of the Tangent Linear Model and Its Adjoint of the Adiabatic Version of the NASA GEOS-1 C-Grid GCM, Version 5.2*. National Aeronautics and Space Administration, Goddard Space Flight Center . . . , 1996.

Paul J Young, Anna B Harper, Chris Huntingford, Nigel D Paul, Olaf Morgenstern, Paul A Newman, Luke D Oman, Sasha Madronich, and Rolando R Garcia. The montreal protocol protects the terrestrial carbon sink. *Nature*, 596(7872):384–388, 2021.

Yuk L. Yung and W.B. Demore. Photochemistry of the stratosphere of venus: Implications for atmospheric evolution. *Icarus*, 51(2):199–247, 1982. ISSN 0019-1035. doi: https://doi.org/10.1016/0019-1035(82)90080-X. URL `https://www.sciencedirect.com/science/article/pii/001910358290080X`.

Yuk L Yung, Jun-Shan Wen, Joseph P Pinto, Mark Allen, Kathryn K Pierce, and Suzanne Paulson. Hdo in the martian atmosphere: Implications for the abundance of crustal water. *Icarus*, 76(1):146–159, 1988.

Kevin Zahnle. Play it again, sam. *Science*, 347(6220):370–371, 2015.

Kevin Zahnle, Richard S Freedman, and David C Catling. Is there methane on mars? *Icarus*, 212(2):493–503, 2011.

Xin Zhang, Xiang-Yu Huang, and Ning Pan. Development of the upgraded tangent linear and adjoint of the weather research and forecasting (wrf) model. *Journal of Atmospheric and Oceanic Technology*, 30(6):1180–1188, 2013.